MEASUREMENTS OF DIFFUSION COEFFICIENTS FOR RUBIDIUM ATOMS IN INERT GAS MIXTURES USING COHERENT SCATTERING FROM OPTICALLY PUMPED POPULATION GRATINGS

ALEXANDER PETER ARMAND POULIOT

A DISSERTATION SUBMITTED TO THE FACULTY OF GRADUATE STUDIES
IN PARTIAL FULFILMENT OF THE REQUIREMENTS
FOR THE DEGREE OF
DOCTOR OF PHILOSOPHY

GRADUATE PROGRAM IN PHYSICS AND ASTRONOMY
YORK UNIVERSITY
TORONTO, ONTARIO

OCTOBER 2025

Abstract

We present comprehensive determinations of the diffusion coefficients for rubidium atoms in six commonly used buffer gases using a newly developed coherent transient technique. The experiments are carried out by establishing a spatially periodic rubidium population grating using two laser beams intersecting at an angle of a few milliradians. The grating decays exponentially in time due to diffusive motion induced by momentum-changing elastic collisions with buffer gas atoms. The decay can be monitored over a large dynamic range using a heterodyne detection system that records the coherently scattered light from the grating. We are able to distinguish the contribution of diffusion from other collisional processes by measuring the characteristic dependence of the decay rate on the angle between excitation beams. These experiments are carried out in a non-magnetic atomic vapour cell manifold that allows magnetic fields and magnetic field gradients to be cancelled so that rubidium atoms can be manipulated in targeted internal ground states in the presence of different inert gases that can be maintained at pressures ranging from a few hundred pascals to one atmosphere. Our measurements agree with theoretical calculations of diffusion coefficients after reconciling key systematic effects, and this agreement appears to resolve both the widespread scatter in the values of diffusion coefficients using other techniques obtained over several decades and their disagreement with theory. Our measurements lay the groundwork for the development of a quantum pressure sensor that will rely on the intrinsic properties of atoms to calibrate commercial pressure gauges and impact emerging quantum technologies

such as magnetometry, spin polarized imaging, and quantum memory that rely on accurate knowledge of diffusion coefficients. We also describe preliminary, comparative studies of a traditional population magnetometer and a unique coherence magnetometer developed by our group, which led to the development of the technique for measuring diffusion. All our experiments were carried out using a low-cost, home-built diode laser system. We present a detailed characterization of this system, which has supported wide-ranging experiments in precision metrology such as optical tweezers-based determination of micro-particle masses, measurements of atomic lifetimes, and atom interferometric measurements of velocity and gravitational acceleration.

To mom, dad, Gabriel, and Christina

Acknowledgements

I am grateful for this opportunity to see through every stage of the scientific process: building an experiment from the ground up, feeling the excitement at the first signal, pushing to publish initial findings, and then revising, rebuilding, and producing mature results.

This was all made possible by my supervisor, Kumar, who is gifted with the ability to work with students for hours on end without requiring a single meal. Seemingly sustained in these periods only by his bottomless enthusiasm for atomic physics, and occasional laps around the lab to "recharge his batteries." He has taught me a lot of physics, but also to be confident in my abilities and to advocate for myself without reservation. I could not have asked for a more supportive and understanding supervisor.

Ultimately however, the quality of the lab is a product of those working in it, and I am grateful to have had the pleasure of working with many amazing physicists over the years. With special mention to Gehrig Carlse who I have been working with in some capacity for this entire thesis, and who has always provided interesting conversations about physics and a wide array of other topics. I also want to thank by name, in chronological order, Gurpreet Singh, Andrew Vorozcovs, Adam Carew, Hermina Beica, Thomas Vacheresse, Eduardo Chomen Ramos, and Jaskaran Randhawa as well as too many others to name who also deserve thanks. I am also indebted to the previous graduate students in Kumar's group, particularly Brynle Barrett, who has provided continuous guidance years after his departure, and Iain Chan, whose work formed the basis of much of my own.

This project would not have been possible without York's technical services: Jerry Grech and Adam McLean in the student machine shop, who have tolerated my roughly annual need to be retrained on how to use the mill, and Dirk Verdoold in the glassblowing shop, who made the glass manifold and also rescued it from the brink of catastrophe. I also want to thank York's administrative staff Marlene Caplan, Janaki De Camillis, and Cristal del Biondo for ensuring deadlines were met, pay-cheques were deposited, and scholarships were applied for.

In addition to my supervisor, this project has been guided by the suggestions and assistance of my supervisory committee. Jim Whiteway has been on-board since this was a lidar project, he also generously loaned the optical table upon which half (and up until the latest iteration—all) of my experiment sits. Louis Marmet has been particularly hands-on; he has helped me hunt down noise sources and eliminate them, solve the mystery of the gas temperature, and countless other things. Every evaluation, Jim Martin has asked the questions I am most afraid of answering, and has thus ensured I have a thorough understanding of the experiment. Although he is not on the committee, I would also like to acknowledge the support and guidance of Tom Kirchner throughout my time at York.

Several others have made significant contributions. The neon was "loaned" from Greg Koyanagi of York University, who also provided assistance with vacuum equipment. The xenon was provided by Brynle Barrett of the University of New Brunswick. The motivation for parts of this project was based on unpublished work done by Unyob Shim and Kumar as well as Sidney Cahn, Andrey Turlapov, and Tycho Sleator at New York University. Krishna Myneni of US Army DEVCOM corrected an error in my spectroscopic pressure measurement, and our correspondence with him improved my understanding of pressure-broadened spectra. Brian Saam of the University of Washington helped us better understand the influence of collisions on spin polarization. This project has benefited tremendously from our collaboration with Eite Tiesinga of NIST, USA and Jacek Kłos of the University of Maryland, who not

only provided a wealth of theoretical results, but also pushed me to continue refining my analysis and devoted valuable time to revising and adding to my work.

Finally, and most importantly, I would not have been able to pursue physics at all were it not for my support network. My mom and dad gave me an environment where education and knowledge were valued, and I felt comfortable pursuing them for their own sake. My brother Gabriel has been my companion and mutual sounding board for all of my life. Growing up, we were unique in our obsessive attention to detail in every niche interest that one has as a child. I'm sure those aspects of my personality, which are key to pulling off any physics experiment, would have been eroded if not for the knowledge that there was at least one other person in the world who was as weird as I am.

Christina, who has been my girlfriend, fiancée, and then wife for this entire degree, has also been my best friend for nearly my entire life. She has always supported me despite a series of baffling decisions (majoring in English literature, switching to physics, doing a 10-year PhD). For (at least) the last 16 years, every single day she has made me laugh, made me think, and made me a better person. There is no hope of capturing a fraction of her impact in this acknowledgements section. For the last several years, her parents, Edmund and Gita, have also supported me in my atypical pursuits, giving me the pleasure of having two sets of amazing parents.

Littlest, but not least, Xavier and Diana, you were the light at the end of the tunnel, and you gave me the push I needed to get to the end.

Contents

List of Tables

List of Figures

Abbreviations

Abbreviation	Definition
AD	Allan Deviation
ALDLS	Auto-Locking Diode-Laser System
AOM	Acousto-Optic Modulator
ASE	Amplified Spontaneous Emission
AV	Allan Variance
BEC	Bose-Einstein Condensate
CW	Continuous Wave
CSV	Comma-Separated Values
ECDL	External Cavity Diode Laser
FFT	Fast Fourier Transform
FWHM	Full-Width at Half-Maximum
IF	Interference Filter
LO	Local Oscillator
MGFID	Magnetic-Grating Free-Induction-Decay
MOPA	Master Oscillator–Power Amplifier
NPBS	Non-Polarizing Beam-Splitter
PBS	Polarizing Beam-Splitter

Abbreviation	Definition
PD	Photo-Diode
PID	Proportional, Integral and Differential
PMT	Photo-Multiplier Tube
RF	Radio-Frequency
SERF	Spin-Exchange Relaxation Free
TA	Tapered Amplifier
ToF	Time of Flight
TTL	Transistor-Transistor Logic
UHV	Ultra-High-Vacuum

Chapter 1

Introduction

1.1 Diffusion and precision metrology

The diffusion of microparticles such as pollen grains first observed by the botanist Robert Brown [1] has been a source of considerable interest because of practical applications and because the investigation of its characteristics is strongly linked to the mathematics of random walk processes [2]. The successful treatment of microparticle diffusion by Einstein [3] showed that the ballistic motion of the particle on short time scales evolves into diffusive behaviour on longer timescales characterized by the famous equation.

$$\bar{x^2} = D\,t \tag{1.1}$$

Here, D is the diffusion coefficient, and the equation predicts that the mean squared displacement $\overline{x^2}$ increases linearly with time t.

Subsequently, there has been considerable interest in understanding the diffusion of atoms for the development of compact vapour cell quantum sensors. These sensors contain trace amounts of alkali-metal atoms in mixtures of inert buffer gases and have been developed into

essential platforms for cutting-edge quantum sensors and precision metrology. Examples of sensors in this category include Spin-Exchange Relaxation Free (SERF) magnetometry [4], the use of spin-polarized noble gases for medical imaging [5], schemes for quantum memory [6] and vapour cell atomic clocks [7, 8]. Vapour cells have also been used to study optical pumping and collisional effects using coherent transient effects including atom interferometry [9–17].

During the last forty years, there have been significant improvements in the sensitivity of a particular class of vapour cell sensors, namely atomic magnetometers used for the detection of small magnetic fields and magnetic anomalies. The development of spin–exchange relaxation—free (SERF) atomic magnetometers has allowed these sensors to reach sensitivities below 1 fT/Hz$^{1/2}$, competing with, and often surpassing, superconducting (SQUID) magnetometers [18] to become the most precise magnetometers in the world [19]. Such magnetometric techniques have also been used to monitor the Earth's ocean currents and interior dynamics [20]. Atomic magnetometers operate by optically pumping alkali vapour into a specific internal state, thereby aligning the individual magnetic dipole moments of atoms. This net magnetic moment will oscillate at the Larmor frequency, which is uniquely determined by the external magnetic field. In a conventional, time–domain magnetometer, the Larmor frequency is measured by observing the absorption of a weak probe laser [21]. SERF magnetometers achieve high precision by preserving the alignment over extended time scales. This is achieved by using high alkali densities and specific concentrations of buffer and quenching gases. Under these conditions, the optically–pumped alkali vapour slowly diffuses with minimal decoherence due to radiation trapping and spin–disrupting collisions.

To optimize magnetometers and other vapour cell sensors, it is critically important to reliably measure binary diffusion coefficients for alkali-metal atoms in inert buffer gases in order to model the many-body evolution in these systems. Models of these systems also require other key parameters such as spectroscopic parameters related to collision-induced broadening, and binary collision cross-sections [22]. Because these observables are ultimately

determined by the electronic potential energy surfaces between alkali-metal atoms and inert buffer-gas atoms or molecules, [23–25] it is possible to compare measurements to *ab-initio* calculations.

1.2 Techniques to calculate and measure atomic diffusion coefficients

Diffusion coefficients can be theoretically calculated from an accurate knowledge of the intermolecular potential of the colliding species by relying on the Chapman–Enskog formalism [22, 26]. Previous measurements of diffusion coefficients have involved analyzing transient signals associated with the optical pumping of alkali vapours [9–13, 27], measuring the amplitude decay of spin echoes in a magnetic gradient [28, 29], and analyzing the spectrum of transmitted probe light well below the shot–noise limit to directly observe atomic motion [30]. Other known methods of inferring diffusion coefficients involve frequency domain measurements of collisional broadening [31] and of collision cross–sections using four-wave mixing [32].

In this thesis, we have developed a distinctive coherent transient technique [33–36] for comprehensive measurements of the binary diffusion coefficients for rubidium atoms near room temperature in the presence of inert gases helium, neon, argon, krypton, xenon, and molecular nitrogen [35] and within the pressure range 50 Torr to 700 Torr, where 1 Torr = 133.322 Pa. Our technique relies on the decay of a coherently scattered signal from a spatially periodic lattice (grating) created by optical pumping. Our measurements relied on theoretical calculations of diffusion coefficients from collaborators at NIST Gaithersburg USA. Their theoretical predictions were based on classical, semi-classical, and quantum mechanical models and relied on the Chapman–Enskog formalism [35, 36]. The agreement

between theory and experiment in 6 atomic systems has made it possible to realize a quantum pressure sensor based on intrinsic atomic properties rather than electromechanical properties of materials used in pressure gauges. Our experimental configuration also proved suitable for comparative investigations of traditional population magnetometers and coherence magnetometer techniques developed in our group [37–39].

1.3 Contributions and key steps in the development of this thesis

When I joined this research group, a commercial Ti:Sapphire laser system that had been used in key measurements for over 14 years had broken down. Therefore, we embarked on a project to develop home-built master-oscillator power-amplifier (MOPA) laser systems. The first step involved the development of external cavity diode lasers (ECDL) and I contributed to this effort by developing home-built controllers. These modules included circuits for stabilizing the diode temperature and current. Scanning modules were built to apply a tuning voltage to a Piezo transducer that controlled the length of the laser cavity. A feedforward circuit was designed to synchronously scan the laser frequency via the diode current and the external cavity to avoid mode-hops. My next major contribution was to develop the protocol for Allan deviation measurements for characterizing the ECDL stability [40]. Our studies indicated that the ECDL had a short-term linewidth of 200 kHz and an Allan deviation floor of 1.5×10^{-12} at 300 s. The Allan deviation code was used for a number of results that support this dissertation, which include tests of laser stability [40], stability of power supplies [41], stability of a rotating knife-edge spatial profiler used for angle measurements in the diffusion experiment [33], and to estimate the uncertainty in atomic lifetime experiment [42].

I then developed a high-power laser system by seeding a commercial semi-conductor

waveguide tapered amplifier (TA) with the ECDL. In this manner, I developed laser systems with power outputs ranging from 2 W to 3 W [41]. I was involved in constructing multiple replicas of this laser system to support four projects in the lab, including my own. These other projects included optical tweezers, atomic lifetime measurements [42] and atom interferometric measurements of gravity [43–46], all of which reached mature stages during the course of my work. In the next phase of my research, I validated the performance of the high-power laser systems by obtaining comparative data from traditional population magnetometers and coherence magnetometers [39]. Using a sealed cell containing isotopically purified ^{87}Rb and nitrogen buffer gas, I carried out a proof-of-concept measurement of the Rb-N_2 diffusion coefficient using coherent scattering from a population grating [33]. The completion of this work required a spectroscopic determination of the buffer gas pressure. Learning from this experiment, we set up a vacuum system in which different buffer gases could be introduced at various pressures. It then became possible to use our coherent transient technique to measure the diffusion coefficient of Rb atoms in six different buffer gas mixtures. A number of systematic effects including transit time corrections [36] were identified so that it was possible to compare with theoretical calculations [35]. The agreement between experiment and theory has paved the way for future experiments to realize a pressure sensor. In a follow-up experiment [47] we were able to use a detection system consisting of a gated photomultiplier tube to replicate the diffusion measurements presented in this work in nitrogen. This experiment will focus on measuring the temperature dependence of the diffusion coefficient, which is an essential step to realize the aforementioned pressure sensor. The spectroscopic measurements of the buffer gas pressure that were completed as part of this work were also compared with readings from a capacitance manometer, and these results have enabled the determination of collisional shift and broadening parameters in six Rb-buffer gas mixtures [48].

1.3.1 Impact of delays

My thesis was considerably impacted by a 15-month shutdown of our research lab during the COVID-19 pandemic from March 2020 to May 2021, only one student was allowed to work in the lab for one day of the week to maintain critical systems. During the period from May to August 2021, only 50% of the research group members were allowed to work in the lab. Although normal operation resumed in September 2021, there was widespread failure of building infrastructure, resulting in unscheduled power outages, water leaks, and the failure of the air conditioning unit in the lab. These failures resulted in damage to the equipment used in the diffusion experiment. It proved time-consuming to slowly repair and replace this equipment because my research group was constrained by a modest operational grant of $34 000 per year and because the university did not provide reimbursements until February 2024. The collective impact of these delays set back my project by about two years.

1.4 Outline of thesis

The thesis is organized as follows: We use the remainder of Chapter 1 to provide an overview of magnetometric techniques and the principles of our coherent transient technique to measure diffusion. Chapter 2 covers the theoretical formalism relevant to magnetometry and the theoretical calculations of diffusion coefficients. Chapter 3 describes the experimental details including key elements of the apparatus. The results and discussion are presented in Chapter 4. The supporting results are described in a series of appendices to ensure that the main body of the thesis is compact and cohesive. Appendix A describes the MOPA system. Appendix B describes the analysis protocol to calculate the Allan deviation to characterize the ECDL stability. We also describe applications in which this protocol was used to characterize the stability of laser-current controllers and a scanning knife-edge beam profiler used to measure the angle between excitation beams in our diffusion experiments.

Appendix C describes the transit time correction to the measured diffusion coefficients due to atoms leaving the interaction volume defined by the laser beams. Appendix D describes the spectroscopic measurements of the pressure. Appendix E summarizes the journal publications and conference proceedings related to this dissertation. In summary, the work described in the appendices relates to some of the most time-consuming developments related to this dissertation. I have described these contributions separately to ensure the readability of the manuscript.

1.5 Overview of atomic magnetometry

1.5.1 Time-domain population magnetometer

Figure 1.1 shows a schematic of a well–understood, time–domain, "population" magnetometer [21]. Here, a continuous wave (CW) diode laser is amplified by a tapered waveguide amplifier (TA) and used to generate a strong pump and a weak probe that are aligned at a small angle through a vapour cell containing an alkali sample such as rubidium. These beams are amplitude–modulated by acousto–optic modulators (AOMs). In this example, the circularly–polarized pump laser is tuned to the ^{85}Rb $F = 3 \rightarrow F' = 4$ transition and is used

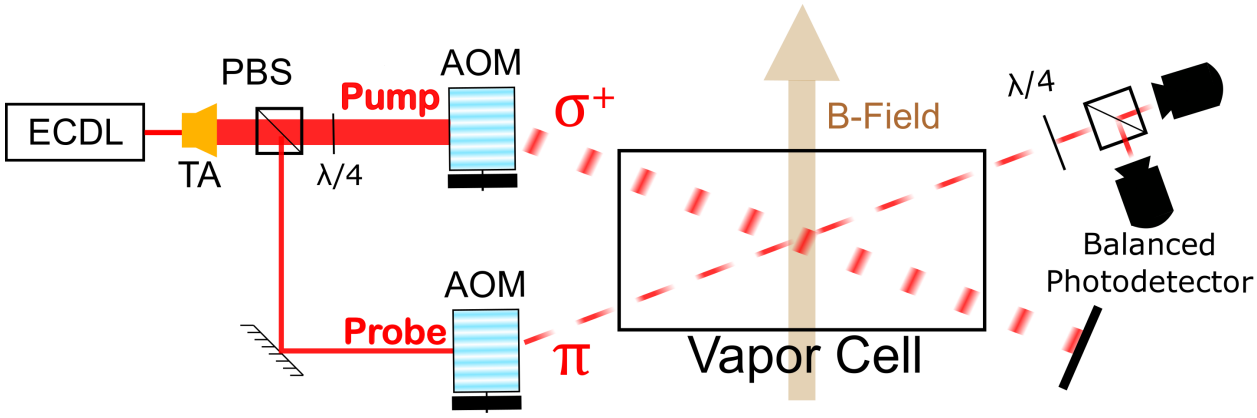

Figure 1.1: Schematic of time–domain population magnetometer.

to optically pump atoms into the $F = 3$, $m_F = 3$ ground state magnetic sub-level, resulting in spin–polarization. If a magnetic field is applied perpendicular to the quantization axis defined by the pump laser, the transfer of population across the ground state manifold and back is modulated at the Larmor frequency $\omega_L = (\vec{\mu_F} \cdot \vec{B})/\hbar$. This population evolution is detected as a periodic variation in the differential transmission of the two orthogonal circular components of the probe beam.

The decay time of the signal—which is modulated at the Larmor frequency—is limited first by the transit time of the atoms through the pumping volume (see Figure 1.2). If the pumping volume is extended to encompass the entire vapour cell, then the measurement time will be limited by the effect of wall collisions that decohere the Larmor oscillations. Although the measurement time can be extended using wall coatings, commonly–available coatings degrade at the high temperatures required for SERF magnetometry [49]. A simpler way to extend the measurement time is to add a high concentration of a *buffer* gas—such as N_2 or a noble gas—whose principal requirement is a low spin–destruction cross–section. Collisions between the alkali atoms and the buffer gas will result in diffusive motion and effectively increase the transit time. Under these conditions, the measurement time is limited by radiation trapping which scrambles the atomic polarization. The addition of a small concentration of *quenching* gas—such as N_2—with a broad range of resonant energies can ensure that collisional de–excitations dominate spontaneous emission while preserving the spin–polarization. In this regime, spin–exchange collisions between rubidium atoms, which result in a transfer to atomic states that precess with the opposite phase, limit the time scale. Even so, this effect can be avoided by increasing the alkali density until the collisional frequency is large enough to re–initialize the phase of the Larmor precession, resulting in the so–called SERF regime.

Other transit time limited experiments involving the configuration in Figure 1.1 have been utilized for precise measurements of atomic g–factor ratios [38, 50]. However, this

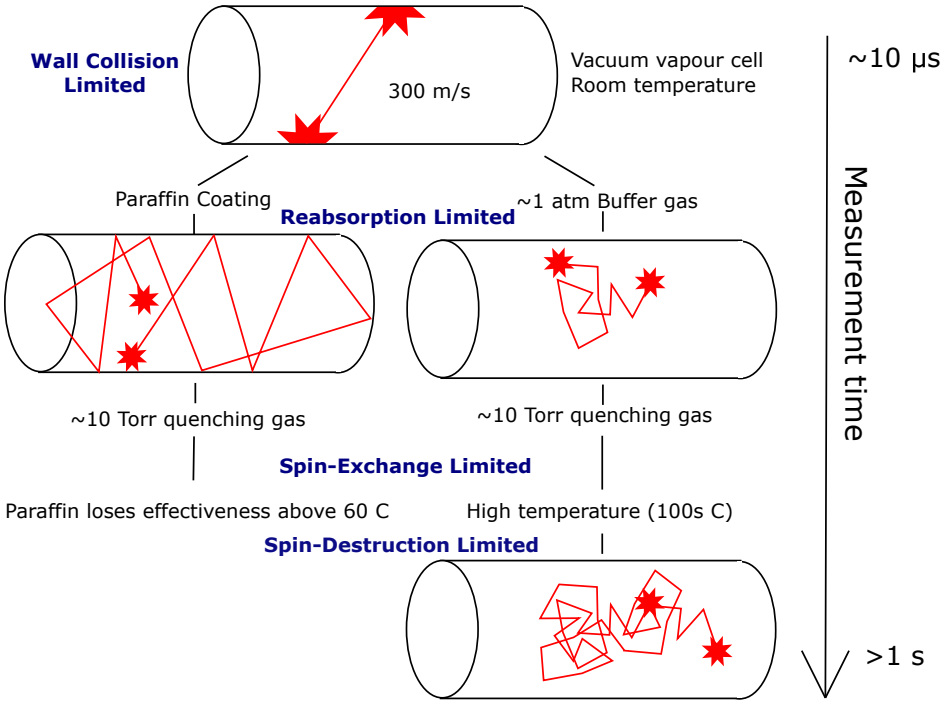

Figure 1.2: Methods to extend the coherence time of magnetometry signals. Collisions with the walls present the fastest source of decoherence, and can be eliminated either by coating the walls so that collisions do not cause decoherence, or by adding a buffer gas to decrease the frequency of wall collisions. Both methods require the addition of a buffer gas with a significant cross-section for *quenching* collisions, in order to limit decoherence due to the reabsorption of spontaneous emission (radiation trapping). The third limiting phenomenon is spin-exchange collisions, which can be overcome by heating the alkali vapour to increase the atomic vapour density. Generally, coatings do not perform well at the required temperatures.

type of magnetometer is not ideally suited for diffusion measurements since the signal decay must be modelled by a complex function which is sensitive to various mechanisms of spin–depolarization in addition to diffusion. Further, the magnetic field response, which is also sensitive to various systematic effects, cannot be decoupled from the signal decay. In general, the transit time of atoms—$\tau_{transit} = fR^2/D$, where R is the beam radius, D is the diffusion coefficient, and f is a form factor—is sensitive to the volume of the pump–probe overlap region. In devices of this type, the geometry of the overlapping region and its corresponding form factor contribute substantial errors into the diffusion measurement. The Rb–N_2 diffusion coefficient has been inferred by experiments of this kind by illuminating an entire vapour cell

of simple geometry, with a circularly–polarized lamp source and monitoring the transmission [11]. These measurements rely on knowledge of the form factor of the cell geometry apart from requiring deconvolution of magnetic field effects and all sources of spin de–polarization.

1.5.2 Coherence magnetometer

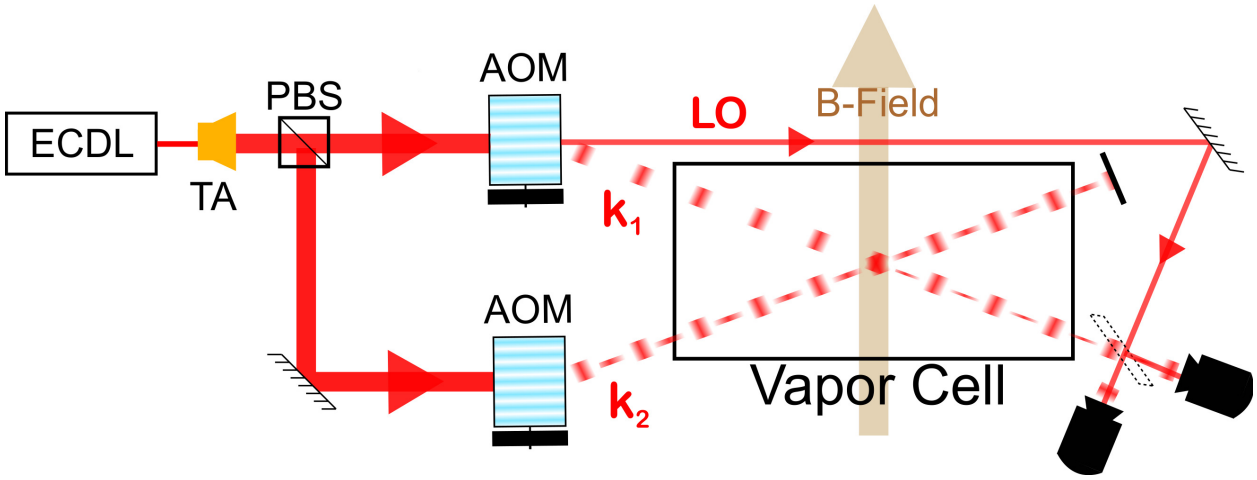

Figure 1.3: Schematic of the coherence magnetometer.

Figure 1.3 shows a schematic of a "coherence" magnetometer [37, 51–53]. Here, a spatially-modulated coherence grating is created between adjacent magnetic sublevels of the $F = 3$ ground state in ^{85}Rb by an excitation pulse that consists of two perpendicular linear-polarized travelling waves, with wave vectors $\vec{k_1}$ and $\vec{k_2}$, aligned at a small angle θ (a few mrad). The grating is formed along the direction $\Delta\vec{k} = \vec{k_1} - \vec{k_2}$ as shown in Figure 1.4 and has a spatial periodicity of $\sim \lambda/\theta$, where $\lambda = 2\pi/k$, and k is the magnitude of the wave-vector $k = |\vec{k_1}| = |\vec{k_2}|$. The grating can be detected by applying a read-out pulse along the direction $\vec{k_2}$, and observing the coherent emission scattered along the phase-matched direction $\vec{k_1}$. This signal, called the magnetic grating free induction decay (MGFID) [54], exhibits a Gaussian decay with a time constant $\tau = 2/ku\theta$, where u is the most probable speed associated with the Maxwell-Boltzmann velocity distribution. This decay corresponds to the thermal motion

of atoms causing the grating to dephase. The scattered electric field from the grating is then given by

$$E(t) = E_0 e^{-(\frac{ku\theta}{2})^2 t^2}. \tag{1.2}$$

If the excitation pulses have opposite circular polarizations, they will excite coherences between magnetic sublevels separated by $\Delta m = \pm 2$, whereas perpendicular linear excitation produces coherences between sublevels separated by $\Delta m = \pm 1$. The signal scattered from these coherence gratings will have the same exponential decay time constant. The dephasing time of the grating has been used to measure the velocity distributions of warm vapour [37, 53], cold atomic gases [38, 52], and atomic beams [51].

In the presence of a magnetic field, the functional form of the coherence can have a complicated dependence, parameterized by the Larmor frequency. This behaviour has been described in references [37, 52] based on the formalism presented in reference [55]. While Equation 1.2 assumes the thermal trajectory of the atoms is uninterrupted over the length scale of the grating, in the presence of a high concentration of buffer gas the mean–free–path of Rb atoms is reduced by collisions and may become much less than the grating spacing. In this limit, the motion of Rb atoms becomes a random walk that can be modelled by the diffusion equation [56–58]. This condition is represented by

$$\frac{\delta u}{\Gamma_{Col}} \ll \frac{1}{k\theta}. \tag{1.3}$$

Here, δu is the average velocity change per collision and Γ_{Col} is the effective collisional rate. When Equation 1.3 is satisfied, the evolution of the ground state density matrix ρ can be described by the diffusion equation,

$$\frac{\partial \rho(x,t)}{\partial t} = -D\nabla^2 \rho(x,t). \tag{1.4}$$

Here, D is the diffusion coefficient, which is inversely proportional to the perturber pressure. D can be accurately converted to its value at atmospheric pressure D_0, using the relationship

$$D_0 P_0 = DP. \tag{1.5}$$

Here, P_0 is atmospheric pressure and P is the buffer gas pressure in the experiment [22, 26]. If the x–axis is along $\vec{\Delta k}$, the spatial dependence of the coherence ρ may be written as $e^{ik\theta x}$. This results in

$$\frac{\partial \rho(x,t)}{\partial t} = -(\theta k)^2 D\rho(x,t). \tag{1.6}$$

The solution to Equation 1.6 is a decaying exponential. The MGFID is therefore given by

$$E(t) = E_0 e^{-(\theta k)^2 Dt}. \tag{1.7}$$

Under these conditions, the coherent scattering from the grating is preserved but the signal exhibits an exponential decay with a characteristic time constant $\tau = 1/(D(k\theta)^2)$. Since $(k\theta)^{-1}$ represents the characteristic length scale in this problem, namely the grating spacing, the scaling law for τ is representative of a random walk. Therefore, the coherence magnetometer offers a direct approach for measuring diffusion rates [57]. However, this method is prone to inaccuracies since the scattered signal has a small amplitude and is sensitive to magnetic field gradients.

1.5.3 Formation of population gratings

Due to the limitations in the measurements of the decay times of coherence gratings, we have exploited an interesting aspect of the lin–perp–lin excitation, namely that it simultaneously produces a population grating with the same spatial period as the coherence grating. Ac-

cordingly, we are able to record decays with much improved signal–to–noise ratios and with greater accuracy due to the insensitivity of the population grating to magnetic fields and field gradients. It should be noted that the population gratings used in this work can be modelled without atomic recoil or matter–wave interference effects [59–63]. By recording the decay time as a function of angle, we rely on Equation 1.7 to measure the diffusion coefficient with a typical statistical uncertainty of 1–3%. The novelty of this technique, its ability to separate the effects of diffusion from other collisional processes, and the detailed comparison with theory are the most salient features of this dissertation.

In our experiments, the population grating forms as the result of a spatially–periodic polarization modulation in the combined (standing–wave) excitation field. This standing–wave potential optically pumps atoms into a spatially–periodic population distribution within the ground state manifold of the Rb atoms.

1.6 Measuring diffusion

Our experiment is schematically shown in Figure 1.4 as described in reference [33]. An optical field with spatially periodic polarization is created by overlapping two laser pulses with perpendicular linear polarizations that intersect at a small angle θ. The laser producing both of these excitation beams is locked 60 MHz below the frequency resonant on the $F = 3 \rightarrow F' = 4$ hyperfine transition of the $5s(^2\mathrm{S}_{1/2}) \rightarrow 5p(^2\mathrm{P}_{3/2})$ or D2 line in ^{85}Rb atoms in a vapour cell with no buffer gas. The excitation beam directions are aligned along $\vec{k}_1$ and $\vec{k}_2$, respectively. Their wavelengths λ and wavenumbers $k = 2\pi/\lambda$ are identical. This beam geometry produces a spatially periodic polarization grating along the direction $\vec{k}_1 - \vec{k}_2$ with a period of $\approx \lambda/\theta$. The angle can be varied between 1.5 mrad and 4.0 mrad so that the number of periods ranges between six and fifteen across the 3 mm spatial extent of the beams in this direction. Due to optical pumping in Rb, spatially periodic gratings are formed

in the populations of the magnetic sublevels m_F of the electronic ground state [33]. Here, the quantization axis for the m_F sublevels is along the lattice direction $\vec{k}_1 - \vec{k}_2$. These Rb population gratings have the same period $\approx \lambda/\theta$ and direction as the polarization grating.

When a read-out pulse is applied later along the direction $\vec{k}_2$, phase-matched coherent scattering from the atomic lattice results in a scattered light signal along $\vec{k}_1$ [54].

The decay of this signal is exponential and has contributions from diffusion and from spin-exchange or spin-destruction collisions, all of which arise from the effect of elastic momentum-changing collisions of Rb with the buffer gas atoms or molecules. Other weaker effects, such as decoherence due to residual light, can also contribute to the decay. Our technique, however, is able to differentiate between diffusion and other decay mechanisms by varying angle θ. Since the grating period scales as θ^{-1}, diffusion leads to a decay time constant τ that is proportional to θ^{-2}. We measure decay rates $1/\tau$ with a precision of a few percent and correct for systematic effects such as the transit time and wavefront curvature. Our first round of measurements was carried out at a fixed pressure [33]; while our second round of measurements was performed in an apparatus that could be filled with a buffer gas to a pressure of up to one atmosphere [35].

We interpret our data on decay rates using the diffusion equation applied to the evolution of number density gradients [54]. We compare the extracted diffusion coefficients with our theoretical calculations of thermalized diffusion coefficients expressed in terms of the microscopic differential cross section [64] determined using accurate inter-atomic and inter-molecular potentials. The agreement between experiment and quantum and classical calculations makes it possible to realize an accurate quantum pressure sensor with an operating range of 50-1000 Torr. Our studies complement efforts to realize pressure standards in ultra-high vacuum (UHV) environments using alkali-metal atoms [65–68]. These efforts involve either lithium or rubidium atoms laser-cooled to temperatures of tens of microkelvin.

The diffusion coefficient is a function of both temperature T and pressure p and is given

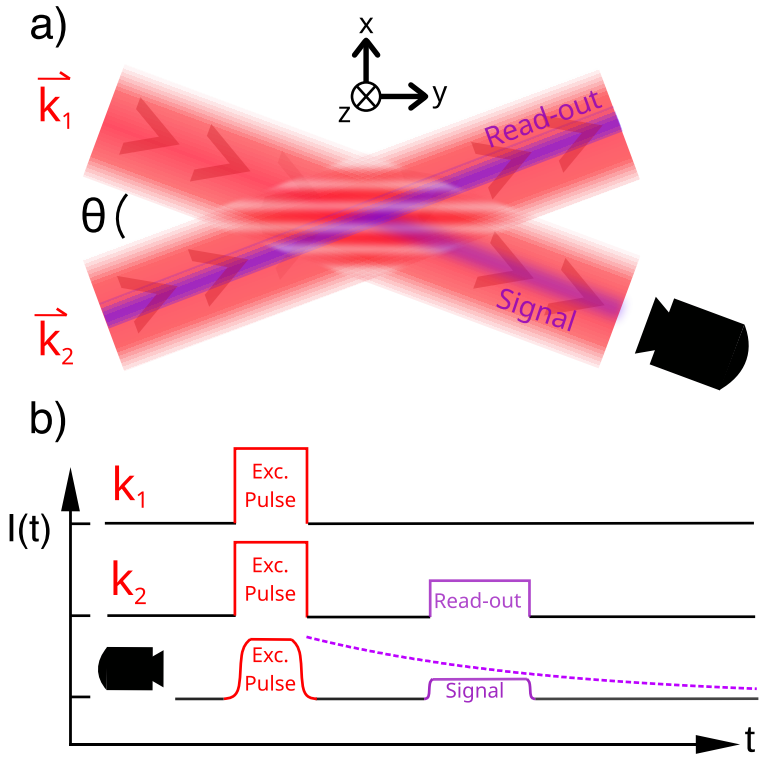

Figure 1.4: a) Diagram of the optical polarization grating formed by two perpendicular linear polarized laser beams with wavevectors $\vec{k}_1$ and $\vec{k}_2$ intersecting at a small angle θ. One laser is polarized in the plane, the other is polarized out of plane. The polarization grating forms along $\vec{k}_1 - \vec{k}_2$ and is indicated by red and white stripes. An excitation pulse is applied along both directions creating a spatial population grating in each m-level of the Rb sample along the same direction. A read-out pulse is applied along $\vec{k}_2$ with variable time delay after the excitation pulse, inducing a coherent scattered signal from the grating in direction $\vec{k}_1$. Fields applied at the time of the excitation pulse are shown in red, while those present at the time of the read-out pulse are shown in purple. All beams have the same spatial profile, but the read-out and signal beams are shown narrower so that they do not obscure the excitation beams. b) Timing diagram for the experiment showing the laser pulses applied along directions $\vec{k}_1$ and $\vec{k}_2$ as well as the intensity of the detected fields. The detector records light incident along direction $\vec{k}_1$. The integrated signal pulse at each read-out delay is indicated by the dotted purple line.

by

$$D(T,p) = \frac{\mathcal{Q}(T)}{n} = \mathcal{Q}(T)\frac{k_{\mathrm{B}}T}{p}. \tag{1.8}$$

Accordingly, we report the diffusion coefficient at standard atmospheric pressure $p_0 \equiv 101\,325$ Pa for the buffer gas, following the convention in the field of pressure metrology. Here, quantity $\mathcal{Q}(T)$ is the pressure invariant diffusion coefficient, and is solely a function of T, n is the number density of the inert gas, and we have used the ideal gas law $p = nk_{\mathrm{B}}T$ in the second equality in Equation 1.8. Another common representation of Equation 1.8 in the literature is

$$D(T,p) = D_0 p_0/p \tag{1.9}$$

where D_0 is the temperature-dependent diffusion coefficient at pressure p_0.

In Table 1.1, we summarize our experimental results on diffusion coefficients $D(T,p)$ for trace amounts of naturally abundant Rb interacting with buffer gases $X =$ He, Ne, N_2, Ar, Kr, and Xe. In this table, we also compare our measurements to existing experimental determinations relying on different physical effects, such as optical pumping, spin echoes, and coherent scattering. The values in Table 1.1 have been scaled to our measurement temperature of $T = 24.0$°C using a buffer-gas dependent power law obtained from our theoretical calculations. Our values are among the most precise and confirm our previous measurement for nitrogen N_2 [33] obtained at a fixed pressure. The data in this thesis are obtained with a single experimental technique, with minimal changes required to interchange buffer gases, resulting in consistency of systematic errors across the six systems. This allows for more complete comparisons with our theoretical results and can serve as a benchmark for future work.

Table 1.1 provides standard statistical uncertainties in parentheses where available. In this table, we quote two results from our 2025 work for each gas, the first being the result without systematic corrections applied, that shows only the statistical uncertainty in parentheses.

The second value is our recommended result, which is a weighted average of two different models for the transit time correction. The first of these models uses rectangular spatial profiles for the population distribution and the readout pulse, and the second model uses Gaussian profiles. The error in the corrected value includes estimates of systematic errors due to the transit time correction and wavefront curvature.

Table 1.1: Measurements of $D(T,p)$ in cm^2/s at standard atmospheric pressure of 101 325 Pa for naturally abundant Rb-inert gas mixtures. The second column gives $D(T,p)$ at $T = 24.0(5)°C$ scaled using the third and fourth columns. We use $D \propto T^\beta/p$, where $\beta = 1.793$, 1.756, 1.730, 1.731, 1.750, and 1.791 for He, Ne, N_2, Ar, Kr, and Xe, respectively, as extracted from our theoretical models.

Buffer gas	D (@ 24 °C)	D (@ T)	T (cited)
Helium (our work 2025) [35]	0.33(2);0.33(5)	0.33(2);0.33(5)	24 °C
Helium (1976) [69]	0.40	0.42	32 °C
Helium (1969) [70]	0.41	0.41	27 °C
Helium (1965) [71]	0.53	0.68	67 °C
Helium (1961) [72]	0.46	0.54	50 °C
Neon (our work 2025) [35]	0.213(7);0.214(14)	0.213(7);0.214(14)	24 °C
Neon (2014) [14]	0.202(5)	0.222(5)	40 °C
Neon (2014) [73]	0.19(2)	0.24(3)	70 °C
Neon (2008) [74]	0.11	0.13	52 °C
Neon (1976) [69]	0.22	0.235	32 °C
Neon (1965)[71]	0.38	0.48	67 °C
Neon (1959) [75]	0.27	0.31	47 °C
Nitrogen (our work 2025) [35]	0.131(3);0.132(7)	0.131(3);0.132(7)	24 °C
Nitrogen (our work 2021) [33]	0.129(1); 0.129(4)	0.1490(14);0.149(5)	50 °C
Nitrogen (2000) [28]	0.1305(16)	0.159(4)	60 °C
Nitrogen (2000) [13]	0.1446(19)	0.30(3)	180 °C
Nitrogen (1994) [12]	0.15	0.28	150 °C
Nitrogen (1985) [11]	0.16	0.20	70 °C
Nitrogen (1976) [69]	0.15	0.16	32 °C
Argon (our work 2025) [35]	0.122(5)0.123(9)	0.122(5)0.123(9)	24 °C
Argon (1976) [69]	0.15	0.16	32 °C
Argon (1972) [76]	0.137(11)	0.139(11)	27 °C
Argon (1965) [71]	0.29	0.37	67 °C
Argon (1959) [75]	0.21	0.21	47 °C
Krypton (our work 2025) [35]	0.092(5);0.093(9)	0.092(5);0.093(9)	24 °C
Krypton (2014) [14]	0.085(3)	0.093(3)	40 °C
Krypton (2014) [73]	0.069(5)	0.089(6)	70 °C
Krypton (2012) [77]	0.033(5)	0.043(7)	70 °C
Krypton (1972) [76]	0.118(10)	0.12(1)	27 °C
Xenon (our work 2025) [35]	0.072(3);0.073(4)	0.072(3);0.073(4)	24 °C
Xenon (2014) [14]	0.0519(9)	0.057(1)	40 °C
Xenon (2014) [73]	0.053(3)	0.068(4)	70 °C

Chapter 2

Theory of formation and decay of optically pumped lattices

This chapter describes the theoretical framework used to design and understand the experiments described in 1. Section 2.1 reviews optical pumping due to the application of multiple laser fields resulting in a spatially periodic population distribution (grating) in each magnetic sub-level of the ground state of the alkali vapour. In what follows, we use the language that optical pumping "polarizes" the sample. We use this terminology to describe any population imbalance between the magnetic sublevels created by the laser fields. In our experiment, we have to consider the effect of two or more laser fields with specific optical polarizations that induce both population transfer and coherences between magnetic sublevels associated with both the ground and excited states. For most of our work, we are interested in the ground-state distribution of magnetic sub-level populations, but the manner in which these distributions are created can be described in a tensor representation [55] with the lowest ordered terms labelled monopole (population), orientation (magnetic dipole) and alignment (magnetic quadrupole). Henceforth we will draw attention to specific aspects of the sample polarization depending on the laser excitation configuration that is used.

Section 2.2 describes how collisions modify the absorption lines of an alkali vapour. The ideas in these two sections are combined in Section 2.3 where our simulations of optical pumping are described. These simulations model the formation of the optically pumped lattices used for our experiments. Section 2.4 describes the decay of the lattices due to diffusion as well as other mechanisms. Finally, in Section 2.5 we discuss how the diffusion coefficient can be calculated.

2.1 Optical pumping

In the absence of external fields, the populations of ground state magnetic sublevels (m_F states) in an atomic vapour are isotopically distributed. Such a distribution can be intuitively understood since the m_F state distributions correspond to the projections of the magnetic dipole moment of an atom onto a particular axis, and we would not expect the magnetic dipole moment to have a preferred direction in the absence of any fields. The application of a near-resonant optical field will generally lift this isotropy, resulting in a redistribution of the sub-level populations which is biased towards certain states and against others. This redistribution is achieved in our case by optical fields that connect the ground states with the excited state.

The direction and magnitude of this bias is dependent on: (i) the absorption strength of every ground-excited transition in the atom, (ii) the probabilities of alternative relaxation channels from the excited state to the ground state (*i.e.* other than spontaneous or stimulated emission of a photon). Both of these mechanisms are strongly influenced by collisions with the buffer gas, in the case of (i) by broadening the line-widths and shifting the line-centres, and in the case of (ii) by providing a potentially significant number of "quenching" collisions, which allow the atom to relax to the ground state without regard to the selection rules for electric dipole transitions.

In this section, we will quantify each of these factors with the goal of simulating the result of optical pumping by a relatively long optical pulse. A long pulse length is defined here as one in which the population of atoms has reached a steady state, and further exposure to the same field will no longer significantly change the population distribution.

2.1.1 Rate equations to model optical pumping

The response of the atom to applied optical fields can be simulated based on the semiclassical model of a multi-level atom. [39, 78]. Ignoring collisions, optical pumping will redistribute atomic populations ρ among ground states with $F = G$, each with magnetic sublevels m_G, and excited states $F = H$, each with magnetic sublevels m_H, following a set of rate equations of the form

$$\begin{aligned}\frac{d}{dt}\rho_{G,m_G} =& \sum_H \Gamma_0 \sum_{q,m_H} \langle G\ m_G\ 1\ q|H\ m_H\rangle^2 \rho_{H,m_H} \\ &+ \sum_H \Gamma_0 \frac{|\chi_{H,G}|^2}{(\frac{\Gamma_0}{2})^2 + \Delta_{H,G}^2} \sum_{q,m_H} |\vec{E}\cdot\epsilon_q|^2 \langle G\ m_G\ 1\ q|H\ m_H\rangle^2 (\rho_{H,m_H} - \rho_{G,m_G})\end{aligned} \tag{2.1}$$

$$\begin{aligned}\frac{d}{dt}\rho_{H,m_H} =& -\Gamma_0 \rho_{H,m_H} \\ &- \Gamma_0 \sum_G \frac{|\chi_{H,G}|^2}{(\frac{\Gamma_0}{2})^2 + \Delta_{H,G}^2} \sum_{q,mG} |\vec{E}\cdot\varepsilon_q|^2 \langle G\ m_G\ 1\ q|H\ m_H\rangle^2 (\rho_{H,m_H} - \rho_{G,m_G}).\end{aligned} \tag{2.2}$$

These rate equations describe the time evolution of the population ρ in hyperfine ground state $|G, m_G\rangle$ 2.1 and excited state $|H, m_H\rangle$ 2.2, in the presence of an applied optical field, where $F = G$ or H and $m_F = m_G$ or m_H are the total angular momentum and magnetic projection quantum numbers, respectively. These relations can be derived from the full set of density matrix equations [39, 78], but since the goal of this simulation is to observe the

steady-state atomic population distribution given by a particular driving field, all atomic coherences are ignored to make computation more efficient. For now, we ignore the effects of collisions on the transfer of atomic populations.

Here, Γ_0 is the natural linewidth of the atoms, $\chi_{H,G}$ is the Rabi frequency, $\Delta_{H,G}$ is the detuning of the optical field from resonance, q is the projection of photon angular momentum $[-1, 0, 1]$, ϵ_q is the unit vector corresponding to the polarization of spin q.

The first term in Equations 2.1 and 2.2 describes relaxation due to spontaneous emission. The excited state decays with a total radiative rate Γ_0 (in vacuum), and the ground state is repopulated from all possible excited states with an effective rate proportional to the Clebsch-Gordan coefficient symbol between initial and final states.

The second term in both Equations describes the interactions of the atoms with the driving optical field, namely the stimulated absorption and emission processes characterized by the effective Rabi frequency $\langle H||\vec{p}\cdot\vec{E}||G\rangle/2\hbar\sqrt{2H+1}$, and the detuning from atomic resonance $\Delta_{H,G} = \omega_{\text{laser}} - \omega_{H,G}$. Here, $\vec{p}$ is the electric-dipole operator, $\vec{E}$ is the electric field strength, ω_{laser} is the laser frequency, and $\omega_{H,G}$ is the atomic resonance frequency between hyperfine states $|H\rangle$ and $|G\rangle$. The inner product $\langle G\ m_G\ 1\ q|H\ m_H\rangle$ is the Clebsch-Gordan coefficient, which describes the transition strength between states with different angular momenta coupled by a photon with spin projection q onto the quantization axis. The Clebsch-Gordan coefficient has the general form $\langle j_1\ m_1\ j_2\ m_2|j_3\ m_3\rangle$ and describes the addition of two angular momenta j_1 and j_2 with projections onto the quantization axis m_1 and m_2 respectively, into a product state with combined angular momentum j_3 and projection m_3. It is non-zero only for electric-dipole-allowed transitions. A time-dependent envelope function is used to model the amplitude of the pumping pulse over time.

We now illustrate the effects of optical pumping in the absence of collisions. These examples are particularly relevant for the description of the magnetometer signals which are outlined in Chapter 1 and described in detail in Chapter 4. Figure 2.1 shows optical pumping

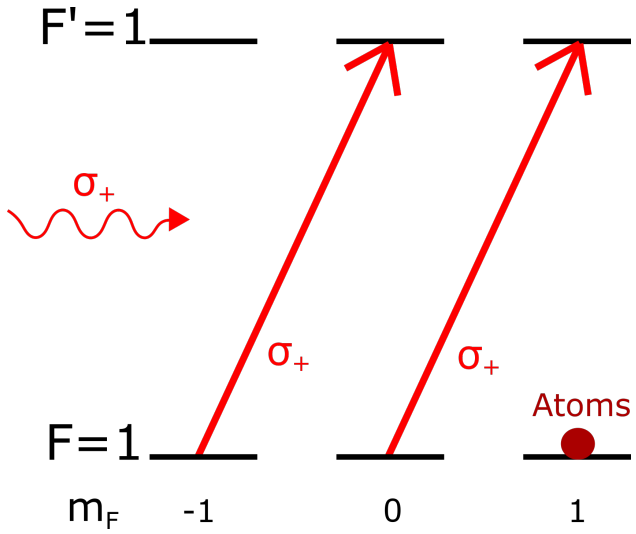

Figure 2.1: An optical pumping scheme with a dark state. The particular circular polarization and frequency of the field can excite atoms out of all ground states except the $m_F = +1$ ground state. As atoms are repeatedly excited and decay, they will all eventually migrate to this dark state. This ideal scheme would be unaffected by collisions to first order.

in the presence of a dark state. This example illustrates the general trend that atoms will collect in ground states that are weakly coupled to the excited state (due to relatively small or non-existent Clebsch-Gordan coefficients). A dark state is an extreme example of this effect as it cannot couple to the excited state at all.

However, as demonstrated in the second example shown in Figure 2.2, atoms are not always biased towards the ground state with the weakest coupling. In this example, where there are no dark states, and the applied field is circularly polarized, ground-excited and excited-ground couplings involve $\Delta m_F = +1$ transitions. In this case, spontaneous emission of a photon is the only other mechanism for decay and it will result in $\Delta m_F = -1, 0$ or 1 transitions with equal probability. This means that the average change in m_F due to spontaneous decay is 0, and thus the angular momentum of the optical field accumulates in the ground state, and atoms eventually migrate to the extreme m_F level, even though this level will also have the strongest coupling to the excited state.

We now consider the effect of collisions. The final example, depicted in Figure 2.3, shows

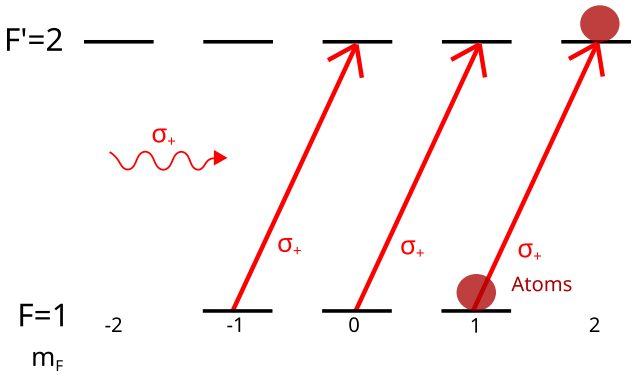

Figure 2.2: A situation where all ground states can be excited. Due to the polarization of the field, an excitation, or a stimulated relaxation, is always accompanied by an increase in the angular momentum projected on to the quantization axis. In the absence of collisions, this results in the migration of atoms into the $m_F = +1$ and $m_{F'} = +2$ states.

one way in which the presence of a buffer gas can dramatically change the result of optical pumping. Here, the applied field and atom are the same as in the previous example, but the addition of a molecular *quenching* gas, with many vibrational excitations, allows the alkali atom to decay via collisions with this gas. Decays via this pathway are generally not limited to the selection rules for an electric dipole transition. Thus, Δm can have a range of values when the atoms decay from the excited state. This effectively eliminates the accumulation of angular momentum seen in the previous example, resulting in a situation similar to the first example, in which the state with the weakest coupling will collect the largest population of atoms.

2.2 Collisional broadening and shifting of spectral lines

The effect of collisions on spectral lines is important for several distinct reasons in this work. First, it is necessary for modelling the optical pumping in the transit-time limited magnetometer experiments. It is also necessary in order to model optical pumping in the diffusive regime, on the basis of which we can understand how spatially periodic population

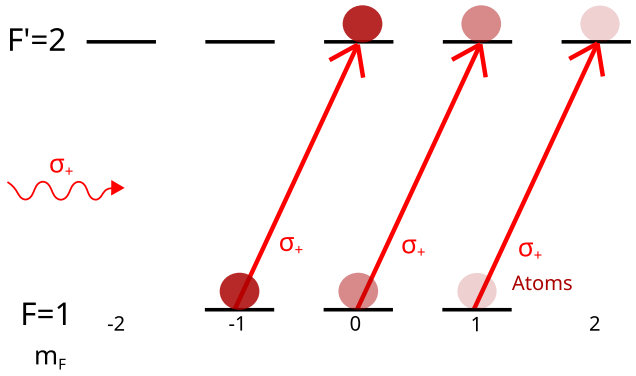

Figure 2.3: If collisions with the buffer gas allow atoms to decay to many ground states with high probability, instead of being limited to transitions $|\Delta m_F| \leq 1$ as is the case for electric dipole transitions, the angular momentum of the applied field is not able to accumulate in the atoms. The Clebsch-Gordan coefficients for σ^+ photons are strongest for the $m_F = +1$ to $m_{F'} = +2$ transition and decrease to the left, so in the absence of accumulation the atomic population will be biased towards the ground states that have the weakest coupling to the excited state, with the $m_F = -1$ having the largest population.

gratings are formed. Finally, measurements of the collisionally broadened line can be used for an independent spectroscopic determination of the buffer gas pressure, which can be compared to the pressure determined on the basis of the diffusion measurement. .

In general, the presence of a buffer gas will cause the Rb spectral lines to broaden and shift. We will briefly review the reasons for these effects in the following section on the basis of reference [79].

2.2.1 Models of collisional broadening and shifting of spectral lines

Theories accounting for the effect of collisions on spectral lines begin with the time domain picture of an atom radiating an infinite train of monochromatic light. The emission spectrum of this overly simplified atom can be obtained by taking the Fourier transform of this sinusoid, which would result in a delta function centred at the frequency of the monochromatic light. Before considering collisions, the first correction to this simple model would be to include the natural exponential decay of the atom determined by the $1/e$ lifetime τ of the excited

state. This modification in the time-domain results in a Lorentzian distribution centred at the frequency of the monochromatic light, and with a full-width at half-maximum (FWHM) $\Gamma_N = 1/2\pi\tau$. The effect of collisions is modelled in a similar way, by modifying the radiation from the atom in the time-domain, and then taking the Fourier transform to find the effect on the emission spectrum.

The simplest model for collisions is the impact approximation, in which the wave-train is interrupted by collisions that occur at a rate and duration determined by a billiard-ball model of atoms. This approach was introduced by Michelson [80] and predicts a broadening proportional to the inverse of the collision rate. By replacing a steady collision rate with a rate characterized by Poisson statistics, Lorentz found the collisionally broadened lineshape takes on the experimentally observed Lorentzian distribution $g(\Delta) = \Gamma/2\pi((\Gamma/2)^2 + \Delta^2)^{-1}$ [81]. Although these models give inaccurate predictions for the spectral broadening and predict no spectral shift, they give an intuitive description of how the observed broadening can arise as a result of collisions, which is not immediately apparent. A slightly more sophisticated approach introduced by Lenz [82, 83] and Lindholm [84] models the effects of collisions as phase shifts instead of abrupt interruptions to the wave-train. The change in the phase of the radiation caused by the interaction between the atom and its surroundings results in a shift of the central frequency.

The simple models described here capture the basic features of collisional effects. More recent, highly sophisticated models have been developed, which predict accurate shifts and widths starting from *ab-initio* calculations of inter-atomic potentials [23]. An additional consideration required to combine the effect of collisional broadening with Doppler broadening (which results in a Gaussian distribution in the absorption profile) is the use of a Voigt profile, which is the convolution of its Lorentzian and Gaussian components [85].

An example of the effect of shifting and broadening of spectral lines due to collisions is shown for naturally abundant ^{85}Rb and ^{87}Rb in Figure 2.5a. Unshifted, Doppler-broadened

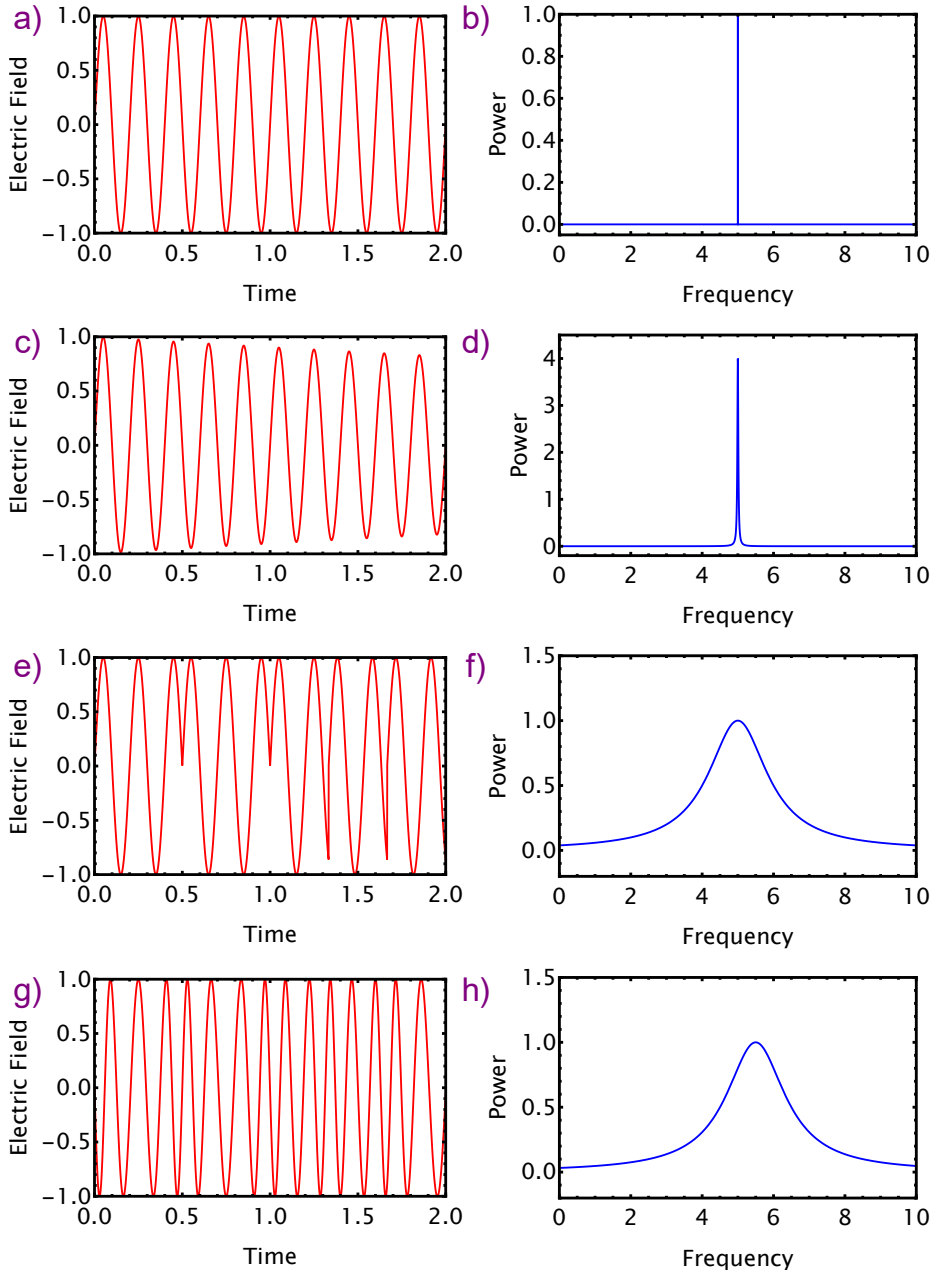

Figure 2.4: Impact of interruptions to the phase of the resonance in the time domain (shown on the left side) on the lineshape observed in the frequency domain (right side). a) and b) show a pure sinusoid, with a delta function lineshape. c) and d) show an exponentially decaying sinusoid, modelling the effect of the excited state lifetime, the result is a Lorentzian lineshape in d). e) demonstrates phase interruptions which manifest as broadening of the lineshape in f). g) demonstrates a continuous phase shift related to the interatomic potential between the atomic gas the perturber, this results in a broadened and shifted lineshape.

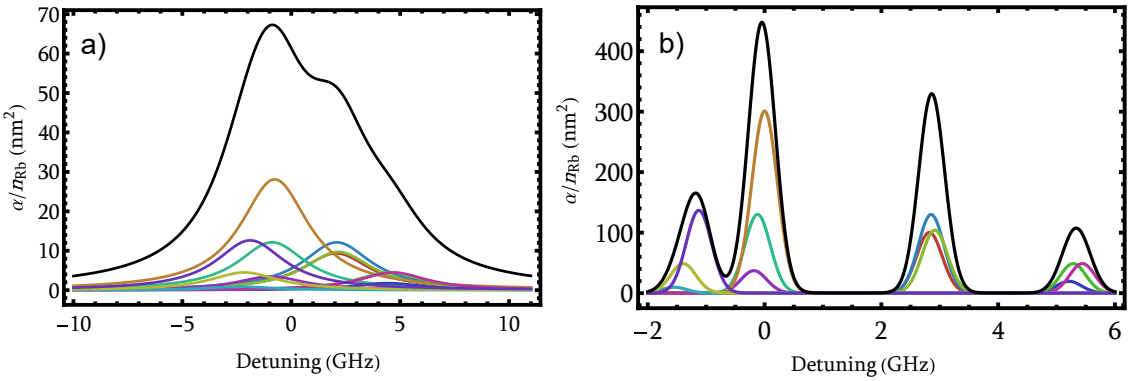

Figure 2.5: a) Collisionally broadened and shifted D2 lines in naturally abundant Rb with 200 Torr of N_2 gas. Individual transitions are shown as coloured lines. The total absorption spectrum is shown in black. b) Doppler broadened D2 lines in naturally abundant Rb at room temperature and Rb vapour pressure with no buffer gas. Individual transitions are shown with the same colours as a). The total absorption spectrum is shown in black. The detuning axis shown relative to $F = 3 \rightarrow F' = 4$ transition in ^{85}Rb.

spectra are shown in Figure 2.5b for comparison.

2.3 Simulations of optical pumping in the presence of collisions

We now modify Equations 2.1 and 2.2 to include the effects of collisions on the spectral line, and include radiative as well as collisional transfer between the ground and excited states. Specifically, we have added the quenching rate Γ_q, a broadening parameter Γ_{col} which appears as part of the total broadened line-width $\Gamma_b = \Gamma_0 + \Gamma_{col}$, and a shift parameter Δ_{col}. All of these parameters are buffer gas dependent and their values are obtained from previous measurements. Reference [86] is used for broadening and shift parameters and reference [87] is used for quenching rates. The collisionally modified rate equations for the ground and excited states are given by

$$\frac{d}{dt}\rho_{G,m_G} = \sum_H \Gamma_0 \sum_{q,m_H} \langle G\ m_G\ 1\ q|H\ m_H\rangle^2 \rho_{H,m_H} + \frac{1}{g_G}\sum_H \Gamma_{\mathrm{q}}\rho_{H,m_H}$$
$$+ \sum_H \Gamma_{\mathrm{b}} \frac{|\chi_{H,G}|^2}{(\frac{\Gamma_{\mathrm{b}}}{2})^2 + (\Delta_{H,G} - \Delta_{\mathrm{col}})^2} \sum_{q,m_H} |\vec{E}\cdot\epsilon_q|^2 \langle G\ m_G\ 1\ q|H\ m_H\rangle^2 (\rho_{H,m_H} - \rho_{G,m_G}) \tag{2.3}$$

$$\frac{d}{dt}\rho_{H,m_H} = -(\Gamma_0 + \Gamma_{\mathrm{q}})\rho_{H,m_H}$$
$$- \Gamma_{\mathrm{b}} \sum_G \frac{|\chi_{H,G}|^2}{(\frac{\Gamma_b}{2})^2 + (\Delta_{H,G} - \Delta_{\mathrm{col}})^2} \sum_{q,mG} |\vec{E}\cdot\varepsilon_q|^2 \langle G\ m_G\ 1\ q|H\ m_H\rangle^2 (\rho_{H,m_H} - \rho_{G,m_G}) \tag{2.4}$$

Here, most of the quantities are defined in Section 2.1.1, and $g = 2G + 1$ gives the degeneracy of a given ground state manifold $|G\rangle$. This term allows all ground states to be populated by any excited state with equal probability, providing a simple model of how quenching collisions redistribute the excited state.

Although this model is simplistic, it is effective in predicting the optical pumping of all magnetic ground-state sublevels on long timescales. A more detailed model of the collisional and radiative transfer gives more accurate predictions for all timescales [78] but this is not necessary for our purposes.

Table 2.1 shows the broadening, shift, and quenching rates used in this simulation.

We apply this model to simulate optical pumping of Rb atoms in the absence of buffer gas or presence of buffer gas in Figures 2.6 and 2.7 respectively.

In Figure 2.6a, a circularly polarized pumping field resonant with the $F = 2 \rightarrow F' = 2$ transition of the $^2\mathrm{5S}_{1/2} \rightarrow ^2\mathrm{5P}_{1/2}$ (or D1) line of ^{87}Rb is applied for 800 ns. The D1 level structure resembles that of Figure 2.1 in that there are the same number of magnetic sublevels

Gas	Γ_{col} (MHz/Torr)[86]	Δ_{col} (MHz/Torr)[86]	Γ_q (MHz/Torr)[87]
N_2	18.9	-8.2	1.2
He	22.5	2.2	4.5×10^{-13}
Ne	9.4	-3.7	2.2×10^{-11}
Ar	19.8	-7.1	2.5×10^{-7}
Kr	17.5	-8.4	3.0×10^{-7}
Xe	19.8	-7.0	1.8×10^{-7}

Table 2.1: Collisional spectroscopic parameters for the buffer gases used in this simulation. Values for Γ_q assume a temperature of 24°C. Other values have not been scaled for temperature since no simple scaling law applies.

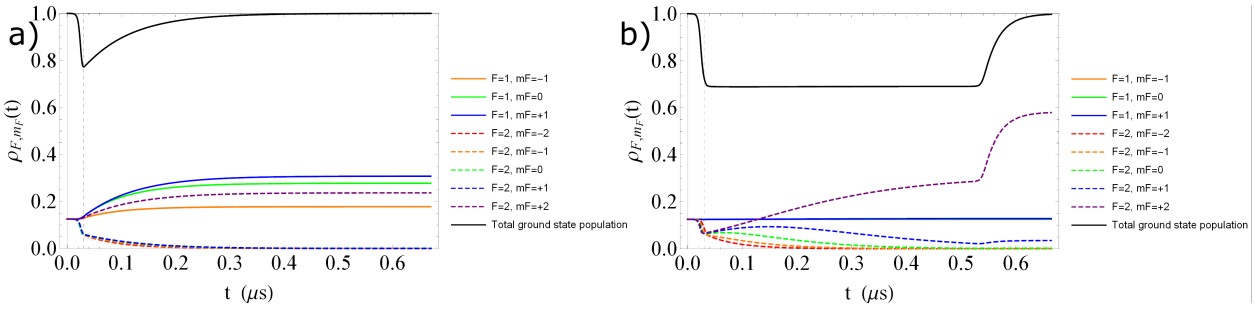

Figure 2.6: Simulation of optical pumping on the D1 and D2 lines in ^{87}Rb in the absence of buffer gas. a) pumping from a circularly polarized optical pulse resonant with the $F = 2 \rightarrow F' = 2$ line on the D1 transition in ^{87}Rb. b) pumping from a circularly polarized optical pulse resonant with the $F = 2 \rightarrow F' = 3$ line on the D2 transition in ^{87}Rb.

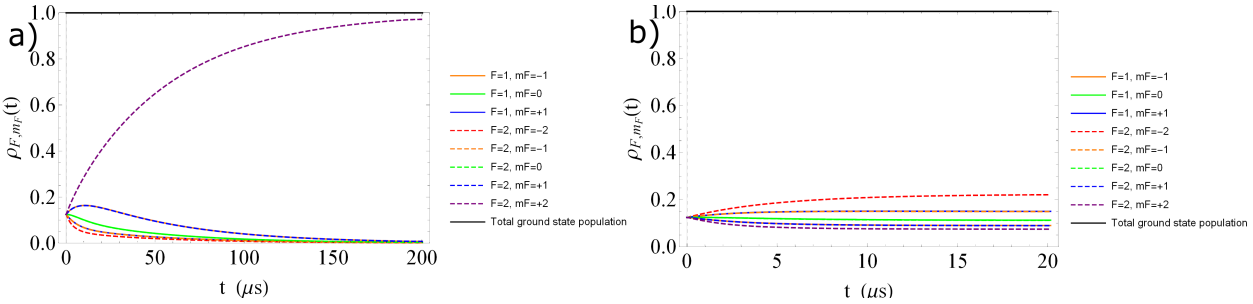

Figure 2.7: Simulation of optical pumping on the D1 and D2 lines in rubidium in the presence of 700 Torr of N_2 gas

in the ground and excited state, thus pumping with circularly polarized light can result in a dark state at one extremum of m_F. However, since there are two hyperfine ground states in ^{87}Rb ($F = 1$ and $F = 2$, and both are accessible from any excited state via spontaneous emission of a photon, a large proportion of the atoms are transferred into the other dark state before they reach the dark state. Since the resonances are narrow at this pressure, atoms in the $F = 1$ ground state interact very weakly with the laser field, and thus will be pumped very slowly into the dark $F = 2$, $m_F = +2$ state (≈ 3 ms). Figure 2.6b simulates optical pumping on the ^{2}5S$_{1/2} \rightarrow ^2$5P$_{3/2}$, or D2 line in ^{87}Rb, caused by a circularly polarized field resonant with the $F = 2 \rightarrow F' = 3$ transition. The D2 level structure resembles Figure 2.2, in which the excited state has additional angular momentum states available, and therefore there are no dark states. Since electric dipole decays from the $F' = 3 \rightarrow F = 1$ level are not allowed, transfer to the $F = 1$ hyperfine level is very slow. The atoms that were initially in the $F = 2$ ground state are efficiently pumped into the $F = 2$, $m_F = +2$ state. When the pulse is shut off at $t = 0.85$µs the excited state, which has been quickly transferred to the $F' = 3$, $m_{F'} = +3$ state decays almost entirely into the $F = 2$, $m_F = +2$ state.

In Figure 2.7a, the same pumping scheme on the D1 line of ^{87}Rb is applied as in Figure 2.6a but with 700 Torr of N_2 buffer gas. The presence of the buffer gas broadens all transitions so that atoms from all ground states are efficiently pumped into the dark ground state.

Figure 2.7b simulates the results of the same optical pumping pulse on the D2 line as in Figure 2.6b with the addition of 700 Torr of N_2 buffer gas. With no dark states, and all states broadened by the buffer gas, the atoms are redistributed into an equilibrium in which the population of each state is inversely proportional to the strength of the transition.

2.3.1 Simulations of lattice formation

We use this model to simulate optical pumping and model the resulting spatial population distribution for each m_F state for the excitation scheme used in our experiment. The excitation scheme was presented in Chapter 1 but is revisited in detail here along with the accompanying Figure 2.8. A spatially periodic polarization grating in the excitation field is produced by overlapping two laser beams with perpendicular linear polarizations, identified by their wavevectors $\vec{k}_1$ and $\vec{k}_2$, at a small angle θ. To find the total polarization created by both fields, we can start by writing the fields in coordinate systems $(\hat{x}', \hat{y}', \hat{z}')$ and $(\hat{x}'', \hat{y}'', \hat{z}'')$, such that $\vec{k}_1 \parallel \hat{z}'$ and $\vec{k}_2 \parallel \hat{z}''$. The electric fields at a particular point can then be written very simply as

$$\vec{E}_{k_1} = A\hat{x}'e^{-i\omega t} \tag{2.5}$$

and

$$\vec{E}_{k_2} = B\hat{y}''e^{-i\omega t}. \tag{2.6}$$

We then rotate each co-ordinate system onto a common co-ordinate system $(\hat{x}''', \hat{y}''', \hat{z}''')$, defined such that the co-linear component of the beams is parallel to $\hat{z}'''$, *i.e.* $\vec{k}_1 + \vec{k}_2 \parallel \hat{z}'''$. This means rotating $\hat{z}'$ by an angle $\theta/2$ and $\hat{z}''$ by $-\theta/2$. The total field can now be written

$$\vec{E}_{\text{com}} = e^{-i\omega t}(\hat{x}'''A\cos(\theta/2) + \hat{y}'''B - \hat{z}'''A\sin(\theta/2)). \tag{2.7}$$

Thus far, we have chosen an arbitrary point in space where the two beams are in phase, however, we can see that the relative phase will shift between the two beams as a function of displacement along $\hat{x}'''$ (the same as $\hat{x}$ in Figure 2.8). This phase difference ϕ is

$$\phi = \frac{2\pi \sin\theta}{\lambda \cos(\theta/2)} \Delta x \approx k\theta \Delta x. \tag{2.8}$$

The total field including this phase difference can be written

$$\vec{E}_{\text{com}} = e^{-i\omega t}(\hat{x}''' A\cos(\theta/2) + \hat{y}''' B e^{-i\phi} - \hat{z}''' A\sin(\theta/2)). \tag{2.9}$$

Finally, we are interested in reflections off of the zy-plane. So, the relevant quantization axis for optical pumping is along the $\hat{x}'''$ axis. The relevant spherical coordinates are

$$\hat{\epsilon}_{\pm} = \frac{1}{\sqrt{2}}(\pm\hat{z}''' - i\hat{y}'''), \tag{2.10}$$

$$\hat{\epsilon}_0 = \hat{x}'''. \tag{2.11}$$

Rewriting in terms of this coordinate system gives us

$$\vec{E}_{\text{com}} = e^{-i\omega t}\left(\left(\frac{1}{\sqrt{2}} A\sin(\theta/2) - iBe^{-i\phi}\right)(\hat{\epsilon}_- - \hat{\epsilon}_+) + A\cos(\theta/2)\hat{\epsilon}_0\right). \tag{2.12}$$

We see that the polarization formed by the small angle geometry in Figure 2.8 is primarily linear everywhere, but has a small component which oscillates between σ^+ and σ^- polarizations, with a period of $\approx \lambda/\theta$ as shown in Figure 2.8. We have simulated the spatially periodic optical pumping for this applied field using rate Equations 2.3 and 2.4, which describe the evolution of the F and m_F populations of ^{85}Rb and ^{87}Rb in a buffer gas, incorporating collisionally broadened and shifted atomic resonances [86] as well as relaxation from collisions

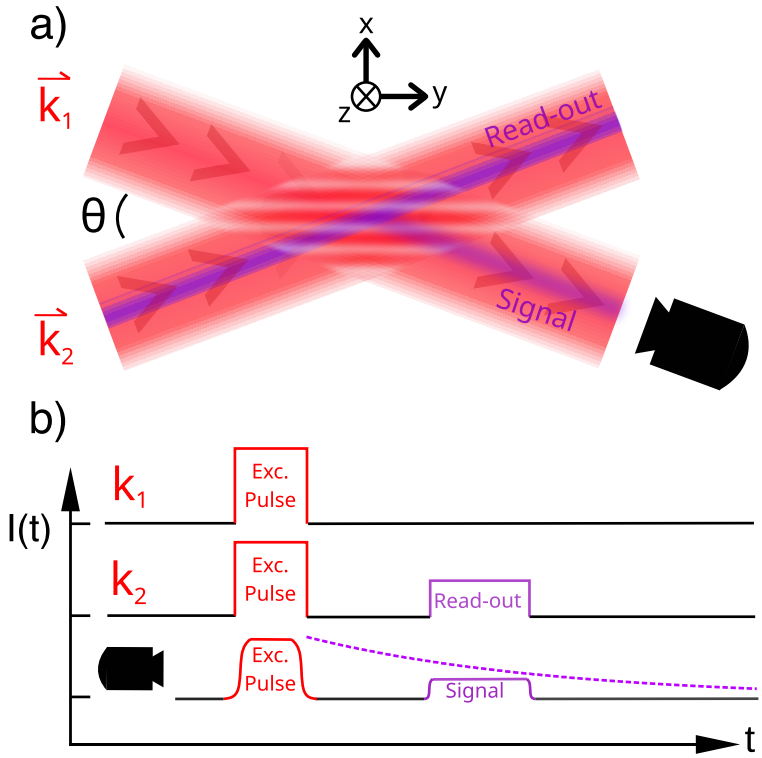

Figure 2.8: a) Diagram of the optical polarization grating formed by two perpendicular linear polarized laser beams with wavevectors $\vec{k}_1$ and $\vec{k}_2$ intersecting at a small angle θ. One laser is polarized in the plane, the other is polarized out of plane. The polarization grating forms along $\vec{k}_1 - \vec{k}_2$ and is indicated by red and white stripes. An excitation pulse is applied along both directions creating a spatial population grating in each m-level of the Rb sample along the same direction. A read-out pulse is applied along $\vec{k}_2$ with variable time delay after the excitation pulse, inducing a coherent scattered signal from the grating in direction $\vec{k}_1$. Fields applied at the time of the excitation pulse are shown in red, while those present at the time of the read-out pulse are shown in purple. All beams have the same spatial profile, but the read-out and signal beams are shown narrower so that they do not obscure the excitation beams. b) Timing diagram for the experiment showing the laser pulses applied along directions $\vec{k}_1$ and $\vec{k}_2$ as well as the intensity of the detected fields. The detector records light incident along direction $\vec{k}_1$. The integrated signal pulse at each read-out delay is indicated by the dotted purple line.

between an electronically excited Rb atom and buffer gas atoms or molecules [87]. This is the effect that creates spatially periodic population gratings that are central to this thesis.

Reference [88],and [86] measure the broadening and shift rates for the buffer gases used in this work at a temperature of $T = 20\,^{\circ}\mathrm{C}$ and $T = 121\,^{\circ}\mathrm{C}$, respectively. Both of these experiments were carried out at pressures ~ 100 Torr. The broadening and shift parameters measured in either [88] or [86] are the same within experimental uncertainties for all F and m_F levels and for both Rb isotopes. However, although the measured shift and broadening rates in these two works are generally similar, they do not typically agree within their error bars.

For nitrogen, the broadening parameters are in agreement, and the shift parameters differ by two standard deviations. Here, we have used 18.9(5) MHz/Torr and 8.2(6) MHz/Torr for pressure broadening and shifts, respectively, from Ref. [88] for N_2 because the temperature in that experiment is better matched to the temperature at which our experiments are carried out. For the entirety of our pressure range, collisional broadening is on the order of several GHz, which is larger than the natural line-width of Rb (≈ 6 MHz), Doppler broadening (≈ 500 MHz), and hyperfine splittings of the $5p(^2\mathrm{P}_{3/2})$ state (≈ 300 MHz) for either isotope. If the pressure exceeds ≈ 250 Torr, collisional broadening is also larger than the $5s(^2\mathrm{S}_{1/2})$ hyperfine splittings (≈ 5 GHz). Our simulations represent a simplified model of the experiment since they ignore effects of the transit of atoms in and out of the volume of the excitation and ignore coherences between magnetic sublevels. Nevertheless, the simulations provide useful insight into the population gratings in our Rb-inert gas mixtures.

The results of these simulations are shown in Figure 2.9 for typical laser parameters used in our experiments. For these parameters, we find that the populations of each ground-state sub-level reach steady-state values so that a larger power or pulse length will not change the distributions. We plot the deviation in m_F level populations from a uniform distribution, $N_F/(2F+1)$ for each level, for projections m_F defined along $\vec{k}_1 - \vec{k}_2$. The simulations

reveal that the spatial gratings of the magnetic sublevels have different amplitudes due to asymmetries in the coupling strengths of the excitation fields. The sum of all F and m_F populations adds to one at all positions corresponding to a constant Rb density profile. The simulations show that the contrast in the $F = 2$ ground state of ^{85}Rb is significantly larger than that for $F = 3$. Similarly, the contrast for the $F = 1$ state of ^{87}Rb is larger than that for $F = 2$. Although the contrast of each F, m_F grating is small, it is still possible to detect a signal because of the phase-matched emission of coherently scattered light, whose intensity exhibits a faster than linear scaling with grating contrast [45, 54, 89].

2.3.2 Formation of the population gratings in collision-free and collisionally broadened regimes

Although all of the experiments described in this work are performed in the presence of a buffer gas, it is useful to describe the formation of Rb population gratings in both the presence and absence of buffer gas collisions for the small angle excitation geometry shown in Figure 2.8. In the absence of a buffer gas and at a low Rb vapour pressure of 3.5×10^{-7} Torr at 24 °C, the Rb spatial population distribution can be assumed to evolve ballistically over the spatial period of our gratings. Under these conditions, the grating contrast in a room temperature Rb vapour cell with no buffer gas decays on a timescale of 1 µs when $\theta \approx 1$ mrad [33]. This effect arises from the thermal motion of the Rb atoms, also known as Doppler dephasing. This timescale is significantly shorter than the ≈ 10 µs transit time for room-temperature Rb atoms to pass through our 3 mm diameter laser beams. All velocity classes along $\vec{k}_1 - \vec{k}_2$ are resonant with the excitation pulses, whereas short optical pulses can ensure that a substantial fraction of the Doppler broadened velocity distribution is excited along the direction of the excitation beams. Although pulses as short as 100 ns are required to observe a signal, the optical pumping process remains incomplete and the grating contrast

is significantly smaller than that shown in Figure 2.9. Under these conditions, scattered light signals from coherence gratings, which have the same period as population gratings and are related to superpositions of adjacent m_F levels, are dominant [54]. These signals have been exploited to measure velocity distributions, magnetic fields, and collision cross-sections in vapour cells, laser-cooled gases, and atomic beams [37, 51–53].

When a small concentration of buffer gas corresponding to a pressure of $\approx 10^{-5}$ Torr is added to the Rb vapour cell, the mean-free path for Rb-X collisions becomes of the order of the spatial period of the gratings. This buffer gas pressure marks the beginning of the diffusive regime [56]. When the buffer gas pressure is further increased to ≈ 100 Torr, the rubidium resonances are collisionally broadened and shifted, such that the excitation and read-out laser pulses couple to all ground and excited hyperfine states of both ^{85}Rb and ^{87}Rb. Under these conditions, all velocity classes are excited within the pulse bandwidth of the excitation pulse.

The transit time of ≈ 2 ms at these pressures is then significantly larger than in the collision-free regime. If the excitation pulses are sufficiently long (> 10 µs), population gratings like those shown in Figure 2.9 are maximized. Further, when ambient magnetic fields are minimized, the contribution to the signal from coherence gratings is reduced [33]. In the presence of a buffer gas, the on-resonance optical depth of the sample is reduced by a factor of ≈ 300 compared to that of a Rb vapour cell without a buffer gas at the same temperature. This effect occurs because the coupling strengths of the Rb hyperfine transitions are distributed over a large spectral width [85], resulting in a reduction in the absorption signal. We compensate by heating the cell so that the Rb number density is increased by about a factor of 10 within the excitation zone defined by the laser beams.

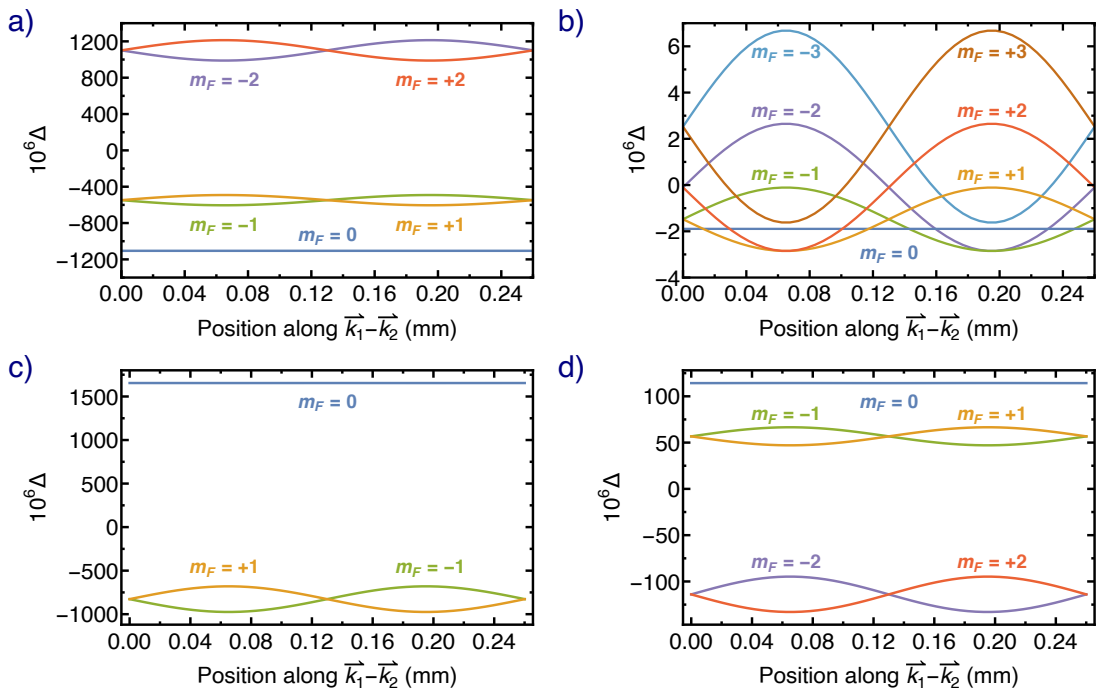

Figure 2.9: Simulation of the population distribution after a 50 µs excitation pulse in the ground-state magnetic sublevels quantized along $\vec{k}_1 - \vec{k}_2$ of ^{85}Rb $F = 2$ (panel a), $F = 3$ (b) and of ^{87}Rb $F = 1$ (c), $F = 2$ (d) as functions of position along $\vec{k}_1 - \vec{k}_2$ for one period of the grating. We have assumed a 200 Torr N_2 buffer gas and an average light intensity of 120 mW/cm^2. The distribution for each level is shown in terms of its deviation Δ from a uniform population in each m_F sub-level for each F state (i.e. a population of $1/(2F+1)$). After the pulse, 96 % of the ^{85}Rb population is pumped into the $F = 2$ ground state and 4 % into the $F = 3$ state. For ^{87}Rb the percentages are 87 % and 13 % for $F = 1$ and 2, respectively. For all four panels, the two linearly polarized laser beams intersect at angle $\theta = 3$ mrad and have a laser frequency that coincides with the $F = 3 \rightarrow F' = 4$ transition for a ^{85}Rb atom in vacuum.

2.4 Decay of population gratings in diffusive regime

In the diffusive regime, the ground-state populations $\rho_{Fm_F}(\vec{x},t)$ for hyperfine state F, m_F of ^{85}Rb or ^{87}Rb at position $\vec{x} = (x, y, z)$ and time t satisfy the diffusion equation

$$\frac{\partial \rho_{Fm_F}(\vec{x},t)}{\partial t} = -D(T,p)\nabla^2 \rho_{Fm_F}(\vec{x},t) \tag{2.13}$$

with coordinates x, y, and z along directions $\vec{k}_1 - \vec{k}_2$, $(\vec{k}_1 + \vec{k}_2)/2$, and $\vec{k}_1 \times \vec{k}_2$, respectively, as shown in Figure 2.8, the populations have an initial spatial dependence given by

$$\rho_{Fm_F}(\vec{x}, t=0) \quad = \quad A_{Fm_F} + B_{Fm_F}\sin(k\theta x) \tag{2.14}$$

where $0 < |B_{Fm_F}| \ll A_{Fm_F}$ as suggested by our simulations in Figure 2.9.

When the read-out pulse is applied along $\vec{k}_2$, as shown in Figure 2.8, the phase matched emission from dipole oscillators interferes constructively along $\vec{k}_1$ [33, 54]. The amplitude of the electric field of the scattered light into this latter direction is measured and is proportional to the $\vec{k}_1 - \vec{k}_2$ Fourier component of the populations $\rho_{Fm_F}(\vec{x},t)$. This signal is

$$E_{\mathrm{C}}(t) = E_0 e^{-(k\theta)^2 D(T,p)t} \tag{2.15}$$

with diffusion time constant $\tau_{\mathrm{D}} \equiv D(T,p)^{-1}(k\theta)^{-2}$. Here, E_0 is the non-negative amplitude which depends on the grating contrast (B_{F,m_F} in Equation 2.14) and the amplitude of the readout field E_{RO}. The corresponding decay rate $1/\tau_D$ scales inversely as a function of the buffer gas pressure since $D_0 p_0 = Dp$ or $D(T,p) = Q(T)k_{\mathrm{B}}T/p$.

In our experiments, we record the decay rate of optically pumped population gratings as a function of the angle θ and the pressure of the buffer gas. There are, however, two additional contributions to the decay rate. The first is due to binary spin-exchange or spin-destruction

collisions between Rb and the inert gas atoms or molecules [76, 90–92]. This process adds a decay rate $n\langle v\sigma_{\text{spin}}\rangle = p\langle v\sigma_{\text{spin}}\rangle/(k_{\text{B}}T)$ to the total decay of the grating. Here, $\langle v\sigma_{\text{spin}}\rangle$ is the thermally averaged rate coefficient for spin-exchange or spin-destruction collisions.

The second additional contribution is caused by leakage of residual laser light after the excitation beams are nominally turned off. Measurements have shown that the intensity of this residual light is no larger than 0.1 mW/cm^2, which is less than 0.3 % of the typical intensity of the excitation pulse. If the residual intensity along the directions $\vec{k}_1$ and $\vec{k}_2$ are closely balanced, the light will contribute to optical pumping and increase the amplitude of the Rb population grating. For unbalanced residual intensities, we find that the light will reduce the grating amplitude. These effects can be modelled by an additional contribution to the decay rate given by $\mathcal{W}(\nu, T, p)\Gamma_{\text{opt}}$, where $\mathcal{W}(\nu, T, p)$ is a collisionally broadened and shifted Voigt profile and Γ_{opt} is a signed optical pumping rate that is a function of both residual intensities [93].

The dimensionless Voigt profile describes the atomic response to the laser light as a function of the laser frequency ν at fixed temperature and buffer gas pressure p [85]. This normalized function is a convolution of a Gaussian distribution, primarily due to Doppler broadening, and a Lorentzian distribution with a width that is primarily due to collisional broadening and thus proportional to p. For our temperature and range of pressures, the Lorentzian component is dominant, and therefore $\mathcal{W}(\nu, T, p)$ has a $1/p$ dependence near atomic resonance. Therefore this term can be approximated as $\mathcal{W}(\nu, T, p) \approx \mathcal{W}(\nu, T, p_{\text{ref}}) \times (p_{\text{ref}}/p)$. Here, p_{ref} is a convenient reference pressure.

The resulting total decay rate of the population grating is

$$\frac{1}{\tau} = \frac{p}{k_{\text{B}}T}\langle v\sigma_{\text{spin}}\rangle + D(T, p)(k\theta)^2 + \mathcal{W}(\nu, T, p)\Gamma_{\text{opt}} \tag{2.16}$$

This expression can be rewritten to explicitly show the dependence on pressure by using

$D(T,p) = Q(T)k_{\mathrm{B}}T/p$, and assuming that $\mathcal{W}(\nu,T,p) \propto 1/p$. Hence,

$$\frac{1}{\tau} = \frac{\langle v\sigma_{\mathrm{spin}}\rangle}{k_{\mathrm{B}}T}p + \mathcal{Q}(T)k_{\mathrm{B}}T\frac{(k\theta)^2}{p} + \mathcal{W}(\nu,T,p_{\mathrm{ref}})\Gamma_{\mathrm{opt}}\frac{p_{\mathrm{ref}}}{p}\,. \tag{2.17}$$

The diffusion coefficient can be unambiguously inferred from Equation 2.17 by measuring this characteristic angle dependence of τ. For decreasing angle θ, however, the number of grating planes in the excitation volume decreases, optical pumping becomes less efficient, and the angle determination is more error prone. For increasing θ, the decay time becomes shorter, which limits the precision. Therefore, we find a balance by operating the experiment over the range $\theta = 1.5$ mrad to 4 mrad. In addition, $D(T,p)$ can also be measured by varying the pressure of the buffer gas when the contributions from spin-exchange, spin-destruction processes, and residual light are small.

2.5 Calculating the diffusion coefficient

In Section 2.4 we calculated the time evolution of the population grating by applying the diffusion equation (2.13). We now discuss how the parameter $D(T,p)$ itself can be calculated from first principles.

As described in reference [64], the diffusion coefficient for a binary mixture is defined by the Chapman-Enskog method for solving the Boltzmann equation, assuming an isotropic, non-reactive, and spin-independent interaction, as given by [94]

$$D(T,p) = \frac{3}{16}\left(\frac{2\pi k_{\mathrm{B}}T}{\mu}\right)^2 \frac{1}{n\mathcal{A}(T)} \tag{2.18}$$

Here, k_{B} is the Boltzmann constant, T is the temperature, $\mu = m_1m_2/(m_1+m_2)$ is the reduced mass of the two colliding species, n is the number density, and $\mathcal{A}(T)$ is the thermally averaged diffusion area which is defined as

$$\mathcal{A}(T) = \frac{\int_0^\infty e^{-E/k_\mathrm{B}T} E^2 \mathcal{A}(E) \mathrm{d}E}{\int_0^\infty e^{-E/k_\mathrm{B}T} E^2 \mathrm{d}E} \tag{2.19}$$

with the diffusion area $\mathcal{A}(E)$

$$\mathcal{A}(E) = \int \mathrm{d}\Omega (1 - \cos\Theta) \frac{\mathrm{d}\sigma}{\mathrm{d}\Omega} \tag{2.20}$$

$$= \frac{4\pi}{k_\mathrm{r}^2} \sum_{\ell=0}^{\infty} (\ell + 1) \sin^2[\eta_{\ell+1}(E) - \eta_\ell(E)] \,, \tag{2.21}$$

where $E = \hbar^2 k_\mathrm{r}/(2\mu)$ is the collision energy with collision wave-number k_r, $\mathrm{d}\sigma/\mathrm{d}\Omega$ is the differential elastic scattering cross section, which now only depends on polar scattering angle Θ, and $\eta_\ell(E)$ is the collisional phase shift for partial wave ℓ and collision energy E. The factor $1 - \cos\Theta$ suppresses the role of small angles Θ in area $\mathcal{A}(T)$ as small angle collisions do not lead to significant diffusion or transfer of momentum between Rb and inert gas atoms or molecules.

Calculations of $D(T, p)$ in this work were carried out by our collaborators at NIST Gaithersburg, Eite Tiesinga and Jacek Kłos [35]. They performed simulations based on *semi-classical*, *classical* and *quantum* models for solving for $\mathcal{A}(T)$ which will be described below.

These models require knowledge of the differential cross section for $^{85}\mathrm{Rb} + X$ as well as $^{87}\mathrm{Rb} + X$ that are based on the electronic potential energy surfaces published by Ref. [25] as well as those by Ref. [24]. The relevant potentials have well depths D_e expressed in energy equivalent temperatures $D_\mathrm{e}/k_\mathrm{B}$ = 1.6 K, 8.8 K, 34 K, 56 K, 97 K, and 150 K for $X = {}^4\mathrm{He}$, $^{20}\mathrm{Ne}$, $^{14}\mathrm{N}_2$, $^{40}\mathrm{Ar}$, $^{84}\mathrm{Kr}$, and $^{132}\mathrm{Xe}$, respectively, and are shallow compared to those of more typical chemical bonds. Moreover, these well depths are smaller than $k_\mathrm{B}T$ for the

temperatures T used in experiments measuring diffusion coefficients in the viscous regime. The standard uncertainties in D_e and, in fact, of the shape of the electronic potential energy surfaces can be found in Ref. [25].

The theoretical simulations involve numerically calculating the regular solutions of radial Schrödinger equations as functions of the separation R between the centre of masses of ^{87}Rb and a noble gas atom or N_2. We thus obtain one equation for each partial wave $\ell = 0, 1, 2, \ldots$. Collisional phase shifts $\eta_\ell(E)$ as functions of collision energy E and ℓ are extracted from the large-R behaviour of these solutions [95]. The reduced mass μ in the kinetic energy operator of the Schrödinger equations is determined from the atomic masses. We have used the atomic masses from Ref. [96] and recommended energy conversion factors from Ref. [97]. Standard uncertainties in the theoretical values for $D(T, p)$ are estimated from scattering calculations performed with the electronic potential energy surfaces obtained from *ab initio* calculations with several basis sets for the electronic wave-functions as described in Ref. [25].

In principle, one would need to determine diffusion coefficients for all isotopologues of systems Rb + X, especially for those elements where more than one isotope has a significant abundance. However, the electronic potential energy surfaces for different isotopologues are the same to a good approximation and we need only to change the reduced mass in the kinetic energy operator of the Schrödinger equations. [35]

2.5.1 Semi-classical approximation

The semi-classical method is analytical, and relies solely on perturbative scattering from the attractive, long-range, van-der-Waals $-C_6/R^6$ component of the electronic potential with a positive dispersion coefficient C_6. The methodology starts with the Born approximation for the phase shift $\eta_\ell(E) = (3\pi/32)(E/E_6)^2/\ell^5$, which is valid for collision energies $E \gg E_6$ and small polar angles $\Theta \ll \pi$ [95]. Here, the van-der-Waals energy is $E_6 = \hbar^2/(2\mu\beta_6^2)$

with van-der-Waals length $\beta_6 = (2\mu C_6/\hbar^2)^{1/4}$, and $\hbar$ is the reduced Planck constant. The van-der-Waals energies for our systems lie between $k_\mathrm{B} \times 0.14$ mK for ^{87}Rb-Xe and $k_\mathrm{B} \times 29$ mK for ^{87}Rb-He. With this ansatz for $\eta_\ell(E)$ and changing the sum over ℓ into an integral, all relevant thermalized quantities can be computed analytically. Specifically, we have for the semiclassical thermalized diffusion area

$$\mathcal{A}_\mathrm{sc}(T) = 3.9728(k_\mathrm{B}T/E_6)^{-1/3}\beta_6^2\,, \tag{2.22}$$

so that $D(T,p) \propto (kT)^{5/6}\mu^{-1/2}C_6^{-1/3}p^{-1}$ (see also Section 2.3.a of Ref. [64]). Although approximate, this model sets expectations for the orders of magnitude of the diffusion coefficients.

2.5.2 Classical and Quantum mechanical models

The classical model is based on the expression for the classical deflection angle in terms of the impact parameter and the collision energy [24, 95]. The classical results are computed numerically using the potentials from Refs. [24, 25]. Again, the differences in values for $D(T,p)$ based on the potentials from Ref. [24] and those from Ref. [25] are smaller than the theoretical uncertainties. It is worth noting that within the classical approximation, Monchick in Ref. [98] found by inspection that for a repulsive exponential potential $V_\mathrm{exp}(R) = V_0\exp(-bR)$ for *all* R, the thermally averaged diffusion coefficient is well described by

$$D(T,p) \propto \frac{(k_\mathrm{B}T)^{3/2}}{[\ln(V_0/k_\mathrm{B}T)]^2 p}\,. \tag{2.23}$$

Here, V_0 and b are the positive parameters of the exponential potential (see also Section 2.3.b of Ref. [64]). This scaling law is appropriate at temperatures above 300 K because the thermal kinetic energy is much larger than the depth of the attractive part of the interaction

potentials.

The quantum calculations are divided into two parts. The first corresponds to "exact" numerical solutions of Schrödinger equations using the most-accurate electronic potentials from Refs. [24, 25] for tens of thousands of pairs ℓ and E with ℓ up to 950 for our heaviest system, and $E < k_{\rm B} \times 3000$ K. The differences in values for $D(T, p)$ based on the potentials from Ref. [24] and those from Ref. [25] are smaller than the theoretical uncertainties. For the second quantum results, we replace the shallow electronic potentials with ones that are purely repulsive. That is, the repulsive wall of the electronic potentials from Ref. [25] for $V(R) > k_{\rm B} \times 45$ K are kept and smoothly connected to a repulsive exponential potential for larger separations. The potential energy at the connection point was chosen to be smaller than our collision energies at room temperature [35].

2.5.3 Results of simulations

Figure 2.10 shows "weighted" differential cross sections $(1 - \cos\Theta)\mathrm{d}\sigma/\mathrm{d}\Omega$ for our ^{87}Rb+X systems as functions of polar scattering angle Θ for collision energy $E = k_{\rm B} \times 300$ K. These differential cross sections are determined using the quantum-mechanical method and using the most-accurate electronic potentials by Ref. [25]. They have a complex, fast oscillatory behaviour for polar angles up to 15° for ^{87}Rb+He and even up to 60° for ^{87}Rb+Xe. Moreover, the amplitude of these oscillations increases with the mass of the inert gas atom or molecule. These oscillations correspond to glory scattering from interferences between waves reflected at different atom-atom separations R [95]. For larger angles the "weighted" differential cross sections are slowly increasing smooth functions. These behaviours are in sharp contrast to those for $\mathrm{d}\sigma/\mathrm{d}\Omega$, which is extremely large and highly peaked for $\Theta < 1°$, *i.e.* near forward scattering. Integrated over all angles, however, the total cross section $\sigma(E) = \int \mathrm{d}\Omega\,(\mathrm{d}\sigma/\mathrm{d}\Omega)$ is only two to three times larger than the diffusion area $\mathcal{A}(E)$ at the same E. Unsurprisingly,

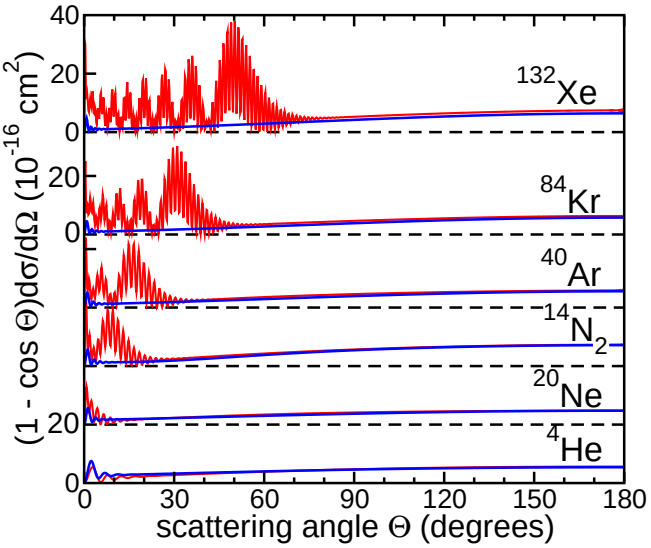

Figure 2.10: "Weighted" differential cross sections $(1-\cos\Theta)\mathrm{d}\sigma/\mathrm{d}\Omega$ at a collision energy of $k_\mathrm{B} \times 300$ K as functions of polar scattering angle Θ for systems $^{87}\mathrm{Rb} + X$, where $X = {}^4\mathrm{He}$, ${}^{20}\mathrm{Ne}$, ${}^{14}\mathrm{N}_2$, ${}^{40}\mathrm{Ar}$, ${}^{84}\mathrm{Kr}$, and ${}^{132}\mathrm{Xe}$. The red curves are obtained from quantum scattering calculations using the most-accurate electronic potentials by Ref. [25]. Blue curves are obtained with quantum scattering calculations using a purely repulsive potential derived from the repulsive wall of the potential for this system (see text for details). Data for the various systems have the same vertical scale but are displaced by unequal amounts for clarity. Dashed black lines correspond to the zero values for the relevant data.

$\mathcal{A}(E) < \sigma(E)$ as small angle Θ scattering does not lead to significant diffusion or transfer of momentum between Rb and inert gas atoms or molecules.

Figure 2.10 also shows $(1 - \cos\Theta)\mathrm{d}\sigma/\mathrm{d}\Omega$ for $^{87}\mathrm{Rb} + X$ systems, where the electronic potential has been replaced by the purely repulsive shape. We find that the rapid oscillations in the forward scattering region are mostly absent, but that for larger polar scattering angles the "weighted" differential cross sections based on the "exact" potential and the repulsive potential are in agreement.

We compare thermalized diffusion coefficients $D(T, p)$ at standard atmospheric pressure as functions of temperature T obtained with *quantum, classical*, and *semi-classical* theoretical methods , along with those measured experimentally over the past fifty years for $^{87}\mathrm{Rb} + {}^{14}\mathrm{N}_2$ in Figure 2.11 [35]. Firstly, we observe that the quantum and classical diffusion coefficients based on the most-accurate potential energy surfaces are identical to within our uncertainties and are slowly increasing. The less than 0.5 % standard uncertainties in $D(T, p)$ for the temperature range shown in the figure are due to uncertainties in the ^{87}Rb-N_2 potential energy surface from Ref. [25]. For temperatures between 300 K and 500 K, classical simulations of $D(T, p)$ are more than adequate. Now, however, we can quantify the degree of agreement using our quantum results.

The blue lines in Figure 2.11 also show $D(T, p)$ based on the quantum-mechanical calculations using the purely repulsive potential. These values are systematically larger than those based on calculations using the most-accurate potential energy surface but have visually identical temperature dependencies. A larger $D(T, p)$ is consistent with the observations in Figure 2.10 for $^{87}\mathrm{Rb} + {}^{14}\mathrm{N}_2$. That is, the difference in $D(T, p)$ for the two calculations is due to differences in the behaviour of $(1 - \cos\Theta)\mathrm{d}\sigma/\mathrm{d}\Omega$ at relatively small polar angles.

The observation regarding the temperature dependence of $D(T, p)$ in the previous paragraph led Eite us to try to fit the theoretical $^{87}\mathrm{Rb} + {}^{14}\mathrm{N}_2$ quantum data in Figure 2.11 to the analytical expression for $D(T, p)$ for an exponential potential given in Equation 2.23.

The fit with its two adjustable parameters reproduces our theoretical data to within their uncertainties, thereby validating the results of Ref. [98]. A naive fit to $(k_{\mathrm{B}}T)^{3/2}$, however, is insufficient to reproduce theoretical results.

Next, Figure 2.11 shows the semi-classical, analytical estimates for $^{87}\mathrm{Rb} + {}^{14}\mathrm{N}_2$. They are significantly lower than the quantum and classical results, *e.g.*, by about 30 %, and have a noticeably weaker T dependence than that found with the quantum or classical simulations. For the ^{87}Rb and rare-gas-atom systems, the analytical estimates are similarly too small. We conclude from the calculations with the purely repulsive potential and the semi-classical, analytical estimates that the diffusion coefficients are mainly determined by the inner repulsive wall of the potential energy surfaces.

Finally, Figure 2.11 shows the available experimental diffusion coefficients for $\mathrm{Rb} + \mathrm{N}_2$ as measured over the past fifty years and over a temperature range between 300 K and 460 K. Our measurement performed at 24 °C is the smallest studied temperature [35]. The experimental data is consistently larger than the theoretical values. The experimental data for other $\mathrm{Rb} + X$ systems do not necessarily follow this pattern, as we will show and discuss in Chapter 4. However, we find our measured $D(T, p)$ to be in agreement with the quantum and classical theoretical calculations after correcting for systematic effects.

We conclude this chapter with some qualitative comments that capture our overall understanding. We started with an investigation of the semiclassical treatment based on an attractive, $1/r^6$ van-der-Waals potential. This approach has been very successful in modelling cold collisions that involve interactions between atoms at long range (small angle scattering) such as in references [99–101]. However, our diffusion measurements and the quantum and classical theoretical calculations disagreed with the $\mu^{-1/2}$ scaling of $D(T, p)$ predicted by the semiclassical theory. The disagreement, while within a factor of two, was still severe, with the semiclassical calculation predicting diffusion coefficients that were about 35% lower than experiment and the quantum and classical theory.

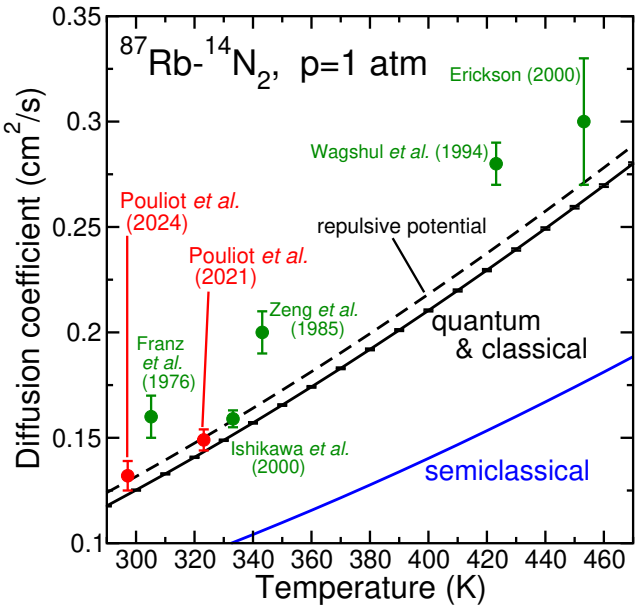

Figure 2.11: Thermalized diffusion coefficients as functions of temperature T for ^{87}Rb+^{14}N$_2$ and at the standard atmospheric pressure of $p = 101\,325$ Pa. The solid black curve with small standard-uncertainty error bars correspond to our quantum simulations as well as the (nearly) indistinguishable classical simulations from Ref. [24]. The dashed black curve corresponds to a quantum simulation using the purely repulsive potential constructed from our most-accurate electronic potential. The blue curve corresponds to the semi-classical, analytical estimate. Two overlapping red markers with standard uncertainties just below $T = 300$ K are from Ref. [33] and [35]. Green markers with standard uncertainties and author labels at higher temperatures correspond to measurements found in Table 1.1. For publications that did not supply an uncertainty budget we assume standard uncertainty 1 in the last significant digit.

The differential cross-sections for the quantum mechanical calculations show a high degree of complexity over a fairly large range of angles (see red curves in Figure 2.10). However, if the electronic potential is replaced by a repulsive barrier in the spirit of hard sphere models, we obtain a much less complex differential cross section (see blue curves in Figure 2.10), which gives similar predictions for $D(T, p)$ as those obtained using the potentials which are the basis for the red curves in Figure 2.10. This observation suggests that diffusion coefficients are mainly determined by the inner repulsive wall of the potential energy surface.

Chapter 3

Experimental apparatus

In this chapter, we describe the two experimental apparatuses used in this work. In Section 3.1 we describe the apparatus used in reference [33] to measure diffusion of ^{87}Rb in a N_2 buffer gas, and compare magnetometer signals based on the evolution of atomic populations or coherences. For these experiments, the Rb-N_2 mixture is contained in a sealed cell, which was also used to compare population and coherence magnetometry. In Section 3.2 we describe the apparatus used in reference [35] to measure diffusion of naturally abundant Rb atoms in the presence of N_2, He, Ne, Ar, Kr, and Xe.

3.1 Apparatus for comparison of population and coherence magnetometers and demonstration of diffusion measurement technique

The first apparatus relies on a home-built external-cavity diode laser (ECDL) [40] that seeds a tapered amplifier (TA) with ≈15 mW of light to produce an output power of 2 W [41].

The ECDL is frequency stabilized with respect to the $F = 2 \rightarrow F' = 2, 3$ crossover peak

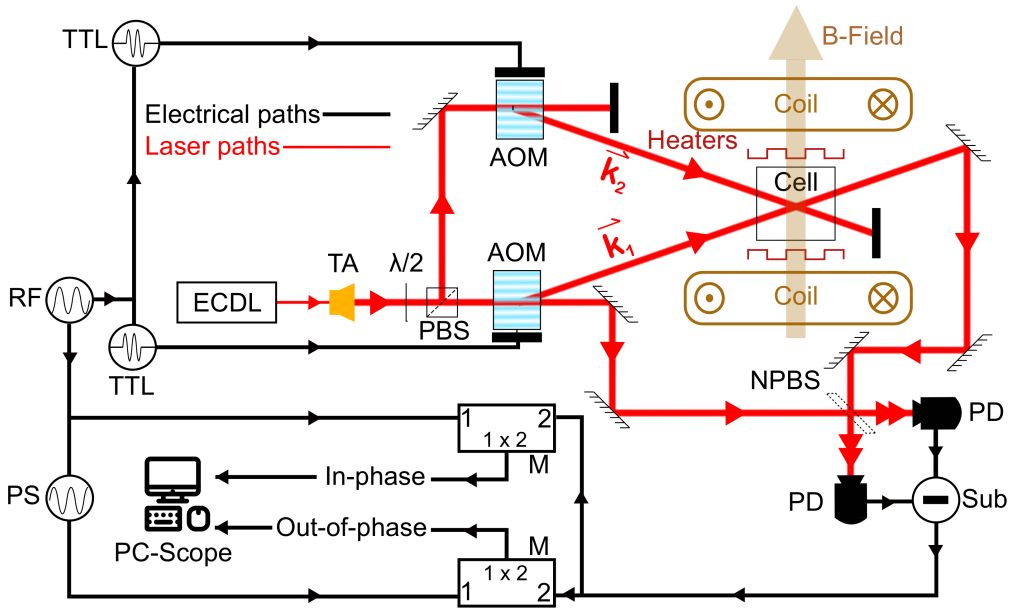

Figure 3.1: Schematic of the experimental set–up. The laser (ECDL) seeds the TA, the output of which is split by half wave plate ($\lambda/2$)—polarizing beam splitter (PBS) and sent to the two AOMs. The two AOMs are driven by 80 MHz pulses produced by the RF generator (RF), and their respective TTL switches. In the diffusion measurements, the coils minimize the external field ($B \approx 0$). The signal from the cell is overlapped with an optical LO (undiffracted beam from the k_1 AOM) on a non-polarizing beam splitter (NPBS) to produce a heterodyne signal recorded on two photodiodes (PD). These signals are subtracted to remove DC amplitude fluctuations. The subtracted signal, which is an amplitude modulated 80 MHz beat-note, is mixed down using RF mixers (M) to DC using the RF oscillator diving the AOMS, and a 90° phase shifted oscillator produced by phase–shifting cable (PS). The in–phase and out–of–phase components of the signal are obtained in this manner. These mixed–down signals are recorded and analyzed on the PC oscilloscope.

on the D2 line in ^{87}Rb (see Figure 3.4) using saturated absorption in a 5 cm-long vapour cell. The output of the TA is split into two beams, each amplitude modulated by an 80-MHz acousto-optic modulator (AOM) as shown in Figure 3.1. The AOMs are driven by a radio frequency (RF) network consisting of an RF generator, RF amplifiers, transistor-transistor logic (TTL) switches, and pulse generators. By adjusting the power and timing of the RF pulses, the power and pulse sequence of the (diffracted) AOM outputs may be varied. The up-shifted beams from these AOMs, which are at a frequency of 53 MHz below the $F = 2 \rightarrow F' = 3$ resonance, are aligned along directions $\vec{k}_1$ and $\vec{k}_2$ through a 10-cm, quartz,

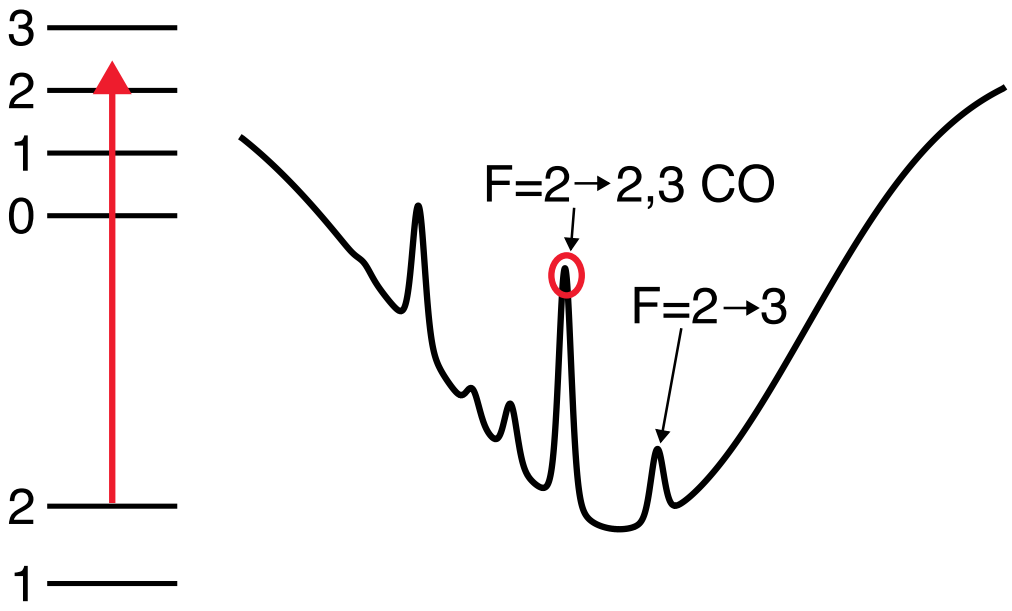

Figure 3.2: Level diagram showing the energy of the optical field relative to the ^{87}Rb hyperfine $5^2S_{1.2} \rightarrow 5^2P_{3/2}$ transitions. The right side shows the saturated absorption profile for the ^{87}Rb $F = 2 \rightarrow F'$ transitions where F' is $1, 2, 3$ including the crossover peaks induced by simultaneous excitation of *different* velocity classes by the counter-propagating pump and probe laser beams. The laser frequency is locked to the highlighted $F = 2 \rightarrow 2, 3$ crossover peak.

vapour cell containing isotopically pure ^{87}Rb and 564 ± 2 Torr of N_2. The isotopic purity of the cell simplifies its magnetic response, but it is not a primary requirement for the diffusion measurement, which is insensitive to magnetic fields and isotopic differences.

3.1.1 Pressure measurement

To determine the pressure in the sealed cell, we scanned a free-running laser diode with an estimated linewidth of 50 MHz across the pressure-broadened (and pressure-shifted) resonances in the isotopically purified ^{87}Rb. This technique is described in detail in Appendix C, and is shown schematically in Figure 3.3. Absorption spectra were recorded on a photomultiplier tube (PMT) for a range of logarithmically varied laser powers from 1 – 2 µW, for which there are no detectable optical pumping effects. Optical pumping is observed as a narrowing of the collisionally broadened absorption line, as atoms in a state that is currently being addressed by the laser are quickly pumped into a state with a resonance farther from the laser frequency. By recording absorption spectra with logarithmically varied laser powers of 1 pW up to 1 mW, we were able to identify the 1–2 µW range being low enough that optical pumping does not distort the absorption line while also providing a good signal-to-noise ratio on the PMT.

The laser diode was scanned at rates of 21–106 Hz with 10,000–30,000 samples per sweep, and the laser frequency was scanned over a range of ≈60 GHz. The spectrum was obtained by averaging 560–1660 sweeps of the frequency range. To provide a frequency calibration, a reference scan was simultaneously recorded in a vapour cell containing a natural isotopic abundance of Rb at room temperature. A photodiode was used to record the laser intensity variation during the scan. This information was used to model frequency dependent intensity variations of the laser diode, such as those caused by etalon effects and the diode gain curve. To infer the N_2 gas concentration from the measured spectrum, as well as the N_2 pressure in

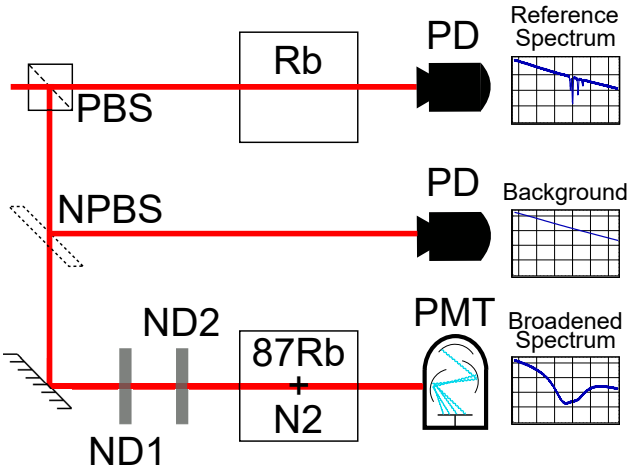

Figure 3.3: Schematic of experimental set up to measure the pressure in the isotopically purified ^{87}Rb cell. A diode laser is scanned over ~ 60 GHz by scanning the current. The power of the laser is attenuated using two 13 dB ND filters to avoid spectral distortions due to optical pumping. The frequency scan is calibrated using the spectrum of a low–pressure reference cell. Power fluctuations in the laser output are calibrated by recording the laser intensity on a photodiode. The pressure–broadened spectrum of the ^{87}Rb cell is recorded using a PMT.

the cell, we perform a fit to the collisionally broadened and shifted profile of ^{87}Rb as shown in Figure 3.4.

3.1.2 Signal detection

The isotopically pure experimental cell is insulated and maintained at a temperature of 50 ± 2 °C using a resistive heater. As shown in Figure 3.1, the cell is placed in a constant magnetic field transverse to the direction of laser propagation. The B field is produced by a pair of "racetrack" coils with an elliptical cross section. The undiffracted beam from the $\vec{k_1}$ AOM, at a frequency 80 MHz below the frequency of the diffracted beam, bypasses the cell and is combined with the beam along $\vec{k_1}$ on a beam-splitter downstream from the cell. The outputs of the beam-splitter that contain a heterodyne signal with a beat frequency of 80 MHz are incident on a balanced detector. This detector consists of two Si:PIN photodiodes with 1-ns rise times that are biased to produce signals with opposite polarity. The combined,

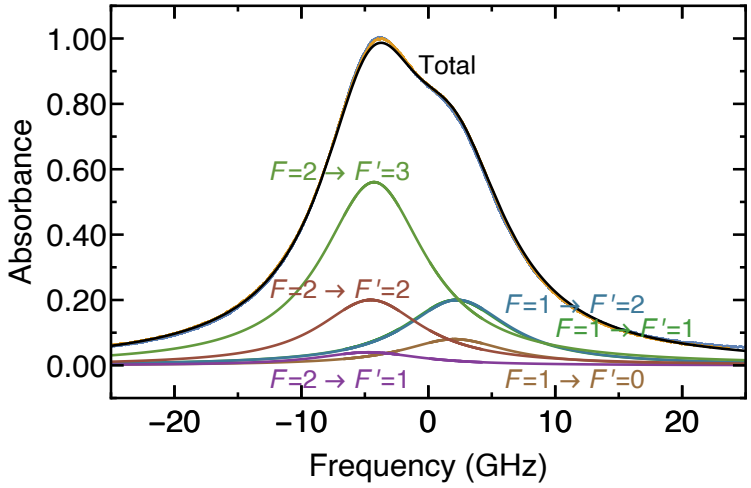

Figure 3.4: Absorption spectrum from the isotopically pure experimental cell fitted to composite spectrum for ^{87}Rb resonances. Blue and yellow curves show data from the upward and downward frequency scan respectively, the best fit to both of these curves is shown in black. Individual resonances are shown with broadening and shift parameters determined by the fit and strengths and centres relative to each other taken from reference [102]. The frequency axis is relative to the $F = 2 \rightarrow F' = 3$ transition on the D2 line ($5^2S_{1/2} \rightarrow 5^2P_{3/2}$) in ^{87}Rb.

80-MHz signal from the photodiodes is amplified and mixed down to DC to generate the in-phase and $\pi/2$ out-of-phase components. These signal envelopes are further amplified and recorded on a 12-bit analog to digital converter (ADC) with a bandwidth of 125 MHz corresponding to a two-channel acquisition rate of 250 million samples per second. The total amplitude a_T is obtained by adding the two signal components a_1 and a_2 in quadrature $a_T = \sqrt{a_1^2 + a_2^2}$. The experiment is operated at approximately 1-kHz repetition rates using digital delay generators. The time base of these generators is referenced to a 10-MHz rubidium atomic clock [103] with an Allan deviation floor value of 3×10^{-13} at 1 h. The pulses from the delay generators are coupled to the AOMs using TTL switches. The RF generator that produces the 80 MHz AOM drive frequency is also phase locked to the same 10-MHz output of the rubidium clock. This practice ensures phase noise makes a negligible contribution to the error of this measurement.

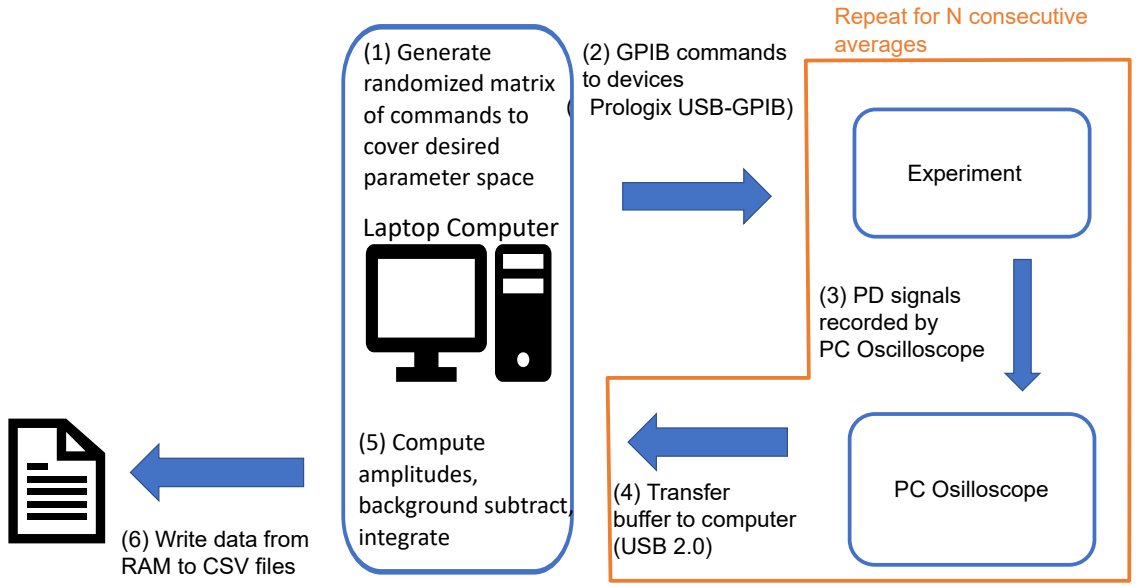

Figure 3.5: Schematic of automated data acquisition loop used in reference [33]. Pulse generators, power supplies and data acquisition oscilloscope were controlled using LabView on laptop computer. Commands to pulse generators and power supplies were issued over GPIB using a USB-GPIB controller. Commands to PC oscilloscope were issued over USB. Background subtraction and integration was done in real time in LabView and saved in comma-separated variable (CSV) files. All raw data also saved as CSV files for error diagnostics and further analysis.

The same setup was used to generate signals from the coherence grating (MGFID) and the population grating (as shown in Figure 1.3 of Chapter 2. The quartz vapour cell was replaced with a pyrex cell containing a natural abundance of ^{85}Rb and ^{87}Rb isotopes and no buffer gas to record reference MGFID signals. The important difference between this cell and the previously mentioned cell is the absence of a buffer gas. For studies of the population magnetometer (see Figure 1.1 in Chapter 1), which were carried out in the quartz cell containing isotopically pure ^{87}Rb vapour, the k_2 beam was circularly polarized and served as the pump, while the k_1 beam was linearly polarized and attenuated to serve as the probe. The signal was recorded by measuring the differential absorption of the oppositely polarized circular components of the probe beam that are split by the $\lambda/4$ waveplate-cube beam splitter combination shown in Figure 1.1.

In all of these experiments, the decay of the signal is recorded by varying the delay time of the read-out or probe pulses and recording the average of 80–100 repetitions. This process was automated by a LabView program running on a laptop computer. The data acquisition loop is shown in Figure 3.5.

3.1.3 Angle Measurement

The angle between $\vec{k_1}$ and $\vec{k_2}$ was measured using a scanning knife edge profiler with a rotation frequency of ≈10 Hz. The separation between the beams was measured at two locations separated by ≈2 m. The centre of each beam was located using Gaussian fits to the profiler output, allowing the separation between beams to be determined. The variation in the rotation frequency as a function of time was characterized by an Allan deviation plot (see Appendix B). The errors in the rotation frequency and separation were then propagated and combined in quadrature to obtain the error in the angle. To ensure that the condition for diffusion (Equation 1.3) was met for the 564 Torr cell, the selected angles ranged from 1.5 to 9 mrad, corresponding to grating spacings of 10–80 µm, about two orders of magnitude greater than the mean-free path for 564 Torr of N_2 (≈280 nm)

3.2 Apparatus for pressure varied diffusion measurements with different buffer gases

The second apparatus is also based on the same home-built ECDL [40] and MOPA system [41]. However, instead of sealed cells containing rubidium samples, the experiment is performed in a vacuum system which includes an experimental cell containing naturally abundant Rb vapour and in which the pressure of the inert gases can be varied. In this apparatus, the cell is maintained at a temperature of 24°C.

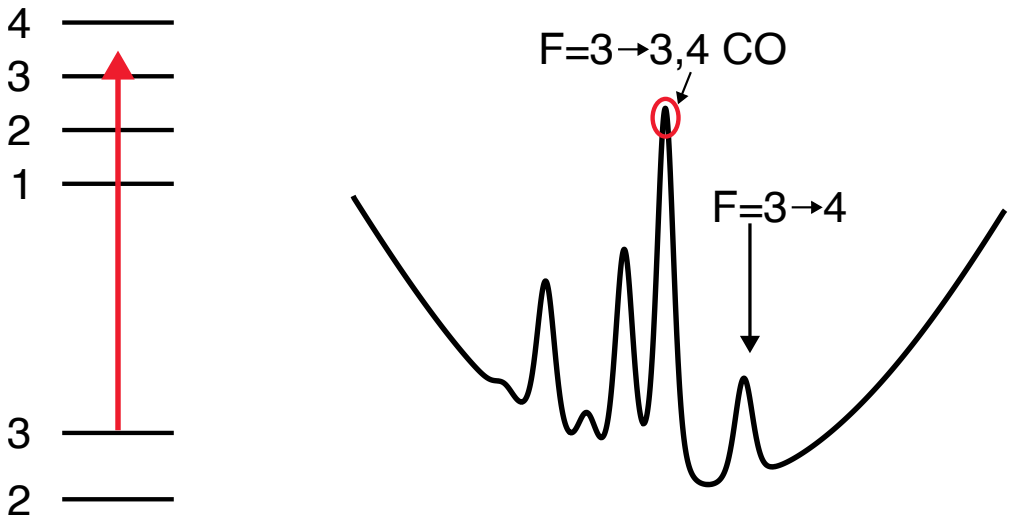

Figure 3.6: Level diagram showing the energy of the optical field relative to the ^{85}Rb hyperfine $5^2S_{1.2} \rightarrow 5^2P_{3/2}$ transitions. The right side shows the saturated absorption profile for the ^{85}Rb $F = 3 \rightarrow F'$ transitions where F' is $2, 3, 4$ including the crossover peaks induced by simultaneous excitation of *different* velocity classes by the counter-propagating pump and probe laser beams. The laser frequency is locked to the highlighted $F = 3 \rightarrow 3, 4$ crossover peak.

The ECDL is frequency stabilized with respect to a D2 line in ^{85}Rb using saturated absorption spectroscopy in a 5 cm long Rb reference cell that contains no buffer gas. The lock point coincides with the peak of the $F = 3 \rightarrow F' = 3, 4$ crossover resonance in ^{85}Rb, which is 60.3 MHz red detuned from the $F = 3 \rightarrow F' = 4$ transition for a ^{85}Rb atom at rest (see Figure 3.6). The output of the TA is split into two beams, each amplitude modulated by an 80-MHz AOM.

The AOMs are driven by an RF network consisting of an RF synthesizer, RF amplifiers, transistor-transistor logic (TTL) switches, and pulse generators. This RF network is depicted in Figure 3.7. The sinusoidal 80 MHz sinusoid is created by the waveform generator. This signal is then sent to a coupler, the coupled (≈10% of input power) output is used to trigger the pulse generators, the main output (≈90% of the input power) is sent to an amplifier. The amplified signal is sent to a second coupler, whose main output is used to mix down measured signals (see Figure 3.14), while the coupled output continues to a splitter/combiner

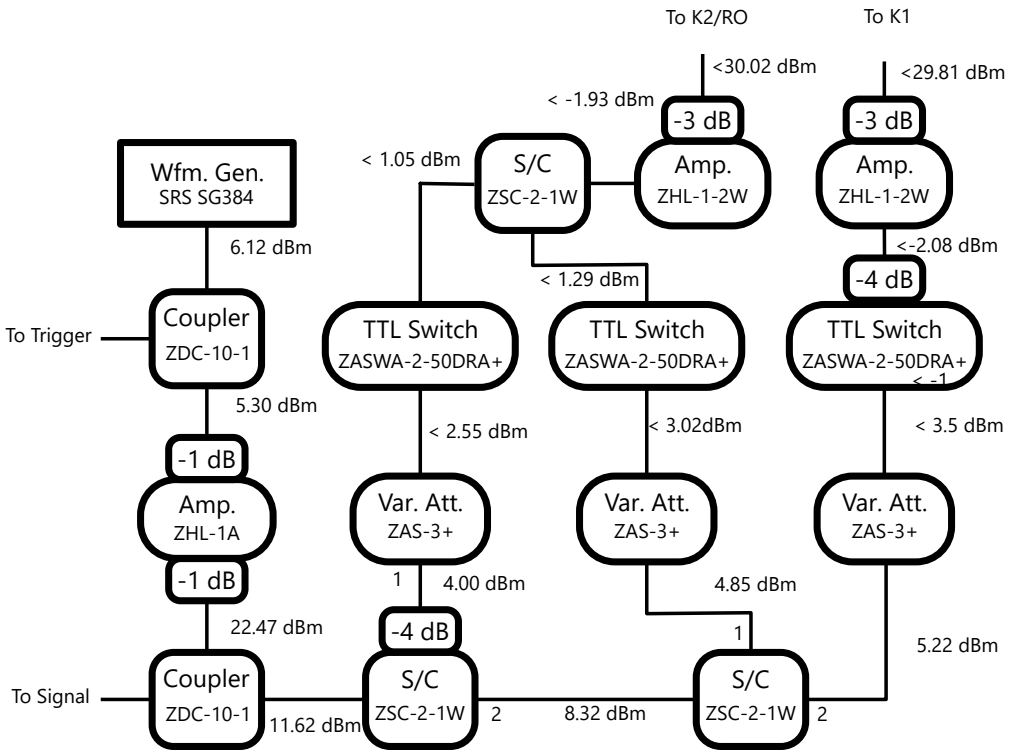

Figure 3.7: RF network for driving AOMs in diffusion experiment. 80 MHz RF signal from the waveform generator (Wfm. Gen.), is sent through a network of Couplers, amplifiers (Amp.), splitter/ combiners (S/C), variable attenuators (Var. Att.) and TTL switches to provide the desired driving frequencies. Passive xdB attenuators are labelled "-x dB". Portions of the RF signal split off to trigger the pulse generators and to mix down the signal from the photodiodes.

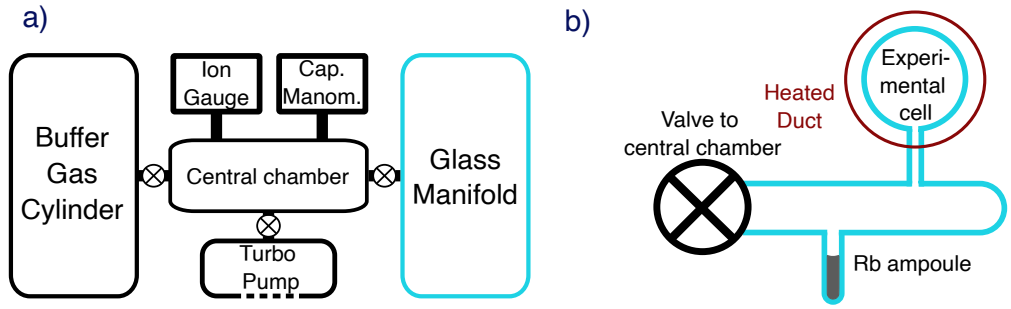

Figure 3.8: a) Sketch of gas handling apparatus including the glass manifold. Gate valves are represented by circles with crosses. A capacitance manometer ("Cap. Manom." in the figure) measures pressures in the central chamber between 0.1 Torr and 1000 Torr, while an ion gauge measures pressures from 10^{-9} Torr to 10^{-4} Torr. b) Detailed sketch of the glass manifold with the valve connecting the manifold to the central chamber shown in panel a). The cylindrical out-of-plane heated duct (red circle) helps maintain a constant rubidium vapour density in the experimental cell.

(S/C). One output of the splitter is sent to a second splitter. The resulting three outputs are each sent to a variable attenuator, whose control voltage is set by the pulse generators. From this point onward, powers in Figure 3.7 are quoted as less than their maximum value, which corresponds to the minimum attenuation level of the attenuator. The three attenuated signals are sent to TTL switches which apply the pulse envelopes defined by the pulse generators. After this, two of the three pulsed signals are combined, these are the readout and $\vec{k}_2$ pulses. The cable lengths carrying these pulses are adjusted to ensure that the phase difference between them is close to π, this ensures that if the pulses accidentally overlap, that they do not interfere constructively and produce a potentially damaging pulse power. The combined pulses are sent to the $\vec{k}_2/RO$ AOM, while the third pulse is sent to the $\vec{k}_1$ AOM.

The frequency up-shifted, 3 mm diameter laser beams emerging from the two AOMs are aligned along the nearly parallel directions $\vec{k}_1$ and $\vec{k}_2$, respectively, and aligned through the atomic vapour cell.

The vacuum system is schematically shown in Figure 3.8a with a more detailed diagram of the Pyrex glass manifold shown in Figure 3.8b. The cylindrical experimental atomic vapour

cell has a diameter of 5.1 cm, a length of 5.1 cm, and circular end-faces of thickness 0.3 cm. This cell is attached to a Pyrex manifold by a thin stem of length 4.4 cm and an outer diameter of 0.3 cm, located halfway along the length of the cylinder. The $\vec{k}_1$ and $\vec{k}_2$ laser beams are well collimated (with a Rayleigh range of ≈ 1 m), aligned perpendicular to the end-faces of the experimental cell, and strongly overlapped over the cell length. One end of the Pyrex manifold, which has a glass-to-metal graded seal, is attached to a gate valve. A glass ampoule containing a sample of natural isotopic abundance Rb is fused to the cylinder below the experimental cell as shown in Figure 3.8b. A gate valve attaches the glass manifold to a small stainless-steel central vacuum chamber. The glass manifold can be evacuated by a turbo pump and then filled with rubidium as described below. The central chamber can also be filled with inert gases from a high-pressure gas cylinder via a stainless-steel gas line through a second gate valve.

The pressure in the experimental cell is measured using a capacitance manometer in the central chamber with the connecting valve open. The manometer has an operating range between 0.1 Torr and 1000 Torr with at worst a 0.2 % fractional standard uncertainty. The central chamber and glass manifold can be evacuated to $\approx 10^{-8}$ Torr by a turbo pump with a pumping speed of 70 L/s. Our base, or lowest-achievable pressure, is 5×10^{-9} Torr. When the vacuum system is operated below 10^{-4} Torr, *e.g.* while pumping out the central chamber and glass manifold, a micro-ion gauge is used to monitor the pressure. The turbo pump is attached to a roughing pump rated at 200 L/s through a fore-line bellows hose (not shown in Figure 3.8). The fore-line pressure is monitored by a Pirani gauge.

Before a buffer gas can be introduced into the experimental cell from the central chamber, rubidium vapour is cycled into the experimental cell by repeatedly heating the rubidium ampoule and the glass walls of the manifold for ten minutes at a time, in order to create thermal gradients between the pyrex manifold and the experimental cell that speed up the introduction of the Rb vapour into the cell. This loading procedure is necessary because the

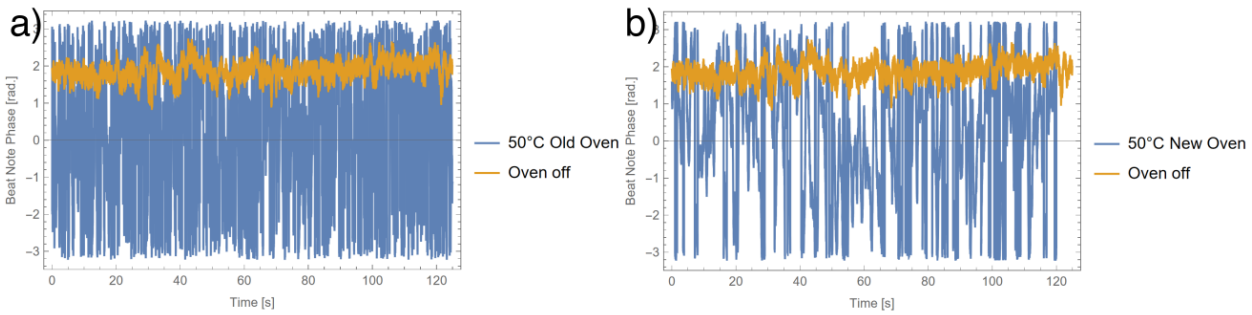

Figure 3.9: Comparison of the phase noise between the local oscillator and excitation beams in a) an oven design based on an insulated box fed forced air from a heat gun begin controlled by a PID loop and b) an aluminum duct wrapped in heater tape with a constant current. The phase noise is measured by running the $\vec{k}_1$ and LO beams CW and overlapping them to observe their beat-note. The noise is compared to the baseline beat-note when the oven is not running.

migration of rubidium is highly restricted due to collisions after the buffer gas is added [104].

3.2.1 Heating the experimental cell

Stable and sufficiently large rubidium vapour pressures in the experimental cell are needed to optimize the observed signals. This is accomplished by surrounding the cylindrical experimental cell with a heated cylindrical aluminum duct, 10.1 cm in diameter and protruding 20 cm on either side of the length of the experimental cell. Earlier designs of the oven utilized forced hot air from a heat gun attached to an insulated box surrounding the glass manifold via aluminum ducts. The heat gun was incorporated in a PID loop to stabilize the temperature of a thermocouple located inside the insulated box. This design had to be abandoned as it was found that the hot air currents introduced significant phase noise between the excitation and signal beams and the local oscillator. The heterodyne detection method is extremely sensitive to this phase noise as shown in Figure 3.9. The final design with no forced air, and the local oscillator passing through the oven, was chosen over similar designs because it was able to minimize this phase noise.

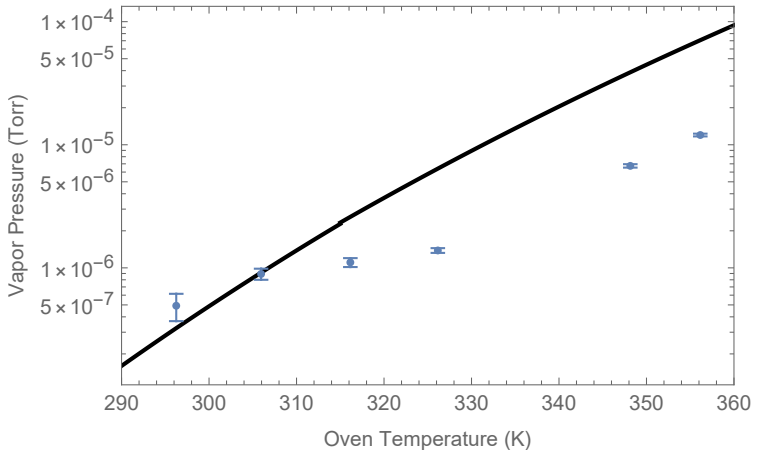

Figure 3.10: Rb vapour pressure as the duct temperature is increased from 23 °C to 83 °C (blue points) in the presence of 416 Torr of N_2 gas. The black line shows the expected vapour pressure curve for Rb as a function of temperature. Deviations from the black line are attributed to insufficient Rb coating the walls of the experimental cell and the gradual migration of Rb out of the experimental cell.

To minimize phase noise, one would ideally create an air-tight chamber around the cell and surround it with heater tape, which would minimize the possibility of bulk air currents in the beam paths. However, it was not possible to create such an airtight box around the delicate glass manifold. Future measurements are being performed with a PMT which is not sensitive to the phase of the signal [47].

In the final design, the duct has a circular hole of diameter 4 cm to accommodate the thin glass stem of the experimental cell. The duct is wrapped in resistive heater tape and the air just inside the duct is maintained at a temperature of 50(2) °C as measured by a thermocouple between the top of the experimental cell and the heated duct. As a result of the 4 cm hole in the duct, there is a steady-state convective flow of air from the surrounding laboratory at $T_{\text{lab}} = 23$ °C in through the hole and out through the ends of the heated duct. Under these conditions, the walls of the experimental glass cell are coldest near the stem, and hottest on the opposite, upper side. In recent work [47], this oven design has been successfully modified to achieve uniform high temperatures throughout the cell.

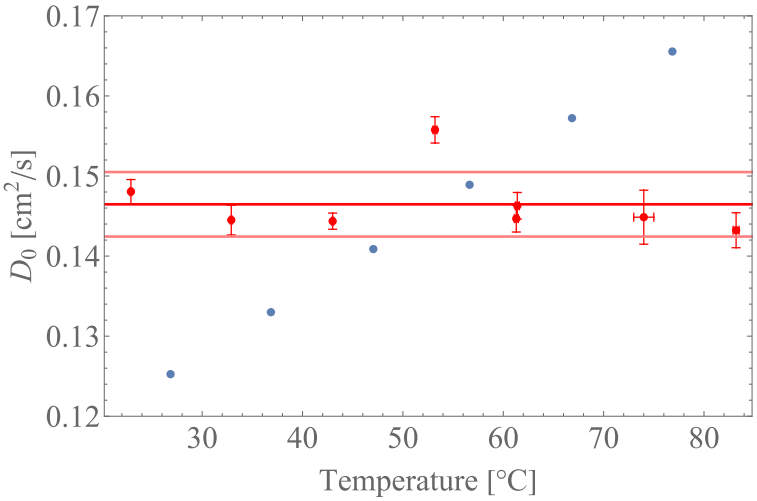

Figure 3.11: Measured diffusion values (red points) in the presence of 416 Torr of N_2 as a function of the temperature as measured by the thermocouple in the air between the heated duct and the top of the experimental cell. Since these diffusion values are taken from single measurements (instead of by varying the angle) the effect of residual light optical pumping cannot be meaningfully subtracted. The values shown assume there is no residual light pumping, as such their absolute values are not meaningful, but their trend as a function of temperature is meaningful. Thick red line shows the mean of the measured diffusion values, and fainter red lines show one standard deviation above and below the mean. Blue points indicate the theoretical value of Rb-N_2 diffusion as a function of temperature at this pressure. Comparing the trends of the blue and red points demonstrates that although the temperature outside the experimental cell is changing by 60 °C, the temperature inside the cell (conservatively) cannot change by more than $\approx$ 5 °C (the theoretical change in temperature corresponding to the standard deviation of the measured values)

This configuration ensures that the rubidium density at the centre of the cell is enhanced by the vapour leaving the hottest surface. The absorption spectra of a probe laser passing through the centre of the cell indicate that the rubidium density is about a factor of 10 larger than its value without heating. The estimated rubidium density as a function of temperature is plotted in Figure 3.10. The process to obtain the density spectroscopically is described in detail in Appendix C. Despite the increased Rb density, the gas mixture near the centre of the cell illuminated by the laser beams is inferred to be at a temperature of 24.0(5) °C.

This inference is supported by two separate considerations. Firstly, we find that measurements of $D(T, p)$ in N_2 remain unchanged within experimental uncertainty of 1 % for a fixed

angle and pressure when the temperature of the duct is increased from 23 °C to 83 °C. In contrast, for this temperature variation, $D(T, p)$ is expected to increase by 42 % for N_2 based on the theoretical predictions and experimental data shown in Figure 2.11. We compare our measured diffusion to the expected diffusion at the temperature measured by the oven thermocouple in Figure 3.11. A stable measured $D(T, p)$ with its 1 % accuracy then implies that the temperature of the gas mixture at the centre of the cell can be no higher than 24 °C for the typical duct temperature of 50 °C. In addition, the room temperature of 23 °C places a lower bound on the gas temperature. Secondly, a simulation based on the heat equation and the steady-state Navier-Stokes equations, that uses measured temperatures around the cell and the thermal conductivities of the gas and Pyrex glass, provides confirmation of this temperature range.

We observe a gradual depletion of rubidium vapour in the experimental cell over the course of days due to the thermal gradients. These observations are consistent with a non-equilibrium distribution of rubidium. Under these conditions, the rubidium density is strongly influenced by the hottest surfaces of the cell. We monitor the rubidium density in the experimental cell by measuring collisionally broadened Rb spectra [33]. When the Rb is depleted, we evacuate the system to base pressure and reintroduce rubidium and buffer gas.

3.2.2 Cancellation of ambient magnetic fields and gradients

We cancel ambient magnetic fields using three pairs of square magnetic-field coils, oriented along three orthogonal axes and with currents running in the same direction as depicted in Figure 3.12. The coils in each pair are separated by 0.55ℓ, where ℓ is the side length of the square, and are centred on the experimental cell. We cancel linear magnetic field gradients using three additional coil pairs in the same geometry. These additional coils have currents in opposite directions.

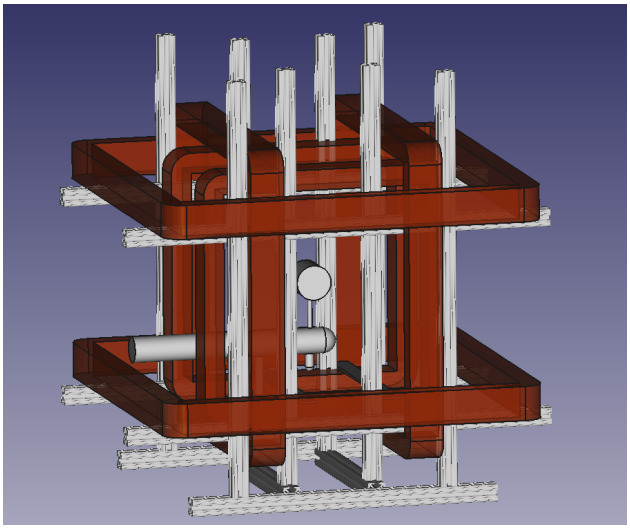

Figure 3.12: CAD drawing of cell inside field coils. The coils centred on the front-back axis have 100 turns in the Helmholtz (current in the two coils same direction) configuration and 60 turns in the anti-Helmholtz configuration (current in two coils go in opposite directions). They have an interior side-length of 50.6 cm and a thickness of 5.0 cm. The coils centred on the left-right axis have 100 turns Helmholtz and 50 turns anti-Helmholtz. They have an interior side-length of 40.5 cm and a thickness of 5.0 cm. The coils centred on the front-back axis have 100 turns Helmholtz and 40 turns anti-Helmholtz. They have an interior side-length of 30.6 cm and a thickness of 5.0 cm. The experimental cell in the centre of the coils has a length of 5.1 cm and a diameter of 5.1 cm.

A finite magnetic field and gradient are initially set to easily record an oscillatory signal associated with Rb Larmor precession from a coherence grating magnetometer, as in the experiments carried out using the apparatus described in Section 3.1. Subsequently, the field and gradient are iteratively reduced to zero to maximize the coherently scattered light signal from the Rb population grating. In the current work, this iterative procedure is applied to all three axes, whereas in Section 3.1 we only reduced the magnetic field and gradient along the direction $\vec{k}_1 - \vec{k}_2$.

3.2.3 Pressure measurement

The pressure of the inert gas in the experimental cell is measured using the capacitance manometer and is independently verified, typically to within 20 %, using atomic spectroscopy of Rb resonances similar to what was performed in Section 3.1 and described in detail in Appendix C. In this latter approach, the pressure is determined from a fit to the collisionally broadened and shifted rubidium lines. Figure 3.13 shows an example of such a Rb spectrum for trace amounts of Rb in a N_2 buffer gas as well as a fit to the spectrum [34]. Using the shift and broadening parameters from Ref. [86] and assuming that these parameters are independent of temperature for the relevant temperature range, the fit gives a N_2 pressure of 145.7(5) Torr while the capacitance manometer reading is 134.10(5) Torr. Moreover, we determine the Rb number density to be $8.2(4) \times 10^{10}$ cm^{-3}, from the fitted signal amplitude of the spectrum. The Rb density can be inferred from the amplitude using the known length of the experimental cell, D2 transition dipole moments of ^{85}Rb and ^{87}Rb [102, 105], and the isotopic abundances of ^{85}Rb and ^{87}Rb.

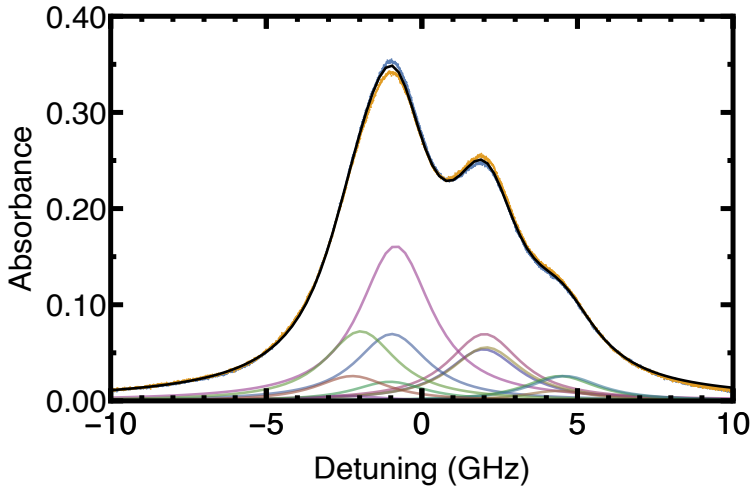

Figure 3.13: Rubidium absorption spectra a cell of length 5 cm at $T = 24.0(5)$ °C and a pressure of 134.10(5) Torr of N_2 buffer gas as measured by the capacitance gauge. The plot shows absorbance $-\ln(I/I_0)$ as a function of laser detuning, where I and I_0 are the transmitted and off-resonant transmitted laser intensities, respectively, and the laser detuning is relative to the $F = 3 \rightarrow F' = 4$ hyperfine transition frequency of the D2 line in ^{85}Rb in its rest frame and absent any buffer gas. Blue and yellow traces correspond to data from upward and downward scans of the laser frequency. A fit of both traces to the composite spectrum for collisionally broadened and shifted ^{85}Rb and ^{87}Rb D2 hyperfine transitions is shown in black [33]. Individual D2 hyperfine line profiles are also shown as coloured lines, the most prominent of these coloured lines is the collisionally broadened and shifted $F = 3 \rightarrow F' = 4$ line in ^{85}Rb.

3.2.4 Signal detection

The heterodyne detection technique is illustrated in Figure 3.15. The undiffracted laser beam from the $\vec{k}_1$ AOM, at a frequency 80 MHz below the frequency of the diffracted $\vec{k}_1$ beam, serves as a local oscillator (LO) and travels through the air gap between the heated duct and the glass cell. The LO is combined with the beam along $\vec{k}_1$ that passes through the centre of the experimental cell on a beam-splitter downstream from the cell. Among other possible configurations, this path of the LO minimizes phase noise relative to the $\vec{k}_1$ beam. The two outputs of the beam splitter, which consist of heterodyne signals that have a relative π phase shift and a beat frequency of 80 MHz, are incident on the two photodiodes of a balanced detector. These Si:PIN photodiodes have 1 ns rise times and are reverse-biased with voltages of opposite polarity. As a result, the combined heterodyne signals of the two photodiodes add in phase, while their DC offsets cancel.

The combined 80 MHz signal from the photodiodes is gated by a TTL switch so as to shield the downstream amplifiers from the intense excitation pulse, while allowing the scattered signal to pass through at the time the read-out pulse is applied. The signal from the switch is then amplified and mixed down to DC using the RF oscillator that drives the AOMs to generate the in-phase and $\pi/2$-out-of-phase components. The RF network performing this function is shown in Figure 3.14. The mixed down signal envelopes are further amplified and recorded using an 8-bit analog to digital converter (ADC) with a bandwidth of 125 MHz at a sample acquisition rate of 500×10^6 per second in each channel.

3.2.5 Data acquisition

The experiment is operated at an approximately 1 kHz repetition rate using digital delay generators. The time base of these generators is synchronized to the 10 MHz clock of a radio-frequency synthesizer [106]. The delay generators are also triggered by the clock signal

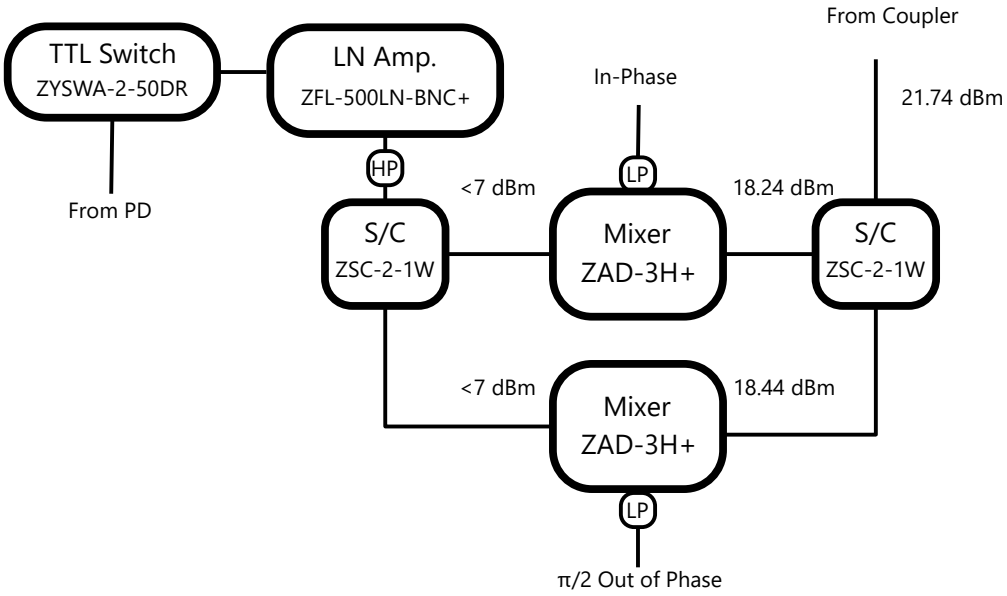

Figure 3.14: RF network for mixing down heterodyne signal. Photodiode signal is gated by a TTL switch to protect amplifiers from the high-power excitation pulse. The signal is amplified by a low noise amplifier (LN Amp.), and sent through a 150 kHz high pass filter (HP) to remove slow drifts. The signal is the split, and combined with mixers, whose local oscillator inputs are driven by RF from the AOM driving RF network (Figure 3.7). The cable lengths of the local oscillators are adjusted so that there is a relative $\pi/2$ phase shift in the 80 MHz signals, while the cable lengths carrying the signal are set to ensure there is no phase difference. The mixed down output goes through a 22 MHz low pass filter (LP) to remove leakage of the 80 MHz LO.

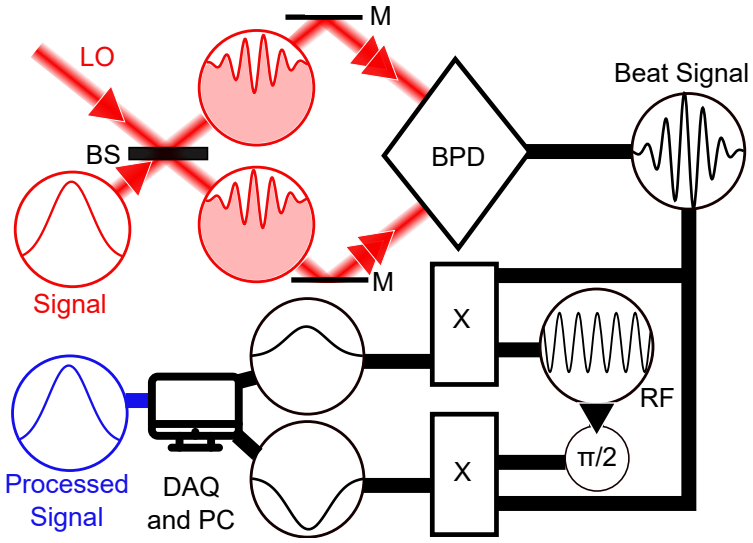

Figure 3.15: Simplified diagram of our heterodyne detection setup. Optical signals are shown in red, analog electronic signals are shown in black, and digital electronic signals are shown in blue. LO - local oscillator light from the $\vec{k}_1$ AOM; BS - 50:50 beamsplitter; BPD - balanced photodiodes; M - mirrors; RF - RF signal used to drive the AOMs, and used here to demodulate the heterodyne signal $\pi/2$ - $\pi/2$ phase shifter; X - RF mixers.

to reduce jitter. The pulses from the delay generators are coupled to the AOMs using TTL switches with an RF extinction ratio of 80 dB. Nevertheless, this optical setup produces residual scattered light along $\vec{k}_1$ and $\vec{k}_2$ at the level of a few µW even when the AOMs are turned off. The level of the background light depends on alignment and varies on a timescale of days.

Data acquisition is controlled and automated by a LabView program that features numerous improvements over the one that was used in Section 3.1.2. The data acquisition loop is shown in Figure 3.16 with improvements over the previous system highlighted in red. The experiments in the pressure-varied apparatus required measurements taken over a much larger range in parameter space than the experiments in the sealed N_2 cell. For example, the diffusion measurement in Section 3.1 ultimately relied on 20 measured grating decays, while for the pressure varied experiments, a minimum of 50 decays would be needed for each of the

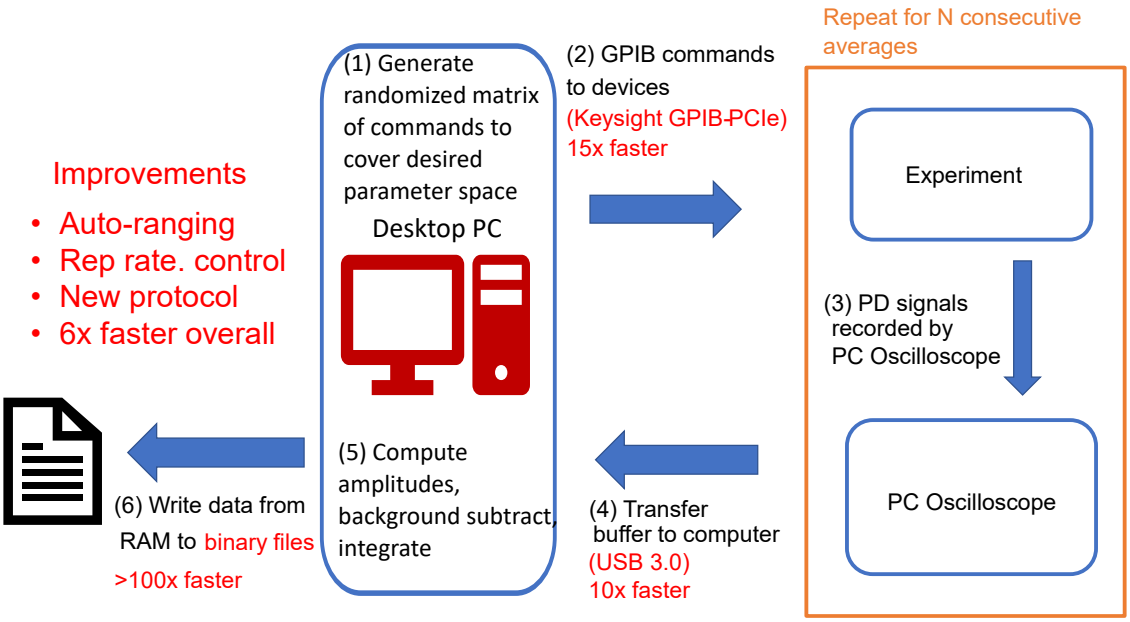

Figure 3.16: Schematic of automated data acquisition loop used in reference [35]. Improvements over the loop in Figure 3.5 are highlighted in red. Pulse generators, power supplies and data acquisition oscilloscope were controlled using LabView on desktop PC. Commands to pulse generators and power supplies were issued over GPIB. Commands to PC oscilloscope were issued over USB. Background subtraction and integration was done in real time in LabView and saved in binary TDMS files. All raw data are also saved as binary files for error diagnostics and further analysis

six buffer gases, and ultimately more than 100 decays were required in some gases in order to obtain a clear picture. While measurement times of 30-45 minutes per decay were acceptable in the experiments in Section 3.1 that would not be feasible in this round of measurements.

The primary bottleneck in the data acquisition loop in Figure 3.5 was the saving of data to CSV files. The LabView program was modified to save binary files in the National Instruments TDMS format. The time required to save files went from being a bottleneck to being negligible. This change also resulted in a substantial reduction in the hard-drive space required to store the data. In order to read and analyze the TDMS data files, I wrote a package to open and manipulate TDMS files in Mathematica. The LabView program was also modified to only transfer data from the PC oscilloscope to the PC after it had completed all N acquisitions at a certain set of device parameters (consecutive signals or backgrounds at a particular delay). Other improvements were related to the upgrade of the controlling computer from a laptop to a desktop PC with a GPIB-PCIe card and USB 3.0 support. These features of the new computer enable faster data transfer to the controlled devices and faster transfer from the acquisition oscilloscope respectively.

3.2.6 Angle Measurement

The angle θ between $\vec{k}_1$ and $\vec{k}_2$ is measured using a beam profiler attached to an automated, motorized translation stage as shown in Figure 3.17. The stage moves the beam profiler repeatably between two points along the beam path separated by ≈ 82 cm. The centre of each beam is found using Gaussian fits to the profiler output at these two points. In order to ensure that the beams have Gaussian profiles and their centres can be determined accurately, the beams have been spatially filtered using an iris during the angle measurement. Since the irises are fully open during the diffusion measurement, a potential systematic effect due to wavefront curvature arises which is quantified in Chapter 4. By comparing the separation of

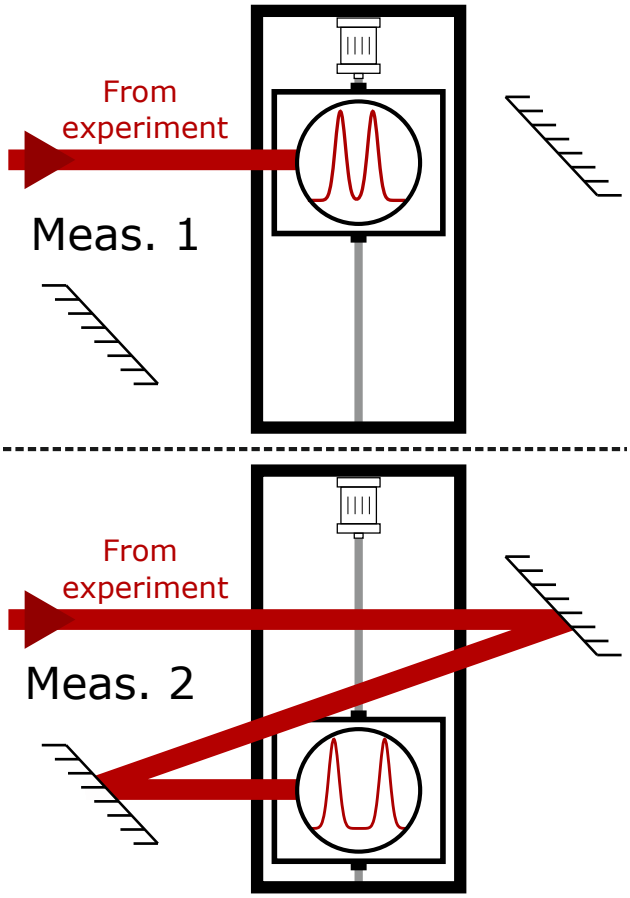

Figure 3.17: Schematic representing the angle measurement protocol using two measurement steps. The two nearly parallel lasers, indicated by red beam paths coming from the left, are operated in cw mode and a motorized translation stage (thick rectangular box) moves a spatial beam profiler (circle inside a square with red signal traces.) between two points along the beam path. The angle is calculated from Gaussian fits to the double-peaked beam-profiler signal. The path distance between the two points is approximately 82 cm and is measured with a precision of 0.3 cm.

the beams at the two locations to the measured distance between the locations, we determine the angle between the excitation beams.

Chapter 4

Results and discussion

This section will discuss the key experimental results of this thesis in the order they were obtained. Section 4.1 describes the initial demonstration of the population magnetometer using the home-built MOPA system [39, 41]. Section 4.2 describes the initial demonstration of the coherence magnetometer signal using the same MOPA system and compares the signal with the widely used population magnetometer [33]. Section 4.3 discusses the proof-of-concept measurement of the Rb-N_2 diffusion coefficient in a sealed cell containing ^{87}Rb at a fixed N_2 pressure [33]. Section 4.4 presents measurements of the Rb-X diffusion coefficients using the gas manifold where X is He, Ne, Ar, Kr, Xe, and N_2 [35, 36]. Section 4.5 discusses the impact of the results, and we provide concluding remarks in Section 4.6.

4.1 Demonstration of population magnetometer using home-built MOPA system

The initial magnetometry work demonstrated the capability of our home-built MOPA system to be deployed in a magnetometer [39]. Magnetometry signals were obtained in a vapour cell containing naturally abundant Rb at room temperature vapour pressure, as well as in the

quartz cell containing isotopically purified ^{87}Rb vapour in addition to 553 Torr of N_2 buffer gas.

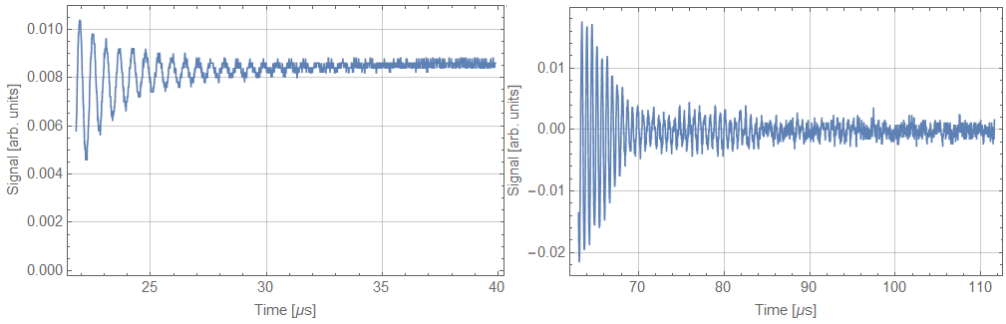

Figure 4.1: Time-domain magnetometry signals detected by measuring differential probe absorption in ^{87}Rb. (a) Signal for a room temperature vapour cell with no buffer gas. (b) Signal for a cell with 553 Torr of N_2 at 40 °C. The applied magnetic field is approximately 3 G in both cases

Figure 4.1 shows a comparison of magnetometer signals from the two vapour cells in a magnetic field of approximately 3 G. The signal decay time in the buffer gas cell is approximately a factor of two larger. This behaviour is consistent with the expectation that the transit-time-limited signal will be considerably extended due to diffusion through the buffer gas. Additionally, the rate of collisional de-excitation in the buffer gas cell exceeds the rate of spontaneous emission. Under these conditions, radiation trapping is not expected to limit the decay time. The signal amplitude in the buffer gas data is notably larger due to the higher vapour pressure associated with the high temperatures. Applying this technique in the vacuum cell yields a reduced decay time limited by the transit time of free-moving particles. Other factors that limit the decay time include the probe intensity and the magnetic gradients across the cell length due to the field coils, the cell heaters, and magnetized materials near the cell. Based on the results of the simulations in Chapter 2, we expect that operating on the D1 transition under the same conditions will result in a larger signal amplitude, thereby permitting the signal decay to be observed over a longer timescale.

Figure 4.2 shows the Fourier transform of the signal in Figure 4.1(b). The data are fit

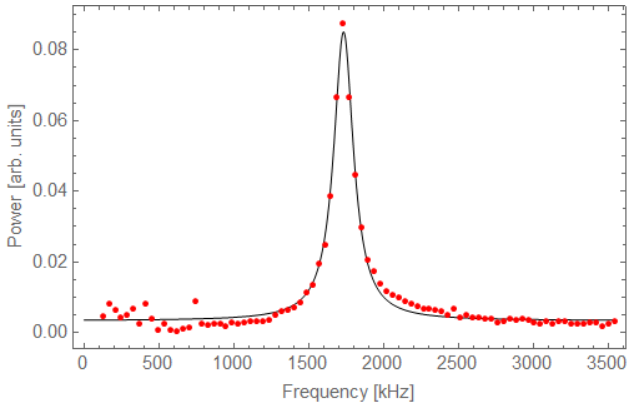

Figure 4.2: Fourier transform and fit corresponding to the time domain signal in Figure 4.1b

to a Lorentzian function added to a $1/f$ decay to account for noise. Datasets like this one show a single-peaked spectrum, but at lower magnetic fields (1 G) two peaks spaced by approximately 100 kHz are distinguishable. This effect is attributed to the presence of a magnetic field gradient across the cell.

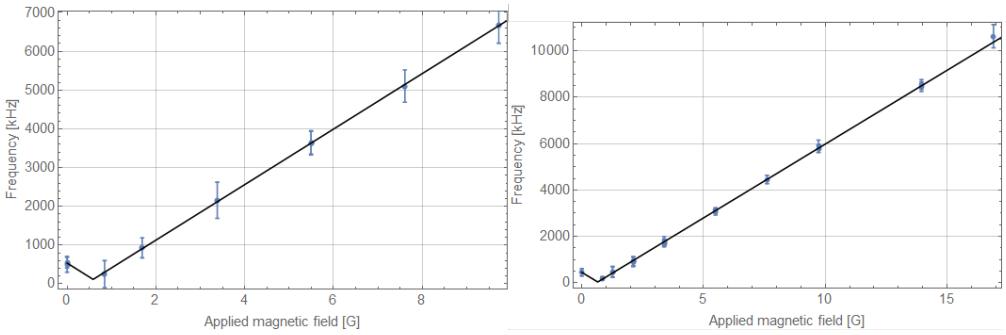

Figure 4.3: Larmor frequency as a function of the applied magnetic field. (a) Data from a room temperature vapour cell with no buffer gas. (b) Data from a vapour cell containing 553 Torr of N_2 at a temperature of 40° C.

Figure 4.3 shows the measured Larmor frequency as a function of the applied magnetic field in the two vapour cells. In Figure 4.3(a) a linear fit to the form $|sB_y + B_{y0}| + B_x$ gives a slope of $s = 716 \pm 5$ kHz/G based on a current-to-field calibration of 42.3 G/A. This coil calibration was verified at the 10% level using a Hall sensor. The error bars in this fit have been weighted by the full-width at half maxima of the Lorentzian fits. While these error bars

probably overestimate the uncertainty in the centre frequency, we have been conservative in these estimates to account for errors due to uncontrolled magnetic field gradients including those that arise from the shape of the coil. The slope is comparable to the expected value of ≈ 700 kHz/G for the ^{87}Rb $F = 3$ atom, and the measured deviation is entirely consistent with the uncertainty in the magnetic field due to the coil calibration and spatial gradients. Figure 4.3(b) shows similar data for the cell containing buffer gas. Here we find a slope of 636 ± 3 kHz/G. The uncertainty of each frequency measurement is reduced due to the extended timescale of the signal. However, the overall quality of the fit is comparable for both datasets. We attribute the deviation with respect to the expected slope of 700 kHz/G to the fact that the coils had to be displaced slightly to accommodate the heaters used for the buffer gas cell.

4.2 Comparison of coherence and population magnetometers

Using a redesigned apparatus, the coherence magnetometer method was demonstrated using the same MOPA system and compared to the signals obtained using the population magnetometer method. Signals from the optically pumped lattice formed in the coherence magnetometer method, which can be observed by using small external magnetic fields. When the magnetic fields are annulled, the resulting population gratings are found to be particularly well suited for measuring diffusion coefficients [33].

Figure 4.4 shows representative signals of the coherent transients obtained from the population magnetometer method, the coherence magnetometer method, and from population gratings. Figure 4.4(a) shows the population magnetometer signal recorded in the Pyrex vapour cell without a buffer gas. The duration of the pump pulse was 300 ns and the

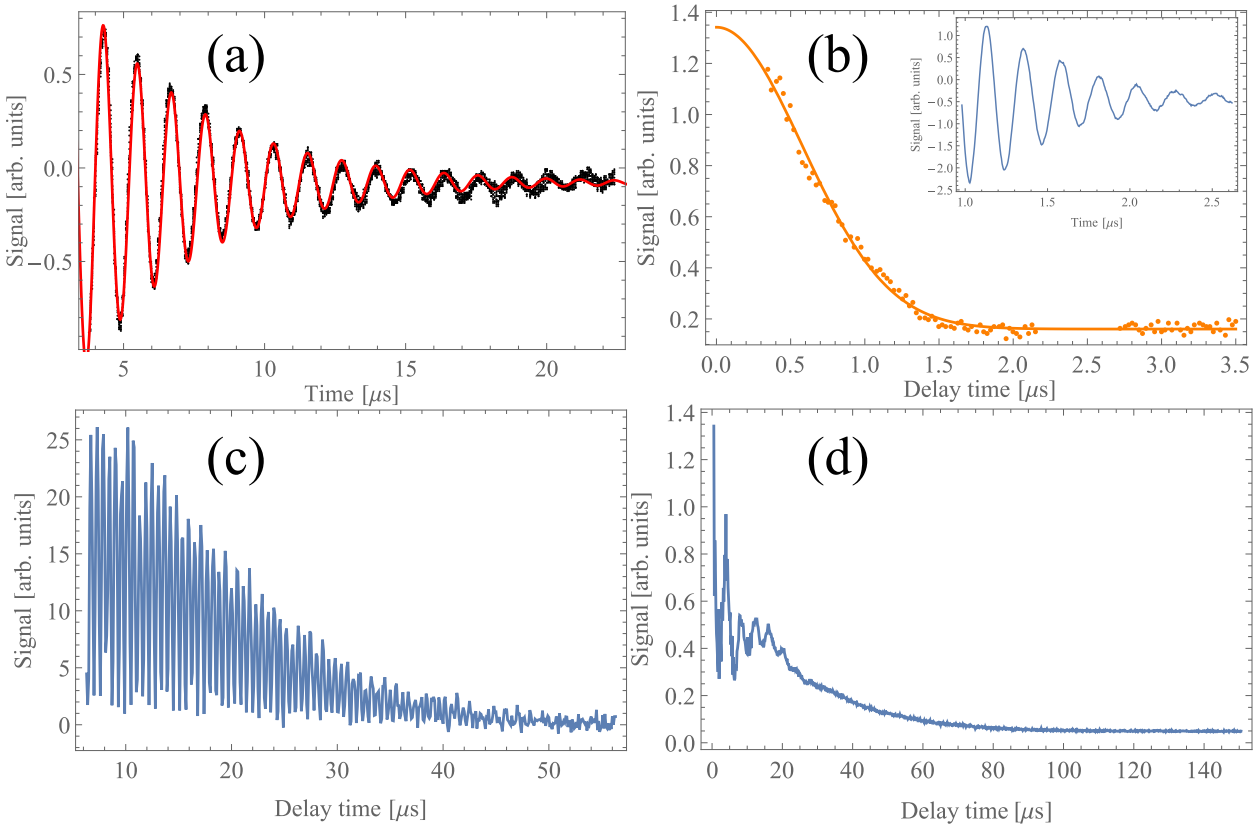

Figure 4.4: Representative responses of the coherence and population magnetometers. Field strengths are varied to clearly demonstrate the magnetic field response over the varied timescales. (a) Decay of the spin–polarization of a population magnetometer in the pyrex vapour cell containing natural abundance of Rb and no buffer gas. With a magnetic field of 0.2 G, the observed Larmor frequency (0.433 MHz) is consistent with this field. (b) Gaussian decay of the total signal of the coherence magnetometer (MGFID) in the same cell. The magnetic field is zeroed to minimize Larmor oscillations in the decay and infer the most probable speed. The excitation pulse width is 70 ns and $\theta = 2$ mrad. The fit gives $u = 246$ m/s, which corresponds to a temperature of 30°C, agreeing with the cell temperature. Inset shows the MGFID signal in a magnetic field of 13.8 G. The Larmor oscillation frequency is 6.5 MHz. (c) The response of the coherence magnetometer (MGFID) in a magnetic field of 1.25 G with 553 Torr of N_2 buffer gas. The excitation pulse width is 1 µs, which ensures that the signal from the population grating is small. The Larmor oscillation of 1.7 MHz is consistent with the applied magnetic field. (d) The response of the coherence magnetometer with a longer excitation pulse (80 µs), $\theta = 5.23$ mrad, and magnetic field of 0.17 G. The magnetic field response is visible at early times but the coherent scattering from the population grating dominates at later times.

duration of the weak probe pulse was 100 µs. Here, the signal represents the intensity of the differential absorption of the two polarization components of the probe pulse. The decay time is principally limited by the estimated transit time across the 3 mm × 3 mm probe beam (approximately 12 µs). The frequency of the Larmor oscillations is consistent with the applied magnetic field. The data illustrates the difficulty of using this signal for measurements of diffusion. Firstly, the magnetic field response must be de-convolved. Secondly, to relate the decay time to the diffusion coefficient, one must solve the diffusion equation for the expansion of the optically pumped cloud. This kind of calculation is performed in Appendix D, where it is shown that the resulting decay has a complicated dependence on the diffusion coefficient. These requirements add significant uncertainty to any diffusion measurement. Figure 4.4(b) shows the MGFID of the coherence magnetometer recorded in the same cell as in 4.4(a), with k_1 and k_2 excitation pulse widths of 70 ns. Each point was recorded by varying the delay of an intense, 70 ns read-out pulse, then integrating and adding the two components in quadrature to obtain the total intensity. These measurements were carried out by annulling the ambient magnetic field to avoid Larmor oscillations from the coherence grating. A Gaussian fit to the intensity gives a temperature of 30 °C which is consistent with the cell temperature. The $1/\theta$ dependence of the decay time has been verified in reference [57]. The inset shows the in-phase component of the MGFID signal in a magnetic field (13.8 G). The Larmor oscillation frequency of 6.5 MHz is consistent with the expected value of 6.43 MHz for this field. The inset data were taken with a single, long, weak read–out pulse, as was done for Figure 4.4(a).

Figure 4.4(c) shows the MGFID signal in the presence of a magnetic field of 1.25 G, from isotopically pure ^{87}Rb vapour in 553 Torr of N_2 gas. Here, the k_1 and k_2 excitation pulse widths were 1 µs. The delay time of a 100 ns, intense, read-out pulse was varied to record the signal decay. As in Figure 4.4(b), the total intensity of the scattered signal is displayed. The frequency of the Larmor oscillations (1.7 MHz) is once again consistent with the applied magnetic field. Although this signal could be used for a diffusion measurement, it is necessary

to remove the effects of the magnetic field and residual field gradients to obtain smooth decays. This process can be error-prone and can only be avoided by good magnetic shielding. However, a population grating, which is formed by the same excitation configuration by spatially dependent optical pumping, is insensitive to magnetic field effects and does not have shielding requirements. Additionally, as we will show, a much larger signal-to-noise ratio can be realized using a population grating. In Figure 4.4(d) the width of the excitation pulse is extended to 80 µs and the magnetic field is reduced to 0.17 G. The coherent scattering is recorded in the same manner as in Figure 4.4(b) and 4.4(c) by varying the delay time of an intense 100 ns read-out pulse. The coherent scattering from the magnetic field–dependent coherence grating is visible at early time delays while the scattering from the population grating dominates at later times. It is evident that the signal from the population grating can be observed on much longer timescales since it has a greater amplitude than the signal from the coherence grating for suitably long excitation pulses.

4.3 Measurement of Rb-N_2 diffusion coefficients in sealed cells

Figure 4.5(a) shows the signal from a long-lived population grating recorded by varying the delay time of an intense 100 ns read-out pulse. This data was recorded over a timescale of ∼1 hour by randomizing 1000 delay times. Over this duration, we verified that the uncertainty in θ is less than 0.01 mrad by sampling the beam profile on a profile analyzer. The signal exhibits the expected exponential decay curve represented by the fit line. Here, the angle θ between $\vec{k_1}$ and $\vec{k_2}$ was adjusted to be 1.31 ± 0.01 mrad. The magnetic fields were also minimized using a single pair of coils to reduce the amplitude of Larmor oscillations that are visible at the beginning of the curve in Figure 4.4d. These kinds of decay curves were used in

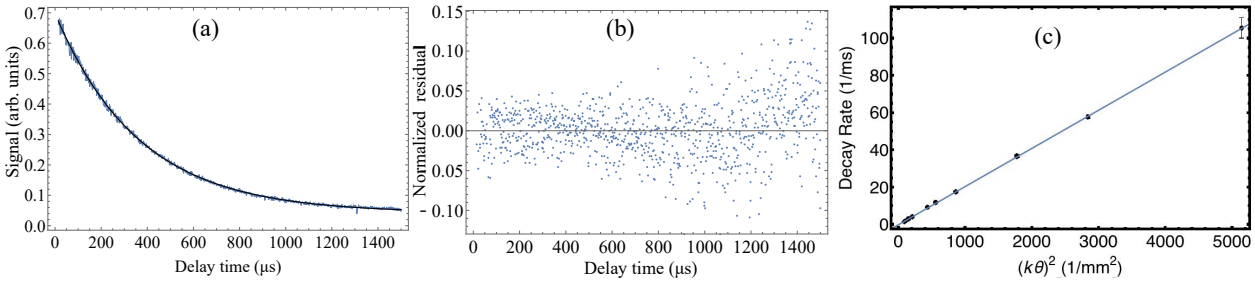

Figure 4.5: (a) Exponential signal decay of a population grating at 553 Torr N_2. The excitation pulse width is 80 μs and the delay of a 100 ns read–out pulse is varied. Here, each excitation pulse has a single–photon, average Rabi frequency $\Omega \approx 10\Gamma$, where Γ is the radiative rate of the excited state. The dataset consists of 1000 points. Here, $\theta = 1.31 \pm 0.01$ mrad and the decay time $\tau = 363 \pm 1$ μs, which together give $D = 0.246$ cm^2/s. (b) Normalized fit residuals of the exponential decay. (c) Fit to the decay rate $(1/\tau)$ of the density grating as a function of $(k\theta)^2$ showing a linear dependence. The slope gives $D = 0.2049 \pm 0.0019$ cm/s^2, which represents a statistical error of 1%. Scaling to atmospheric pressure gives $D_0 = 0.1490 \pm 0.0014$ cm^2/s.

the diffusion measurement. The measured decay time constant τ is 363 μs with a fit error of ±1 μs. The value of D (at 553 Torr) extracted from the fit $f(t; a, \tau, \sigma_{\rm bg}) = \sqrt{ae^{-2t/\tau} + \sigma_{\rm bg}^2}$ to the dataset y_i on the basis of Equation 1.7 is 0.2049 ± 0.0019 cm^2/s. Figure 4.5(b) shows the normalized fit residuals $(f(t_i) - y_i)/f(t_i)$ which demonstrate that the model based on an exponential fit agrees with the data.

Figure 4.5(c) shows the decay time constant measured as a function of angle θ and plotted as a function of $1/\theta^2$. This trend demonstrates one of the key advantages of this technique, namely the ability to change the length scale on which diffusion occurs. We note that this length scale (the grating spacing) is significantly smaller than the beam diameter of 3 mm. Over the range of angles, this ratio of the beam size to grating spacing varies from 27 to 360, suggesting that the transit time correction is small. We have calculated a correction for the transit time outlined in Section 4.4.1 and described in detail in Appendix D, and shown that the correction for these nitrogen measurements is less than 0.4% of the measured value. The linear dependence confirms the characteristic scaling law expected for a diffusion–dominated system (Equation 1.7). The slope of this line gives $D = 0.2049 \pm 0.002$ cm^2/s,

which represents a statistical uncertainty of 1%. We scale this to atmospheric pressure and obtain $D_0 = 0.149$ cm^2/s. The combined error in k, θ and τ, computed in quadrature, is 0.9%, which is consistent with the observed statistical error. Additionally, the variation in cell temperature is 0.5%. These factors contribute to an overall uncertainty of 1.3% (assuming a $T^{1.730}$ scaling law for D, see Chapter 2), giving an absolute error of ± 0.005 cm^2/s when added to the systematic errors discussed in Section 4.4.1.

4.3.1 Pressure measurement in the sealed cell

To infer the N_2 gas concentration from the measured spectrum, we perform a fit to the collisionally broadened and shifted profile of ^{87}Rb. The profile is fit to the spectra from the experimental cell to the composite lineshape obtained by shifting and broadening the underlying resonances (see Figure 4.6) and determining the broadening and shift by comparing the underlying features to their counterparts in the unbroadened, reference spectrum (see Appendix C. All line profiles share the same Lorentzian width and shift parameters, which are defined by a single pressure parameter that uses the relationships measured in reference [86]. The line strengths and splittings are taken from reference [102]. We also use a scalable background term based on the measured laser intensity. To ensure that the fit parameters are strongly constrained, datasets obtained by increasing and decreasing the laser frequency during the scan are fit simultaneously. The pressure is extracted from fits such as the one shown in Figure 4.6. This fit is superimposed on an illustration showing the component line-shapes which add to form the composite spectrum.

Figure 4.7 shows the inferred pressure obtained with laser powers ranging from $1 - 2$ µW and an effective temperature of 47°C. We find that the fit errors typically range from 0.07% to 0.2%. The scatter in the data can be attributed to temperature fluctuations of ± 1.5°C over the time in which the data was acquired. The average value was determined to be 544 ± 2 Torr

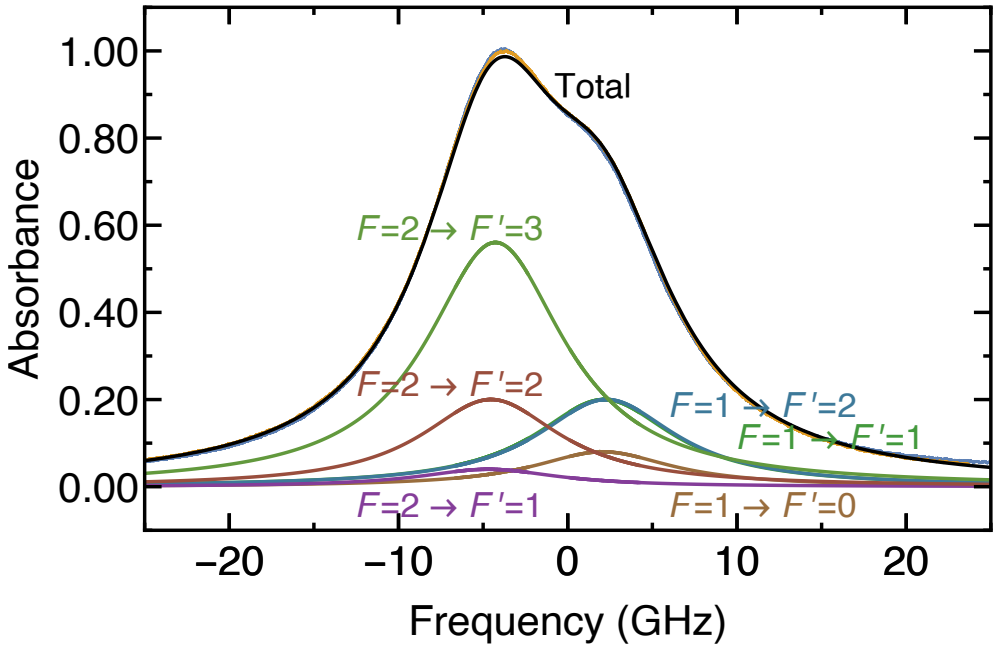

Figure 4.6: Data from the experimental cell fitted to composite spectrum for ^{87}Rb resonances in the isotopically purified cell. Blue and yellow curves show data from the upward and downward frequency scan respectively, the best fit to both of these curves is shown in black. Individual resonances are shown with broadening and shift parameters determined by the fit and strengths and centres relative to each other taken from reference [102]. The frequency axis is relative to the $F = 2 \rightarrow F' = 3$ transition on the D2 line ($5^2S_{1/2} \rightarrow 5^2P_{3/2}$) in ^{87}Rb.

at 47°C. Using the ideal gas law, this value can be scaled to the cell temperature during the diffusion measurement (50°C) giving a pressure of 553±2 Torr. This is lower than the bound provided by the cell manufacturer when scaled to a temperature of 50°C (650 ± 65 Torr). It is significant that the statistical uncertainty in the pressure measurement has reduced the dominant systematic uncertainty in the measurement of the diffusion coefficient from 10% to 0.4%, resulting in a negligible contribution to the overall error.

The final value, $D_0 = 0.149 \pm 0.005$ cm$^2/s$, has been rescaled using $D_0 = D' \frac{P'}{P_0}$, where D' is the diffusion coefficient measured at 50 °C and P' is the pressure inside the cell at this temperature, inferred from the pressure measurement at 47 °C. Here, D_0 and P_0 represent the values at atmospheric pressure.

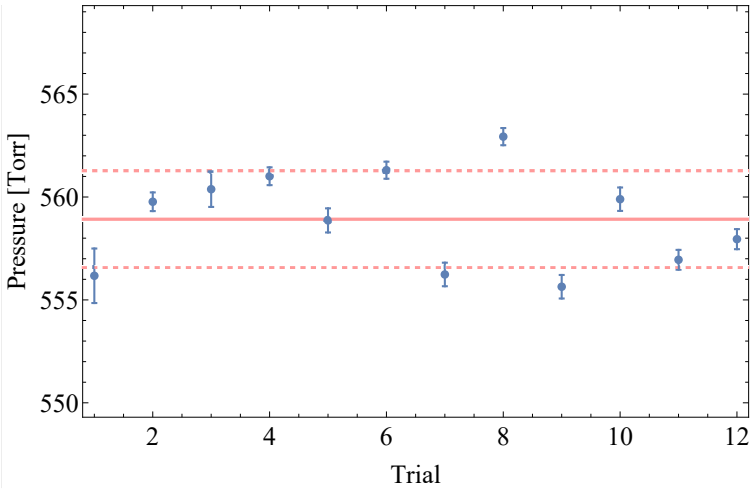

Figure 4.7: Distribution of pressure measurements taken at varying input laser powers (between 1-2 µW) and laser scan rates of 106 Hz or 21 Hz, at an effective temperature of 47°C. The fit errors in the pressure parameter of the Voigt profiles are shown as error bars. The additional spread is attributed to the ±1.5% temperature fluctuations in the cell. The mean value of 544.0 Torr is indicated by a pink line. The standard deviation of ±2.3 Torr is indicated by the dashed pink lines.

4.4 Measurement of diffusion coefficients in Rb-X mixtures

As explained in Chapter 3, the apparatus was substantially modified to measure the diffusion coefficient in a Pyrex cell where the pressure and composition of the buffer gas could be freely varied [35]. The cell contained a naturally abundant mixture of ^{85}Rb and ^{87}Rb. The method of data acquisition and analysis was also further refined and optimized.

The combined amplitude of the Rb population gratings in each m level is measured by applying a read-out pulse with a rise-time of ≈ 67 ns and a duration of ≈ 50 ns. The read-out pulse has an intensity of 120 mW/cm^2 optimized to maximize the scattered light signal. The read-out delay time relative to the excitation pulse is varied in a random sequence over $N \approx 1500$ delays. For each delay, the scattered light signal $E_C(t)$ of Equation 1.7 is acquired by averaging four consecutive repetitions at the ≈ 1 kHz repetition rate of the experiment.

We then acquire the background signal E_{BG} by turning off the $\vec{k}_2$ excitation pulse for the same delay time. The switching process requires ≈ 10 ms. The signal E_{BG} is also acquired by averaging four consecutive repetitions. We limit the number of consecutive traces to four because the phases of these electric fields are well correlated on timescales of ≈ 20 ms. This limitation is imposed by variations in the optical path length between the excitation and LO beams caused by convection currents caused by the heated oven. To improve statistics, each of the N time delays is repeated four times in a random sequence of $4N$ acquisitions. It takes ≈ 150 ms to transfer data and switch to a different delay time. As a consequence, the acquisition time for the entire decay curve ranges from 5 min to 15 min. This data acquisition procedure was modified only in nitrogen, for which the signal strength was the largest. In this case, the signal and background were acquired on the basis of 50 consecutive repetitions which were not repeated.

For delay time t, signals E_{C} and E_{BG} are detected as a heterodyne beatnote at 80 MHz and mixed down to DC using the 80 MHz RF oscillator driving the AOMs (see Figure 3.15. The resulting in-phase, V_{p}, and $\pi/2$-out-of-phase, V_{q}, homodyne signals are added in quadrature $\sqrt{V_{\mathrm{p}}^2 + V_{\mathrm{q}}^2}$ to obtain non-negative electric field amplitudes. The associated phases $\phi_{\mathrm{C}}(t)$ and ϕ_{BG} are $\arctan(V_{\mathrm{p}}/V_{\mathrm{q}})$ when $V_{\mathrm{q}} > 0$ and $\arctan(V_{\mathrm{p}}/V_{\mathrm{q}}) + \pi$ when $V_{\mathrm{q}} < 0$. We have made it explicit that $E_{\mathrm{C}}(t)$ and $\phi_{\mathrm{C}}(t)$ depend on delay time t and, in practice, $0 \leq E_{\mathrm{BG}} \ll E_{\mathrm{C}}(t)$. The non-negative background-subtracted (BS) signal amplitude is

$$E_{\mathrm{BS}}(t) = |E_{\mathrm{C}}(t)e^{i\phi_{\mathrm{C}}(t)} - E_{\mathrm{BG}}e^{i\phi_{\mathrm{BG}}}| \tag{4.1}$$

as a function of delay time and $|z|$ is the absolute value of the complex argument z.

In the presence of amplitude and phase noise, the background signal can be described by probability density $p_{\mathrm{BG}}(E_{\mathrm{BG}}, \phi_{\mathrm{BG}}) = e^{-E_{\mathrm{BG}}^2/(2\sigma_{\mathrm{BG}}^2)}/(2\pi\sigma_{\mathrm{BG}}^2)$. This corresponds to a Gaussian distribution with a zero mean and a standard deviation σ_{BG} for $E_{\mathrm{BG}}e^{i\phi_{\mathrm{BG}}}$. The acquired,

background-subtracted signal $E_{\mathrm{aq}}(t)$ becomes

$$E_{\mathrm{aq}}(t) = \int_0^\infty E_{\mathrm{BG}} \mathrm{d}E_{\mathrm{BG}} \int_0^{2\pi} \mathrm{d}\phi_{\mathrm{BG}}\, p_{\mathrm{BG}}(E_{\mathrm{BG}}, \phi_{\mathrm{BG}}) E_{\mathrm{BS}}(t)\,. \tag{4.2}$$

No closed form is available for this two-dimensional integral, but some algebra shows that the background-subtracted signal amplitude satisfies

$$E_{\mathrm{aq}}(t) = \begin{cases} \sqrt{\dfrac{\pi}{2}}\sigma_{\mathrm{BG}} \left[1 + \dfrac{1}{4}\left(\dfrac{E_{\mathrm{C}}(t)}{\sigma_{\mathrm{BG}}}\right)^2\right] & \text{for } E_{\mathrm{C}}(t) \ll \sigma_{\mathrm{BG}} \\ E_{\mathrm{C}}(t) \left[1 + \dfrac{1}{2}\left(\dfrac{\sigma_{\mathrm{BG}}}{E_{\mathrm{C}}(t)}\right)^2\right] & \text{for } E_{\mathrm{C}}(t) \gg \sigma_{\mathrm{BG}} \end{cases} \tag{4.3}$$

omitting terms of higher order in $E_{\mathrm{C}}(t)/\sigma_{\mathrm{BG}}$ and $\sigma_{\mathrm{BG}}/E_{\mathrm{C}}(t)$ for the two limits, respectively.

Since we have not taken data for $E_{\mathrm{C}}(t) \ll \sigma_{\mathrm{BG}}$, we fit the measured $E_{\mathrm{aq}}(t)$ to

$$E_{\mathrm{aq}}(t) = \sqrt{E_{\mathrm{C}}(t)^2 + \sigma_{\mathrm{BG}}^2} \tag{4.4}$$

ensuring that we reproduce the first two terms of Equation 4.3 when $E_{\mathrm{C}}(t) \gg \sigma_{\mathrm{BG}}$, while still predicting a finite, although incorrect $E_{\mathrm{aq}}(t)$ for small $E_{\mathrm{C}}(t)$. The standard deviation σ_{BG} is an adjusted parameter in addition to those of $E_{\mathrm{C}}(t)$ in Equation 1.7 with decay rate $1/\tau$ of Equations 2.16 or 2.17.

The inset of Figure 4.8a shows data for a typical example of the background-subtracted signal amplitude, obtained for the delay time $t = 41.33$ µs at a pressure of 342.70(5) Torr of neon buffer gas and $T = 24.0(5)$ °C. Each point on this curve has an error bar that represents the standard deviation of the 16 measurements. The integrated area under such curves $S_i = S(t_i)$ is computed for each delay time t_i, $i = 1, \ldots, N$. The results are shown in Figure 4.8a. Each point S_i has an error bar representing the standard uncertainty $u(S_i) = u(S(t_i))$ of the integrated area, calculated as the quadrature sum of the error bars in

the inset.

Using Equations 1.7 and 2.16, we extract the decay time constant τ by minimizing the chi square, calculated as

$$\chi^2 = \sum_{i=1}^{N} \frac{(S_i - E_{\mathrm{aq}}(t_i; E_0, \sigma_{\mathrm{BG}}, \tau))^2}{u^2(S_i)}\,, \tag{4.5}$$

where for the acquired, background-subtracted signal $E_{\mathrm{aq}}(t; E_0, \sigma_{\mathrm{BG}}, \tau) = \sqrt{E_{\mathrm{C}}(t)^2 + \sigma_{\mathrm{BG}}^2} = \sqrt{E_0^2 \exp(-2t/\tau) + \sigma_{\mathrm{BG}}^2}$ we have made the dependence on the adjustable parameters E_0, σ_{BG}, and τ apparent.

For the data shown in Figure 4.8, where the non-exponential behaviour for large delay times is clearly visible, we find that the standard uncertainty at a delay time, $u(S_i)$, generally underestimates the deviation from the fit value, *i.e.* the residual $S_i - E_{\mathrm{aq}}(t_i; E_0, \sigma_{\mathrm{BG}}, \tau)$. This effect is quantified by the Birge ratio of the fit given by $\sqrt{\chi^2/(N-3)} = 3.7$, which is significantly larger than 1 for our $N \gg 1$. We attribute this inconsistency to the time-correlation between the consecutively acquired samples for each delay time, an effect that arises due to the phase drifts associated with the convection currents from the oven. In fact, from analyses of the fit residuals, we find that the residuals are proportional to $\sqrt{S_i}$, with a few exceptions in the nitrogen data at large angle for which the residuals are proportional to S_i.

Figure 4.8b shows the *normalized* residuals $r_i = [S_i - E_{\mathrm{aq}}(t_i; E_0, \sigma_{\mathrm{BG}}, \tau)]/u(S_i)$ as a function of delay time t_i. Their standard deviation $\sqrt{\langle r_i^2 \rangle} = \sqrt{\chi^2/N}$ is clearly larger than 1. More importantly, the figure shows that there exist no obvious correlations among the data. In fact, the residuals are well represented by a normal distribution. To account for the observed large residuals and to obtain a satisfactory fit, the standard uncertainty of the decay time constant τ from the fit is multiplied by the Birge ratio. We find that the typical Birge ratio for each gas is near 3.7, but it is as high as 5.6 in helium.

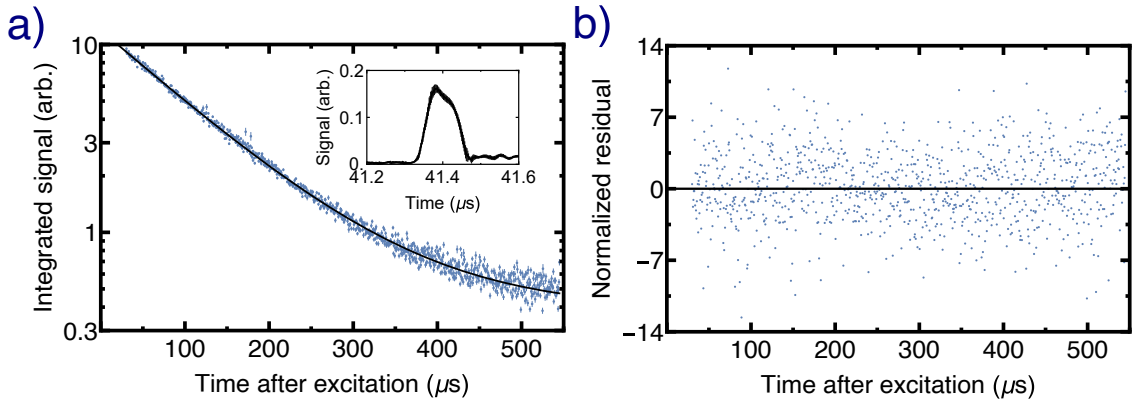

Figure 4.8: a) Decay of the square of the amplitude of the optically pumped grating, the integrated signal $\mathcal{S}(t_i)$, with 341.70(5) Torr of neon buffer gas at $T = 24.0(5)$ °C as function of time after excitation or delay time t_i. The excitation beams are aligned with an angle $\theta = 1.61(2)$ mrad. Here, the parentheses represent one standard deviation of statistical and systematic uncertainty due to wavefront curvature as explained in the text. A fit to $\sqrt{E_0^2 \exp(-2t/\tau) + \sigma_{\rm BG}^2}$ gives a decay time constant of 123.0(4) µs. Inset of panel a) shows the background-subtracted signal amplitude produced by a 50 ns readout pulse with a delay of 41.33 µs after the excitation pulses. The rise time of read out pulse is 67 ns. Such signals are integrated and squared to obtain each point in panel a). b) Normalized residuals $(\mathcal{S}(t_i) - E_{\rm aq}(t_i; E_0, \sigma_{\rm BG}, \tau))/u(S_i)$ of our fit as a function of t_i.

Figure 4.9 presents *all* measured decay rates τ and their standard uncertainties for the six inert buffer gases and a large set of pressures p and angles θ. These measurements have been obtained at a temperature of 24.0(5) °C and with the laser locked to the $F = 3 \rightarrow F' = 3, 4$ crossover peak in ^{85}Rb (Figure 3.6). Figures 4.9a and 4.9b show observed decay rates as the pressure of each gas is varied at constant angle. Figures 4.9c and 4.9d show the data as a function of the angle between laser beams at constant pressure. For each buffer gas, we measure decay rates at l pairs (p, θ). These data are fit to Equation 2.17 with positive fit parameters $\langle v\sigma_{\rm spin}\rangle_{\rm exp}$ and $\mathcal{Q}_{\rm exp}(T)$, and signed parameters $(\mathcal{W}\Gamma_{\rm opt}p_{\rm ref})_i$, where index $i = 1, \ldots, m$ corresponds to data taken on different days and models changes in residual light due to small deviations in the alignments of the AOMs. For each buffer gas, the number of fit parameters $m + 2$ is significantly smaller than the number of measured decay rates l.

To better visualize the p and θ dependencies of the decay rates, we have plotted a modified

decay rate in Figure 4.9. First, we subtracted $(\mathcal{W}\Gamma_{\rm opt}p_{\rm ref})_i/p$ from each measured $1/\tau$ using the corresponding fitted value $(\mathcal{W}\Gamma_{\rm opt}p_{\rm ref})_i$. Then, for Figure 4.9a and b, the resulting decay rates have been scaled to a common angle of $\theta' = 2$ mrad. Here, the scaled rate $(1/\tau)'$ is determined by

$$\left(\frac{1}{\tau}\right)' = \left(\frac{1}{\tau}\right)\frac{g(p,\theta',T)}{g(p,\theta,T)}, \tag{4.6}$$

where $g(p,\theta,T)$ corresponds to the first two terms on the right-hand side of Equation 2.17 using the fitted values for $\langle v\sigma_{\rm spin}\rangle$ and $\mathcal{Q}(T)$. In a similar manner, the decay rates in Figures 4.9c and d have been scaled to a common pressure $p' = 200$ Torr. As a result, a positive modified decay rate for $\theta \to 0$ in Figures 4.9c and d indicates the presence of spin-exchange and spin-destruction collisions.

We note that in Figures 4.9a and 4.9b the lowest pressures at which we can observe a signal are buffer-gas dependent. They are determined by the limited efficiency of optical pumping for small collisional shifts and broadening, as discussed in Chapter 2.

Based on Equation 2.17, we infer that the contributions from the Rb spin-exchange and spin-destruction collisions are small compared to that of Rb diffusion and residual light. For the heavier argon, krypton, and xenon gases, the decay rates in Figure 4.9b exhibit a component proportional to p, which is apparent at our larger pressures. We interpret this trend as evidence of the influence of spin-exchange and spin-destruction collisions. In Figure. 4.9c and 4.9d the linear increase with $(k\theta)^2$ is solely due to diffusion. While this dependence can be used to determine $D(T,p)$ even without the data in Figure. 4.9a and 4.9b, the quality of the fits improves by including all data.

Figure 4.9d shows our nitrogen data as well as data from our previous determination in reference [33] as functions of angle θ. The data from reference [33], taken at a temperature of 50 °C, has been scaled to 24.0(5) °C using the procedure described in the caption of Table 1.1. The fit to the nitrogen data gives $D(T,p) = 0.131(3)$ cm^2/s at standard pressure, which

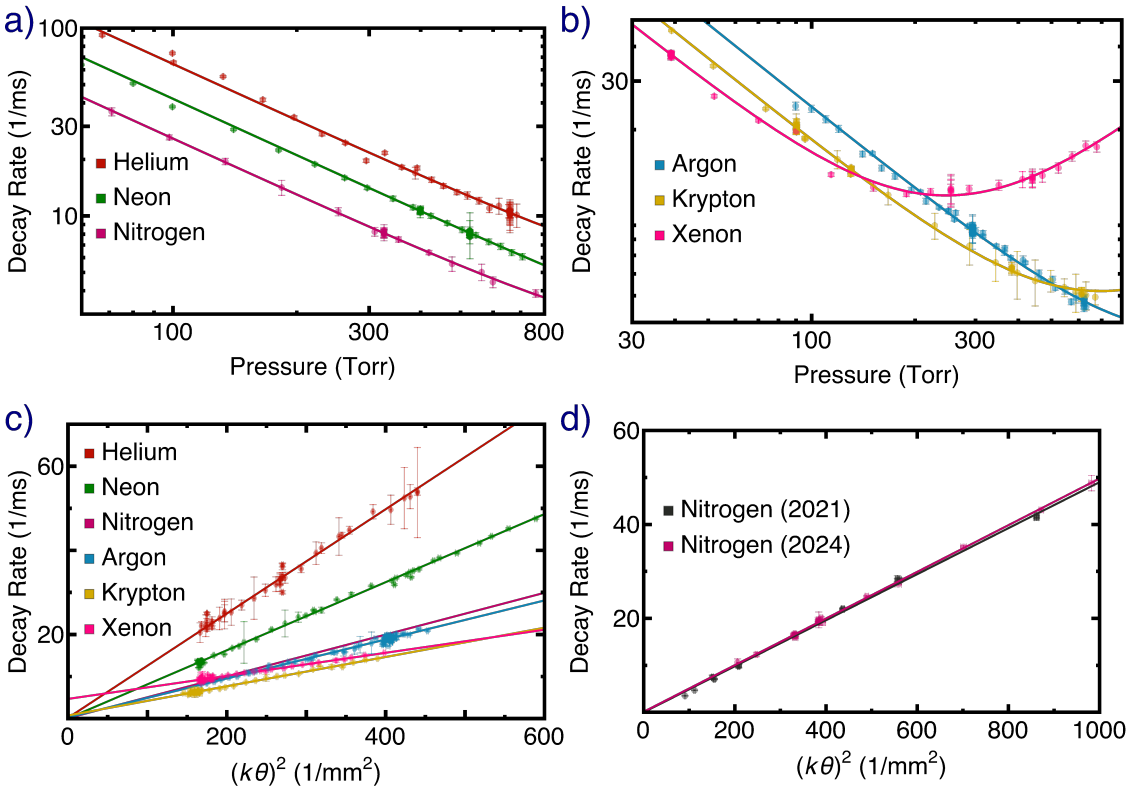

Figure 4.9: Data for naturally abundant Rb-X systems at $T = 24.0(5)$ °C with fits based on Equation 2.17 as described in the text. a) Decay rates for helium, neon, and nitrogen buffer gases as functions of buffer gas pressure for angle $\theta = 1.88$ mrad, 1.60 mrad, and 2.34 mrad, respectively. b) Decay rates in argon, krypton, and xenon as functions of buffer gas pressure for $\theta = 2.49$ mrad, 1.57 mrad, and 1.63 mrad, respectively. For all the angles reported here, the statistical uncertainty is small compared to the systematic uncertainty of 1.5 % which arises due to wavefront curvature as explained in text. For ease of comparison, decay rates in panels a) and b) have been scaled to correspond to data taken at a common angle of 2 mrad. c) Decay rates as functions of $(k\theta)^2$ for helium, neon, argon, krypton, and xenon taken at buffer gas pressure 659.0(5) Torr, 526.73(1) Torr, 294.292(1) Torr, 90.27(1) Torr, and 38.953(1) Torr, respectively. Only the best fit to the nitrogen data is shown in this panel. The nitrogen experimental data is displayed separately in panel d). d) Decay rates as function of $(k\theta)^2$ for a nitrogen buffer gas at 325.97(2) Torr for this work and 552.4 Torr for our previous determination [33]. Four data points from the previous determination fall outside the plot range. For ease of comparison, decay rates in panels c) and d) have been scaled to correspond to data taken at a common buffer gas pressure of 200 Torr. The error bars in all panels represent one-standard-deviation uncertainties obtained from fits such as that shown in Figure 4.8a.

agrees with the reported 0.129(1) cm^2/s in reference [33]. We summarize the data from Figure 4.9 in Table 4.1 where the second column represents the values of $D(T, p)$ extracted from the fits to Equation 2.17 with statistical uncertainty shown in parentheses. The second column of Table 4.2 shows the values of $\langle v\sigma_{\mathrm{spin}} \rangle$.

4.4.1 Systematic Corrections

A transit time correction is estimated by simulating the signal decay based on two analytical models that attempt to account for the spatial expansion or diffusion of the Rb population grating beyond the extent of the read-out beam, as described by Equation D.1. A detailed derivation of these models can be found in Appendix D and in reference [36]. In both models, the analytical signal $E(t)$ is given by the $\vec{k}_1 - \vec{k}_2$ Fourier component of the product of population grating $\rho_{Fm_F}(\vec{x}, t)$ and the profile of the electric field amplitude of the read-out beam $E_{\mathrm{RO}}(\vec{x})$.

In the first model, we assume that the spatial amplitudes B_{Fm_F} of the initial population gratings in Equation 2.14 and $E_{\mathrm{RO}}(\vec{x})$ are finite and positive on the same rectangular cuboid and are zero elsewhere. This cuboid reflects the spatial volume of the Gaussian laser beams, within which the atomic transitions are saturated and a grating is formed, and the volume from which coherent light scattering can be detected. The cuboid is assumed to be infinitely long along $(\vec{k}_1 + \vec{k}_2)/2$, but has finite sizes $w_x = 3$ mm and $w_z = 4$ mm along directions $\vec{k}_1 - \vec{k}_2$ and $\vec{k}_1 \times \vec{k}_2$, respectively, based on our measurements of the beam intensity profile and simulations of optical pumping that show the saturated area of Rb.

This first model predicts that the decay of the scattered field will be the real component

of

$$E_{\rm rect}(t) = E_0 \left[\mathrm{erf}(d_z(t)/2) - \frac{2}{\sqrt{\pi} d_z(t)} [1 - e^{-d_z^2(t)/4}] \right] \left[- \frac{2}{\sqrt{\pi} d_x(t)} \left(1 - e^{-d_x^2(t)/4} \cos(k\theta w_x) \right) + e^{-\Delta^2(t)} \left(1 - 2i \frac{\Delta(t)}{d_x(t)} \right) \left(\mathrm{erf}(d_x(t)/2 - i\Delta(t)) + \mathrm{erf}(i\Delta(t)) \right) \right] \tag{4.7}$$

with the dimensionless time-dependent functions

$$\Delta(t) = k\theta \sqrt{D(T,p)t}\,, \tag{4.8}$$

$$d_i(t) = w_i / \sqrt{D(T,p)t} \tag{4.9}$$

with $i = x$ and z. Here, $\mathrm{erf}(z)$ is the error function of a complex variable z, $\mathrm{erfi}(z) = -i\,\mathrm{erf}(iz)$, $\mathrm{Re}[z]$ and $\mathrm{Im}[z]$ are the real and imaginary components of the complex variable z. Note that with $\mathrm{erf}(z) \to 1 - \exp(-z^2)/\sqrt{\pi} z$ for $z \to \infty$ Equation (4.7) approaches Equation (1.7) when $w_i \to \infty$.

In the second model, we assume that the spatial amplitudes B_{Fm_F} of the initial population gratings in Equation 2.14 and $E_{\rm RO}(\vec{x})$ have the same Gaussian profile along orthogonal directions $\vec{k}_1 - \vec{k}_2$ and $\vec{k}_1 \times \vec{k}_2$. The profiles of B_{Fm_F} are assumed to be dictated by the laser intensity profile, which has a measured $1/e^2$ full width of $W_x = 2.4$ mm and $W_z = 2.4$ mm along these two directions, respectively. The profile of $E_{\rm RO}(\vec{x})$ is the square root of the measured intensity profile and thus has a $1/e$ full width of $W_x = 2.4$ mm and $W_z = 2.4$ mm. This model predicts a modified decay given by signal

$$E_{\mathrm{Gauss}}(t) = E_0 \frac{W_x\sqrt{w_x^{**}}(t)}{w_x^*(t)} \frac{W_z\sqrt{w_z^{**}}(t)}{w_z^*(t)} \times \exp\left(\frac{W_x^4 - [w_x^*(t)]^2}{12 w_x^*(t) w_x^{**}(t)} W_x^2 (k\theta)^2 + \frac{4W_x^2 - 3w_x^{**}(t)}{3w_x^{**}(t)} (k\theta)^2 D(T,p)t\right), \tag{4.10}$$

where $w_i^*(t) = W_i^2 + 8D(T,p)t$ and $w_i^{**}(t) = W_i^2 + 8D(T,p)t/3$ for $i = x$ and z.

The signals $E_{\mathrm{rect}}(t)$ and $E_{\mathrm{Gauss}}(t)$ are non-exponential in delay time t. We then construct the acquired, background-subtracted signal as

$$\sqrt{[E_\alpha(t) e^{-\langle v\sigma_{\mathrm{spin}}\rangle pt/k_{\mathrm{B}}T}]^2 + \mathrm{BG}_{\mathrm{sim}}^2}\,, \tag{4.11}$$

where $\alpha =$ rect or Gauss, in analogy to the expression for the signal in Equation (4.4). Here, factor $\exp(-\langle v\sigma_{\mathrm{spin}}\rangle pt/k_{\mathrm{B}}T)$ accounts for the effects of spin-destruction collisions and $\sigma_{\mathrm{BG\text{-}sim}}$ represents the phase and amplitude noise of the heterodyne detection. We do not directly fit our experimental data to these model signals, but instead generate discrete noisy datasets based on Equation (4.11) for each pair of (p,θ) for which a time trace was acquired. To generate these datasets, we use estimates for $\mathcal{Q}$ and $\langle v\sigma_{\mathrm{spin}}\rangle$, and assume a one-dimensional normal distribution for $\mathrm{BG}_{\mathrm{sim}}$ with a mean of zero and width given by σ_{BG} for that time trace. We take the average of 16 of these simulated time traces and fit the averaged datasets to the Equation (4.4) with an exponential signal $E_{\mathrm{C}}(t)$ and obtain a modified rate τ' and σ'_{BG} for each time trace. Next, we fit the values of τ' as a function of θ and p to Equation (2.17) to obtain output values for $\mathcal{Q}'$ and for $\langle v\sigma_{\mathrm{spin}}\rangle'$, which are now systematically offset from $\mathcal{Q}$ and $\langle v\sigma_{\mathrm{spin}}\rangle$ due to the effects of transit time and the heterodyne noise.

We adjust our input values for $\mathcal{Q}$ and $\langle v\sigma_{\mathrm{spin}}\rangle$ in Equation (4.11) until we arrive at a range of simulated values of $\mathcal{Q}'$ and $\langle v\sigma_{\mathrm{spin}}\rangle'$ that match our experimental observations of $\mathcal{Q}_{\mathrm{exp}}$ and $\langle v\sigma_{\mathrm{spin}}\rangle_{\mathrm{exp}}$ within the experimental error bar. The mean of the estimates which

satisfy this condition is taken as the corrected values of $\mathcal{Q}$ and $\langle v\sigma_{\rm spin}\rangle$. The uncertainty in the corrected values has been evaluated by simulating a library of decay curves obtained by varying input parameters p, θ, w_i, W_i, $\mathcal{Q}$, and $\langle v\sigma_{\rm spin}\rangle$ based on their uncertainties.

The transit time corrected values of $D(T,p)$ for each model are displayed in columns 3 and 4 of Table 4.1 [35, 36]. The uncertainty in these values has been added in quadrature to the statistical error in column one of Table 4.1 to obtain the error values reflected in columns three and four. Similarly, the transit time corrected values of $\langle v\sigma_{\rm spin}\rangle$ and their associated uncertainties are displayed in columns 3 and 4 of Table 4.2.

We observe that the corrected values of $D(T,p)$ in columns 3 and 4 of Table 4.1 are larger than the uncorrected values. This behaviour arises from the functional form of the non-exponential decay curves predicted by the models, which exhibit a more rapid decay for short delay times and a less rapid decay for longer delay times.

Column 5 of Table 4.1 represents the final experimental value for $D(T,p)$ given by the weighted average of the results of the two models for the transit time correction. We observe that the Gaussian model predicts a very small correction, whereas the correction is substantial in the rectangular model. Since we do not know which of these models is correct, we choose the conservative option of reporting the weighted average. The error in this value is computed as the quadrature sum of the error in the rectangular model, the error in the Gaussian model, and half the difference between the corrected value given by these two models. Column 5 of Table 4.2 shows the final experimental value for $\langle v\sigma_{\rm spin}\rangle$ using the same procedure.

A second systematic effect relates to the curvature of the laser wavefronts that are incident on the aperture used to spatially filter the excitation beams in order to measure angle θ. This effect does not change the fitted value of τ but does introduce an additional fractional uncertainty of 1.5 %, which is added in quadrature to the statistical uncertainty in column two of Table 4.1, and reflected in columns three through five. To obtain this uncertainty, we translate the circular aperture across the excitation beam profiles and find that the measured

Table 4.1: Measured Rb-inert gas diffusion coefficients $D(T,p)$ for naturally abundant Rb and our calculated ^{87}Rb-inert gas diffusion coefficients at standard atmospheric pressure and $T = 24.0(5)$°C. Values and uncertainties in parenthesis are reported in cm^2/s. The diffusion coefficients with their statistical uncertainties inferred from fits are reported in column two. Columns three and four show $D(T,p)$ corrected for transit time effects using two models as explained in the text. Column five shows our recommended value, a weighted average of columns three and four, with errors in parentheses calculated as described in the text. Diffusion coefficients for ^{87}Rb-X systems calculated using the quantum mechanical model are shown in the last column.

Gas	$D(T,p)$	$D(T,p)$ corrected (rect.)	$D(T,p)$ corrected (Gaus.)	$D(T,p)$ recommended	$D(T,p)$ quantum
He	0.33(2)	0.34(4)	0.33(2)	0.33(5)	0.3768(16)
Ne	0.213(7)	0.217(11)	0.213(8)	0.214(14)	0.212(3)
N_2	0.131(3)	0.134(5)	0.131(4)	0.132(7)	0.1257(3)
N_2 [33]	0.129(1)	0.130(3)	0.129(2)	0.129(4)	
Ar	0.122(5)	0.124(7)	0.122(5)	0.123(9)	0.1329(13)
Kr	0.092(5)	0.096(7)	0.092(5)	0.093(9)	0.0960(11)
Xe	0.072(3)	0.074(3)	0.072(3)	0.073(4)	0.0709(5)

angle varies by as much as 130 µrad per mm of translation. As the maximum uncertainty in the placement of the aperture (with diameter ≈ 0.1 mm) is 0.2 mm, the maximum systematic uncertainty in the angle is 26 µrad. The impact of this effect on $D(T,p)$ as a function of θ and p is as large as 1.5 %.

Finally, we compare our weighted experimental values reported in column five of Table 4.1, to those predicted by the quantum theory in Chapter 2. We find deviations from the experimental determinations of 0 % to 12 % for the six gases, all of which are in agreement within experimental errors.

From the compilation of $\langle v\sigma_{\rm spin}\rangle$ in Table 4.2, we find our measurements show increasing positive values as a function of the mass of the buffer gas. However, the values are also consistent with zero. This is likely due to the fact that we operate under conditions in which diffusion dominates other decay rates and thus limits our sensitivity to $\langle v\sigma_{\rm spin}\rangle$. For Kr and

Table 4.2: Measured $\langle v\sigma_{\text{spin}}\rangle/k_{\text{B}}T$ in unit $\text{s}^{-1}\text{Torr}^{-1}$ at $T = 24.0(5)$ °C for spin-exchange and spin-destruction processes of trace amounts of naturally abundant Rb in inert buffer gases X. The fitted values are shown in column two with their statistical uncertainties in parenthesis. Columns three and four show values after correcting for systematic errors due to transit time using two models as described in the text. Column five shows our recommended value, a weighted average of columns three and four as explained in text. Our rate coefficients are compared to those measured by reference [76] in column six where available. Note that $\langle v\sigma_{\text{spin}}\rangle/(k_{\text{B}}T)$ expressed in unit $\text{s}^{-1}\text{Torr}^{-1}$ is equivalent to $\langle v\sigma_{\text{spin}}\rangle$ expressed in unit 3.08×10^{-17} cm^3/s at 24 °C.

Gas X	$\langle v\sigma_{\text{spin}}\rangle/(k_{\text{B}}T)$	$\langle v\sigma_{\text{spin}}\rangle/(k_{\text{B}}T)$ corrected (rect.)	$\langle v\sigma_{\text{spin}}\rangle/(k_{\text{B}}T)$ corrected (Gaus.)	$\langle v\sigma_{\text{spin}}\rangle/(k_{\text{B}}T)$ recommended	$\langle v\sigma_{\text{spin}}\rangle/(k_{\text{B}}T)$ [76]
He	0(11)	0(11)	0(11)	0(16)	-
Ne	0(2)	0(2)	0(2)	0(3)	-
N_2	1(3)	0(4)	1(3)	0(5)	-
Ar	2(2)	2(3)	2(2)	2(4)	0.95(3)
Kr	4(3)	4(4)	4(3)	4(5)	33.2(1.5)
Xe	23(15)	22(21)	23(15)	23(26)	185(10)

Xe, our values deviate significantly from previous measurements at a similar temperature of 27 °C by reference [76]. While we do not have an adequate explanation, we note that the values of the diffusion coefficients are not impacted by the values of $\langle v\sigma_{\text{spin}}\rangle$ and vice-versa. As shown in Equation 2.17, this is because the decay rate due to diffusion scales as p^{-1} and θ^2, while the decay rate due to $\langle v\sigma_{\text{spin}}\rangle$ scales only as p, with no known coupling between these two effects. We speculate that the discrepancy between our values of $\langle v\sigma_{\text{spin}}\rangle$ and previous measurements arises from the fact that the measurements in reference [76] were carried out using highly polarized Rb in the presence of a small, 1 Torr concentration of buffer gas leading to longer timescales τ and thus greater sensitivity to $\langle v\sigma_{\text{spin}}\rangle$. Measurements of $\langle v\sigma_{\text{spin}}\rangle$ at a higher temperature [92] are also discrepant with our values when scaled to the same temperature.

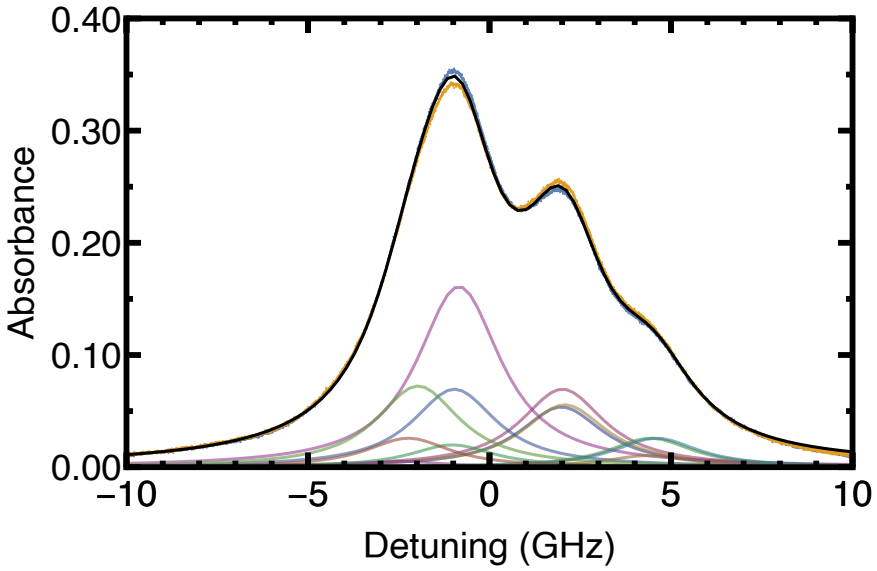

Figure 4.10: Rubidium absorption spectra a cell of length 5 cm at $T = 24.0(5)$ °C and a pressure of 134.10(5) Torr of N_2 buffer gas as measured by the capacitance gauge. The plot shows absorbance $-\ln(I/I_0)$ as a function of laser de-tuning, where I and I_0 are the transmitted and off-resonant transmitted laser intensities, respectively, and the laser de-tuning is relative to the $F = 3 \rightarrow F' = 4$ hyperfine transition frequency of the D2 line in ^{85}Rb in its rest frame and absent any buffer gas. Blue and yellow traces correspond to data from upward and downward scans of the laser frequency. A fit of both traces to the composite spectrum for collisionally broadened and shifted ^{85}Rb and ^{87}Rb D2 hyperfine transitions is shown in black [33]. Individual D2 hyperfine line profiles are also shown as coloured lines, the most prominent of these coloured lines is the collisionally broadened and shifted $F = 3 \rightarrow F' = 4$ line in ^{85}Rb.

4.4.2 Pressure measurement in the gas manifold

The pressure of the inert gas in the experimental cell is measured using the capacitance manometer and is independently verified, typically to within 20 %, using atomic spectroscopy of Rb resonances [33]. In this latter approach, pressure is determined from a fit to the collisionally broadened and shifted rubidium lines. Figure 4.10 shows an example of such a Rb spectrum for trace amounts of Rb in a N_2 buffer gas as well as a fit to the spectrum [34]. Using the shift and broadening parameters from reference [86] and assuming that these parameters are independent of temperature for the relevant temperature range, the fit gives a N_2 pressure of 145.7(5) Torr while the capacitance manometer reading is 134.10(5) Torr. Moreover, we determine the Rb number density to be $8.2(4) \times 10^{10}$ cm^{-3}, from the fitted signal amplitude of the spectrum. The Rb density can be inferred from the amplitude using the known length of the experimental cell, D2 transition dipole moments of ^{85}Rb and ^{87}Rb [102, 105], and the isotopic abundances of ^{85}Rb and ^{87}Rb.

4.5 Discussion of diffusion results

Our results allow us to make detailed comparisons between theory and experiment involving six distinct Rb-X systems. Figure 4.11 shows $D(T, p)$ for all six buffer gas systems with data from our experiments, our values from quantum mechanical calculations, and results of other experiments (see Table 1.1). Here, the vertical axis is dimensionless and represents the ratio $D(T, p)/D_{\mathrm{vdW}}$, where the van-der-Waals diffusion coefficient $D_{\mathrm{vdW}} = \beta_6 v_6$, with relative van-der-Waals velocity $v_6 = \sqrt{2E_6/\mu}$ so that $D_{\mathrm{vdW}} = \hbar/\mu$, which only depends on the reduced mass μ of the system. This ratio, with most values between 2500 and 7500, allows us to compare the six buffer gas systems on the same vertical scale. Our experimental values for $D(T, p)$ agree with the quantum mechanical calculations across all of the different gases. We also find a similar systematic variation in both experiment and theory as a function of

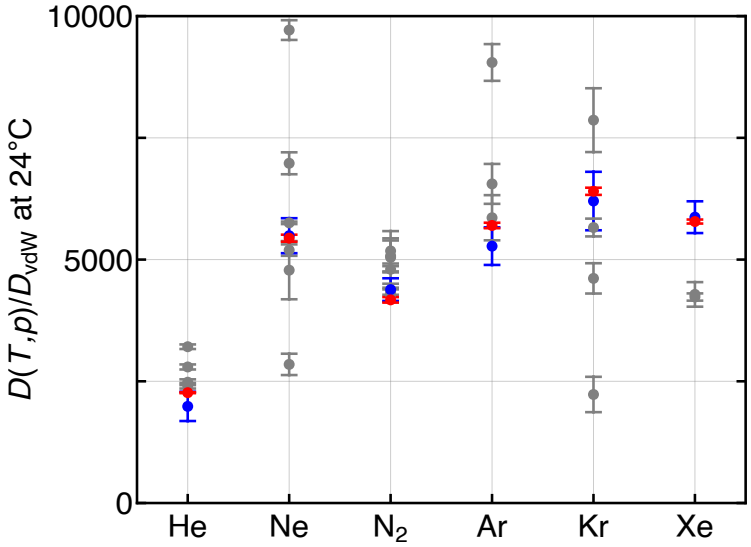

Figure 4.11: Ratio $D(T,p)/D_{\mathrm{vdW}}$, where $D_{\mathrm{vdW}} = \beta_6 v_6 = \hbar/\mu$, for all six naturally abundant Rb+X systems. Filled blue circles with error bars show this ratio based on the experimental determinations presented in this paper. The ratios based on quantum theoretical values for ^{87}Rb-X systems are shown as red circles with error bars. We also display the same ratios with respect to other experimental results (in Table 1.1) as grey circles with error bars, where we assume a standard uncertainty of 1 in the last significant digit for publications that did not supply an uncertainty. The diffusion coefficients $D(T,p)$ are at standard atmospheric pressure and measured at or scaled to $T = 24.0(5)$°C.

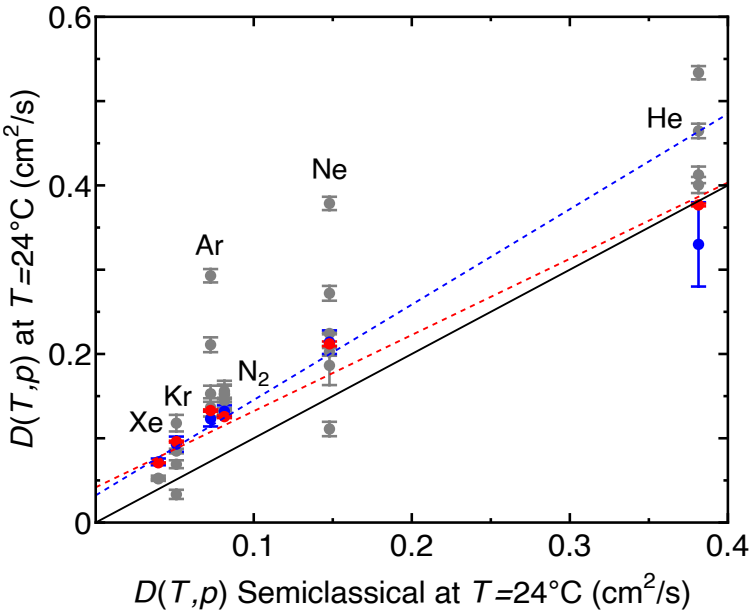

Figure 4.12: Measured $D(T,p)$ for six natural abundance Rb-X systems and theoretical ^{87}Rb-X diffusion coefficients from quantum mechanical simulations at standard atmospheric pressure and $T = 24$ °C plotted as functions of the corresponding semi-classical values for $D(T,p)$. Blue and red markers with error bars representing standard uncertainties correspond to our experimental and quantum theoretical values, respectively. Gray markers correspond to previous measurements found in Table 1.1, where for publications that did not supply an uncertainty budget we assume a standard uncertainty of 1 in the last significant digit. The dotted blue and red lines correspond to linear least-squares fits to the blue and red markers, respectively. The solid black line represents the semiclassical value for $D(T,p)$

the mass of the buffer gas. The other historical measurements of $D(T,p)$, however, show a much larger spread of values relative to the theoretical predictions.

In the semiclassical formalism, an analytical expression for $D(T,p)$ follows from the expression for the thermally averaged cross section $\mathcal{A}(T)$ in Equations 2.18 and 2.22. It is then instructive, as shown in Figure 4.12, to plot the measured $D(T,p)$ along with those from our quantum theoretical calculations as functions of $D(T,p)$ from the semiclassical treatment at one standard atmospheric pressure and $T = 24\,°\mathrm{C}$. The graph shows that the experimental and semiclassical values agree to within a factor of two for all inert buffer gases, as already discussed for nitrogen in Figure 2.11. It is worth noting that the semiclassical

diffusion coefficients depend on both μ and the van der Waals coefficient C_6. In fact, we recall that the semiclassical $D(T,p)$ scales as $\mu^{-1/2}C_6^{-1/3}$.

Linear fits to our experimental and quantum diffusion coefficients with respect to the semiclassical values are also shown in Figure 4.12. The slopes for the experimental and quantum predictions are unitless and have values of 1.13(16) and 0.90(7) respectively, both of which differ from the semiclassical slope of unity.

In addition to the tabulated systematic uncertainties, we have examined additional systematic effects that can affect the experimental diffusion coefficients. Firstly, we have investigated the role of broadband background light due to, for example, amplified spontaneous emission (ASE) from our tapered amplifier by spatially filtering the excitation and readout beams using an optical fibre. Reference [39] has shown that the spectral intensity of ASE can be reduced by a factor of 5.8 by using an optical fibre. However, spatial filtering did not affect the values for $D(T,p)$.

We have also considered two other systematic effects that can potentially impact the diffusion coefficients. These are i) spin decoherence due to the formation of Rb + X van der Waals molecules [69, 76, 90–92, 107] and ii) the redistribution of light due to radiation trapping, including the role of quenching and mixing collisions. These effects can modify the formation of the population grating by depopulating the excited state and redistributing light and result in an inverse pressure dependence. The first of these two effects is known to be small at the typical, >10 Torr buffer gas pressures used in this work [90]. Secondly, based on reference [108], we have determined that the lifetime of the excited state of Rb within the cylindrical excitation volume is only extended by a factor of ≈ 3 due to radiation trapping. This timescale is three orders of magnitude smaller than the timescale of diffusion and is therefore unlikely to play a role in the observed decays. As collisional quenching and mixing are only relevant when radiation trapping is prominent, these effects can be ruled out for the same reason. Additionally, reference [87] suggests that collisional quenching rates in noble

gases are of order 200 Hz at 760 Torr, which is too small to affect our measurements even at the upper limit of our experimental pressure range. We conclude that these processes have not influenced our measurements.

We conclude this subsection by describing a possible application of our setup, namely, the realization of a quantum pressure sensor that depends on the intrinsic properties of atomic interactions. Since experiment and theory are in agreement, it is possible to solve Equations 1.8 and 2.18 directly for p by first determining $\mathcal{Q}(T)$ by recording decay curves over a range of angles and using the calculated value of $\mathcal{A}(T)$. By following this procedure, one can infer the absolute value of the pressure of a buffer gas X in a Rb-X mixture, over the effective pressure range of the technique. In this manner, our technique can serve as a basis for a quantum pressure sensor. Such an effort would complement other techniques that have been recently developed to realize pressure sensors using ultra-cold atoms under high vacuum conditions [65–68].

4.6 Conclusions and future research

We have presented unified measurements of diffusion coefficients near room temperature along with theoretical predictions using quantum, semiclassical, and classical models for six inert buffer gases and trace amounts of natural abundance rubidium using a single experimental apparatus. Our experiment relies on creating spatial population gratings in each m-level of the rubidium gas and measuring its decay or diffusion using two nearly parallel optical laser beams. The decay rate is proportional to the diffusion coefficient and the square of the small angle between the laser beams.

By accounting for systematic effects we have resolved discrepancies between the experimental and theoretical diffusion coefficients for six buffer gases, which provides the basis for a pressure sensor. A practical realization of this idea requires confirmation of the predicted

temperature dependence of $D(T,p)$. Such a confirmation would require an improved oven design which can produce a uniform temperature profile throughout the gas manifold. A new round of experiments will be able to realize greater precision as the optical pumping simulations in Figure 2.9 suggest that an increase in the signal to noise ratio may be possible by tuning the read-out and excitation pulses to be resonant with separate ground state hyperfine levels. Systematic effects due to signal offsets, as shown in Figure 4.8, can be avoided by using a detection system consisting of a photomultiplier tube with an electronic gate and an AOM shutter as in reference [44]. It may also be possible to reduce the effect of wavefront curvature on the systematic error in the angle θ by spatially filtering the excitation and readout beams using optical fibres. A better description of the effects of residual laser light on the rubidium atoms can be based explicitly on the line-shape function as described by the last term in Equation 2.16 instead of the approximation described by the last term in Equation 2.17. Such an improved description, which must include all magnetic sublevels and their relative populations, may allow us to reduce the error associated with this effect.

Some of the improvements proposed here have been realized in a new round of measurements [47]. Here, gated PMT detection was used to measure $D(T,p)$ in a Rb-N_2 mixture using a modified oven which allowed a uniform temperature profile over the range of 24°C to 80°C. Measurements of $D(T,p)$ reported in reference [47] at $T = 24.0(5)$°C agree with the measurements obtained in this dissertation [33, 35] and the preliminary results for the temperature dependence are consistent with the temperature scaling predicted in Figure 2.11 by the quantum and classical models.

Chapter 5

Bibliography

[1] R. Brown, "Xxvii. a brief account of microscopical observations made in the months of June, July and August 1827, on the particles contained in the pollen of plants; and on the general existence of active molecules in organic and inorganic bodies," The philosophical magazine **4**, 161 (1828).

[2] T. Li and M. G. Raizen, "Brownian motion at short time scales," Annalen der Physik **525**, 281 (2013), https://onlinelibrary.wiley.com/doi/pdf/10.1002/andp.201200232 .

[3] A. Einstein, "On the theory of the Brownian movement," Ann. Phys **19**, 371 (1906).

[4] J. C. Allred, R. N. Lyman, T. W. Kornack, and M. V. Romalis, "High-sensitivity atomic magnetometer unaffected by spin-exchange relaxation," Phys. Rev. Lett. **89**, 130801 (2002).

[5] T. G. Walker and W. Happer, "Spin-exchange optical pumping of noble-gas nuclei," Rev. Mod. Phys. **69**, 629 (1997).

[6] A. I. Lvovsky, B. C. Sanders, and W. Tittel, "Optical quantum memory," Nature Photonics **3**, 706 (2009).

[7] J. Kitching, S. Knappe, and L. Hollberg, "Miniature vapor-cell atomic-frequency references," Applied physics letters **81**, 553 (2002).

[8] M. Abdel Hafiz, G. Coget, P. Yun, S. Guérandel, E. de Clercq, and R. Boudot, "A high-performance Raman-Ramsey Cs vapor cell atomic clock," J. Appl. Phys. **121** (2017).

[9] R. J. McNeal, "Disorientation cross sections in optical pumping," J. Chem. Phys. **37**, 2726 (1962).

[10] F. A. Franz and C. E. Sooriamoorthi, "Analytic expressions for transient signals in the optical pumping of alkali-metal vapors," Phys. Rev. A **8**, 2390 (1973).

[11] X. Zeng, Z. Wu, T. Call, E. Miron, D. Schreiber, and W. Happer, "Experimental determination of the rate constants for spin exchange between optically pumped K, Rb, and Cs atoms and ^{129}Xe nuclei in alkali-metal–noble-gas van der Waals molecules," Phys. Rev. A **31**, 260 (1985).

[12] M. E. Wagshul and T. E. Chupp, "Laser optical pumping of high-density Rb in polarized ^{3}He targets," Phys. Rev. A **49**, 3854 (1994).

[13] C. J. Erickson, *MEASUREMENTS OF THE MAGNETIC FIELD DEPENDENCE OF THE SPIN RELAXATION RATE IN ALKALI METAL VAPORS*, PhD dissertation, Princeton University (2000).

[14] M. Parniak and W. Wasilewski, "Direct observation of atomic diffusion in warm rubidium ensembles," Appl. Phys. B **116**, 415 (2014).

[15] T. Mossberg, A. Flusberg, R. Kachru, and S. R. Hartmann, "Total scattering cross section for Na on He measured by stimulated photon echoes," Phys. Rev. Lett. **42**, 1665 (1979).

[16] R. A. Forber, L. Spinelli, J. E. Thomas, and M. S. Feld, "Observation of quantum diffractive velocity-changing collisions by use of two-level heavy optical radiators," Phys. Rev. Lett. **50**, 331 (1983).

[17] G. Biedermann, H. McGuinness, A. Rakholia, Y.-Y. Jau, D. Wheeler, J. Sterk, and G. Burns, "Atom interferometry in a warm vapor," Physical Review Letters **118**, 163601 (2017).

[18] R. L. Fagaly, "Superconducting quantum interference device instruments and applications," Rev. Sci. Inst. **77**, 101101 (2006).

[19] D. Budker and M. Romalis, "Optical magnetometry," Nat. Physics **3**, 227 (2007).

[20] J. M. Higbie, S. M. Rochester, B. Patton, R. Holzlöhner, D. Bonaccini Calia, and D. Budker, "Magnetometry with mesospheric sodium," Proc. Natl. Acad. Sci. USA **108**, 3522–3525 (2011).

[21] D. Suter, M. Rosatzin, and J. Mlynek, "Optically driven spin nutations in the ground state of atomic sodium," Phys. Rev. A **41**, 1634 (1990).

[22] S. Chapman, T. Cowling, and D. Burnett, *The Mathematical Theory of Non-uniform Gases: An Account of the Kinetic Theory of Viscosity, Thermal Conduction and Diffusion in Gases*, 3rd ed. (Cambridge University Press, 1990).

[23] L. Blank, D. E. Weeks, and G. S. Kedziora, "M+Ng potential energy curves including spin-orbit coupling for M = K, Rb, Cs and Ng = He, Ne, Ar," J. Chem. Phys. **136**, 124315 (2012).

[24] A. A. Medvedev, V. V. Meshkov, A. V. Stolyarov, and M. C. Heaven, "Ab initio interatomic potentials and transport properties of alkali metal (M = Rb and Cs)–rare gas (Rg = He, Ne, Ar, Kr, and Xe) media," Phys. Chem. Chem. Phys. **20**, 25974 (2018).

[25] J. Kłos and E. Tiesinga, "Elastic and glancing-angle rate coefficients for heating of ultracold Li and Rb atoms by collisions with room-temperature noble gases, H_2, and N_2," J. Chem. Phys. **158**, 014308 (2023).

[26] E. L. Cussler, *Diffusion: Mass Transfer in Fluid Systems*, 3rd ed., Cambridge Series in Chemical Engineering (Cambridge University Press, 2009).

[27] M. Parniak and W. Wasilewski, "Direct observation of atomic diffusion in warm rubidium ensembles," Appl. Phys. B **116**, 415 (2014).

[28] K. Ishikawa and T. Yabuzaki, "Diffusion coefficient and sublevel coherence of Rb atoms in N_2 buffer gas," Phys. Rev. A **62**, 065401 (2000).

[29] K. Ishikawa, "Spin-polarized lithium diffusion in a glass hot-vapor cell," Appl. Phys. B **122**, 224 (2016).

[30] K. Aoki and T. Mitsui, "Observing random walks of atoms in buffer gas through resonant light absorption," Phys. Rev. A **94**, 012703 (2016).

[31] Allard, N. F., Myneni, K., Blakely, J. N., and Guillon, G., "Temperature and density dependence of line profiles of sodium perturbed by helium," A and A **674**, A171 (2023).

[32] L. J. Rothberg and N. Bloembergen, "High-resolution four-wave light-mixing studies of collision-induced coherence in Na vapor," Phys. Rev. A **30**, 820 (1984).

[33] A. Pouliot, G. Carlse, H. C. Beica, T. Vacheresse, A. Kumarakrishnan, U. Shim, S. B. Cahn, A. Turlapov, and T. Sleator, "Accurate determination of an alkali-vapor–inert-gas diffusion coefficient using coherent transient emission from a density grating," Phys. Rev. A **103**, 023112 (2021), corrected in [34].

[34] A. Pouliot, G. Carlse, H. C. Beica, T. Vacheresse, A. Kumarakrishnan, U. Shim, S. B. Cahn, A. Turlapov, and T. Sleator, "Erratum: Accurate determination of an alkali-vapor–inert-gas diffusion coefficient using coherent transient emission from a density grating [Phys. Rev. A 103, 023112 (2021)]," Phys. Rev. A **111**, 039903 (2025).

[35] A. Pouliot, E. Chomen Ramos, G. Carlse, T. Vacheresse, J. Randhawa, L. Marmet, A. Kumarakrishnan, J. Kłos, and E. Tiesinga, "Measurements of diffusion coefficients for rubidium–inert-gas mixtures using coherent scattering from optically pumped population gratings," Phys. Rev. A **111**, 033108 (2025).

[36] A. Pouliot, G. Carlse, E. Chomen Ramos, T. Vacheresse, J. Randhawa, A. Kumarakrishnan, J. Kłos, and E. Tiesinga, "Transit time corrections to the diffusion of atomic lattices," JOSA B (2025), submitted.

[37] I. Chan, A. Andreyuk, S. Beattie, B. Barrett, C. Mok, M. Weel, and A. Kumarakrishnan, "Properties of magnetic sublevel coherences for precision measurements," Phys. Rev. A **78**, 033418 (2008).

[38] I. Chan, B. Barrett, and A. Kumarakrishnan, "Precise determination of atomic g-factor ratios from a dual isotope magneto-optical trap," Phys. Rev. A **84**, 032509 (2011).

[39] A. Pouliot, H. C. Beica, A. Carew, A. Vorozcovs, G. Carlse, B. Barrett, and A. Kumarakrishnan, "Investigations of optical pumping for magnetometry using an auto-locking laser system," in *Laser Technology for Defense and Security XIV*, Vol. 10637, edited by M. Dubinskiy and T. C. Newell, International Society for Optics and Photonics (SPIE, 2018) pp. 40–47.

[40] H. C. Beica, A. Pouliot, A. Carew, A. Vorozcovs, N. Afkhami-Jeddi, T. Vacheresse, G. Carlse, P. Dowling, B. Barron, and A. Kumarakrishnan, "Characterization and

applications of auto-locked vacuum-sealed diode lasers for precision metrology," Rev. Sci. Inst. **90**, 085113 (2019).

[41] A. Pouliot, H. C. Beica, A. Carew, A. Vorozcovs, G. Carlse, and A. Kumarakrishnan, "Auto-locking waveguide amplifier system for lidar and magnetometric applications," in *High-Power Diode Laser Technology XVI*, Vol. 10514, edited by M. S. Zediker, International Society for Optics and Photonics (SPIE, 2018) pp. 152 – 159.

[42] H. C. Beica, A. Pouliot, P. Dowling, A. Carew, T. Vacheresse, G. Carlse, L. Marmet, and A. Kumarakrishnan, "Development of a technique for the precise determination of atomic lifetimes based on photon echoes," Phys. Rev. A **101**, 033408 (2020).

[43] G. Carlse, A. Pouliot, T. Vacheresse, A. Carew, H. C. Beica, S. Winter, and A. Kumarakrishnan, "Technique for magnetic moment reconstruction of laser-cooled atoms using direct imaging and prospects for measuring magnetic sublevel distributions," J. Opt. Soc. Am. B **37**, 1419 (2020).

[44] G. Carlse, J. Randhawa, E. Ramos, T. Vacheresse, A. Pouliot, A. C. Carew, and A. Kumarakrishnan, "Role of optical channeling in contrast enhancement of echo interferometers," Phys. Rev. A **109**, 043307 (2024).

[45] G. Carlse, J. Randhawa, E. Ramos, T. Vacheresse, A. Pouliot, A. C. Carew, A. Kumarakrishnan, and B. Barrett, "Optimization of Bragg scattering from atomic gratings for echo interferometry," Phys. Rev. A **110**, 043306 (2024).

[46] G. Carlse, J. Randhawa, E. Ramos, T. Vacheresse, A. Pouliot, and A. Kumarakrishnan, "Velocimetry using free-induction decay of matter-wave lattices," Phys. Rev. A **111**, L021304 (2025).

[47] E. Chomen Ramos, A. Pouliot, G. Carlse, T. Vacheresse, J. Randhawa, M. Belen Llaguno, and A. Kumarakrishnan, "Temperature dependence of diffusion coefficients for rubidium-inert gas mixtures using coherent scattering," in *Division of Atomic, Molecular and Optical Physics* (2025).

[48] A. Pouliot, E. Chomen Ramos, G. Carlse, T. Vacheresse, J. Randhawa, and A. Kumarakrishnan, "Collisional broadening and shift parameters for Rb D2 line," Atoms (2025), in preparation.

[49] S. J. Seltzer and M. V. Romalis, "High-temperature alkali vapor cells with antirelaxation surface coatings," J. Appl. Phys. **106**, 114905 (2009).

[50] J. Mora, A. Cobos, D. Fuentes, and D. F. Jackson Kimball, "Measurement of the ratio between g-factors of the ground states of ^{87}Rb and ^{85}Rb," Ann. Phys. (Leipzig) **531**, 1800281 (2019).

[51] A. Tonyushkin, A. Kumarakrishnan, A. Turlapov, and T. Sleator, "Magnetic coherence gratings in a high-flux atomic beam," Eur. Phys. J. D **58**, 39 (2010).

[52] A. Kumarakrishnan, S. B. Cahn, U. Shim, and T. Sleator, "Magnetic grating echoes from laser-cooled atoms," Phys. Rev. A **58**, R3387 (1998).

[53] A. Kumarakrishnan, U. Shim, S. B. Cahn, and T. Sleator, "Ground-state grating echoes from Rb vapor at room temperature," Phys. Rev. A **58**, 3868 (1998).

[54] P. R. Berman and B. Dubetsky, "Magnetic grating free induction decay and magnetic grating echo," Laser Phys. **4**, 1017 (1994).

[55] B. Shore, *The Theory of Coherent Atomic Excitation, 2 Volume Set*, The Theory of Coherent Atomic Excitation (Wiley, 1990).

[56] P. R. Berman, "Collisional decay and revival of the grating stimulated echo," Phys. Rev. A **49**, 2922 (1994).

[57] U. Shim, A. Kumarakrishnan, A. V. Turlapov, S. B. Cahn, and T. Sleator, "Collisional revival of magnetic grating free induction decay," (2005), (Unpublished).

[58] U. Shim, *COHERENT TRANSIENT EFFECTS IN LASER COOLED AND ROOM TEMPERATURE ATOMS*, PhD dissertation, New York University (1997).

[59] S. B. Cahn, A. Kumarakrishnan, U. Shim, T. Sleator, P. R. Berman, and B. Dubetsky, "Time-domain de Broglie wave interferometry," Phys. Rev. Lett. **79**, 784 (1997).

[60] B. Barrett, I. Chan, C. Mok, A. Carew, I. Yavin, A. Kumarakrishnan, S. Cahn, and T. Sleator, "Chapter 3 - time-domain interferometry with laser-cooled atoms," in *Advances in Atomic, Molecular, and Optical Physics*, Advances In Atomic, Molecular, and Optical Physics, Vol. 60, edited by E. Arimondo, P. Berman, and C. Lin (Academic Press, 2011) pp. 119–199.

[61] B. Barrett, A. Carew, H. C. Beica, A. Vorozcovs, A. Pouliot, and A. Kumarakrishnan, "Prospects for precise measurements with echo atom interferometry," Atoms **4**, 19 (2016).

[62] B. Barrett, A. Carew, S. Beattie, and A. Kumarakrishnan, "Measuring the atomic recoil frequency using a modified grating-echo atom interferometer," Phys. Rev. A **87**, 033626 (2013).

[63] C. Mok, B. Barrett, A. Carew, R. Berthiaume, S. Beattie, and A. Kumarakrishnan, "Demonstration of improved sensitivity of echo interferometers to gravitational acceleration," Phys. Rev. A **88**, 023614 (2013).

[64] T. R. Marrero and E. A. Mason, "Gaseous Diffusion Coefficients," J. Phys. Chem. Ref. Data **1** (1972).

[65] V. B. Makhalov, K. A. Martiyanov, and A. V. Turlapov, "Primary vacuometer based on an ultracold gas in a shallow optical dipole trap," Metrologia **53**, 1287 (2016).

[66] J. Scherschligt, J. A. Fedchak, D. S. Barker, S. Eckel, N. Klimov, C. Makrides, and E. Tiesinga, "Development of a new UHV/XHV pressure standard (cold atom vacuum standard)," Metrologia **54**, S125 (2017).

[67] P. Shen, K. W. Madison, and J. L. Booth, "Realization of a universal quantum pressure standard," Metrologia **57**, 025015 (2020).

[68] L. H. Ehinger, B. P. Acharya, D. S. Barker, J. A. Fedchak, J. Scherschligt, E. Tiesinga, and S. Eckel, "Comparison of two multiplexed portable cold-atom vacuum standards," AVS Quantum Science **4**, 034403 (2022).

[69] F. A. Franz and C. Volk, "Spin relaxation of rubidium atoms in sudden and quasimolecular collisions with light-noble-gas atoms," Phys. Rev. A **14**, 1711 (1976).

[70] Aymar, M., Bouchiat, M.A., and Brossel, J., "Étude expérimentale de la relaxation du rubidium en présence d'hélium," J. Phys. France **30**, 619 (1969).

[71] F. A. Franz, "Rubidium spin relaxation in the rare gases under ultraclean conditions," Phys. Rev. **139**, A603 (1965).

[72] R. A. Bernheim, "Spin Relaxation in Optical Pumping," J. Chem. Phys. **36**, 135 (1962).

[73] R. Chrapkiewicz, W. Wasilewski, and C. Radzewicz, "How to measure diffusional decoherence in multimode rubidium vapor memories?" Opt. Commun. **317**, 1 (2014).

[74] M. Shuker, O. Firstenberg, R. Pugatch, A. Ron, and N. Davidson, "Storing images in warm atomic vapor," Phys. Rev. Lett. **100**, 223601 (2008).

[75] W. Franzen, "Spin relaxation of optically aligned rubidium vapor," Phys. Rev. **115**, 850 (1959).

[76] M. A. Bouchiat, J. Brossel, and L. C. Pottier, "Evidence for Rb-Rare-Gas Molecules from the Relaxation of Polarized Rb Atoms in a Rare Gas. Experimental Results," J. Chem. Phys. **56**, 3703 (1972).

[77] D. B. Higginbottom, B. M. Sparkes, M. Rancic, O. Pinel, M. Hosseini, P. K. Lam, and B. C. Buchler, "Spatial-mode storage in a gradient-echo memory," Phys. Rev. A **86**, 023801 (2012).

[78] P. R. Berman, G. Rogers, and B. Dubetsky, "Rate equations between electronic-state manifolds," Phys. Rev. A **48**, 1506 (1993).

[79] N. Allard and J. Kielkopf, "The effect of neutral nonresonant collisions on atomic spectral lines," Rev. Mod. Phys. **54**, 1103 (1982).

[80] A. A. Michelson, "On the Broadening of Spectral Lines," Astrophysical Journal **2**, 251 (1895).

[81] H. A. Lorentz, "The absorption and emission lines of gaseous bodies," KNAW, Proceedings **8 II**, 591 (1906).

[82] W. Lenz, "Einige korrespondenzmäßige betrachtungen," Zeitschrift für Physik **25**, 299 (1924).

[83] W. Lenz, "Allgemeine theorie der verbreiterung von spektrallinien," Zeitschrift für Physik **80**, 423 (1933).

[84] E. Lindholm, "Pressure broadening of spectral lines," Ark. Mat. Astron. Fys. **32A** (1945).

[85] A. Corney, *Atomic and Laser Spectroscopy*, Oxford science publications (Clarendon Press, 1977).

[86] M. D. Rotondaro and G. P. Perram, "Collisional broadening and shift of the rubidium D1 and D2 lines ($5^2S_{1/2} \rightarrow 5^2P_{1/2}, 5^2P_{3/2}$) by rare gases, H_2, D_2, N_2, CH_4 and CF_4," J. Quant. Spectrosc. Radiat. Transfer **57**, 497 (1997).

[87] E. Speller, B. Staudenmayer, and V. Kempter, "Quenching cross sections for alkali-inert gas collisions," Z. Phys. A **291**, 311 (1979).

[88] V. Belov, "Application of the magnetic-scanning method to the measurement of the broadening and shift constants of the rubidium D2 line (780.0 nm) by foreign gases," Optics and Spectroscopy **51**, 22 (1981).

[89] S. Slama, C. von Cube, M. Kohler, C. Zimmermann, and P. W. Courteille, "Multiple reflections and diffuse scattering in Bragg scattering at optical lattices," Phys. Rev. A **73**, 023424 (2006).

[90] W. Happer, E. Miron, S. Schaefer, D. Schreiber, W. A. van Wijngaarden, and X. Zeng, "Polarization of the nuclear spins of noble-gas atoms by spin exchange with optically pumped alkali-metal atoms," Phys. Rev. A **29**, 3092 (1984).

[91] G. D. Cates, R. J. Fitzgerald, A. S. Barton, P. Bogorad, M. Gatzke, N. R. Newbury, and B. Saam, "Rb$-^{129}$Xe spin-exchange rates due to binary and three-body collisions at high Xe pressures," Phys. Rev. A **45**, 4631 (1992).

[92] I. A. Nelson and T. G. Walker, "Rb-Xe spin relaxation in dilute Xe mixtures," Phys. Rev. A **65**, 012712 (2001).

[93] P. R. Berman and V. S. Malinovsky, *Principles of laser spectroscopy and quantum optics* (Princeton University Press, 2011).

[94] W. A. Hamel, J. E. M. Haverkort, H. G. C. Werij, and J. P. Woerdman, "Calculation of alkali-noble gas diffusion cross sections relevant to light-induced drift," J. Phys. B **19**, 4127 (1986).

[95] M. S. Child, *Molecular collision theory* (Academic Press, London and New York, 1974).

[96] M. Wang, W. Huang, F. Kondev, G. Audi, and S. Naimi, "The AME 2020 atomic mass evaluation (II). tables, graphs and references*," Chinese Phys. C **45**, 030003 (2021).

[97] E. Tiesinga, P. J. Mohr, D. B. Newell, and B. N. Taylor, "CODATA recommended values of the fundamental physical constants: 2018," Rev. Mod. Phys. **93**, 025010 (2021).

[98] L. Monchick, "Collision integrals for the exponential repulsive potential," Phys. Fluids **2**, 695 (1959).

[99] K. Gibble, "Scattering of cold-atom coherences by hot atoms: Frequency shifts from background-gas collisions," Phys. Rev. Lett. **110**, 180802 (2013).

[100] A. Derevianko, S. G. Porsev, and J. F. Babb, "Electric dipole polarizabilities at imaginary frequencies for hydrogen, the alkali–metal, alkaline–earth, and noble gas atoms," Atomic Data and Nuclear Data Tables **96**, 323 (2010).

[101] M. Bouledroua, A. Dalgarno, and R. Côté, "Diffusion and excitation transfer of excited alkali-metal atoms," Phys. Rev. A **65**, 012701 (2001).

[102] D. Steck, "Rubidium 87 D line data," https://steck.us/alkalidata/ (2023), Rubidium-87 D Line Data (Version 2.3.2).

[103] *Model PRS10 Rubidium Frequency Standard*, Stanford Research Systems (2015).

[104] J. Ma, A. Kishinevski, Y.-Y. Jau, C. Reuter, and W. Happer, "Modification of glass cell walls by rubidium vapor," Phys. Rev. A **79**, 042905 (2009).

[105] D. Steck, "Rubidium 85 D line data," https://steck.us/alkalidata/ (2023), Rubidium-85 D Line Data (Version 2.3.2).

[106] *SG380 Series RF Signal Generators (SG384)*, Stanford Research Systems (2021).

[107] F. Hartmann and F. Hartmann-Boutron, "Shift and broadening of the ^{87}Rb 0-0 line due to collisions with krypton buffer-gas atoms," Phys. Rev. A **2**, 1885 (1970).

[108] T. Holstein, "Imprisonment of resonance radiation in gases," Phys. Rev. **72**, 1212 (1947).

[109] X. Baillard, A. Gauguet, S. Bize, P. Lemonde, P. Laurent, A. Clairon, and P. Rosenbusch, "Interference-filter-stabilized external-cavity diode lasers," Optics Communications **266**, 609 (2006).

[110] M. Gilowski, C. Schubert, M. Zaiser, W. Herr, T. Wübbena, T. Wendrich, T. Müller, E. Rasel, and W. Ertmer, "Narrow bandwidth interference filter-stabilized diode laser systems for the manipulation of neutral atoms," Optics Communications **280**, 443 (2007).

[111] R. A. Nyman, G. Varoquaux, B. Villier, D. Sacchet, F. Moron, Y. Le Coq, A. Aspect, and P. Bouyer, "Tapered-amplified antireflection-coated laser diodes for potassium and rubidium atomic-physics experiments," Review of Scientific Instruments **77** (2006).

[112] K. Fukuda, M. Tachikawa, and M. Kinoshita, "Allan-variance measurements of diode laser frequency-stabilized with a thin vapor cell," Applied Physics B **77**, 823 (2003).

[113] S. Kunze, S. Wolf, and G. Rempe, "Measurement of fast frequency fluctuations: Allan variance of a grating-stabilized diode laser," Optics communications **128**, 269 (1996).

[114] L. D. Turner, K. Weber, C. Hawthorn, and R. E. Scholten, "Frequency noise characterisation of narrow linewidth diode lasers," Optics communications **201**, 391 (2002).

[115] D. Voigt, E. Schilder, R. Spreeuw, and H. Van Linden van den Heuvell, "Characterization of a high-power tapered semiconductor amplifier system," Applied Physics B **72**, 279 (2001).

[116] G. Carlse, K. B. Borsos, H. C. Beica, T. Vacheresse, A. Pouliot, J. Perez-Garcia, A. Vorozcovs, B. Barron, S. Jackson, L. Marmet, *et al.*, "Technique for rapid mass determination of airborne microparticles based on release and recapture from an optical dipole force trap," Physical Review Applied **14**, 024017 (2020).

[117] D. W. Allan, "Statistics of atomic frequency standards," Proceedings of the IEEE **54**, 221 (1966).

[118] W. J. Riley and D. A. Howe, *Handbook of frequency stability analysis*, Vol. 1065 (US Department of Commerce, National Institute of Standards and Technology ..., 2008).

[119] J. Randhawa, G. Carlse, J. Cuzzupoli, E. Ramos, T. Vacheresse, A. Pouliot, and A. Kumarakrishnan, "Homebuilt laser system for frequency domain measurements of gravity using echo atom interferometry," in *Division of Atomic, Molecular and Optical Physics* (2025).

[120] S. P. Maddipatla, H. Haeri, K. Jerath, and S. Brennan, "Fast Allan variance (FAVAR) and dynamic fast Allan variance (D − FAVAR) algorithms for both regularly and irregularly sampled data"," IFAC-PapersOnLine **54**, 26 (2021), modeling, Estimation and Control Conference MECC 2021.

[121] C. Chiarella and A. Reichel, "On the evaluation of integrals related to the error function," Mathematics of Computation **22**, 137 (1968).

[122] S. Abrarov, B. Quine, and R. Jagpal, "Efficient application of the Chiarella and Reichel series approximation of the complex error function," arXiv preprint arXiv:1208.2062 (2012).

[123] M. V. Romalis, E. Miron, and G. D. Cates, "Pressure broadening of Rb D_1 and D_2 lines by ^{3}He, ^{4}He, N_2, and Xe: Line cores and near wings," Phys. Rev. A **56**, 4569 (1997).

[124] J. L. Cohen and P. R. Berman, "Transit-time effects in coherent transient spectroscopy," Phys. Rev. A **54**, 5262 (1996).

[125] V. Shukla and A. Ray, "Experimental study on transit time broadening in rubidium 5s-5d excitation," Applied Optics **61**, 4719 (2022).

[126] J. C. Bergquist, "13 - Doppler-free spectroscopy," in *Atomic, Molecular, and Optical Physics: Atoms and Molecules*, Experimental Methods in the Physical Sciences, Vol. 29, edited by F. Dunning and R. G. Hulet (Academic Press, 1996) pp. 255–272.

[127] M. Levenson, *Introduction to Nonlinear Laser Spectroscopy* (Academic Press, 2012).

[128] M. Bruvelis, J. Ulmanis, N. Bezuglov, K. Miculis, C. Andreeva, B. Mahrov, D. Tretyakov, and A. Ekers, "Analytical model of transit time broadening for two-photon excitation in a three-level ladder and its experimental validation," Phys. Rev. A **86**, 012501 (2012).

[129] J. E. Thomas and R. A. Forber, "Transverse atomic motion in transient polarization phenomena," Opt. Lett. **9**, 56 (1984).

[130] I. Yavin, M. Weel, A. Andreyuk, and A. Kumarakrishnan, "A calculation of the time-of-flight distribution of trapped atoms," American Journal of Physics **70**, 149 (2002), https://pubs.aip.org/aapt/ajp/article-pdf/70/2/149/7420972/149_1_online.pdf .

[131] I. Yavin, T. Mikaelian, and A. Kumarakrishnan, "Calculation of the transfer efficiency between dual magneto-optical traps and simulation of a Ioffe trap for Bose Einstein condensation," Canadian journal of physics **81**, 651 (2003).

[132] G. Carlse, J. Randhawa, A. Pouliot, E. Ramos, T. Vacheresse, and A. Kumarakrishnan, "Measurement of gravitational acceleration using an echo atom interferometer," Physical Review A (2025), submitted.

[133] B. Barrett, I. Chan, and A. Kumarakrishnan, "Atom-interferometric techniques for measuring uniform magnetic field gradients and gravitational acceleration," Phys. Rev. A **84**, 063623 (2011).

[134] DLMF, "*NIST Digital Library of Mathematical Functions*," `https://dlmf.nist.gov/`, Release 1.2.4 of 2025-03-15 (2025), f. W. J. Olver, A. B. Olde Daalhuis, D. W. Lozier, B. I. Schneider, R. F. Boisvert, C. W. Clark, B. R. Miller, B. V. Saunders, H. S. Cohl, and M. A. McClain, eds.

[135] E. W. Ng and M. Geller, "A table of integrals of the error functions," Journal of Research of the National Bureau of Standards-B. Mathematical Sciences **73B**, 1 (1969).

Appendices

Appendix A

Characterization of tapered amplifier system

A.1 Development of master oscillator, power amplifier (MOPA) system

There is widespread interest in developing a new generation of spin-exchange free rubidium magnetometers [4] for geophysical exploration. These magnetometers can be used in airborne surveys for the improved detection of metal and mineral deposits. Magnetometers require laser sources for optical pumping. The laser source should be capable of being frequency stabilized with respect to rubidium atomic transitions without the need for human intervention. Additionally, the laser pulses should have pulse widths of about 100 ns, repetition rates of several kilohertz and power outputs of a few Watts. In this appendix, we describe the pulsed laser system based on auto-locked diode laser systems (ALDLS) that we developed [40, 41] that is capable of addressing all the required specifications.

During the last forty years, there have been significant improvements in the sensitivity of

vapour cell magnetometers used for the rapid detection of small magnetic fields in airborne and terrestrial surveys. These surveys are capable of detecting magnetic anomalies and magnetized rocks associated with deposits of metals and minerals. Vapour cell magnetometers rely on optically pumping alkali vapours using high-power light sources. The vapour becomes spin-polarized and transparent to the pump laser when the optical pumping is complete. Therefore, monitoring the transmission of the pump laser serves as a convenient method of probing the atomic polarization due to optical pumping. An external magnetic field drives a periodic change in population between adjacent ground state magnetic sublevels at the Larmor frequency. As a result, the orthogonal, circularly polarized components of the probe laser are differentially absorbed and exhibit Larmor oscillations. A balanced photo-detector can be used to record these Larmor oscillations and measure the magnetic field.

ALDLS units are integrated using components from original equipment manufacturers (OEM) coupled with specially machined parts and powerful central processors. The laser's master oscillator depends on optical feedback from a narrow band interference filter to realize a narrow laser line width (500 kHz)[109, 110]. The thermally stabilized laser cavity can be evacuated within minutes and vacuum-sealed for several months, making the system insensitive to environmental temperature and pressure fluctuations. The optical feedback from the interference filter can be adjusted from outside the cavity using a vacuum feed-through. The ALDLS can be locked or scanned with respect to a spectral line without the need for human intervention using a digital controller that is capable of storing a variety of algorithms in its memory for laser frequency stabilization using techniques such as pattern matching and first or third derivative feedback. The laser cavity relies on an interchangeable optics kit consisting of a laser diode and optical feedback elements to operate in the desired wavelength range. Therefore, the master oscillator can be designed to optically pump both the D2 (780 nm) and D1 (795 nm) absorption lines in rubidium. The laser source can also address spectral lines associated with both ^{85}Rb and ^{87}Rb isotopes. The ALDLS technology

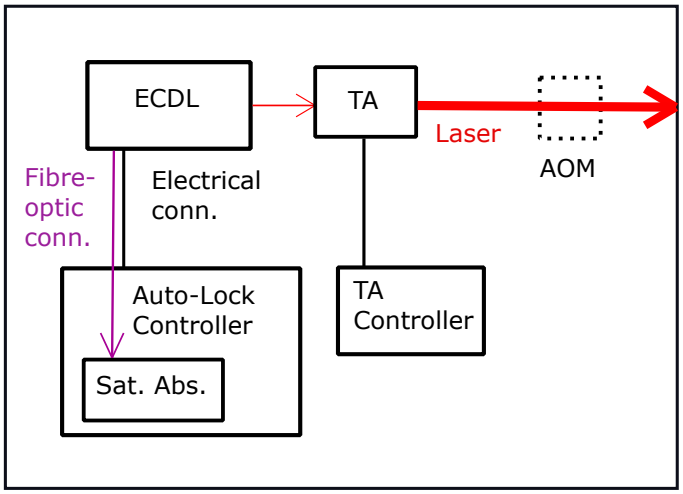

Figure A.1: Schematic of ALDLS system consisting of an external cavity diode laser (ECDL) with an auto-lock controller and waveguide tapered amplifier (TA). Amplitude modulation is achieved by pulsing an acousto-optic modulator (AOM) with RF circuits

enables additional features such as power amplification of the master oscillator's output of 100 mW to several Watts using semiconductor waveguides [111] as well as rapid amplitude modulation using acousto-optic modulators (AOMs) and radio frequency (RF) electronics. A schematic diagram of the pulsed laser system is shown in Figure A.1.

The output of the master oscillator is fibre coupled through a beam splitter into an auto-lock controller containing a saturation-absorption spectrometer and control electronics for frequency stabilization with respect to Rb spectra. Another output of the beam splitter is aligned through a 2-W semiconductor waveguide amplifier to increase the power output. The AOM utilizes TTL switches to produce suitably short pulses for optical pumping.

Optical feedback from a narrowband interference filter [109, 110] is used to realize a laser linewidth of 500 kHz. Laser operation was initially demonstrated at 780 nm and 633 nm based on rubidium and iodine spectroscopy, respectively. We characterized the system performance through measurements of the Allan deviation of the beat note between two lasers,

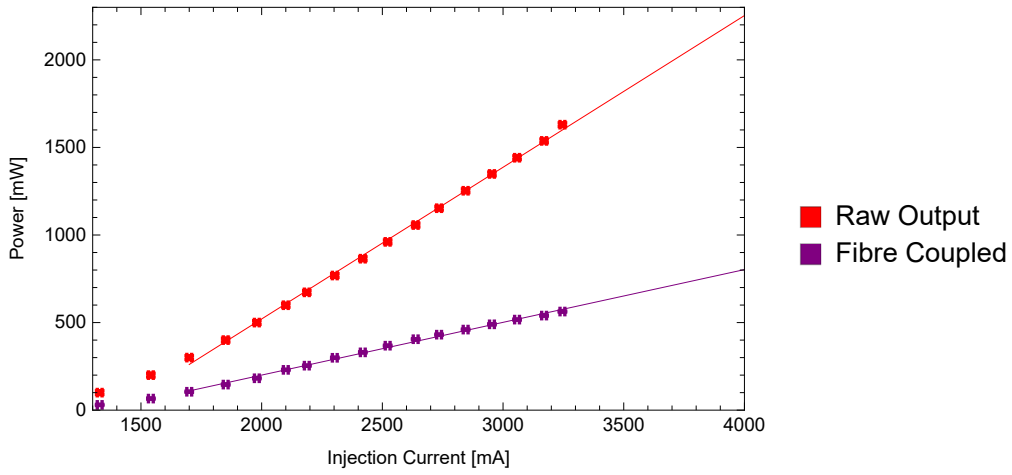

Figure A.2: Output power of 2-Watt tapered amplifier as a function of injection current recorded with and without fibre coupling at a temperature of 16°C. The power input from the seed laser was 17 mW. The straight lines show the extrapolated power output for the maximum allowed injection current

and through a measurement of the Allan deviation of the lock stability of a single laser. The laser frequency was stabilized using different auto-locking algorithms selected from the digital controller's library for these studies. We used third derivative feedback for iodine spectroscopy, and both pattern matching and first derivative feedback for rubidium spectroscopy. The laser linewidth and lock stability allowed precision measurements of gravitational acceleration with an accuracy of 3 parts-per-billion (ppb) using a state-of-the-art industrial sensor. Our studies also showed that the correction signals were reduced by nearly an order of magnitude by evacuating the air in the laser cavity. Under laboratory conditions, the Allan deviation of the beat note between two identical lasers was measured to be 2×10^{-12} for a measurement time $\tau = 40$ s. The Allan deviation of the lock stability of a single laser is 2×10^{-12} for $\tau = 80$ s, which suggests a similar level of performance. These specifications compare favourably with respect to different types of diode lasers[112–114].

The pulsed laser system relies on the amplification of highly monochromatic light from the auto-locking diode laser system (ALDLS) using a tapered, semiconductor waveguide amplifier. The amplifier consists of two sections: a waveguide, and a tapered gain region.

The tapered geometry of the gain region couples the amplified light into several spatial modes. This configuration allows the amplifier to operate at high currents without increasing the energy density of the beam inside the device to the point where non-linear effects can cause catastrophic self-focusing. Spatially filtered laser light from a monochromatic source is coupled into the waveguide section and diffracts into the tapered section such that the tapered gain region is completely filled, allowing maximum amplification of the seed light [111]. Figure A.2 shows the performance of a 2 W tapered amplifier seeded by 17 mW of light from a seed laser locked to a Rb spectral line.

The amplifier introduces two detrimental effects in the seed light. Firstly, the spatial profile of the beam is distorted by the large number of spatial modes associated with the amplifier cavity. Seeding with a filtered TEM00 mode limits the output to a subset of spatial modes, but the beam is still far from Gaussian, assuming a more "flat topped" profile with a few local maxima. Secondly, the spectral profile of the output beam is modified by the broadband amplified spontaneous emission (ASE) from the TA cavity. The simplest way to reduce these effects is to spatially filter the output. This process eliminates undesired spatial modes and a large portion of the ASE as well [115]. However, it comes at the cost of the output power of the beam, as shown in Figure A.2.

We have characterized the relative intensity of the ASE and its reduction through fibre coupling by using a grating spectrometer with a resolution of 1 nm, as shown in Figure A.3. The ASE consists of partially coherent light spanning several nanometers. We find that the intensity of ASE is three to four orders of magnitude smaller than the amplified light at the seed wavelength.

The output power of the amplifier has been measured as a function of the power of the seed laser as shown in Figure A.4. The data show the saturation of the power output of the amplifier as the seed power approaches 30 mW. These results also suggest that a single seed laser (power output of 100 mW) can drive up to three waveguide amplifiers.

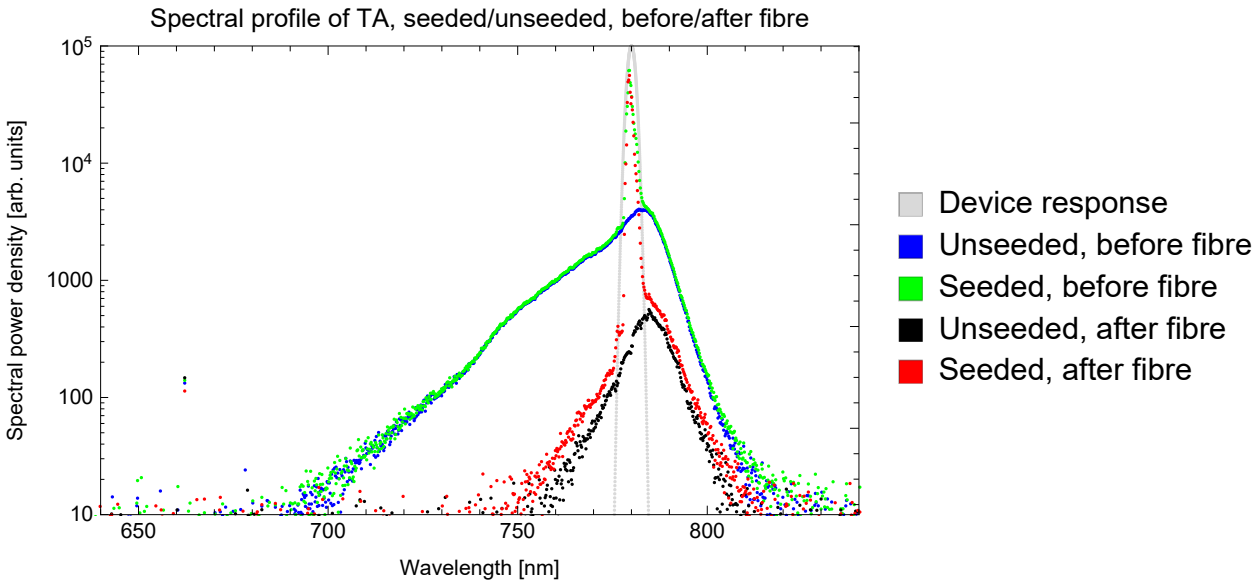

Figure A.3: Spectral characterization of a 2-Watt waveguide amplifier operating at 780 nm with a fibre coupled spectrometer. The full width at half maximum (FWHM) of spectral response function of the spectrometer (1 nm) is shown in grey. This FWHM is much larger than the linewidth (500 kHz) of the seed laser. The spectrometer transmission is recorded before and after an optical fibre that is used to spatially filter the output of the amplifier. At each location, the ASE is recorded by blocking the seed light from the ALDLS. The spectrum of the amplified light is also recorded before and after the fibre.

The effect of the temperature of the tapered amplifier on the power output for constant injection current and seed powers is shown in Figure A.5. The gain-curve of the semiconductor shifts gradually as a function of temperature and we find that for most devices the ideal operating temperature is well below room temperature. The limit on the TA operating current in ambient conditions is then the ambient dew point, since condensation forming on the contacts of the TA will result in catastrophic failure of the device. By operating the TA in a controlled environment (*e.g.* with dry air) one can operate at lower temperatures which will optimize the performance of the device.

Following the development of the laser system, my research group typically used a single ECDL to seed multiple waveguide amplifiers to support four experiments including my own. These experiments included magnetometry/diffusion [33, 35], atom interferometry [43–46],

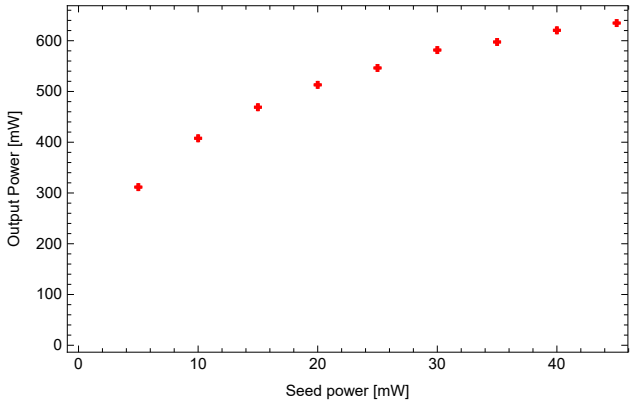

Figure A.4: Waveguide amplifier output as a function of seed-power. This data was recorded with a 2-Watt amplifier driven with an injection current of 1980 mA at a temperature of 16°C

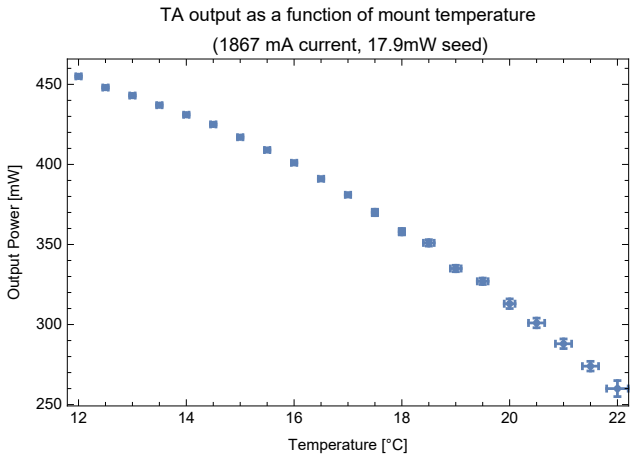

Figure A.5: Output power of 2-Watt waveguide amplifier as a function of temperature

atomic lifetime measurements [42] and optical tweezers [116].

Appendix B

Computing the Allan deviation

B.1 Introduction and outline

The Allan variance σ_{a}^2 and Allan deviation (AD) $\sigma_{\mathrm{a}} = \sqrt{\sigma_{\mathrm{a}}^2}$ were introduced by David Allan as alternatives to the standard variance σ_{s}^2 and standard deviation $\sigma_{\mathrm{s}} = \sqrt{\sigma_{\mathrm{s}}}$ [117]. The problem Allan was trying to address was the non-convergence of the standard deviation in the noise of an oscillator, which is due to successive frequency measurements of an oscillator being an example of a "non-stationary process". Non-stationary processes are commonly encountered in nature; for example, flicker noise (a type of "$1/f$" or "pink noise", described in more detail later) has a divergent standard deviation and is ubiquitous in all electronic systems. Despite the prevalence of these processes, standard methods to characterize them were not developed until it became a necessity in the study of atomic clocks. The noise distribution of an atomic clock is its key figure of merit, and a diverging standard deviation completely fails to characterize this distribution and therefore could not facilitate the comparisons of clocks using different techniques. Since its introduction, the Allan variance and deviation have become adopted as standard methods to analyze the frequency stability of an oscillator [118]. However, the application of the AD does not need to be limited to the stability of an oscillator,

and many systems can benefit from characterization using the AD.

The AD was used in this thesis to characterize the stability of an oscillator, namely the frequency of our home-built diode laser systems described in reference [40] and Appendix A. The algorithms developed for this purpose were used to characterize the stability of a modulation-free laser frequency stabilization setup [119]. We have also broadened our application of the AD to characterize laser current controllers [41, 61], and motorized knife edge profilers used for angle measurements in diffusion experiments [33], and we also used it in the analysis of a precision measurement of atomic excited state lifetimes [42].

In this appendix, we will define the AD and describe its relationship to other metrics commonly used to characterize the noise in a measurement, namely the standard deviation σ_{s}, the power spectral density (PSD) $S_{\vec{y}\vec{y}}(f)$, and the autocorrelation function (ACF) $R_{\vec{y}\vec{y}}(t)$. Unlike most texts on this subject, we will keep this discussion completely general and avoid specifics that are relevant only to measurements of frequency. Next, we will describe practical algorithms for calculating the AD. Finally, we will describe how these methods were applied to achieve various goals in this thesis.

B.2 Stationary processes: The standard variance and standard deviation

We begin by describing the general problem, performing a series of N successive measurements of some system that yields a list $\vec{y}$. For notation and computing purposes, $\vec{y}$ can be considered a vector in N dimensions as

$$\vec{y} = \{y_1, y_2, y_3 \ldots, y_N\} \tag{B.1}$$

For stationary processes, we expect $\vec{y}$ to reflect some underlying probability distribution

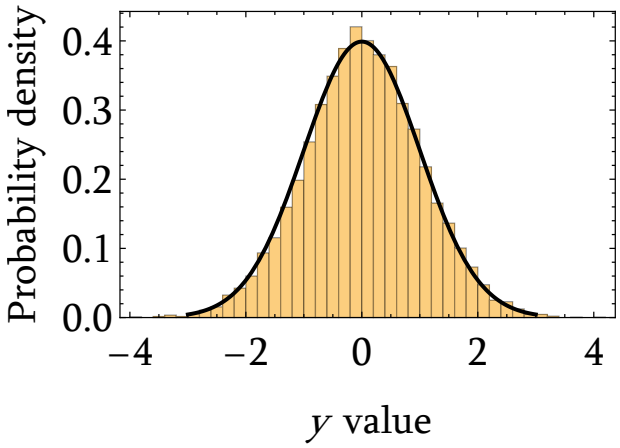

Figure B.1: Example histogram of dataset of 10 000 points with a mean of zero and $\sigma = 1$. The black line shows the underlying probability density function $P(y)$

$P(y)$, most commonly a normal distribution, such that as $N \to \infty$ a histogram of $\vec{y}$ will approach $P(y)$ as shown in Figure B.1.

To be defined as a stationary process it is necessary that every measurement in $\vec{y}$ is *identically distributed*, meaning that the centre and the width of $P(y)$ do not change over time. It is also necessary that the measurements are *independent* meaning that the value of any particular y_n does not affect the probability distribution of any other. Data which conforms to these assumptions is referred to as *Independent, Identically Distributed* (IID) data.

The mean $\bar{y}$ and standard deviation σ_s are the two most commonly applied metrics to quantify this distribution. With $\bar{y}$ defined as

$$\bar{y} = \frac{1}{N} \sum_{n=1}^{N} y_n \tag{B.2}$$

and σ_s defined in relation to the standard variance σ_s^2 as $\sigma_s = \sqrt{\sigma_s^2}$ with

$$\sigma_s^2 = \langle (y_n - \bar{y})^2 \rangle, \tag{B.3}$$

where $\langle x \rangle$ is the expectation value of the expression x. The expectation value is a property of the underlying distribution function, which cannot be obtained from a finite set of measurements. Thus, we use the estimator for the variance of a sample defined as

$$\sigma_{\mathrm{s}}^2 = \frac{1}{N-1} \sum_{n=1}^{n} (y_n - \bar{y})^2. \tag{B.4}$$

Using these tools, one is able to obtain the central value of the distribution from $\bar{y}$ and a quantity describing the width of the distribution from σ_{s}.

However, these metrics will fail if either or both of the assumptions of independence and identical distribution are not true. That is to say, if the process is not stationary.

B.3 Non-stationary processes, the Autocorrelation and Power Spectral Density

Before discussing the AD, which has already been introduced as a method to characterize non-stationary processes, we will describe what it means for a process to be non-stationary using methods that have broader applicability, namely the Power Spectral Density (PSD) $S_{\vec{y}\vec{y}}$ and autocorrelation function (ACF) $R_{\vec{y}\vec{y}}$. We will later show the important relationships between these functions and the AD.

If a dataset $\vec{y}$ is not stationary, it means that there is some kind of time dependence to the measurements y_n. If the measurements y_n are not *independent* it means that obtaining a particular y_n will impact the probability distribution of y_{n+1}, y_{n+2}, ... (and, assuming $\vec{y}$ has time symmetry, y_{n-1}, y_{n-2}, ...). In other words, without the assumption of independence, the specific ordering of $\vec{y}$ is important, and that same process could never produce certain permutations of $\vec{y}$. If each measurement is not *identically distributed*, then that means that there is some time dependence to $P(y)$, such that either the centre or the width of the

distribution changes with time.

B.3.1 Noise classification based on the power spectral density

The standard method to analyze the time dependence of a signal is by examining the signal in the frequency domain by taking the Fourier transform. The discrete Fourier transform $\mathcal{F}(\vec{y})$ is a list of complex elements $\vec{Y} = \{Y_1, Y_2, \ldots, Y_N\}$ where each element Y_k represents a complex frequency and is defined as

$$Y_k = \frac{1}{\sqrt{N}} \sum_{n=1}^{N} y_i \, e^{-i2\pi \frac{k-1}{N}(n-1)} \tag{B.5}$$

The amplitude of each Y_k represents the amplitude of the k^{th} frequency component, which, for a time interval τ between y_n and y_{n+1} has frequency $f(k) = (k-1)/(N\tau)$. The arc-tangent of the ratio of $\text{Re}(Y_k)$ and $\text{Im}(Y_k)$ represents the phase of the k^{th} frequency component. The normalization factor $1/\sqrt{N}$ is chosen so that the inverse transform is unitary, and can be written as

$$y_n = \frac{1}{\sqrt{N}} \sum_{k=1}^{N} Y_k \, e^{i2\pi \frac{k-1}{N}(n-1)}. \tag{B.6}$$

In many applications, the phase is of secondary interest, so focus is placed on the amplitude by looking at the power spectral density $S_{\vec{y}\vec{y}}(f)$, which is defined as

$$S_{\vec{y}\vec{y}}(f) = |\mathcal{F}(\vec{y})|^2 = |\vec{Y}|^2. \tag{B.7}$$

Here, $|z|$ represents the absolute value of the complex argument z. Each value of $S_{\vec{y}\vec{y}}(f)$ can be interpreted as the power density (power per frequency bin) of the signal at a frequency f.

For IID measurements, $S_{\vec{y}\vec{y}}(f)$ shows no trend as a function of f. This is a consequence of our earlier discussion regarding permutations of $\vec{y}$. If, for IID measurements, any permutation

of $\vec{y}$ is equally probable, this means that no matter the time separation between two values y_n and y'_n in the series, they will have the same expected variance. In the frequency domain, this means that the power at all frequencies must be roughly equal.

Processes for which $S_{\vec{y}\vec{y}}(f)$ has no trend in f are called "white noise" processes, or simply "white noise".

Just as $S_{\vec{y}\vec{y}}(f)$ is used to identify stationary processes as white noise, it is also used to classify different types of non-stationary processes. Processes which have a roughly f^{-1} trend in $S_{\vec{y}\vec{y}}(f)$ are referred to as "pink noise" as referenced in the introduction. The name "pink" refers to the fact that it resembles white noise except for a bias toward lower frequencies toward the "red" side of the spectrum. One can see how stronger lower frequencies manifest as a violation of the assumption of IID by looking at the example data in Figure B.2. For pink noise, the time domain signal has an apparent drift in the mean value of the distribution. The slight preference for values taken closer together in time to be similar is common in many physical systems. It is also important to note that pink noise can appear white if we only look at a short enough time interval.

More extreme cases of drift of the mean are identified by a f^{-2} trend in $S_{\vec{y}\vec{y}}(f)$ and referred to as "brown noise". Here, the name "brown" refers to Brownian motion, since this type of spectrum will result from random walk processes.

$S_{\vec{y}\vec{y}}(f)$ with positive trends in f are also observed in nature, although they are less common. A trend of f is named "blue noise" for the same reason the f^{-1} is named "pink." At first glance, blue noise may appear similar to white, and one would assume from looking at the time series that it is IID. However, blue noise is also not strictly a stationary process since, over short time scales (in contrast to long time scales in the case of pink and brown noise) the variance and mean can vary.

It is important to note that these noise types are conceptual constructions and are not strictly followed by any physical process. In addition, a physical process can generally be

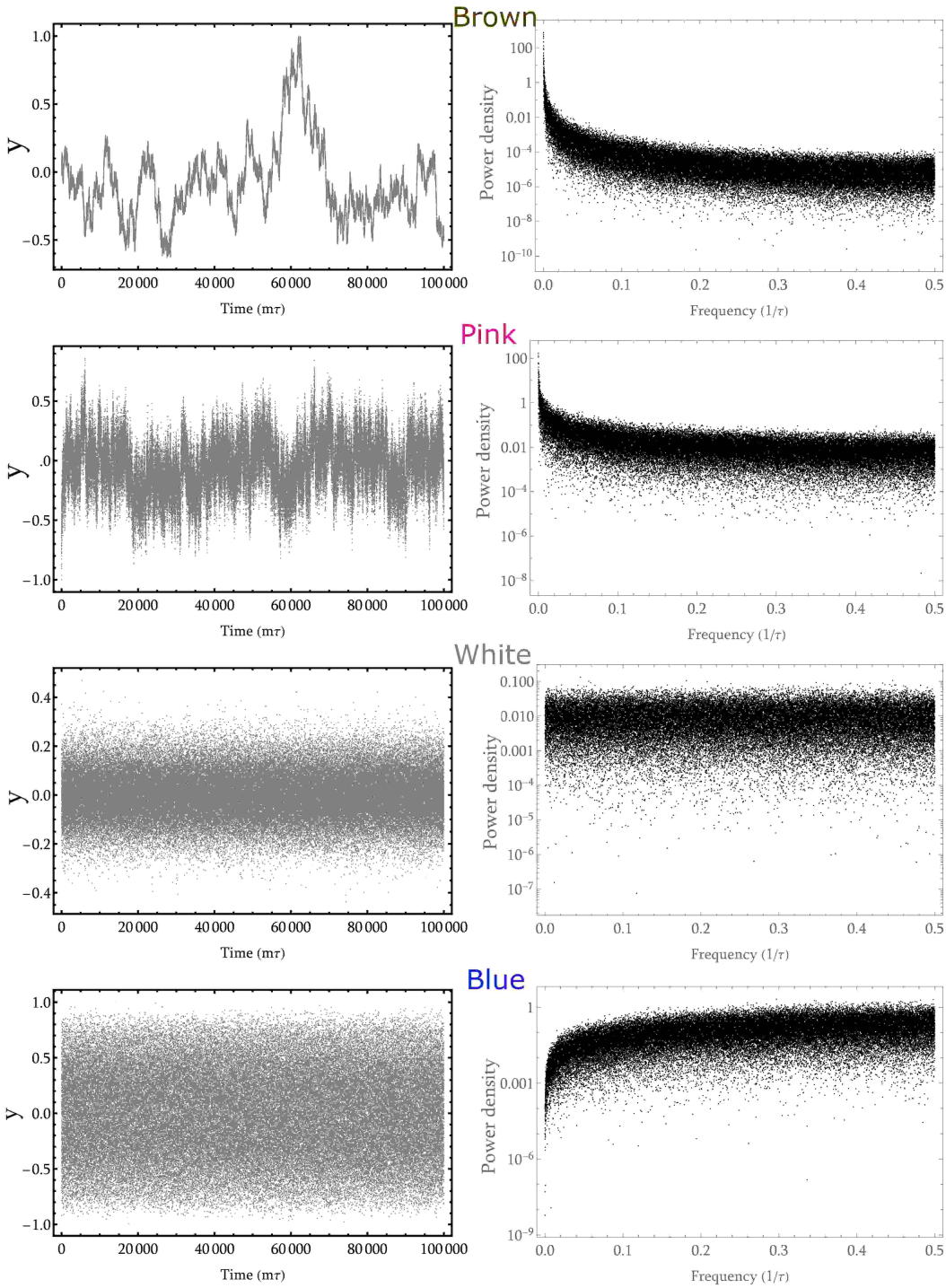

Figure B.2: Examples of randomly generated data with different noise profiles. All datasets have 100,000 points, the time series is shown on the left side, with the x-axis in units of $m\tau$ where τ is the time interval between points. The right side shows the corresponding power series $S_{\vec{y}\vec{y}}$, with the x-axis as fraction of the frequency $1/\tau$.

approximated as one noise type over a particular timescale. Typically, the noise types with higher frequency components (blue and white) will become less prominent at a long enough timescale, then the time series will appear pink and ultimately brown.

B.3.2 The autocorrelation function

Analysis of time series is not restricted to the frequency domain, and the most common time-domain tool is the autocorrelation function $R_{\vec{y}\vec{y}}(l)$, which is defined as

$$R_{\vec{y}\vec{y}}(l) = \langle \vec{y}_n \, \vec{y}^*_{n+l} \rangle. \tag{B.8}$$

Here, l is an integer representing the "lag" between the indices of the two copies of $\vec{y}$, z^* represents the complex conjugate of the complex number z. This plot provides information on the "correlation" between measurements separated by l. As an example, a list of points obeying $\sin(\omega\, t)$ would be highly correlated at times $t = 2\pi/\omega$ and would accordingly have a sharp peak at the corresponding $l = 2\pi/(\omega\tau)$ rounded to the nearest integer, where τ is the time between measurements. The autocorrelation of the data in Figure B.2 is shown in Figure B.3. One can observe that brown and pink noise are significantly correlated over short timescales, while white and blue noise appear to have no correlation whatsoever.

For a dataset of finite length n, we estimate the expectation value as

$$R_{\vec{y}\vec{y}}(l) = \frac{1}{\sqrt{N}} \sum_{n=1}^{N} y_n \, y^*_{n+l}. \tag{B.9}$$

Here, l can take any value from 1 to N, and indices larger than N are "rolled over", i.e. any index n can be interpreted as $y_{\mathrm{mod}(n-1/N)+1}$ where $\mathrm{mod}(q)$ is the modulo function, giving the remainder of the quotient q. The addition and subtraction of 1 make the modulo function compatible with the convention throughout this appendix of starting lists with the index "1".

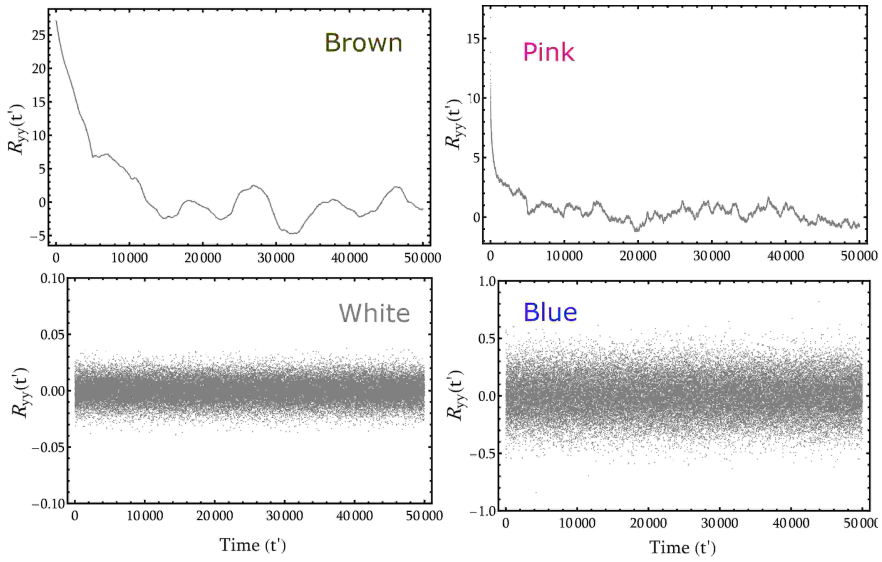

Figure B.3: Comparison of auto-correlation functions for the randomly generated data with different frequency profiles seen in Figure B.2

There are many conventions and standards for normalizing the autocorrelation. We have chosen to normalize by $1/\sqrt{N}$ in order to be consistent with Equation B.5 and make the following alternate definition of the autocorrelation precisely true.

$$R_{\vec{y}\vec{y}}(l) = \mathcal{F}^{-1}(S_{\vec{y}\vec{y}}(f)). \tag{B.10}$$

Here, $\mathcal{F}^{-1}(Y(f))$ is the discrete inverse Fourier transform of Y_k. Thus, the autocorrelation and power spectral density form Fourier transform pairs. The proof of this follows straightforwardly from the convolution theorem. This is very useful for computing the autocorrelation, which typically involves $\sim N^2$ operations. By utilizing this identity, along with fast-Fourier transform (FFT) algorithms, one is able to compute the autocorrelation faster than by direct computation. One may also use an estimator for the autocorrelation which does not "roll over" indices while maintaining Equation B.10 if one defines the discrete Fourier transform and autocorrelation by padding $\vec{y}$ with N zeros.

Ultimately, since the autocorrelation is the product of two displaced vectors, one cannot

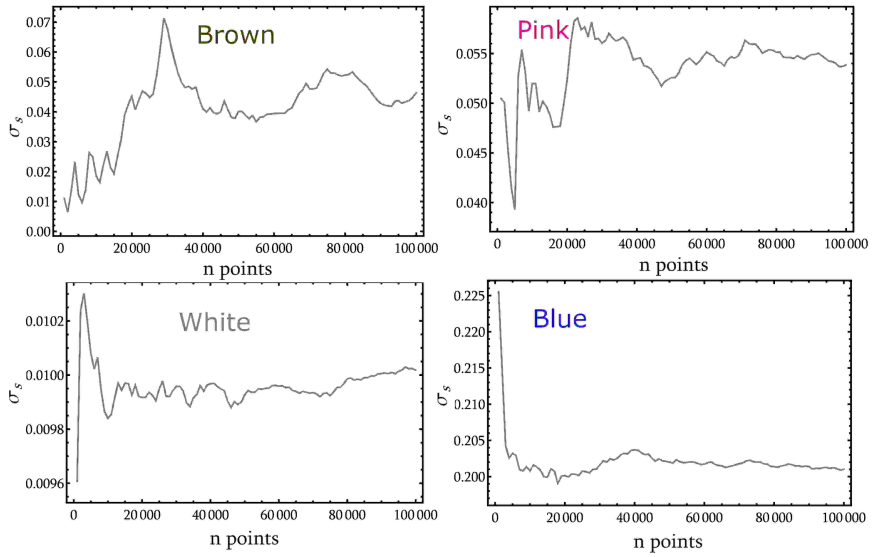

Figure B.4: Comparison of standard variance as the dataset is increased for the randomly generated noise with different frequency profiles seen in Figure B.2

get immediate intuitive quantitative information from its value in the way that one can from the standard deviation, and, as we will show later, the AD. Nevertheless, the autocorrelation function is very effective at identifying precise phase differences in data, such as those caused by the translation of an imaged object. We applied the autocorrelation to complete such a task in reference [116].

B.3.3 Issues in applying the standard variance to non-stationary processes

We have described non-stationary processes, and shown how they can be classified using the power spectral density and autocorrelation function. We will now demonstrate what happens when one tries to apply the standard deviation to these processes. Figure B.4 shows σ_s for the datasets in Figure B.2 as the length for the dataset is increased. One can see that for pink and especially brown noise, the standard variance can change dramatically depending on how long you record data.

Because of this trend, the standard deviation fails to characterize the data in any meaningful way. Additionally, although the variance converges for white and blue noise, the standard deviation provides no way of differentiating these noise types.

B.4 Introduction to the Allan deviation

The Allan variance, $\sigma_{\mathrm{a}}^2(\tau)$, represents the average difference between two consecutive measurements of a quantity, averaged over time τ. Thus, the Allan variance can be computed for all τ from the time-step of the data up to one half the total measurement time of the data. The Allan variance is defined as

$$\sigma_{\mathrm{a}}^2(\tau) = \frac{1}{2}\langle(\overline{y}_{n+1} - \overline{y}_n)^2\rangle, \tag{B.11}$$

where $\overline{y}_{j+1}$ and $\overline{y}_j$ are separated by *and* averaged over the time τ. The Allan deviation (AD), $\sigma_{\mathrm{a}}(\tau)$, is simply the square root of this number.

$$\sigma_{\mathrm{a}}(\tau) = \sqrt{\sigma_{\mathrm{a}^2}(\tau)} \tag{B.12}$$

The AD quantifies the average deviation of a dataset at specific timescales. This is similar to the autocorrelation function but in terms of the *difference* between time-separated values rather than their *product*. It is typically reported as a unit-less, fractional deviation from the mean value of a quantity.

The AD can be used both to *qualify* noise types in data, as the power spectral density and autocorrelation function did in the previous section, and *quantify* the magnitude of deviations, in a manner similar to the role of the standard deviation for stationary processes. In addition to these applications, the AD can also quantify the timescales over which a certain type of noise dominates.

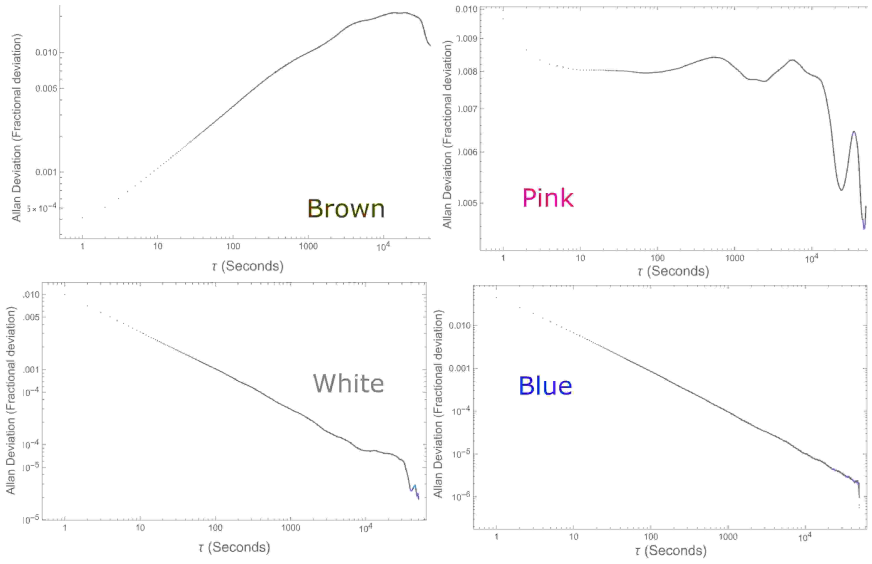

Figure B.5: Comparison of AD as a function of averaging time for the randomly generated datasets with different frequency profiles seen in Figure B.2

Figure B.5 shows the AD for the datasets introduced in Figure B.2. Each type of noise has a characteristic slope in the Log-Log AD plot. Brown, or random walk noise has a slope of 1/2, indicating a trend of $(m\tau)^{1/2}$. Pink, or flicker noise has a slope of zero. White noise has a slope of $-1/2$, or $(m\tau)^{-1/2}$, and blue noise has a slope of -1, or $(m\tau)^{-1}$.

B.4.1 Calculating the Allan deviation

Since the statistical expectation value in Equation B.11 cannot be known for a finite dataset, we use the estimator.

$$\sigma_{\mathrm{a}}^2(\tau) = \frac{1}{2(N-1)} \sum_{n=0}^{N-2} (\overline{y}_{n+1} - \overline{y}_n)^2 \tag{B.13}$$

where N is the total number of measurements.

By averaging m consecutive measurements, we can obtain a new set of consecutive measurements ${}^m\vec{y}$ averaged over time $m\tau$.

This averaging can be completed either by taking consecutive *non-overlapping* subsets

with each element in ${}^{m}\vec{y}$ defined as

$$ {}^{m}\vec{y}_n = \frac{1}{m}\sum_{i=1}^{m} \vec{y}_{m(n-1)+i}. \tag{B.14} $$

This process is visualized in Figure B.6 and results in a vector of length ${}^{m}N = \left\lfloor \frac{N}{m} \right\rfloor$. Here, $\lfloor q \rfloor$ is the floor function of the quantity q, which rounds q down to the nearest integer. Computing the AD from this list would result in ${}^{m}N - 1$ *pairs* to be subtracted in Equation B.13

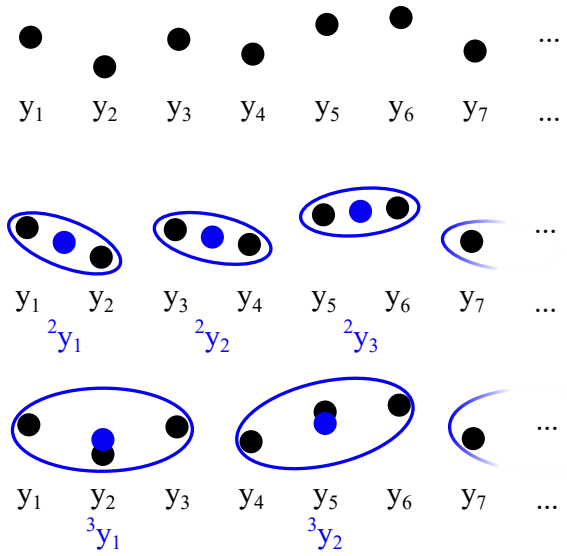

Figure B.6: Averaging a dataset $\vec{y}$ separated by time τ to successive datasets ${}^{m}\vec{y}$ separated by time $m\tau$ without any overlap between averaged data.

Alternatively, one can obtain m different lists ${}^{m,j}\vec{y}$ averaged by $m\tau$ if each list starts on the j^{th} element of the original list, with $1 \leq j \leq m$. This process is visualized in Figure B.7, as we can see these lists have considerable overlap, but as long as the differences used in Equation B.13 are always taken from the same ${}^{m,j}\vec{y}$, they meet the requirements for an AD.

Each term in the overlapping vectors ${}^{m,j}\vec{y}$ is defined as

$$ {}^{m,j}y_n = \frac{1}{m}\sum_{i=1}^{m} y_{m(n-1)+i+(j-1)} \tag{B.15} $$

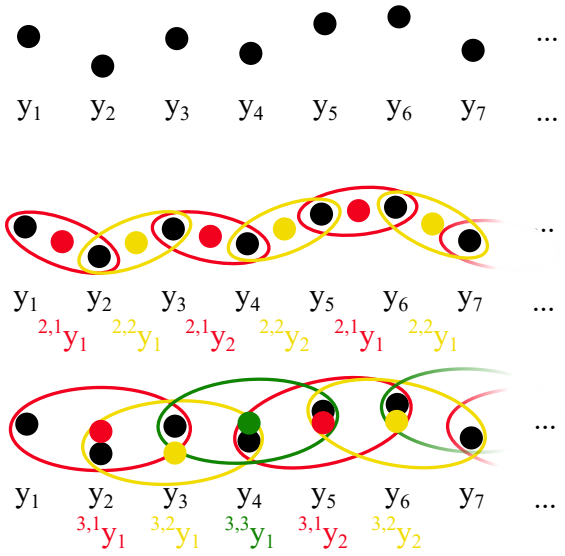

Figure B.7: Averaging a dataset separated by time τ to m successive datasets ${}^{m,j}\vec{y}$ separated by time $m\tau$ and offset by j. These overlapping datasets can be used to calculate the AD as long as consecutive pairs subtracted in Equation B.13 are always taken from the same list ${}^{m,j}\vec{y}$.

The length of all ${}^{m,j}\vec{y}$ is ${}^{m,j}N = N - 2m$, which results in $N - 2m - 1$ pairs to subtract in Equation B.13

ADs obtained from the overlapping method have much better confidence intervals than their non-overlapping counterparts. In standard practice, the AD for $m\tau$ is assumed to be calculated using the *overlapping* method unless specifically stated otherwise.

B.4.2 Relationships between the Allan deviation and other quantities

The expected value of the Allan variance for a finite dataset has a simple relationship with the standard variance. The difference between their expected values is

$$\langle \sigma_a^2 \rangle - \langle \sigma_s^2 \rangle = \langle \vec{y}_n \vec{y}_{n+1} \rangle. \tag{B.16}$$

That is to say, the difference between the expectation values is the autocorrelation for a lag $l = 1$. This explains why the standard variance and Allan variance diverge so much for brown and pink noise, since those noise types are strongly correlated over short timescales.

The Allan variance can also be related to the power spectral density $S_{\vec{y}\vec{y}}$ as

$$\sigma_{\mathrm{a}}^2 = 4 \int_0^\infty S_{\vec{y}\vec{y}}(f) \frac{\sin^4(\pi f \tau)}{(\pi f \tau)^2} df. \tag{B.17}$$

B.4.3 Confidence interval of the Allan deviation

Figure B.5 demonstrates that the AD appears to be less reliable as m approaches its maximum value of $\lfloor N/2 \rfloor$. This begs the question of the error in the AD given the initial sample size N and the averaging length m.

The confidence interval can be calculated using a Chi-Squared distribution. The confidence interval around the measured AD σ_{am}, which includes the true value of the AD σ_{at} with a probability P, can be shown to be

$$\sqrt{\frac{\nu}{\chi^2(\nu, (1+P)/2)}} \sigma_{\mathrm{am}} \leq \sigma_{\mathrm{at}} \leq \sqrt{\frac{\nu}{\chi^2(\nu, (1-P)/2)}} \sigma_{\mathrm{am}}. \tag{B.18}$$

Here, $\chi^2(\nu, Q)$ represents the Q^{th} quantile of a Chi-squared distribution with ν degrees of freedom.

The effective degrees of freedom in the AD depend on the type of noise, as described in Table B.1.

Noise type	ν
White	$\nu \approx \left(\frac{3(N-1)}{2m} - \frac{2(N-2)}{N} \right) \frac{4m^2}{4m^2+5}$
Pink	$\nu \approx \frac{5N^2}{4m(N+3m)}$ if $m \geq 2$
Brown	$\nu \approx \frac{N-2}{m} \frac{(N-1)^2 - 3m(N-1) + 4m^2}{(N-3)^2}$

Table B.1: Effective degrees of freedom ν for the Allan deviation for different noise profiles.

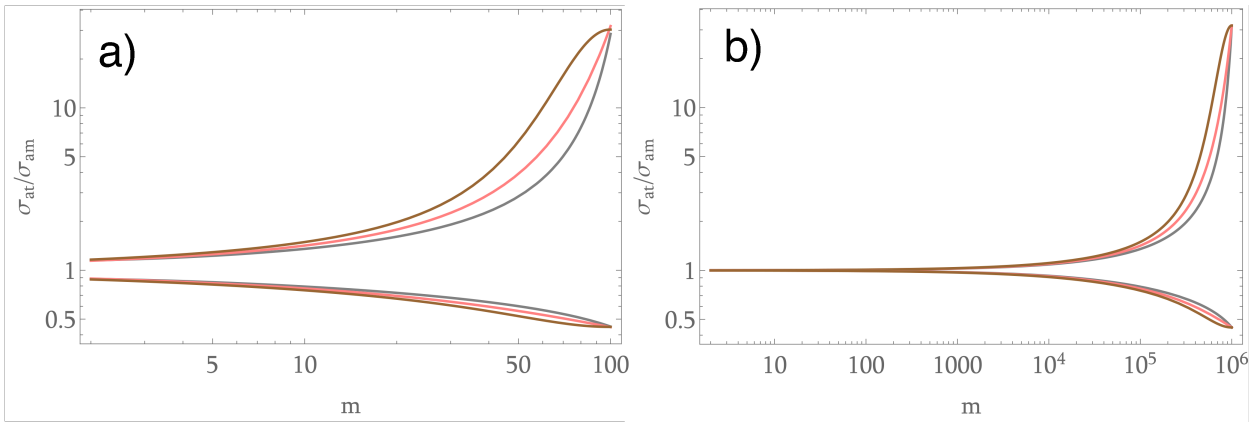

Figure B.8: The interval that contains the true AD σ_{at} 95% of the time as a fraction of the measured AD σ_{am} . Plotted as a function of m for a) $N = 200$ and b) $N = 2 \times 10^6$. The Gray lines indicate the upper and lower bounds of the interval for white noise, the pink lines do the same for pink noise, and the brown lines for brown noise.

Combining Equation B.18 with Table B.1, the 95% confidence intervals for different noise types are plotted for the case of $N = 200$ and $N = 2 \times 10^6$ in Figure B.8. The confidence interval is quite close to the measured value for most values of m, but as $m \to N/2$, the interval spans 3 orders of magnitude. This quantitatively justifies the commonly applied rule of thumb to discard the last quarter of the AD plot. Alternatively, to maximize the information derived from the AD, it is recommended that one display all of the data as well as the confidence interval.

B.5 Algorithms for computing the overlapping Allan deviation

Computation time is often a primary concern when computing the Allan variance. Longer datasets require exponentially more time to compute.

B.5.1 A simple algorithm for computing the Allan deviation

A brute force algorithm for computing the overlapping Allan variance based on Eqs. B.15 and B.13 is demonstrated in algorithm 1.

Algorithm 1 Brute force algorithm for calculating the overlapping Allan deviation

1: Store dataset recorded at intervals τ in a list $\vec{y}$ with length N
2: $\vec{y} = data$
3: $N = \text{Length}(\vec{y})$
4: Calculate the maximum number of points in the Allan deviation M, initialize list for Allan variance $\vec{\sigma_a^2}$ with Length M
5: $M = \left\lfloor \frac{N}{2} \right\rfloor - 1$
6: $\vec{\sigma_a^2} = \{\sigma_a^2[1], \sigma_a^2[2], \ldots, \sigma_a^2[M]\}$
7: Initialize loop to calculate each $\sigma_a^2[m]$
8: **for** $m = 1, 2, 3, \ldots, M$ **do**
9: Initialize loop to calculate all overlapping averages as list $\vec{^m y}$ of length $N - m$
10: **for** $j = 1, 2, 3, \ldots, N - 2m + 1$ **do**
11: Average over m points (or a duration of $m\tau$)
12: $\vec{^m y}[j] \leftarrow \frac{1}{m} \sum_{i=j}^{j+m-1} \vec{y}[i]$
13: **end for**
14: Calculate all differences $\vec{d}$ separated by m points (or a duration of $m\tau$ in $\vec{^m y}$
15: $\vec{d} \leftarrow \vec{^m y}[m+1, m+2, \ldots, N-m+1] - \vec{^m y}[1, 2, \ldots, N-2m+1]$
16: Calculate $\sigma_a^2[m]$ using Eq. B.13
17: $\sigma_a^2[m] \leftarrow \frac{1}{2(N-2m)} \sum_{i=1}^{N-2m+1} \vec{d}[i]^2$
18: **end for**
19: Calculate the Allan deviation $\vec{\sigma}_a$
20: $\vec{\sigma}_a = \sqrt{\vec{\sigma}_a^2}$

B.5.2 More efficient methods of computation

Algorithm 1 is computationally intensive. The approach used for efficiently calculating the autocorrelation, namely, using its relationship to the Fourier transform to take advantage of the efficiency of FFT algorithms, does not work here. This is because the relationship between $S_{\vec{y}\vec{y}}$ and σ_a^2 in Equation B.17 requires recalculating $S_{\vec{y}\vec{y}}$ for each average, and also calculating the value of $\sin^4(\pi f\tau)/(\pi f\tau)$ for all possible values of f. This results in even

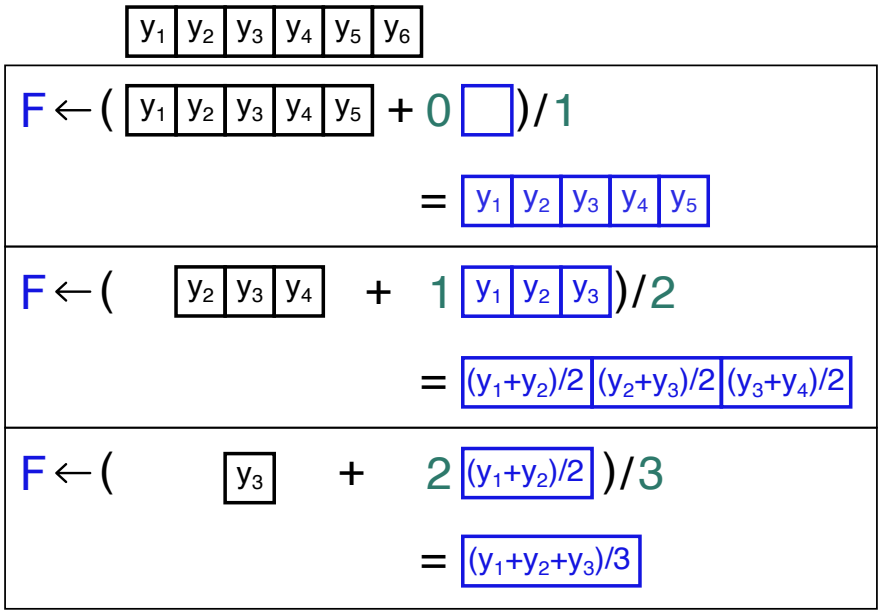

Figure B.9: Demonstration of how successive list of subtrahends, labelled "F" can be calculated from the previous list, (represented by blue boxes) and the original dataset (represented by black boxes) for a dataset of length 6. Teal values increase by one with each iteration. Each average only requires the addition of two numbers, but represents the average of m numbers.

more intensive computation than the brute force algorithm.

Instead, one can efficiently compute the AD by trying to re-use as many calculated averages as possible. For example, if one has already calculated the average of every m consecutive points in $\vec{y}$, and saved it as ${}^{m}\vec{y}$, then to compute the average of $m+1$ points, one only needs to calculate

$$ {}^{m+1}y_n = \frac{m\,{}^{m}y_n + y_{n+m}}{m+1}. \tag{B.19}$$

This allows one to perform the average using one addition operation instead of $m-1$ for every point. This results in substantial gains in efficiency. To implement this in an algorithm, it is convenient to imagine creating a list of averages for the minuend (first term in the difference) in Equation B.13 ${}^{m}\vec{y}_S$ and a separate list for the subtrahends (second term in the difference) ${}^{m}\vec{y}_F$.

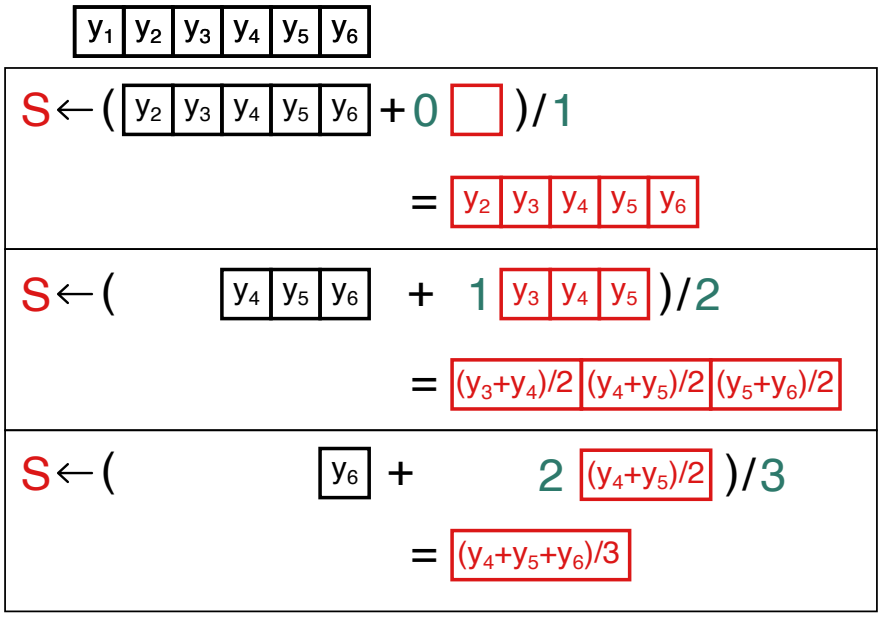

Figure B.10: Demonstration of how successive list of minuends, labelled "S" can be calculated from the previous list (represented by red boxes) and the original dataset (represented by black boxes) for a dataset of length 6. Teal values increase by one with each iteration. Each average only requires the addition of two numbers, but represents the average of m numbers.

Figure B.9 shows an example of how successive lists of subtrahends can be generated for a dataset of length 6, while Figure B.10 shows an example of how successive lists of minuends can be calculated for the same example. Using the ideas in Figures B.9 and B.10, one can improve algorithm 1. An example of an improved algorithm is shown in algorithm 2

Further gains to the efficiency of the AD computation can be made by truncating the datasets and limiting values of $m\tau$ only to values of m for which $2^p = m$, where p is an integer. This approach was used in reference [120] to calculate the AD very quickly for very large datasets. For smaller datasets, however, it is useful to use algorithm 2 in order to cover the full range of m values.

Algorithm 2 Fast algorithm for computing the overlapping Allan variance at all possible values of $m\tau$ by reusing averages

Store dataset recorded at intervals τ in a list $\vec{y}$ with length N
$\vec{y} = data$
$N = \text{Length}(\vec{y})$
Calculate the maximum number of points in the Allan deviation M, initialize list for Allan variance $\vec{\sigma_{\text{a}}^2}$ with Length M
$M = \left\lfloor \frac{N}{2} \right\rfloor - 1$
$\vec{\sigma_{\text{a}}^2} = \{\sigma_{\text{a}}^2[1], \sigma_{\text{a}}^2[2], \ldots, \sigma_{\text{a}}^2[M]\}$
Initialize lists of averaged minuends $\vec{y}_S$ and subtrahends $\vec{y}_F$ using $\vec{y}$
$\vec{y}_F \leftarrow \vec{y}$
$\vec{y}_S \leftarrow \vec{y}$
Initialize loop for calculating each $\vec{\sigma_{\text{a}}^2}[m]$
for $m = 1, 2, \ldots, M$ **do**
    Calculate subtrahends and minuends from the previous iteration as in Figures B.9 and B.10
    $\vec{y}_F \leftarrow \frac{1}{m}(\vec{y}[m \ldots N-m] + (m-1)\vec{y}_F[1 \ldots N-2m+1]+)$
    $\vec{y}_S \leftarrow \frac{1}{m}(\vec{y}[2m \ldots N] + (m-1)\vec{y}_S[2 \ldots N-2m+2]+)$
    Subtract subtrahends from minuends to calculate $\vec{\sigma_{\text{a}}^2}$ using Equation B.13
    $\vec{\sigma_{\text{a}}^2}[m] \leftarrow \frac{1}{2(N-2m)} \sum_{i=1}^{N-2m+1} (\vec{y}_S[i] - \vec{y}_F[i])^2$
end for
Calculate the Allan deviation $\vec{\sigma_{\text{a}}}$
$\vec{\sigma_{\text{a}}} = \sqrt{\vec{\sigma_{\text{a}}^2}}$

B.6 Applications

B.6.1 Characterizing stability

The Allan variance is typically used to measure the stability of an oscillator such as a clock or the frequency of a laser. We applied the results from this appendix work to characterize our home-built laser system [40]. The AD of the laser is shown in Fig. B.11. Typically, the minimum value of the AD (AD floor) is reported, as well as the corresponding averaging time.

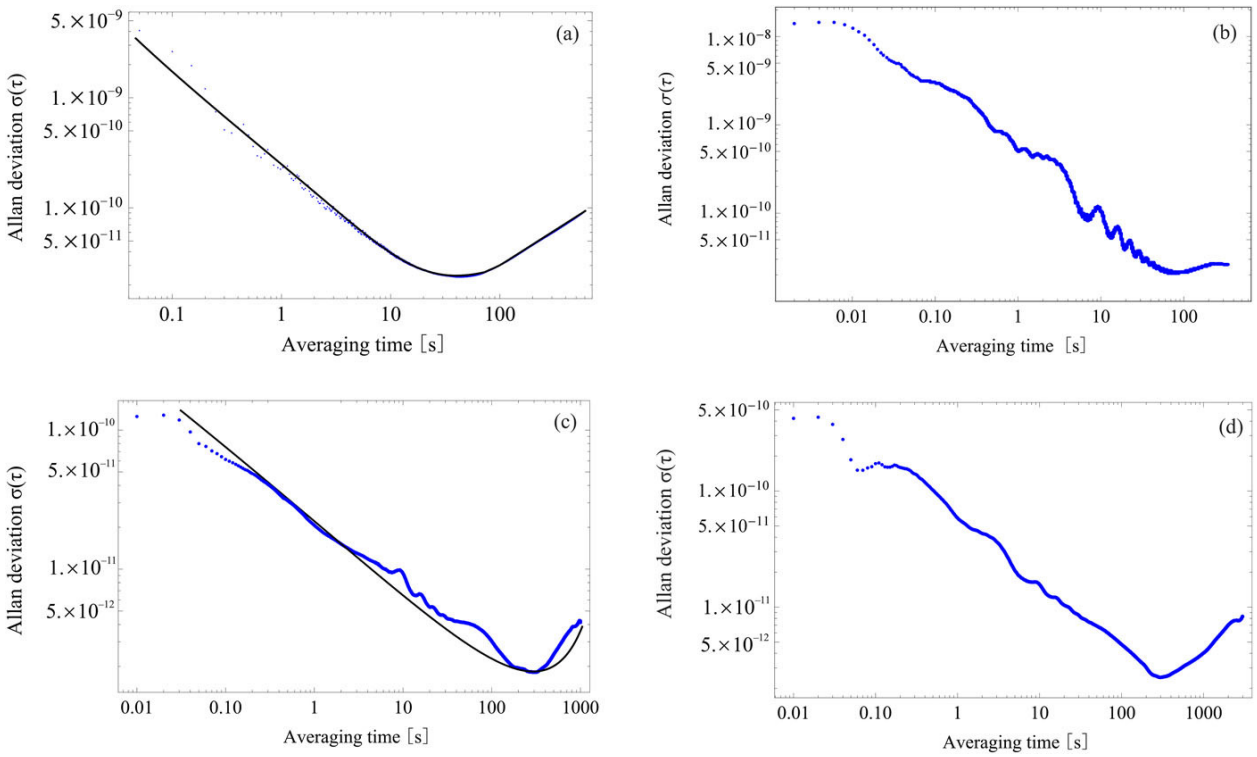

Figure B.11: AD curves obtained using 780 nm IF lasers. (a) and (b) are recorded using current controllers with 200 nA/$\sqrt{\text{Hz}}$ of noise. They show the AD of (a) the beat note between two IF lasers, and (b) the lock signal for a single laser. Ripples in the curve are attributed to the resonant frequency of the vibration isolation platform. (c) and (d) are similar, recorded using a current controller with 100 pA/$\sqrt{\text{Hz}}$ of noise.

The Allan variance can also be used to characterize the stability of other systems for

which the standard deviation does not converge. We applied it in one such case to compare the stability of various laser current controllers (Fig. B.12) [61].

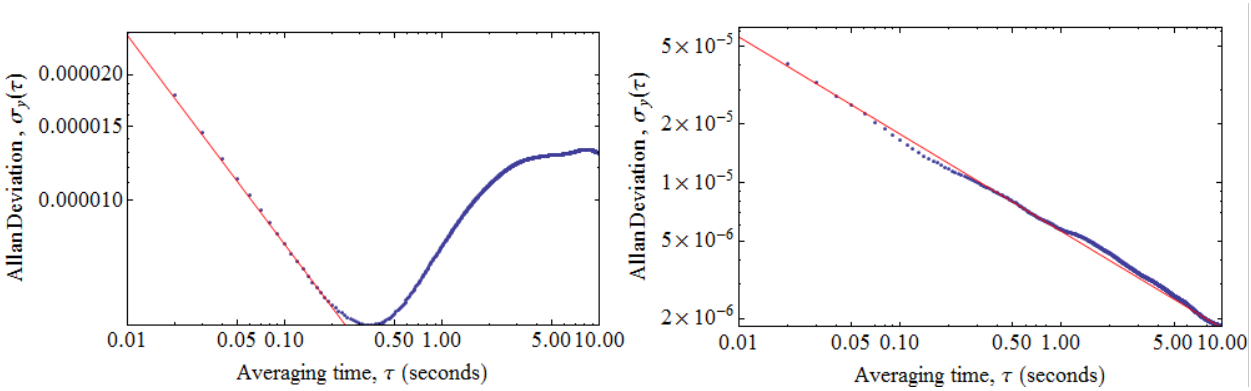

Figure B.12: Comparison of AD plots for integrated Thorlabs controller (left) and commercial ILX laser diode controller (right). The red line shows a $\tau^{-1/2}$ trend-line, characteristic of shot noise. We can see that shot noise dominates for the ILX for all timescales measured, while other sources take over at 0.34 seconds for the Thorlabs controller

B.6.2 Optimizing averaging time

We have also applied the AD in reference [42] to optimize the averaging time in a data acquisition loop. The number of averages taken for each measurement was set to 50000 based on the fact that this represented a minimum in the AD curve.

For typical systems, the AD will decrease until you begin averaging over timescales large enough that pink noise sources begin to dominate. Beyond those timescales, we have shown that the standard deviation will begin to diverge, meaning that further data collection will not result in any further precision.

This presents a method to optimize the statistical uncertainty of a measurement. We utilized this approach when acquiring measurements of the ^{85}Rb $5P_{3/2}$ excited state lifetime in reference [42]. Here, AD was also used to obtain the best estimate for the precision in the lifetime based on successive measurements.

B.6.3 Estimating errors on particular time scale

A final application of the AD is to characterize the error in a device on a particular timescale.

For example, in reference [33] we measured the angular separation of two laser beams using a motorized knife-edge beam profiler. The profiler had to be physically moved from one point in the beam path to another, a process that took 5 minutes from the end of the acquisition of the first point to the second. On this time scale, the motor spinning the knife-edge clearly exhibits drift and random-walk noise as seen in Figure B.13a. Using the AD plot in Figure B.13b, we were able to estimate the average deviation of the profiler on timescales of 5 minutes.

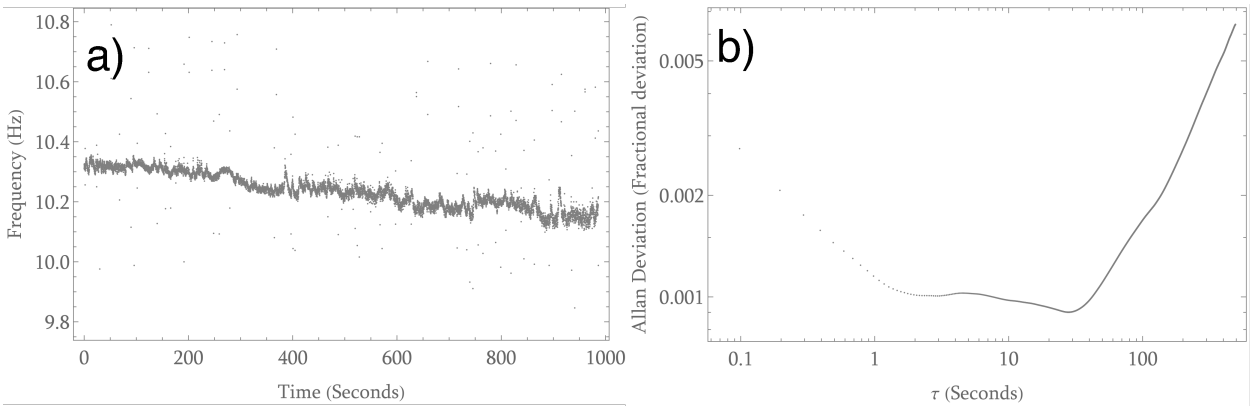

Figure B.13: a) The measured frequency of a motorized knife-edge profiler over a period of 17 minutes. The frequency is measured by timing the interval between pulses of light reaching the photodiode on the inside of the spinning profiler drum from a continuous laser. b) The AD of the data in Figure a

B.7 Conclusion

We have given an overview of the AD and its relationship to the standard deviation, the autocorrelation function, and the power spectral density. We have described methods to efficiently compute the AD as well as various different applications in which these methods have been deployed during the work comprising this thesis.

Appendix C

Collision spectroscopy of rubidium vapour

As described in Section 2.2, the presence of the buffer gas modifies the width and line-centre of the rubidium resonances. Using absorption spectroscopy of the collisionally broadened and shifted rubidium lines in the experimental cell, we were able to determine the pressure of the buffer gas in the cell used in reference [33] which significantly exceeded the value quoted by the commercial manufacturer. We also applied the same technique in reference [35] to verify the capacitance manometer readings and to monitor the rubidium vapour density. Analysis of these data is expected to produce a new determination of line shifts and broadening parameters for the Rb D2 line [48].

C.1 The absorption spectrum of rubidium

Extracting the pressure from absorption spectra requires precise knowledge of line strengths, shifts, and broadening parameters of the rubidium absorption lines. We will outline the established theory here based on a more detailed description in references [85, 102, 105].

For a monochromatic optical field with frequency ω and intensity I_0, the transmitted intensity as a function of ω, through a cell of length l is

$$I(\omega) = I_0 e^{-l\,\alpha(\omega)}. \tag{C.1}$$

Here, $\updownarrow\alpha(\omega)$ is the optical depth in the cell, and we have assumed that the fluorescence from the cell is negligible, which is valid if $I_0 \ll I_{\text{sat}}$, where I_{sat} is the saturation intensity of the spectral lines.

We are concerned with the case where the cell is filled with the vapour of a hydrogen-like atom (such as rubidium), and the frequency ω is near atomic resonances. We must allow this vapour to have different isotopes with nuclear angular momentum I, each having a ground state with electron angular momentum J_G, split into hyperfine ground states with angular momentum $G = \{I - J_G, I - J_G + 1 \ldots I + J_G\}$. The energy of the optical photons $E_{\text{pho}} = \hbar\omega$, with the reduced Planck constant $\hbar$, is close to the energy difference between the ground states and an excited state with electron angular momentum J_H. The excited state is split into hyperfine excited states with angular momentum $H = \{I - J_H, I - J_H + 1 \ldots I + J_H\}$. In this case, $\alpha(\omega)$ can be written in terms of a sum over the atomic resonances for all isotopes I and between all ground and excited states, G and H respectively, within each isotope, so that

$$\alpha(\omega) = \frac{\hbar\omega}{4\pi} \sum_{I,G,H} B_{G,H} n_G \left(1 - \frac{g_G n_H}{g_H n_G}\right) \mathcal{G}(\omega). \tag{C.2}$$

As an aside, in order to avoid overly cluttered subscripts we have omitted the isotope identifier I from all subscripts. Therefore, one must keep in mind that the numbers G and H do not uniquely define a hyperfine state if there are multiple isotopes present. I will continue to be identified in sums when a sum is to be taken over all isotopes. If I is omitted from the subscript of a sum, it is intended that the sum only pertains to the states of a single isotope.

In Equation C.2, $\mathcal{G}(\omega)$ is the atomic response function which describes the shape of the absorption profile near resonance. We will discuss $\mathcal{G}(\omega)$ in detail shortly, but first we will define the rest of the coefficients which together comprise the amplitude of each resonance.

First, $g_F = (2F+1)$ is the magnetic degeneracy factor for the ground state $F = G$ or excited state $F = H$, and n_F is the density of the ground state $F = G$ or excited state $F = H$. The second term in parentheses $(\frac{g_G n_H}{g_H n_G})$ is called the *source function* and is associated with stimulated emission. For small $I_0 \ll I_{\text{sat}}$, the atomic population remains primarily in the ground state so that $n_G \gg n_H$, and this term is approximately zero. Finally, $B_{G,H}$ is the Einstein absorption coefficient in terms of intensity, defined as

$$B_{G,H} = \frac{4\pi^2}{3\epsilon_0 \hbar^2 c} \frac{1}{g_G} S_{G,H}. \tag{C.3}$$

Here, ϵ_0 is the vacuum permittivity, c is the speed of light in vacuum, and $S_{G,H}$ is the line strength, or the square of the electric dipole moment of the ground and excited states, defined as

$$S_{G,H,I} = \sum_{m_G, m_H, q} \left| \langle G\, m_G | e\vec{r} | H\, m_H \rangle \right|^2. \tag{C.4}$$

In Equation C.4, q is the projection of angular momentum of the optical field, $m_G = \{-G, -G+1 \ldots G\}$ are the ground state magnetic sublevels, $m_H = \{-H, -H+1 \ldots H\}$ are the excited state magnetic sublevels, e is the electron charge, and $\vec{r}$ is the electron position relative to the nucleus. Using the Wigner-Eckart theorem, it is possible to write the matrix element $\langle G\, m_G | e\vec{r} | H\, m_H \rangle$ in terms of the reduced matrix element for the electron $\langle J_G || e\vec{r} || J_H \rangle$ as

$$\langle G\, m_G | e\vec{r} | H\, m_H \rangle = (-1)^{m_G + J_G + I} \sqrt{g_H g_G g_{J_G}} \begin{pmatrix} G & 1 & H \\ -m_G & q & m_H \end{pmatrix} \begin{Bmatrix} G & 1 & H \\ J_H & I & J_G \end{Bmatrix} \langle J_G || e\vec{r} || J_H \rangle \tag{C.5}$$

Here, $\begin{pmatrix} G & 1 & H \\ -m_G & q & m_H \end{pmatrix}$ is the Wigner 3-j symbol for combining the angular momentum of the ground state m_G and the excited state m_H with a photon, $\begin{Bmatrix} G & 1 & H \\ J_H & I & J_G \end{Bmatrix}$ is the Wigner 6-j symbol for combining the angular momentum of the electron in the ground and excited states with the angular momentum of the nucleus.

From experimental measurements of the Rb lifetime, the reduced matrix element for the $D2$ transition in rubidium ($5^2\mathrm{S}_{1/2} \rightarrow 5^2\mathrm{P}_{3/2}$) is $\langle J_G = 1/2||e\vec{r}||J_H = 3/2\rangle = 4.22753(62)ea_0$ for ^{85}Rb [105], and $4.22752(62)ea_0$ for ^{87}Rb [102], with a_0 being the Bohr radius.

Thus, every quantity in Equation C.2 is known with the exception of the atomic populations n_G and n_H. By assuming $I_0 \ll I_{\mathrm{sat}}$, we have already established that n_H can be ignored. Using the same assumption, and the additional assumption that isotopically oriented atoms are entering the optical field faster than the field can redistribute atoms into different ground states (as would be the case for a low intensity laser beam in a vapour cell) we can infer that the ground state atoms remain in their initial, isotropic distribution *i.e.* equally populating all magnetic sublevels. This allows us to describe all the populations n_G in terms of the population of the isotope n_I as given by

$$n_G = \frac{g_G}{\sum_G g_G} n_I \tag{C.6}$$

In the case of an isotopically pure vapour, n_I describes the density of the atomic gas. For the case of naturally abundant vapour, we use the fractional occurrence of each isotope $\mathcal{C}_I$ to describe the ground state populations in terms of the density of the gas n_{gas} so that

$$n_G = \frac{g_G}{\sum_G g_G} \mathcal{C}_I n_{\mathrm{gas}}. \tag{C.7}$$

For naturally abundant Rb, $\mathcal{C}_I = \{\mathcal{C}_{3/2}, \mathcal{C}_{5/2}\} = \{0.278, 0.722\}$ for the isotopes ^{87}Rb and ^{85}Rb respectively.

In this manner, we have reduced the number of variables needed to describe the amplitude of absorption features to one, namely the density of the vapour n_{gas}. The shape of the spectrum as a function of frequency is determined by the atomic response function $\mathcal{G}(\omega)$.

C.1.1 The atomic response

As mentioned in Section 2.2, the natural atomic response near a resonance $\omega_{G,H}$ is a Lorentzian line shape with FWHM $\Gamma_{\text{N}} = 1/2\pi\tau$, where τ is the lifetime, so that

$$\mathcal{G}_{\text{N}}(\omega) = \frac{\Gamma_{\text{N}}}{\pi} \frac{1}{\Gamma_{\text{N}}^2 + (\omega - \omega_{G,H})^2}. \tag{C.8}$$

Using this response function for each of the transitions in the Rb D2 line, along with the amplitudes obtained in the previous section, we obtain Figure C.1 for $\alpha(\omega)/n_{\text{Rb}}$ of naturally abundant Rb.

Each of the 12 hyperfine resonances is narrow enough to be individually resolved. In our experiments, $\mathcal{G}(\omega)$ is complicated by the Doppler shift of atoms. An atomic vapour generally has a Maxwell-Boltzmann distribution of velocities $\rho_{\text{gas}}(\vec{v})\, d\vec{v}$. In one dimension $\rho_{\text{gas}}(v_x)\, dv_x$ is a Gaussian distribution with a width determined by the temperature T according to

$$\rho_{\text{gas}}(v_x)\, dv_x = \sqrt{\frac{m_{\text{gas}}}{2\pi k_{\text{B}} T}} e^{-\frac{m_{\text{gas}} v_x^2}{2k_{\text{B}}T}}\, dv_x. \tag{C.9}$$

Here, m_{gas} is the mass of the atom and k_{B} is the Boltzmann constant. Since each atom observes a different ω depending on its velocity, the observed spectrum will be the convolution of the natural lineshape with this Gaussian velocity distribution. The convolution of a Lorentzian $L(\omega;\Gamma)$ and Gaussian $G(\omega;\sigma)$ distribution functions is called a Voigt profile [85]

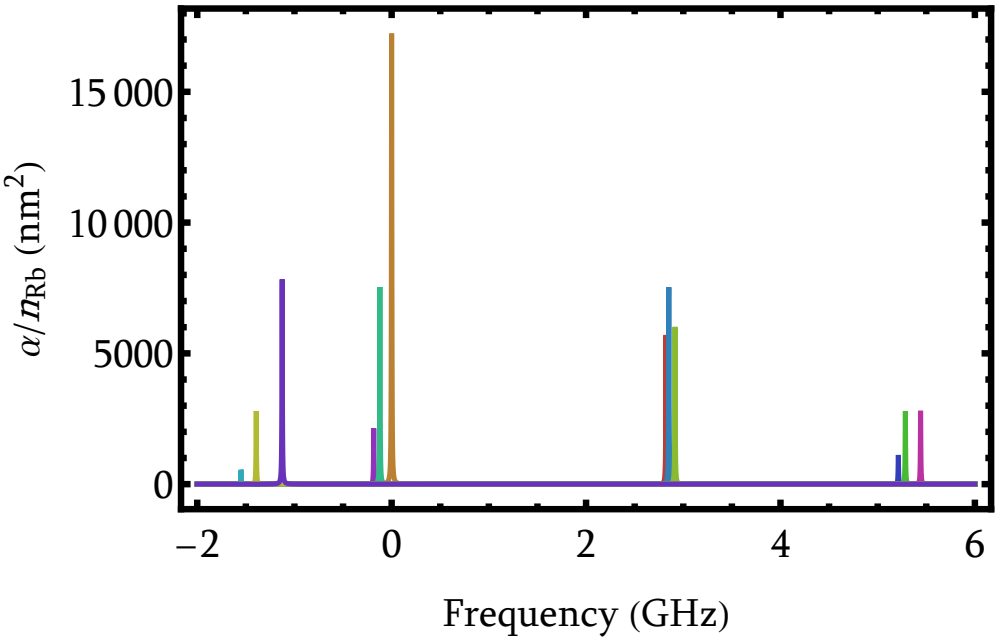

Figure C.1: Absorption spectra in units of α/n_{Rb} for ultra-cold, naturally abundant Rb near the D2 transition. There are 12 resonances clustered into groups of three as each of the two ground states in the two naturally occurring isotopes (four ground states total) has three dipole-allowed excited state transitions. The resonances from left to right are: ^{87}Rb $G = 2 \to H = 1$, ^{87}Rb $G = 2 \to H = 2$, ^{87}Rb $G = 2 \to H = 3$, ^{85}Rb $G = 3 \to H = 2$, ^{85}Rb $G = 3 \to H = 3$, ^{85}Rb $G = 3 \to H = 4$, ^{85}Rb $G = 2 \to H = 1$, ^{85}Rb $G = 2 \to H = 2$, ^{85}Rb $G = 2 \to H = 3$, ^{87}Rb $G = 1 \to H = 0$, ^{87}Rb $G = 1 \to H = 1$, and ^{87}Rb $G = 1 \to H = 2$. The frequency axis is relative to the centre of strongest transition, ^{85}Rb $G = 3 \to H = 4$.

$\mathcal{W}(\omega; \Gamma, \sigma)$.

$$\mathcal{W}(\omega; \Gamma, \sigma) = L(\omega; \Gamma) * G(\omega; \sigma) = \int_{-\infty}^{\infty} L(\omega - \omega'; \Gamma) G(\omega'; \sigma)\, d\omega' \tag{C.10}$$

As a result of Doppler broadening, it is difficult to observe a spectrum like the one shown in Figure C.1. In order to obtain such a spectrum, one must perform spectroscopy in cold atom traps. For room temperature Rb, the spectrum will resemble Figure C.2.

In Figure C.2, $\mathcal{G}(\omega)$ has been modified to include the Doppler shift.

$$\mathcal{G}_{\mathrm{D}} = \left(\frac{\Gamma_{\mathrm{N}}}{\pi} \frac{1}{\Gamma_{\mathrm{N}}^2 + (\omega - \omega_{G,H})^2} \right) * \left(\sqrt{\frac{m_{\mathrm{gas}}}{2\pi k_{\mathrm{B}} T}} e^{-\frac{m_{\mathrm{gas}} v_x^2}{2 k_{\mathrm{B}} T}} \right) \tag{C.11}$$

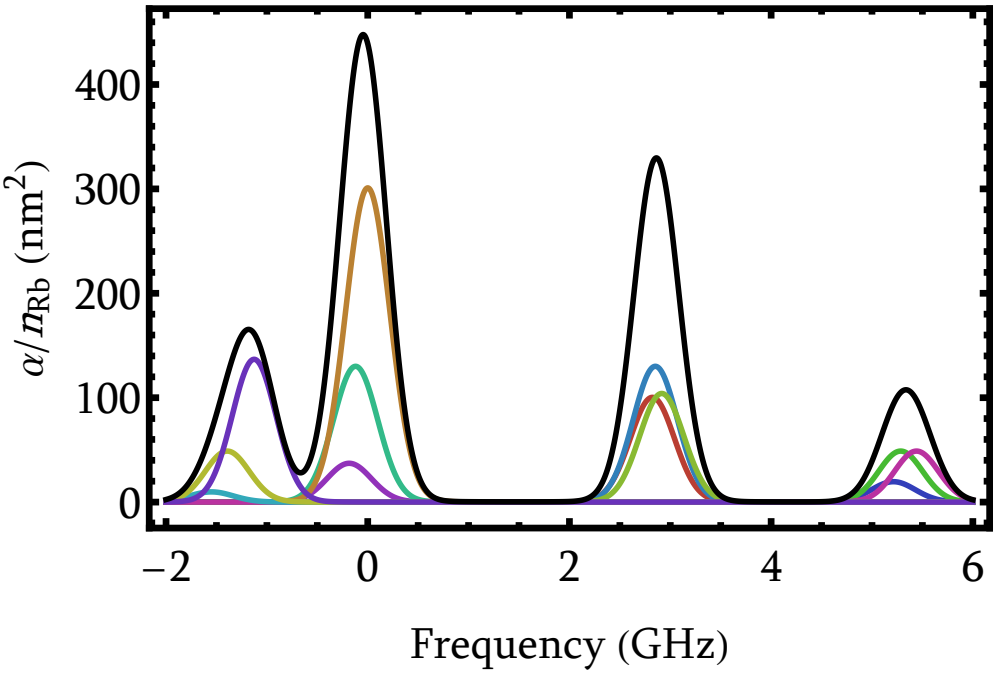

Figure C.2: Absorption in units of α/n_{Rb} for a room temperature vapour cell at Rb vapour pressure near the D2 transition. Individual transitions appear in the same order, and with the same colour, as in Figure C.1. In addition, the black line shows the total absorption due to all transitions. The frequency axis is relative to the centre of strongest transition, ^{85}Rb $G = 3 \rightarrow H = 4$

which is the Voigt profile resulting from the convolution of the natural atomic response $\mathcal{G}_{\mathrm{N}}$, with the normalized Gaussian velocity distribution along the direction of propagation of the optical field.

The lines in Figure C.2 are no longer individually resolvable. Instead, each cluster of three lines associated with the four ground states now features considerable overlap. Due to this, the spectrum one observes is the sum of the overlapping transitions, indicated by the black line in Figure C.2. We also note that in this case, the Gaussian width parameter $\sigma = k_{\mathrm{B}}T/m_{\mathrm{Rb}}\frac{\omega_{G,H}}{2\pi c}$ is much larger than the Lorentzian linewidth Γ_{N}. Thus, the Voigt profiles resemble Gaussian distributions because the Gaussian factor dominates the convolution .

The final complication that we must consider in the atomic response is how it is modified by pressure. In section 2.2 we noted that the atomic lineshape is broadened and shifted due

to collisions with an inert buffer gas. The broadened and shifted lineshape has the form

$$\frac{1}{\pi}\frac{\Gamma_{\mathrm{N}}+\gamma_{\mathrm{b}}p}{(\frac{\Gamma_{\mathrm{N}}+\gamma_{\mathrm{b}}p}{2})^2+(\Delta_{H,G}-\delta_{\mathrm{col}}p)^2}. \tag{C.12}$$

which resembles the natural lineshape but with additional buffer gas dependent broadening and shift rates as a function of pressure, γ_{b} and δ_{col} respectively. Using this function as the Lorentzian component of the Voigt profile allows us to predict the spectrum of naturally abundant, or isotopically pure Rb at any temperature and pressure. Figure C.3 shows an example at room temperature, with 200 Torr of N_2 buffer gas.

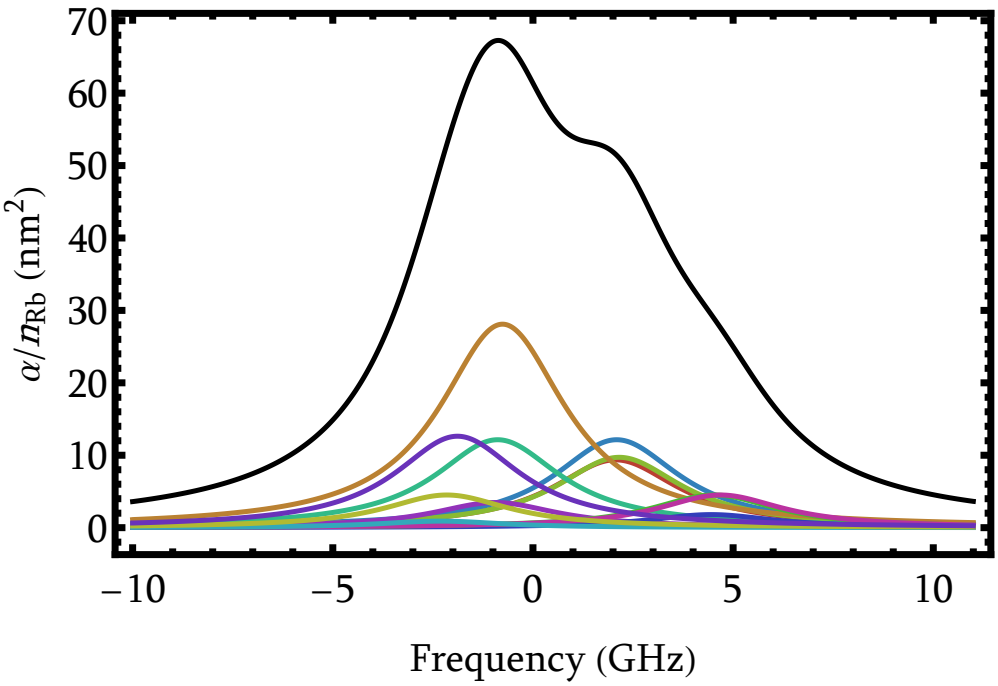

Figure C.3: Absorption in units of α/n_{Rb} for a room temperature Rb vapour with 200 Torr of N_2 buffer gas near the D2 transition. Individual transitions appear in the same order, and with the same colour, as in Figure C.1. In addition, the black line shows the total absorption due to all transitions. The frequency axis is relative to the centre of strongest transition, ^{85}Rb $G = 3 \rightarrow H = 4$

C.2 Procedure for obtaining spectra

Spectra were acquired using slightly different techniques for the experiments in the cell containing isotopically pure ^{87}Rb and for the experiments in the glass manifold containing a natural abundance of Rb.

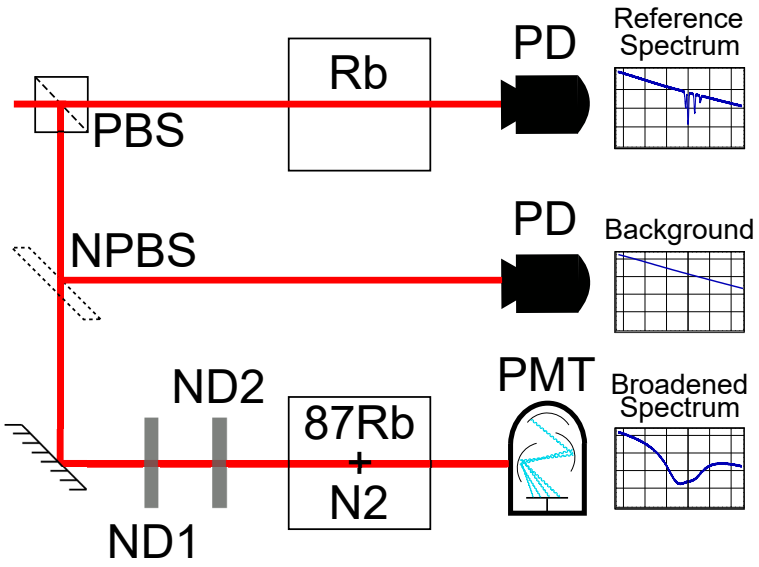

Figure C.4: Schematic of experimental set up to measure the pressure in the isotopically purified ^{87}Rb cell. A diode laser is scanned over $\sim$ 60 GHz by scanning the current. The power of the laser is attenuated using two 13 dB ND filters to avoid spectral distortions due to optical pumping. The frequency scan is calibrated using the spectrum of a low–pressure reference cell. Power fluctuations in the laser output are calibrated by recording the laser intensity on a photodiode. The pressure–broadened spectrum of the ^{87}Rb cell is recorded using a PMT.

A schematic showing the experimental setup in the isotopically purified ^{87}Rb cell is shown in Figure C.4. To record these spectra, with a scan range of several GHz, the external cavity feedback of a homebuilt ECDL was defeated, and the laser frequency was scanned by using the diode current. In this configuration, the linewidth of the laser diode is $\approx$ 50 MHz. However, this resolution is more than adequate for recording these spectral features which, at minimum, have a Doppler width of 500 MHz, and at high pressures can have collisional linewidths of as much as 20 GHz.

The spectra from the experimental cell were recorded on a photomultiplier tube (PMT) for a range of logarithmically stepped laser powers ranging from $1 - 2\ \mu$W, at which there are no detectable optical pumping effects. The laser diode was scanned with a triangle wave scan at rates of $21 - 106$ Hz, with $10,000 - 30,000$ samples per sweep. The spectrum was obtained by averaging 560-1660 sweeps. To provide a frequency calibration, a reference scan was simultaneously recorded in a vapour cell containing a natural isotopic abundance of Rb at room temperature. A photodiode was used to record the laser intensity variation during the scan. This information was used to model frequency-dependent intensity variations of the laser diode, such as those caused by etalon effects, optical filters, and the diode gain curve.

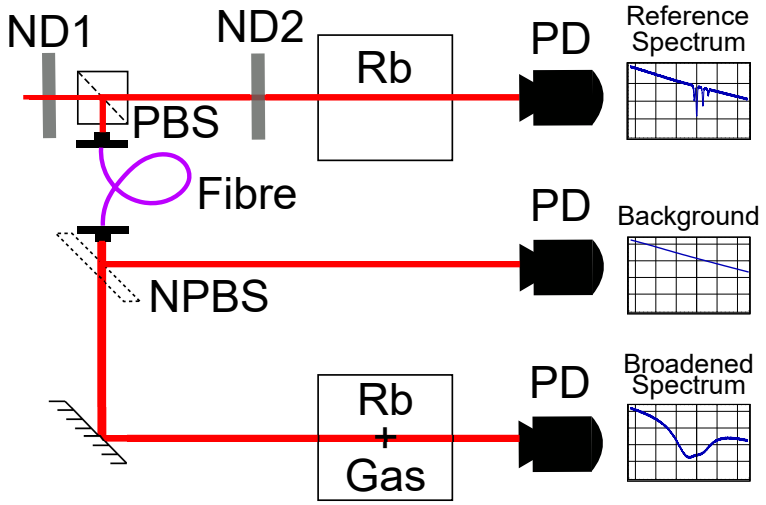

Figure C.5: Schematic of experimental set up to measure the pressure in the gas manifold with naturally abundant Rb. A diode laser is scanned over ~ 60 GHz by scanning the current. The power of the laser is attenuated using polarization beam splitters to avoid spectral distortions due to optical pumping. The frequency scan is calibrated using the spectrum of a low–pressure reference cell. Power fluctuations in the laser output are calibrated by recording the laser intensity on an amplified photodiode. The pressure–broadened spectrum of the ^{87}Rb cell is recorded using an amplified photodiode.

In the glass manifold, the experimental cell contained both Rb isotopes in natural abundance, and the same process was streamlined. A diagram relating to these pressure measurements is shown in Figure C.5. All measurements were taken with a laser power of

≈ 400 nW. The spectra were recorded on a photo-diode with a trans-impedance amplifier. This detector had a faster recovery time than the PMT. The laser scan ramp was changed from a triangle to a sinusoidal form to try to reduce hysteresis and avoid abrupt changes in current. The power was reduced using optical filters that were placed before the beam paths were split to ensure that intensity variations related to the filters are common to all paths so that they can be subtracted in post-processing.

C.3 Fitting to the broadened spectra

We now discuss how the spectroscopic data was processed and fitted. We begin by outlining our technique for fitting to the Voigt profile in Section C.3.1. We then describe the pre-processing done on the data in Section C.3.2. Finally, we describe the regression model and show example fits in Section C.3.3

C.3.1 Fitting to Voigt profiles

Fitting to a sum of Voigt profiles can be computationally intensive. To understand why, we revisit our previous description of the Voigt profile in Section C.1.1. The convolution described in that section has the analytical solution

$$\mathcal{W}(\omega;\Gamma,\sigma) = L(\omega;\Gamma) * G(\omega;\sigma) = \frac{1}{\sqrt{2\pi}\sigma}\,\mathrm{Re}(w(z)) \tag{C.13}$$

where $w(z)$ is the Faddeeva function, with the argument

$$z = \frac{\omega + i\Gamma}{\sqrt{2}\sigma} \tag{C.14}$$

The Faddeeva function itself is defined as

$$w(z) = e^{z^2}\,\mathrm{erfc}(-iz) \tag{C.15}$$

with $\mathrm{erfc}(z)$ being the complementary error function

$$\mathrm{erfc}(z) = 1 - \mathrm{erf}(z) \tag{C.16}$$

Since the error function does not have an analytical form, performing linear regression is inefficient.

To improve curve fitting, we used the series expansion of the Faddeeva function derived in reference [121] for large imaginary components of the argument z, and improved upon in reference [122] to be accurate for all z

$$w(z) \approx i\frac{1 - e^{i\tau_m z}}{\tau_m z} + i\frac{\tau_m^2 z}{\sqrt{\pi}} \sum_{n=1}^{N} a_n \frac{(-1)^n e^{i\tau_m z} - 1}{n^2\pi^2 - \tau_m^2 z^2}. \tag{C.17}$$

Here, τ_m and N are parameters of the approximation that can be adjusted to increase the precision. We have chosen values of $\tau_m = 12$ and $N = 24$, which align with the choices in reference [122]. The Fourier expansion coefficients a_n can be approximated as

$$a_n \approx \frac{2\sqrt{\pi}}{\tau_m} e^{-\frac{n^2\pi^2}{\tau_m^2}}. \tag{C.18}$$

This approximation can be rapidly computed and is accurate to 15 decimal places across three orders of magnitude of z, as shown in reference [122].

C.3.2 Data pre-processing

The first step in preparing the data is splitting all data into upward frequency scans and downward frequency scans. Due to laser diode hysteresis, $\frac{d\omega}{dI_{\mathrm{las}}}$ for the laser current I_{las} cannot be assumed to be equivalent, and the upward and downward scans must be treated separately.

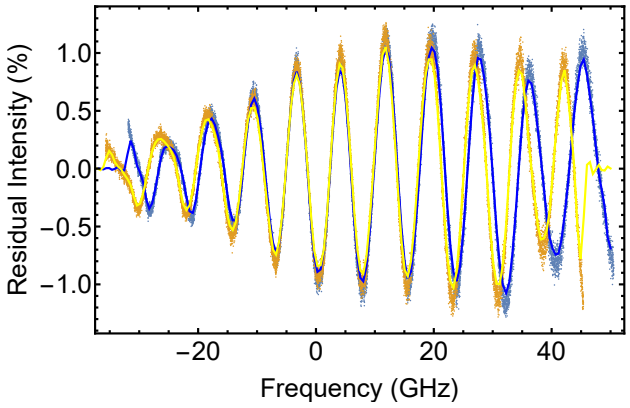

Figure C.6: Intensity variation due to etalon effects in the laser beam path. Data points are shown as percentage of the component of the intensity caused by the current scan determined. Blue points show the upward frequency scan and yellow points are the downward frequency scan. The solid blue line indicates the Fourier series approximation to the upward scan and the solid yellow line shows the same for the downward scan. The frequency axis is labelled in reference to the $G = 3 \rightarrow H = 4$ transition in ^{85}Rb. Both upward and downward scans show linear current-frequency scaling but also show evidence of nonlinear scaling at the extremes. Since the scan is wider than necessary these non-linearities should have a minimal effect on the fit.

The next step is to calibrate each dataset. The scan of the room temperature vapour cell is fit to Equation C.2, with free parameters n_{Rb} and T. The Lorentzian component of the Voigt profile is assumed to have width Γ_{N}. Since the cell is at Rb vapour pressure, which will cause some degree of collisional broadening, this broadening will be small compared to the Doppler width $\sigma = k_{\mathrm{B}}T/m_{\mathrm{Rb}}\frac{\omega_{G,H}}{2\pi c} \approx 200$ MHz.

We then characterize the intensity fluctuations in the laser. To first order, the intensity scales proportionally to the laser frequency. However, etalon effects along the beam path add small periodic intensity fluctuations as a function of frequency. These small fluctuations will interfere with the fits to the composite pressure-broadened lineshape and must be first removed. To do this, we make a Fourier series approximation of the laser intensity (Figure C.6). This analytical expression is incorporated into the fit to the pressure-broadened spectrum, with the only free parameter being its overall amplitude.

For the data from the manifold, the spectrum was acquired with a current scan that is

sinusoidal in time. As a result, the acquired frequency-intensity points are closer together in frequency space near the anti-nodes of the scan, and farther apart at the nodes. Since the discrete Fourier transform requires even spacing of points, the points are binned and averaged to achieve this.

Having calibrated the frequency axis and determined the intensity profile of the light entering the cell, the broadened spectrum is ready to be fitted.

C.3.3 Fitting to the pressure broadened spectra

We fit the spectra using Equation C.2, with Voigt profiles as described in Section C.3.1, using the measured hyperfine splittings between Rb spectral lines [102, 105]. The fit function is given by

$$f(\omega; s, o, r, n_{\mathrm{Rb}}, p) = (s\, I_i(\omega) - o)(\exp(-l\, \alpha(\omega; n_{\mathrm{Rb}}, p, T = 297.15, \gamma_{\mathrm{b}}, \delta_{\mathrm{col}}) + r) \qquad \text{(C.19)}$$

Here, $I_i(\omega) = I_{\mathrm{up}}(\omega)$ or $I_{\mathrm{down}}(\omega)$ is the laser intensity of the upward and downward scans that were previously determined, $l = 5.1$ cm is the length of the cell, γ_{b} is the broadening parameter for the gas in the cell, and δ_{col} is the shift parameter. The broadening and shift parameters used can be found in Chapter 2. The free parameters of the fit are the rubidium density n_{Rb}, the buffer gas pressure p, and background light parameters, s, o, and r. The upward and downward scans are fit simultaneously to the same free parameters; the only distinction between the fits is the previously determined laser intensity functions. Fitting to the downward and upward scans simultaneously causes irregularities in the laser current-frequency function to average out and increases the precision.

The absorption coefficient $\alpha(\omega)$ includes only transitions in ^{87}Rb when fitting to data from the cell containing isotopically pure ^{87}Rb (Figure C.7), and includes transitions in ^{85}Rb

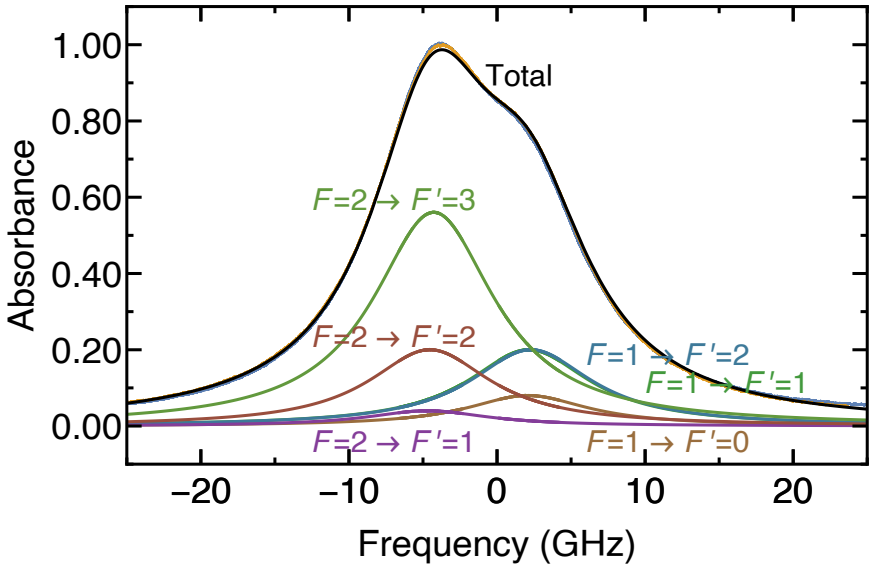

Figure C.7: Data from the experimental cell fitted to composite spectrum for ^{87}Rb resonances. Blue and yellow curves show data from the upward and downward frequency scan respectively, the best fit to both of these curves is shown in black. Individual resonances are shown with broadening and shift parameters determined by the fit and relative line-strengths and centres taken from reference [102]. The frequency axis is relative to the $F = 2 \rightarrow F' = 3$ transition on the D2 line ($5^2S_{1/2} \rightarrow 5^2P_{3/2}$) in ^{87}Rb.

and ^{87}Rb in their natural abundance when fitting to data taken from the glass manifold (Figure C.8).

In reference [33], the broadened spectrum was recorded on a PMT, while the laser intensity was recorded on a photodiode. Since the PMT had a slower response time than the photodiode, an additional delay parameter was added to the fit to account for the time delay. The time delay had the same magnitude but opposite sign for the upward and downward fits.

Using this method we are able to determine the buffer gas pressure p and n_{Rb} with 1% precision. This method has the advantage of being able to measure the pressure and Rb density directly along the beam path used in the diffusion experiment. This contrasts with methods that rely on pressure gauges located some distance from the experimental region. However, the accuracy of our technique is limited by the accuracy of the measured

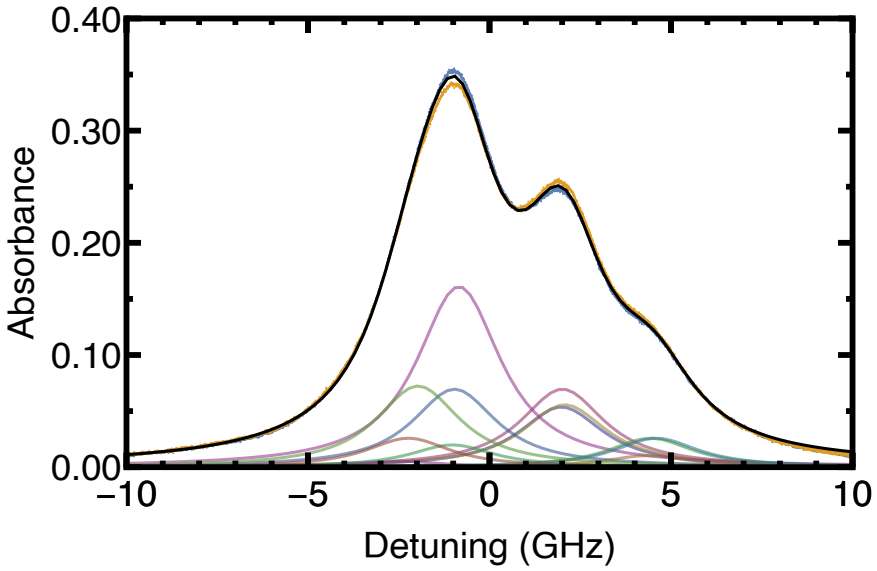

Figure C.8: Rubidium absorption spectra a cell of length 5.1 cm at $T = 24.0(5)$ °C and a pressure of 134.10(5) Torr of N_2 buffer gas as measured by the capacitance gauge. The plot shows absorbances $-\ln(I/I_0)$ as a function of laser detuning, where I and I_0 are the transmitted and off-resonant transmitted laser intensities, respectively, and the laser detuning is relative to the $F = 3 \rightarrow F' = 4$ hyperfine transition frequency of the D2 line in ^{85}Rb in its rest frame and without any buffer gas. Blue and yellow traces correspond to data from upward and downward scans of the laser frequency. A fit of both traces of the composite spectrum for collisionally broadened and shifted ^{85}Rb and ^{87}Rb D2 hyperfine transitions is shown in black. Individual D2 hyperfine line profiles are also shown as coloured lines, the most prominent of these coloured lines is the collisionally broadened and shifted $F = 3 \rightarrow F' = 4$ line in ^{85}Rb.

broadening and shift parameters. These parameters disagree in their reported error bars for references [88] and [86]. There are also further variations for measurements obtained at different temperatures such as in reference [123]. The discrepancies in the literature provide a strong motivation for using our data and fits to infer collisional shift and broadening rates for the Rb D2 line and to enable better comparisons with theory.

Appendix D

Diffusive transit-time corrections to the scattering from one-dimensional, periodic population distributions in a finite volume

D.1 Introduction

The effects of transit times of atoms either when passing through laser beams, moving from one laser beam to another, or between temporal laser pulses have received considerable interest in the fields of laser spectroscopy and precision metrology [124–128]. For example, a variety of coherent transient experiments that rely on photon echoes [129] require knowledge of state-prepared atoms that leave the interaction zone defined by excitation laser beams to estimate systematic effects. Another example involves atom trapping experiments, where the time-of-flight (ToF) distribution of cold atoms released from the trap is often of interest. Atom clouds are released from their traps, allowed to expand for a variable amount of time, and then imaged by fluorescence using resonant laser beams [130]. Knowledge of ToF distributions is also useful for calculating the transfer efficiencies of atoms from a low-vacuum chamber to

an ultra-high-vacuum (UHV) chamber for Bose-Einstein condensate experiments [131]. Atom interferometers that measure atomic recoil [62], gravity [63, 132], magnetic gradients [133] as well as velocimeters operating at room temperature [37] or with ultracold atoms [46] are all fundamentally limited in precision by the transit time of atoms.

Transit time corrections are also important for a variety of optical pumping experiments [5, 11, 73, 76, 91] and in coherent transient investigations of diffusion [33–35]. In this appendix, we study the diffusive motion of localized, spatially periodic density profiles of dilute Rb samples in the presence of an inert buffer gas near ambient temperatures. The density profile, or lattice, is detected by coherently scattering light from a readout laser pulse applied after an initial excitation laser pulse, which created the profile. We show that the corrections depend on the spatial profile of the initial density distribution as well as the readout laser beam. These corrections were crucial for reconciling our measurements of Rb$-X$ diffusion coefficients $D(T, p)$, as a function of temperature T and pressure p, with theoretical calculations [33, 35]. These reconciliations have enabled us to propose the realization of a quantum pressure sensor operating in the range 7,000 Pa to 90,000 Pa.

We focus on the diffusion measurements presented in this dissertation, in which we studied coherent light scattering from one-dimensional (1-D) periodic population distributions in trace Rb vapour at $\sim 10^{-5}$ Pa in the presence of an inert buffer gas at a pressure that is at least six orders of magnitude larger than the Rb vapour pressure. In this appendix, we examine the corrections to the decay of such scattered signals due to the transit of a localized spatial distribution of atoms probed by an optical field with a well-defined spatial profile [36].

The remainder of this appendix is structured as follows: In Section D.2, we describe the theoretical approach used to calculate the evolution of spatial population distributions. We review the case when there is no transit time correction in Section D.3. In Section D.4, we calculate the evolution of the population distribution when the initial distribution and the readout beam have 2-dimensional Gaussian profiles with related width parameters. In

Section D.5, we study the evolution of the population distribution for an initial distribution and readout beam with the same rectangular cuboid spatial profile. The experimental configurations realized in this work lie somewhere between these two geometries. We describe the impact of these corrections in Section D.6.

D.2 Theoretical approach and assumptions

We consider Rb-based diffusion experiments where the gases are at or near room temperature, buffer gas pressures are greater than 7,000 Pa, and lattices have periods near 100 µm, which is much larger than the mean free path for Rb atoms scattering from buffer gas atoms or molecules [56]. Moreover, we can assume that the Rb atoms do not collide with each other during the measurement procedure. Under these conditions, the evolution of the Rb number density $\rho(\vec{r},t)$ at position $\vec{r}$ and time t is described by the equation

$$\frac{\partial\rho(\vec{r},t)}{\partial t} = D(T,p)\nabla^2\rho(\vec{r},t)\,, \tag{D.1}$$

where the diffusion coefficient $D(T,p)$ is inversely proportional to pressure p.

D.2.1 Establishing an initial population distribution

In references [33, 35], the initial Rb population distribution is established by two orthogonally polarized excitation pulses directed along $\vec{k}_1$ and $\vec{k}_2$ at a small angle $\theta \sim 1$ mrad as shown in Figure D.1. These beams originate from a common laser, and therefore have nearly identical spatial profiles. We choose $\vec{k}_1+\vec{k}_2$ along our $\hat{z}$ axis, $\vec{k}_1-\vec{k}_2$ is along our $\hat{x}$ axis, and $k = k_1 = k_2$. If the readout pulse, which has the same spatial profile as the excitation beam along $\vec{k}_2$, is turned on, the coherently scattered signal is produced along the phase-matched direction $\vec{k}_1$. In this case, the Rb population grating is formed along our $\hat{x}$ axis and has a wavevector

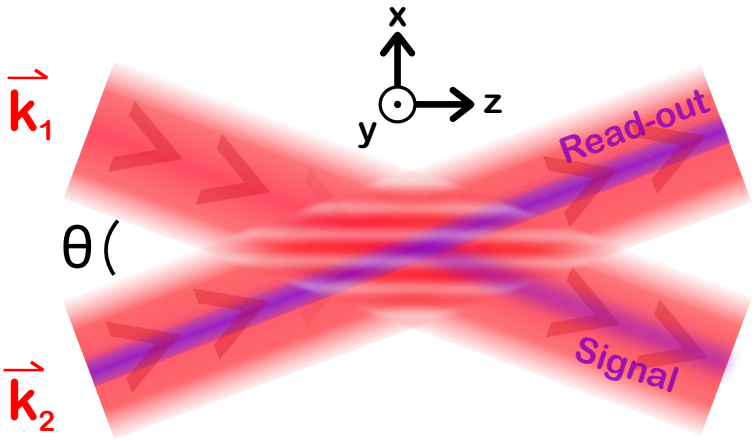

Figure D.1: Realistic depiction of the shapes and directions of Gaussian or cuboid excitation, readout and signal laser beams, shown as red or purple regions, in the experiments. The periodic Rb population distribution (white/red gradient in the centre) forms in the overlapping region of the spatial profiles of the two excitation beams with directions $\vec{k}_1$ and $\vec{k}_2$. The purple beams indicate the readout and scattered fields. They have the same propagation vectors as the excitation fields.

$\kappa = k \sin\theta \approx k\theta$.

D.3 Evolution without transit time corrections

The simplest periodic number density profile is created by assuming that the initial excitation laser pulses in Figure D.1 are plane waves. Figure D.2 demonstrates this condition, including definitions of a convenient coordinate system, orientations of the density profile, and propagation directions of the various light beams. The number density profile at time $t = 0$ is then a 1-D sinusoidal function with wavenumber κ along direction $\hat{x}$ is

$$\rho_{\mathrm{pw}}(\vec{r}, t = 0) = \rho_0 + \rho_{\mathrm{A}} \cos(\kappa x). \tag{D.2}$$

Here, $\vec{r} = x\hat{x} + y\hat{y} + z\hat{z}$, where $\hat{x}$, $\hat{y}$, and $\hat{z}$ form an orthonormal set of unit vectors. Furthermore, ρ_0 and ρ_{A} are the positive mean number density and lattice amplitude, respectively. The choice of the phase of the lattice relative to the origin $\vec{x} = \vec{0}$ and orientation along $\hat{x}$ is

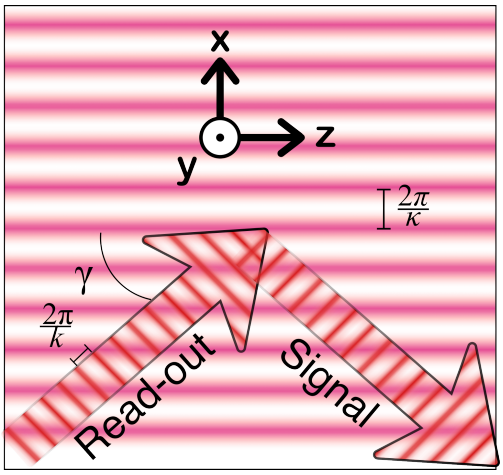

Figure D.2: Sketch of Rb lattice generated by plane-wave excitation laser beams (not shown) as well as the orientations of plane-wave readout and signal fields. The horizontal red and white bands represent the sinusoidal Rb population distribution directed along our $\hat{x}$ axis and has a wavenumber κ. The bands extent all along the y axis, out of the plane of the page. Wide arrows with narrow red stripes represent the directions in the xz plane of the plane wave readout and scattered (or signal) laser fields with wavenumber k. The directions of the two fields have polar angle γ from the positive z direction. Their azimuthal angles differ by π radian.

arbitrary. We also assume $|\rho_{\mathrm{A}}| < \rho_0$.

D.3.1 Time evolution of a plane-wave number density distribution

The time evolution of the number density distribution in Equation D.2 is governed by Equation D.1. Therefore, the $t > 0$ solution is given by

$$\rho_{\mathrm{pw}}(\vec{r}, t) = \rho_0 + \rho_{\mathrm{A}} e^{-D\kappa^2 t} \cos(\kappa x). \tag{D.3}$$

Here, we have omitted the arguments of the diffusion coefficient for clarity. Equation D.3 predicts an exponential reduction in the lattice amplitude with a time constant $\tau = 1/(D\kappa^2)$ without a change in the lattice period, which is visualized in Figure D.3. Measuring τ and κ can then be used to find D. Our choices for D and κ in the figure are typical for Rb diffusion

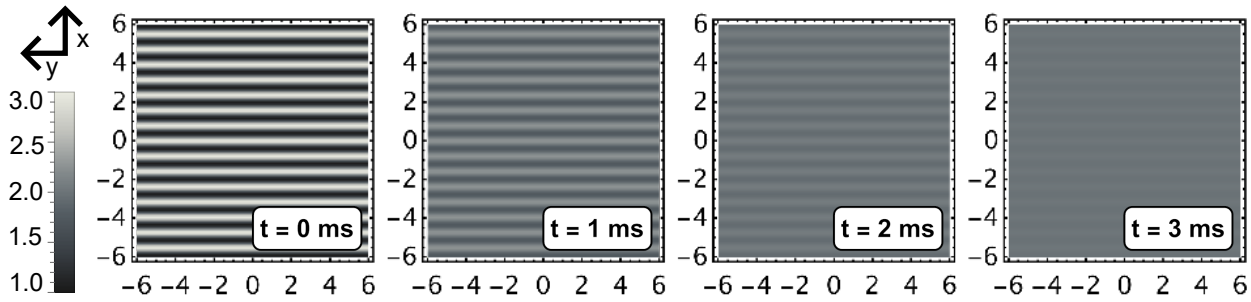

Figure D.3: Snapshots of the lattice amplitude of a plane-wave Rb number density distribution at four times at and after the excitation pulses. The lattice wavenumber and diffusion coefficient are 8 mm^{-1} and 20 mm^2/ms, respectively. The panels shows the amplitude in the xy plane with lengths in units of mm. The colour scale indicates the number density distribution with $\rho_0 = 2$ and $\rho_\text{A} = 1$ in arbitrary units.

in inert buffer gases at atmospheric pressure and ambient temperatures, the relevant optical transition frequency of Rb, and the small angle between the two excitation laser beams.

D.3.2 Bragg-like scattering from the plane-wave number distribution

The coherent optical field of the read-out pulse, with wavenumber k, is then applied at some later time. It is propagating in the xz plane with an angle γ relative to the positive $\hat{z}$ direction. Coherent scattering of this field by the Rb atoms will be sharply peaked into a single direction. This direction is set by the Bragg or phase-matching condition for constructive interference given by [54, 56]

$$m\frac{2\pi}{k} = 2\frac{2\pi}{\kappa}\sin\gamma\,, \tag{D.4}$$

where m is an integer. We choose the angle γ such that this condition is satisfied for $m = 1$. The direction of this signal or scattered light is shown in Figure D.2.

The experiments use detectors that are aligned in such a manner that they collect only the coherently scattered light. In fact, we use a heterodyne detection system that is sensitive to the amplitude of the scattered electric field $E(t)$. The amplitude of this electric field is proportional to the amplitude of the Fourier component of the spatially periodic gratings in

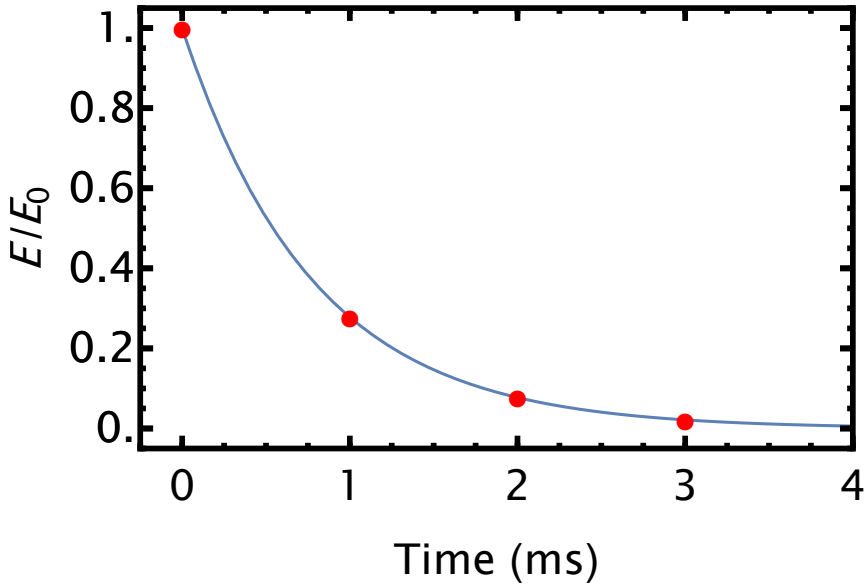

Figure D.4: Scattered electric field amplitude E from a plane wave Rb population distribution as a function of time. This curve is based on the same values for ρ_{A}, ρ_0, κ, and D as used to generate Figure D.3. The times of each snapshot in Figure D.3 are highlighted by red dots.

the populations of the magnetic sublevels m_F of the electronic ground state [33, 54]. Here, the quantization axis for the m_F sublevels is along the lattice direction $\vec{k}_1 - \vec{k}_2$. For the plane wave case, the time dependence of the $\kappa\hat{x}$ Fourier component can be found by inspecting Equation D.3, resulting in a scattered signal of the form

$$E(t) = E_0 e^{-D\kappa^2 t}\,, \tag{D.5}$$

where E_0 is the electric field amplitude at time $t = 0$. This decay is shown in Figure D.4 for the same parameters as in Figure D.3.

D.4 Gaussian distribution of populations and readout with Gaussian spatial profile

Our first attempt at a more realistic treatment of the experiments, in accordance with the geometrical constraints in Figure D.1, will assume that the excitation and readout beams are Gaussian laser beams that have the same two-dimensional Gaussian intensity profile in the xy plane and have an intensity profile that is independent of z along $\hat{z}$. Here, we have relied on observations that, in practice, the Rayleigh ranges of the beams are significantly longer than their beam waists and that we can ignore the effects due to the small angle θ between the excitation beams relative to the z axis. In fact, in our experiments, the Rayleigh ranges are 20 times longer than the length of the glass cell containing our inert buffer gases and Rb atoms. Consequently, the Rb transit times along the $\hat{x}$ and $\hat{y}$ directions will be much smaller than those for atoms reaching the vapour cell windows along $\hat{z}$.

The amplitude of the sinusoidal contribution to the initial population distribution $\rho_{\mathrm{G}}(\vec{r},0)$ is proportional to the intensity profile of the excitation beams for low laser intensities. Since the measured signal is proportional to the scattered electric field (and not the intensity) and the readout beam has the same spatial profile as the excitation beams, the $1/e$ widths of the initial population distribution of Rb and the electric field amplitude of the readout beam will differ by a factor of $\sqrt{2}$. We allow the $1/e$ widths to differ along the x and y axes in order to account for the asymmetric beam profile measured in the experiment. The $1/e$ widths of the electric field will be denoted by lengths a and b, respectively. Therefore, we write the electric field amplitude of the readout beam as

$$E_{\mathrm{RO}}(\vec{r}) = E_{\mathrm{RO}}(\vec{0})e^{-(x/a)^2-(y/b)^2}\,, \tag{D.6}$$

where $E_{\mathrm{RO}}(\vec{0})$ is the electric field strength at the centre of the beam profile, and the initial

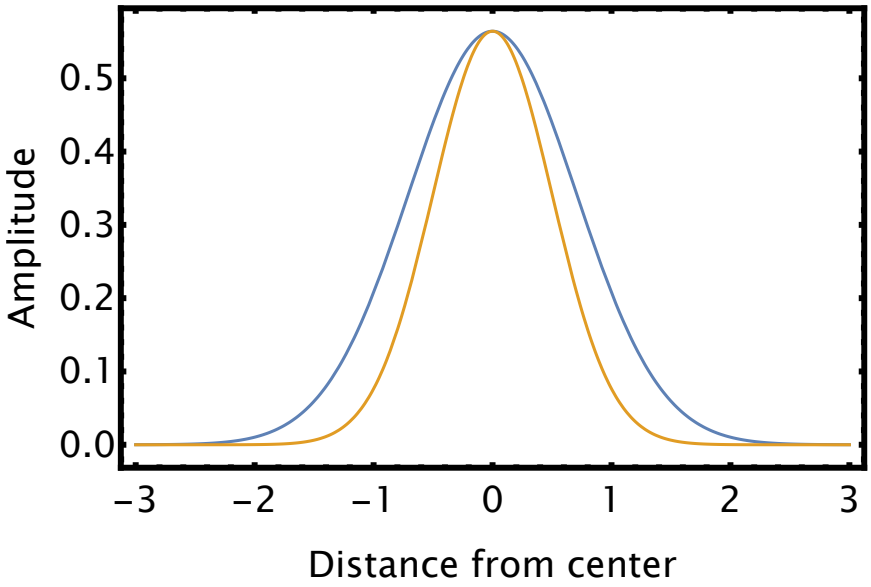

Figure D.5: Electric field (blue) and intensity profiles (orange) of a Gaussian laser beam as functions of distance from the centre of the profile and perpendicular to the propagation direction. The two functions are normalized to have the same value at the centre and distances are in units of the $1/e$ beam radius of the electric profile. The envelope of the initial Rb population distribution will be proportional to the intensity profile for low laser intensities.

population distribution as

$$\rho_{\mathrm{G}}(\vec{r},0) = \rho_0 + \rho_{\mathrm{A}} e^{-2(x/a)^2-2(y/b)^2} \cos(\kappa x)\,. \tag{D.7}$$

This expression represents the lattice amplitude ρ_{A}, as defined in Equation D.2, multiplied by the intensity profile.

D.4.1 Time evolution of Gaussian population distribution

Unlike in Section D.3, the more complicated form of the initial density distribution in Equation D.7 forces us to employ the general solution to Equation D.1. We express this

general solution in terms of the 3-D Fourier transform $P(\vec{q})$ of $\rho(\vec{r},0)$ as

$$\rho(\vec{r},t) = \frac{1}{(2\pi)^3}\int \mathrm{d}^3q\, P(\vec{q})e^{i\vec{q}\cdot\vec{r}}e^{-q^2Dt}\,, \tag{D.8}$$

where the wavenumber vector $\vec{q} = q_x\hat{x} + q_y\hat{y} + q_z\hat{z}$. For the Gaussian Rb number density profile in Equation D.7, $P(\vec{q})$ is

$$P_{\mathrm{G}}(\vec{q}) = (2\pi)^3\left\{\rho_0\delta(\vec{q}) + \frac{ab}{16\pi}\rho_{\mathrm{A}}e^{-a^2(q_x+\kappa)^2/8}\left(1+e^{a^2\kappa q_x/2}\right)e^{-b^2q_y^2/8}\delta(q_z)\right\}, \tag{D.9}$$

where $\delta(q_z)$ and $\delta(\vec{q})$ are the one- and three-dimensional delta function, respectively, resulting in the solution

$$\rho_{\mathrm{G}}(\vec{r},t) = \rho_0 + \frac{ab}{\sqrt{A(t)B(t)}}e^{-\kappa^2Dta^2/A(t)}\rho_{\mathrm{A}}\cos(\kappa x a^2/A(t))e^{-2x^2/A(t)-2y^2/B(t)} \tag{D.10}$$

with time-dependent areas $A(t) = a^2 + 8Dt$ and $B(t) = b^2 + 8Dt$.

The quantity $\rho_{\mathrm{G}}(\vec{r},t) - \rho_0$ based on Equation D.10 is visualized in Figure D.6 for typical parameter values of our systems. We observe that the lattice period along the $\hat{x}$ axis and the widths of the spatial Gaussians are increasing as a function of time t, first slowly and then linearly for longer times. The amplitude of the number density distribution decreases, first exponentially but then slowly as $1/t$ for longer times t. In contrast, the amplitude of the number density distribution decreases exponentially for all time in the plane wave case.

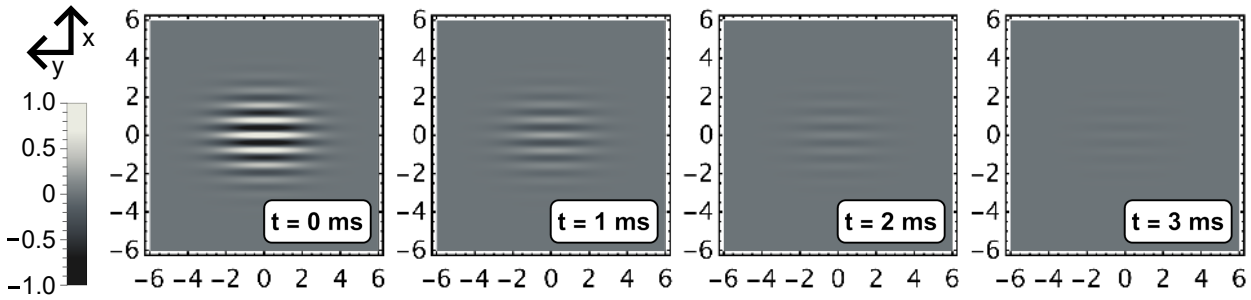

Figure D.6: Snapshots of the lattice amplitude in the xy plane given by the term proportional to ρ_{A} in Equation D.10 for an initial Gaussian population distribution. We used $\kappa = 8$ mm^{-1}, $D = 0.2$ cm^2/s as well as $a = 2.5$ mm and $b = 3$ mm. The horizontal and vertical axes in the snapshots shows lengths in mm and correspond to our $\hat{x}$ and $\hat{y}$ directions, respectively. The colour scale indicates the lattice amplitude with $\rho_{\mathrm{A}} = 1$ in arbitrary units.

D.4.2 Scattering of a Gaussian readout field from an expanding Gaussian Rb lattice

As in Section D.3, our observed signal will be proportional to the $\kappa\hat{x}$ Fourier component of the Rb population distribution. Unlike in Section D.3, however, only the portion of the Rb number distribution that is illuminated by the readout beam produces coherently scattered light. So, to find the time dependence of the scattered field, we take the product of $E_{\mathrm{RO}}(\vec{r})$ and $\rho_{\mathrm{G}}(\vec{r}, t)$ and then find its Fourier component at $\kappa\hat{x}$. The result is

$$E_{\mathrm{G}}(t) \propto \int \mathrm{d}^3 r \, \rho_{\mathrm{G}}(\vec{r}, t) E_{\mathrm{RO}}(\vec{r}) e^{-i\kappa x} \,, \tag{D.11}$$

which can be solved using

$$\int_{-\infty}^{\infty} \mathrm{d}x e^{-(x/s)^2 - ikx} = \sqrt{\pi} s e^{-s^2 k^2/4}$$

to obtain the scattered electric field as a function of time. It is given by

$$E_{\rm G}(t) \propto E_{\rm RO}(\vec{0})\rho_0\pi abLe^{-a^2\kappa^2/4} + E_{\rm RO}(\vec{0})\rho_{\rm A}\pi abL\frac{ab}{\sqrt{\mathcal{A}(t)\mathcal{B}(t)}}e^{-\kappa^2 Dta^2/A(t)} \quad \text{(D.12)}$$
$$\times e^{-a^2\kappa^2(1+a^4/A^2(t))A(t)/4\mathcal{A}(t)}\cosh\left(a^4\kappa^2/2\mathcal{A}(t)\right),$$

where areas $\mathcal{A}(t) = 3a^2 + 8Dt$, $\mathcal{B}(t) = 3b^2 + 8Dt$ and length L is the size of the glass cell along the $\hat{z}$ direction. The result in Equation D.12 represents a more accurate version of Equation 4.10. Here, a and b correspond to $W_{\rm x}$ and $W_{\rm y}$ in Chapter 4 respectively, and $\mathcal{A}(t)$ should not be confused with the diffusion area $\mathcal{A}(T)$ in Chapter 2. Also, $\mathcal{A}(t)$ and $\mathcal{B}(t)$ correspond to $3w_{\rm x}^{**}$ and $3w_{\rm y}^{**}$ in Chapter 4 respectively. The expressions given here and in Chapter 4are similar enough to produce the same transit time corrections.

For early times when $Dt \ll a^2$ and assuming that $a \sim b$, $a\kappa \gg 1$ to have several periods over beam radius a, and $\rho_0 \exp(-a^2\kappa^2/4)$ the time-independent background signal is $\ll \rho_{\rm A}/6$, so that

$$E_{\rm G}(t) \propto \frac{1}{6}\pi abLE_{\rm RO}(\vec{0})\rho_{\rm A}e^{-\kappa^2 Dt} \times \left(1 + c_1\frac{Dt}{a^2} + c_2\frac{D^2t^2}{a^4} + O(D^3t^3/a^6)\right) \quad \text{(D.13)}$$

with negative

$$c_1 = -\frac{4}{3}\left(1 + \frac{a^2}{b^2}\right) \quad \text{(D.14)}$$

and positive

$$c_2 = \frac{8}{3}(\kappa a)^2 + 2 + \frac{16}{9}\frac{a^2}{b^2} + 2\frac{a^4}{b^4} \quad \text{(D.15)}$$

resulting in a function that has the same short time dependence as in the plane-wave case *i.e.* $e^{-\kappa^2 Dt}$. Here, symbol O represents the big O notation. For typical values of a, b, κ, and D, the term proportional to $\rho_{\rm A}$ in Equation D.12 will be many orders of magnitude larger than that from ρ_0 and $a\kappa \gg 1$. This observation agrees with the intuition that the periodic

component of the density distribution will have a much greater impact than the constant offset component.

Figure D.7 shows the ratio of Equation D.12 and Equation D.5 obtained in the plane-wave case as a function of time, normalizing the electric fields to have the same value at $t = 0$. Figure D.7 also shows the ratio of the quadratic approximation in Equation D.13 to Equation D.5 in the plane-wave case. The approximation is in close agreement with the other curve for the timescales typical of the diffusion measurements. Formally, we are in the regime $a \sim b$, $Dt \ll a^2$ and $Dt \gg 1/\kappa^2$ for the largest time shown in Figure D.7 consistent with the requirements for the validity of Equation D.13.

Although the deviation from the plane-wave case is as high as 15% for the time scale shown, this amounts to a modest correction to the diffusion coefficient. Nevertheless, it is statistically significant in precise determinations of $D(T, p)$ [35].

D.5 Rectangular population distribution and readout with rectangular distribution

The Gaussian population envelope assumed in Section D.4 is not accurate for typical operating parameters due to saturation of optical pumping among the hyperfine states F, m_F of the electronic ground state of Rb at high excitation laser intensities. Typically, these lasers are tuned to the $5s$ to $5p$ electronic transition of the ^{85}Rb isotope. Simulations of optical pumping, following the procedures described in Chapter 2 based on [78] and shown in Figure D.8, demonstrate that most of the population is in hyperfine states with a grating envelope that has developed a top-hat shape. The width of this rectangle depends on the power of the excitation lasers as well as the pressure of the buffer gas.

We will now carry out calculations of transit-time corrections assuming an initial rectan-

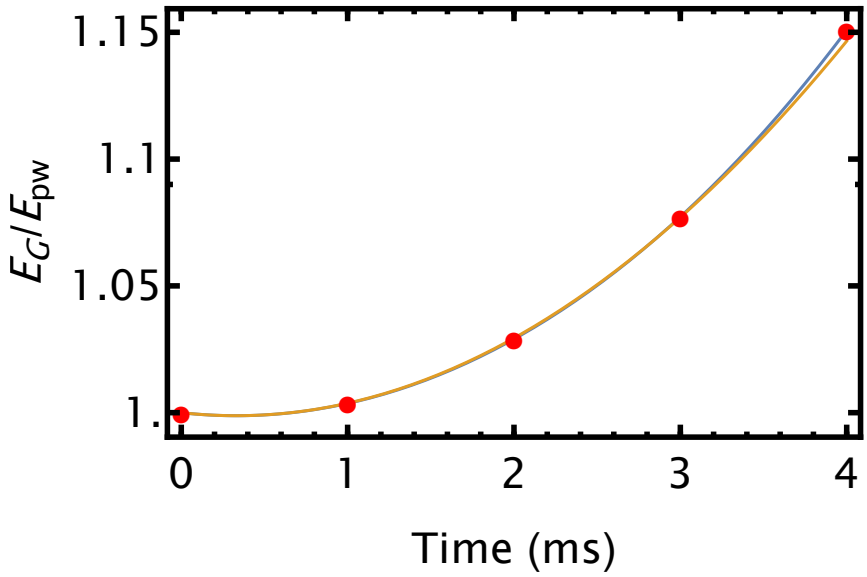

Figure D.7: Ratio of reflected electric fields from the plane-wave distribution E_{pw} and the Gaussian distribution with a Gaussian readout E_{G} as described by Equation D.12 as a function of time (blue). The quadratic approximation to this ratio, as shown in the parentheses of Equation D.13 (orange). All curves use the beam shape and diffusion parameters of Figure D.6. The electric fields have been normalized to have the same value at $t = 0$. The four left-most red points represent the times of the snapshots in Figures D.3 and D.6.

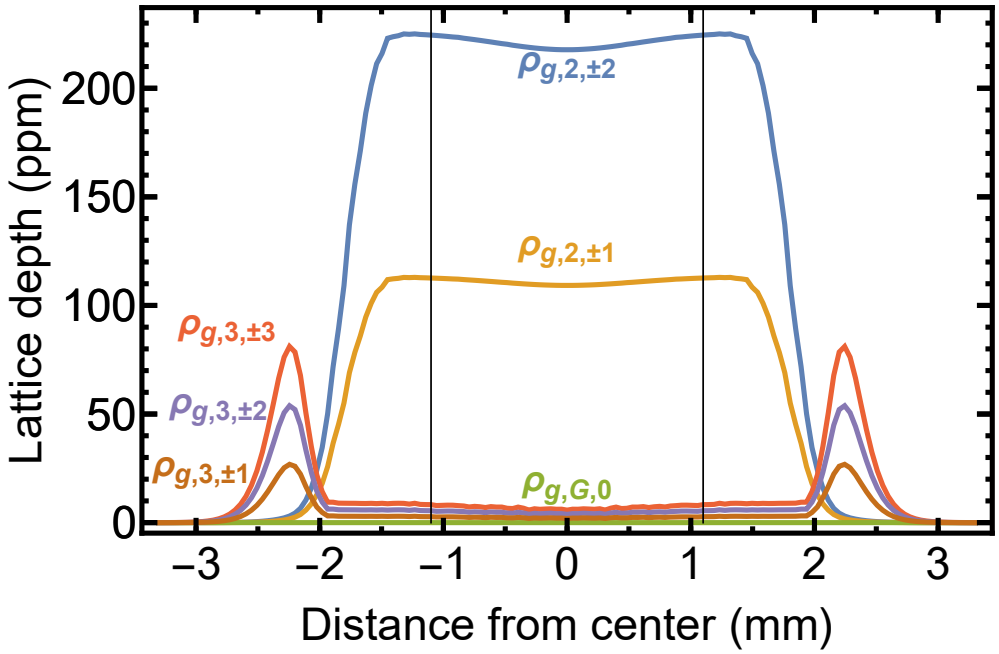

Figure D.8: Spatial dependence of the population for each F, m_F magnetic sublevel of the electronic ground state of ^{85}Rb along $\hat{x}$ with $y = z = 0$, *i.e.* the lattice depth or amplitude for each sublevel, obtained by rate equation simulations assuming Gaussian excitation pulses. The lattice depth is expressed in units of parts per million (ppm) of the total number of Rb atoms. The black vertical lines indicate the $1/e$ radius of 1.1 mm of the electric field of the excitation lasers. We have used typical pulse and buffer gas parameters used in our experiments (50µs pulse length, 70 mW total power, and 26,700 Pa of N_2 buffer gas).

gular lattice envelope with spatial dimensions α and β along the x and y axes, respectively. This is given by

$$\rho_{\text{rect}}(\vec{r},0) = \rho_0 + \begin{cases} \rho_{\text{A}}\cos(\kappa x) & \text{if } |x| \le \alpha/2 \;\&\; |y| \le \beta/2 \\ 0 & \text{otherwise} \end{cases}. \tag{D.16}$$

D.5.1 Time evolution of rectangular distribution

Using the same procedure as Section D.4, we first find $P_{\text{rect}}(\vec{q})$ from the Fourier transform of $\rho_{\text{rect}}(\vec{r},0)$ to be

$$\begin{aligned} P_{\text{rect}}(\vec{q}) =& (2\pi)^3\rho_0\delta(\vec{q}) \\ &+ \rho_{\text{A}}\alpha\beta\pi\left\{\text{sinc}\left(\frac{[q_x+\kappa]\alpha}{2}\right) + \text{sinc}\left(\frac{[q_x-\kappa]\alpha}{2}\right)\right\}\text{sinc}\left(\frac{q_y\beta}{2}\right)\delta(q_z). \end{aligned} \tag{D.17}$$

Here, $\text{sinc}(z) = \sin(z)/z$. We then proceed to derive the time-dependent $\rho_{\text{rect}}(\vec{r},t)$ and obtain

$$\begin{aligned} \rho_{\text{rect}}(\vec{r},t) \;=\; & \rho_0 + \frac{1}{4}\rho_{\text{A}}e^{-\kappa^2 Dt}\left(\text{erf}([y+\beta/2]/\sqrt{4Dt}) - \text{erf}([y-\beta/2]/\sqrt{4Dt})\right) \\ & \times \text{Re}\left\{e^{i\kappa x}\left[\text{erf}\left(\frac{x+\alpha/2}{\sqrt{4Dt}} + i\kappa\sqrt{Dt}\right) - \text{erf}\left(\frac{x-\alpha/2}{\sqrt{4Dt}} + i\kappa\sqrt{Dt}\right)\right]\right\}, \end{aligned} \tag{D.18}$$

where $\text{erf}(z)$ is the error function with $\text{erf}(-z) = -\text{erf}(z)$ and $\text{erf}(x) \to \pm(1 - e^{-x^2}/\sqrt{\pi}x)$ for real $x \to \pm\infty$, respectively, based on Chapter 7 of reference [134] and we used reference [135] to perform the integrals. Equation D.18 is even in both x and y.

The predictions of Equation D.18 are visualized in Figure D.9. We again observe that the amplitude of the sinusoidal pattern decays over time with limited expansion in the x and y directions.

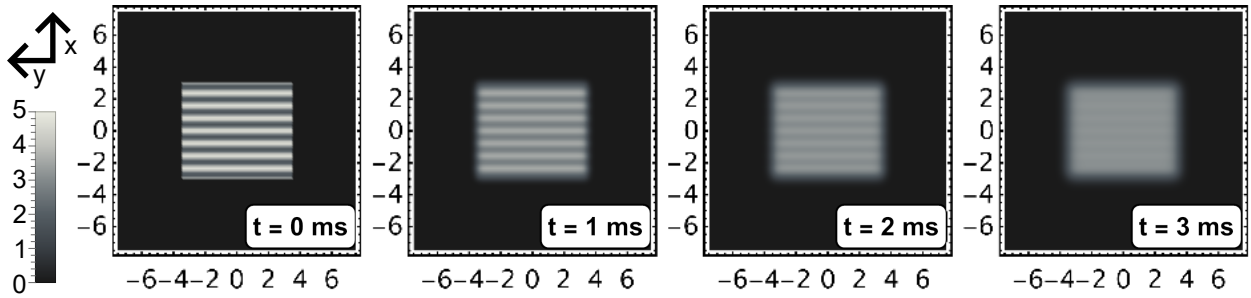

Figure D.9: Snapshots of the Rb lattice amplitude in the xy plane for an initial rectangular population distribution at times $t = 0$ ms, 1 ms, 2 ms, 3 ms. The lattice wavenumber is 8 mm^{-1}, $\alpha = 6$ mm, $\beta = 7$ mm, and the diffusion coefficient is 0.2 cm^2/s. Lengths are in units of mm and the colour scale indicates the population in arbitrary units.

D.5.2 Scattering of a rectangular readout field from an expanding rectangular Rb lattice

The spatial profile of a rectangular readout beam with dimensions α and β along $\hat{x}$ and $\hat{y}$, respectively, is given by

$$E_{\mathrm{RO}}(\vec{r}) = E_{\mathrm{RO}}(\vec{0}) \tag{D.19}$$

when $|x| \leq \alpha/2$ and $|y| \leq \beta/2$ and zero otherwise. This expression replaces the E_{RO} defined in Equation D.6 for the Gaussian case. We can then obtain the scattered field using the "rectangular" version of Equation D.11. This results in

$$\begin{aligned} E_{\mathrm{rect}}(t) \propto\ & \alpha\beta L E_{\mathrm{RO}}(\vec{0})\rho_0 \,\mathrm{sinc}(\kappa\alpha) \\ & + \frac{1}{2}\alpha\beta L E_{\mathrm{RO}}(\vec{0})\rho_{\mathrm{A}} e^{-\kappa^2 Dt}\left[\mathrm{erf}(\beta/\sqrt{4Dt}) - \frac{\sqrt{4Dt}}{\beta\sqrt{\pi}}\left(1 - e^{-\beta^2/4Dt}\right)\right] \\ & \times \left[-\frac{2}{\sqrt{\pi}} e^{\kappa^2 Dt}\left(1 - e^{-\alpha^2/(4Dt)}\cos(\kappa\alpha)\right)\sqrt{\frac{Dt}{\alpha^2}} - \left(\frac{\cos(\kappa\alpha)}{\kappa\alpha} - 2\kappa\alpha\frac{Dt}{\alpha^2}\right)\mathrm{erfi}(\kappa\sqrt{Dt})\right. \\ & \left. + \mathrm{Re}\left\{\left(1 + 2i\kappa\alpha\frac{Dt}{\alpha^2} - i\frac{e^{i\kappa\alpha}}{\kappa\alpha}\right)\mathrm{erf}\left(\frac{\alpha}{\sqrt{4Dt}} + i\kappa\sqrt{Dt}\right)\right\}\right], \end{aligned} \tag{D.20}$$

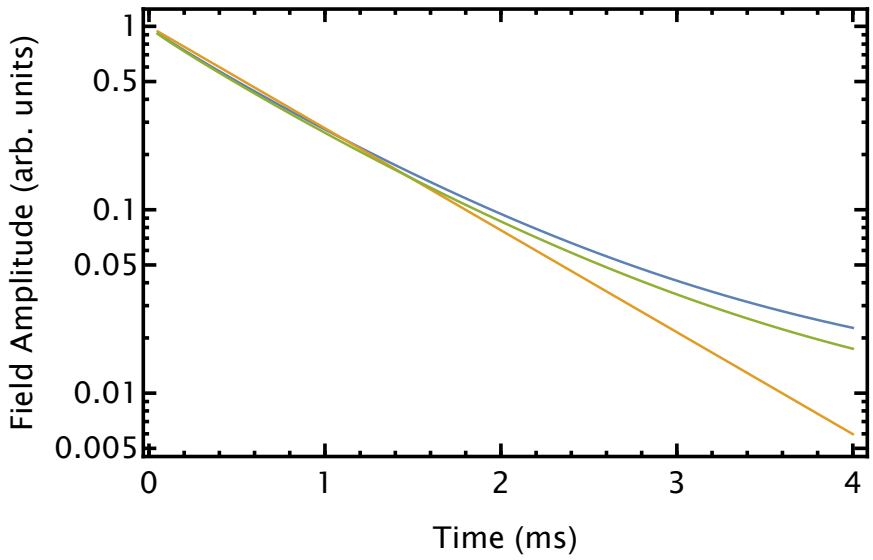

Figure D.10: Comparison of the scattered electric field as described by Equation D.12 (green), Equation 4.7 (blue) and the plane-wave solution Equation D.5 (orange). Curves are shown with a Log vertical scale.

where the imaginary error function $\mathrm{erfi}(z) = \mathrm{erf}(iz)/i$, which is real-valued for real arguments. The result in Equation D.20 amounts to a slight difference from Equation 4.7, as shown in Figure D.10. The parameters α and β in Equation D.20 correspond to w_x and w_y in Chapter 4. Here, we show the decay curves predicted by Equation D.20, Equation 4.7 and Equation D.5 on a log scale. However, the discernible differences between the predictions of Equation D.20 and Equation 4.7 result in corrected diffusion values that agree within the error bars quoted in Chapter 4.

We see that for early times with $Dt \ll \alpha^2$ and $Dt \ll \beta^2$, Equation D.20 with a negligible contribution from the term proportional to ρ_0 leads to

$$E_{\mathrm{rect}}(t) \propto \frac{1}{2}\alpha\beta L E_{\mathrm{RO}}(\vec{0})\rho_{\mathrm{A}} e^{-\kappa^2 Dt}\left(1 - \frac{2}{\sqrt{\pi}}\sqrt{\frac{Dt}{\beta^2}}\right) \times \left[d_0 + d_1\sqrt{\frac{Dt}{\alpha^2}} + d_3\left(\frac{Dt}{\alpha^2}\right)^{3/2} + d_5\left(\frac{Dt}{\alpha^2}\right)^{5/2} + O\left(\left(\frac{Dt}{\alpha^2}\right)^3\right)\right] \quad \text{(D.21)}$$

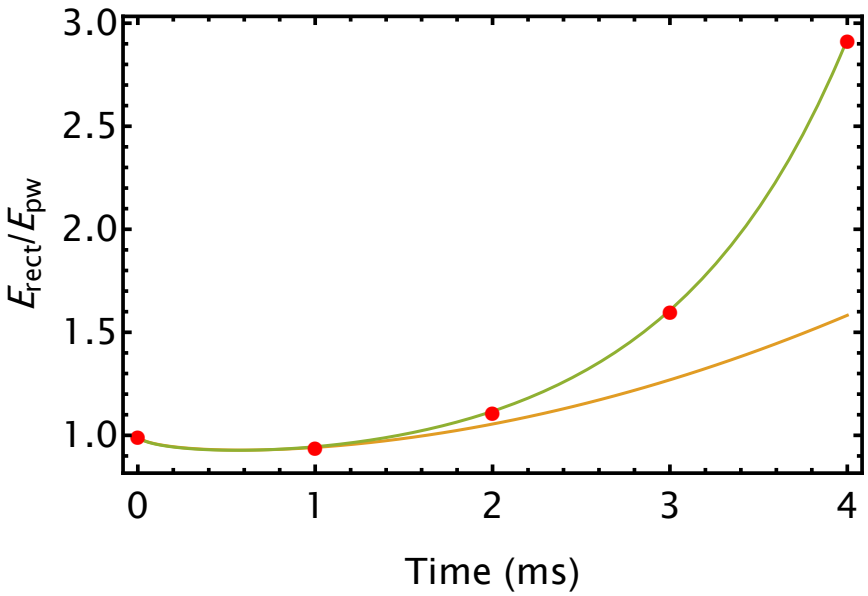

Figure D.11: Ratio of scattered electric fields from the rectangular distribution with a rectangular readout profile, E_{R}, and the plane-wave distribution, E_{pw}, as a function of time (green). Ratio of the non-analytic approximation in Equation D.21 and the plane-wave distribution, E_{pw} (orange). The electric fields have been normalized to have the same value at $t = 0$ and system parameters are those used in Figure D.9.

with

$$d_0 = 1 + \frac{\sin(\kappa\alpha)}{\kappa\alpha}\,, \tag{D.22}$$

$$d_1 = -\frac{2}{\sqrt{\pi}}\left(1 + \cos(\kappa\alpha)\right)\,, \tag{D.23}$$

$$d_3 = \frac{2}{\sqrt{\pi}}(\kappa\alpha)^2\left(1 - \frac{1}{3}\cos(\kappa\alpha)\right)\,, \tag{D.24}$$

and

$$d_5 = \frac{1}{3\sqrt{\pi}}(\kappa\alpha)^4\left(1 - \frac{3}{5}\cos(\kappa\alpha)\right)\,. \tag{D.25}$$

Hence, the early time behaviour of $E_{\mathrm{rect}}(t)$ is nonanalytic in time, which, as we will show next, leads to significant deviations from the ideal exponential behaviour observed for models assuming the plane-wave and Gaussian laser beam profiles.

In Figure D.11 we show the ratio of Equation D.20 and Equation D.5 in green and the

ratio of the non-analytic approximation shown in Equation D.21 and Equation D.5 in orange over the same time interval as for the Gaussian model of transit time corrections. We see that the rectangular model described by Equation D.20 leads to a deviation from the plane-wave case that reaches nearly 300 % at the largest timescale. This contrasts with the Gaussian case shown in Figure D.7 with similar system parameters. The Gaussian model predicts a ratio close to one over the same time interval. The impact of these differences can be seen in Table 4.1. Since the approximation given by Equation D.21 is significantly different from the predictions of Equation D.20, we do not use it further.

We note that the rectangular model contributes to a larger correction to the diffusion values than the Gaussian model. We now discuss the implications of this larger correction. In reference [35], we use the weighted averages of the corrections predicted by the Gaussian and the rectangular models. We reported an error bar that was computed as the quadrature sum of (i) the error in the rectangular model, (ii) the error in the Gaussian model, and (iii) half the difference between the corrected values given by these two models. Therefore, the rectangular model produces a larger transit-time correction and, as a result, reduces the accuracy of the corrected diffusion coefficients. Nevertheless, the corrections predicted by Equation 4.7 and Equation D.20 are the same within error, as discussed in the context of Figure D.10.

D.6 Conclusions

We have outlined the effects of transit-time corrections on measurements of diffusion coefficients of trace amounts of Rb vapour in inert gases. Although we have presented improved models for the Gaussian and rectangular cases, these improvements do not significantly impact the corrections to diffusion coefficients based on the calculations presented in Chapter 4. These models will support future experimental work to reduce the impact of transit time

effects. As described in references [33, 35], measurements of these diffusion coefficients can be used to realize a quantum pressure sensor for the calibration of pressure gauges if the accuracy of these determinations can reach the level of 0.5%. Transit time corrections are also of interest to a wider class of diffusion experiments that rely on optical pumping [5, 11, 73, 76, 91].

Appendix E

List of publications

E.1 First author publications

- A. Pouliot, G. Carlse, E. Chomen Ramos, T. Vacheresse, J. Randhawa, A. Kumarakrishnan, J. Kłos, and E. Tiesinga, "Transit time corrections to the diffusion of atomic lattices," JOSA B (2025), submitted.

- A. Pouliot, E. Chomen Ramos, G. Carlse, T. Vacheresse, J. Randhawa, L. Marmet, A. Kumarakrishnan, J. Kłos, and E. Tiesinga, "Measurements of diffusion coefficients for rubidium–inert-gas mixtures using coherent scattering from optically pumped population gratings," Phys. Rev. A **111**, 033108 (2025).

- A. Pouliot, G. Carlse, H. C. Beica, T. Vacheresse, A. Kumarakrishnan, U. Shim, S. B. Cahn, A. Turlapov, and T. Sleator, "Erratum: Accurate determination of an alkali-vapor–inert-gas diffusion coefficient using coherent transient emission from a density grating [Phys. Rev. A 103, 023112 (2021)]," Phys. Rev. A **111**, 039903 (2025).

- A. Pouliot, G. Carlse, T. Vacheresse, and A. Kumarakrishnan, "Accurate determination of an alkali-vapor-inert-gas diffusion coefficient using coherent transient emission from

a density grating," in *Optical and Quantum Sensing and Precision Metrology II*, Vol. 12016 (SPIE, 2022) pp. 162–166.

- A. Pouliot, G. Carlse, H. C. Beica, T. Vacheresse, A. Kumarakrishnan, U. Shim, S. B. Cahn, A. Turlapov, and T. Sleator, "Accurate determination of an alkali-vapor–inert-gas diffusion coefficient using coherent transient emission from a density grating," Phys. Rev. A **103**, 023112 (2021), corrected in [34]

- A. Pouliot, H. C. Beica, A. Carew, A. Vorozcovs, G. Carlse, B. Barrett, and A. Kumarakr- ishnan, "Investigations of optical pumping for magnetometry using an auto-locking laser system," in *Laser Technology for Defense and Security XIV* , Vol. 10637, edited by M. Dubinskiy and T. C. Newell, International Society for Optics and Photonics (SPIE, 2018) pp. 40–47

- A. Pouliot, H. C. Beica, A. Carew, A. Vorozcovs, G. Carlse, and A. Kumarakrishnan, "Auto-locking waveguide amplifier system for lidar and magnetometric applications," in *High-Power Diode Laser Technology XVI* , Vol. 10514, edited by M. S. Zediker, International Society for Optics and Photonics (SPIE, 2018) pp. 152 – 159.

E.2 First-author publications in preparation

- A. Pouliot, B. Barron, G. Carlse, T. Vacheresse, E. Chomen Ramos, J. Randhawa, and A. Kumarakrishnan, "Efficient algorithms for calculations of the Allan deviation," American Journal of Physics (2025), in preparation

- A. Pouliot, E. Chomen Ramos, G. Carlse, T. Vacheresse, J. Randhawa, and A. Kumarakrishnan, "Collisional broadening and shift parameters for the Rb D2 line," Atoms (2025), in preparation.

E.3 Co-authored publications

- J. Randhawa, G. Carlse, M. Llaguno, J. Cuzzupoli, E. Ramos, T. Vacheresse, A. Pouliot, and A. Kumarakrishnan, "Laser system for frequency domain velocimetry and atom interferometry experiments," Review of Scientific Instruments (2025), submitted.

- G. Carlse, J. Randhawa, A. Pouliot, E. Ramos, T. Vacheresse, and A. Kumarakrishnan, "Measurement of gravitational acceleration using an echo atom interferometer," Physical Review A (2025), submitted.

- G. Carlse, J. Randhawa, E. Ramos, T. Vacheresse, A. Pouliot, and A. Kumarakrishnan, "Velocimetry using free-induction decay of matter-wave lattices," Phys. Rev. A **111**, L021304 (2025).

- G. Carlse, J. Randhawa, E. Ramos, T. Vacheresse, A. Pouliot, and A. Kumarakrishnan, "Contrast enhancement of echo atom interferometers using optical channeling and optimization of near resonant Bragg scattering," in *Optical Sensing and Precision Metrology*, Vol. 13380 (SPIE, 2025) p. 1338002.

- G. Carlse, J. Randhawa, A. Pouliot, T. Vacheresse, E. Ramos, and A. Kumarakrishnan, "Techniques for sensitive measurements of gravitational acceleration using single state echo atom interferometers," in *Quantum Sensing, Imaging, and Precision Metrology III*, Vol. 13392 (SPIE, 2025) pp. 19–24.

- G. Carlse, J. Randhawa, E. Ramos, T. Vacheresse, A. Pouliot, A. C. Carew, A. Kumarakrishnan, and B. Barrett, "Optimization of Bragg scattering from atomic gratings for echo interferometry," Phys. Rev. A **110**, 043306 (2024).

- G. Carlse, J. Randhawa, E. Ramos, T. Vacheresse, A. Pouliot, A. C. Carew, and A. Kumarakrishnan, "Role of optical channeling in contrast enhancement of echo

interferometers," Phys. Rev. A **109**, 043307 (2024)

- G. Carlse, J. Randhawa, A. Pouliot, T. Vacheresse, E. Ramos, A. Carew, and A. Kumarakrishnan, "Improving the sensitivity grating-echo atom interferometers for measurements of gravity," in *Quantum Sensing, Imaging, and Precision Metrology II*, Vol. 12912 (SPIE, 2024) pp. 152–156

- G. Carlse, K. Borsos, T. Vacheresse, A. Pouliot, E. Ramos, J. Randhawa, C. Walsh, and A. Kumarakrishnan, "Time domain metrology with optical tweezers," in *Quantum Sensing, Imaging, and Precision Metrology*, Vol. 12447 (SPIE, 2023) pp. 80–86.

- H. C. Beica, S. Winter, C. Mok, B. Barrett, R. Berthiaume, A. Vorozcovs, F. Yachoua, N. Afkhami-Jeddi, M. Aggarwal, G. Carlse, A. Pouliot, K. B. Borsos, T. Vacheresse, R. Marants, and A. Kumarakrishnan, "Laboratory courses on laser spectroscopy and atom trapping," Atoms **8** (2020)

- G. Carlse, K. B. Borsos, H. C. Beica, T. Vacheresse, A. Pouliot, J. Perez-Garcia, A. Vorozcovs, B. Barron, S. Jackson, L. Marmet, et al., "Technique for rapid mass determination of airborne microparticles based on release and recapture from an optical dipole force trap," Physical Review Applied **14**, 024017 (2020).

- G. Carlse, A. Pouliot, T. Vacheresse, A. Carew, H. C. Beica, S. Winter, and A. Kumarakrishnan, "Technique for magnetic moment reconstruction of laser-cooled atoms using direct imaging and prospects for measuring magnetic sublevel distributions," J. Opt. Soc. Am. B **37**, 1419 (2020).

- H. C. Beica, A. Pouliot, P. Dowling, A. Carew, T. Vacheresse, G. Carlse, L. Marmet, and A. Kumarakrishnan, "Development of a technique for the precise determination of atomic lifetimes based on photon echoes," Phys. Rev. A **101**, 033408 (2020).

- H. C. Beica, A. Pouliot, A. Carew, A. Vorozcovs, N. Afkhami-Jeddi, T. Vacheresse, G. Carlse, P. Dowling, B. Barron, and A. Kumarakrishnan, "Characterization and applications of auto-locked vacuum-sealed diode lasers for precision metrology," Rev. Sci. Inst. **90**, 085113 (2019).

- H. Beica, A. Carew, A. Vorozcovs, P. Dowling, A. Pouliot, B. Barron, and A. Kumarakrishnan, "An auto-locked diode laser system for precision metrology," in *Laser Radar Technology and Applications XXII*, Vol. 10191 (SPIE, 2017) pp. 143–148.

- H. Beica, A. Carew, A. Vorozcovs, P. Dowling, A. Pouliot, B. Barron, and A. Kumarakrishnan, "An auto-locked diode laser system for precision metrology," in *Laser Radar Technology and Applications XXII*, Vol. 10191 (SPIE, 2017) pp. 143–148.

- B. Barrett, A. Carew, H. C. Beica, A. Vorozcovs, A. Pouliot, and A. Kumarakrishnan, "Prospects for precise measurements with echo atom interferometry," Atoms **4**, 19 (2016)

Appendix F

List of presentations

- A. Pouliot, E. Chomen Ramos, G. Carlse, T. Vacheresse, J. Randhawa, L. Marmet, A. Kumarakrishnan, J. Kłos and E. Tiesinga, “Diffusion coefficients of Rb-inert gas mixtures using coherent scattering from optically pumped population gratings”, DAMOP 2025, Portland OR USA, June 2025 (Oral)
- A. Pouliot, G. Carlse, T. Vacheresse, E. Ramos, J. Randhawa, and A. Kumarakrishnan, “Measurements of Rb-Inert Gas Diffusion Coefficients Using Coherent Emission from Optical Lattices", ICOLS 2023, Estes Park CO USA, June 2023 (Poster)
- A. Pouliot, G. Carlse, T. Vacheresse, H. C. Beica, and A. Kumarakrishnan, “Determination of alkali-vapour–inert-gas diffusion coefficients using coherent transient emission from a density grating", DAMOP 2022, Orlando FL USA, May 2022. (Oral)
- A. Pouliot, H. C. Beica, A. Carew, A. Vorozcovs, N. Afkhami-Jeddi, T. Vacheresse, G. Carlse, P. Dowling, B. Barron, and A. Kumarakrishnan, “Characterization and Applications of Auto-locked Vacuum Sealed Diode Lasers for Precision Metrology", DAMOP 2022, Orlando FL USA, May 2022 (Poster)
- A. Pouliot, H. C. Beica, G. M.I. Carlse, S. Winter, C. Mok, B. Barrett, R.t Berthiaume,

A. Vorozcovs, F. Yachoua, N. Afkhami-Jeddi, M. Aggarwal, K. B. Borsos, T. M. Vacheresse, R. Marants, and A. Kumarakrishnan, “An Effective Approach for Teaching Laboratory Courses on Laser Spectroscopy and Atom Trapping", DAMOP 2022, Orlando FL USA, May 2022 (Poster)

- A. Pouliot, G. Carlse, H.C. Beica, T. Vacheresse, and A. Kumarakrishnan, “Comparative Investigations of Magnetometers based on Atomic Populations and Coherences ", Rochester Conference on Coherence and Quantum Optics XI, Rochester NY USA, August 2019 (Poster)

- A. Pouliot, H. C. Beica, A. Carew, A. Vorozcovs, G. Carlse, B. Barrett, and A. Kumarakrishnan, “Auto-locking diode laser system for lidar and magnetometric applications," SPIE DCS Defense + Security, Orlando FL USA, April 2018 (Oral)

- A. Pouliot, H. C. Beica, A. Carew, A. Vorozcovs, G. Carlse, and A. Kumarakrishnan, “Auto-locking Waveguide Amplifier system for lidar and magnetometric applications," SPIE Photonics West (LASE), San Francisco CA USA, February 2018 (Oral)